Systems Biology of Chemotherapy in Hypoxia Environments

A THESIS
SUBMITTED TO THE UNIVERSITY OF MANCHESTER
FOR THE DEGREE OF
DOCTOR OF PHILOSOPHY (PHD)
IN THE FACULTY OF ENGINEERING AND PHYSICAL SCIENCES

2012

Helen Laura Kotze

School of Chemical Engineering and Analytical Science

Contents

List of figures

List of tables

List of equations

The University of Manchester
Faculty of Engineering and Physical Sciences

ABSTRACT OF THESIS submitted by Helen Laura Kotze
For the degree of Doctor of Philosophy
and entitled Systems biology of chemotherapy in hypoxia environments
Date of submission September 2012

Introduction: Hypoxia is found in solid cancerous tumours. The presence of hypoxia within tumours inhibits anti-cancer treatment strategies such as chemotherapy from being completely effective and it is suspected that multiple mechanisms contribute to the resistance.

Methods: In this project a systems biology approach was applied to determine how the toxicity of doxorubicin is affected by hypoxia at the metabolome level. A multitude of analytical techniques were applied to analyse the intracellular metabolism of a monolayer of cancer cells (MDA-MB-231). Metabolic profiling was used to determine metabolite markers related to hypoxia-induced chemoresistance. For this gas chromatography mass spectrometry (GC-MS) and ultra high performance liquid chromatography mass spectrometry (UHPLC-MS) were used. Furthermore, network-based correlation analysis was developed as a novel tool to bridge the gap between metabolomics dataset and systems biology modelling. This methodology was applied to elucidate novel metabolic pathways as potential therapeutic targets to overcome hypoxia-induced chemoresistance. This algorithm determines significant correlation differences between different physiological states, and through applying graph-theory on large genome scale models; it is possible to construct a metabolic network of the pathways connecting the pair-wise correlation. Finally, imaging mass spectrometry using time-of-flight secondary ion mass spectrometry (ToF-SIMS) was developed as a tool for *in situ* metabolite analysis to investigate the metabolic response to chemotherapy in multi-tumour spheroids (MTSs).

Results: Metabolic fingerprinting analysis characterised a snapshot of cells exposed to various environmental perturbations. Metabolite markers associated with hypoxia-induced chemoresistance were related to metabolic pathways including gluconeogenesis, DNA synthesis and fatty acid synthesis. Furthermore, network-based correlation analysis revealed specific metabolites in the fatty acid synthesis pathways were contributing to drug resistance, which included malonyl-CoA, 3-oxoeicosanoyl-CoA, stearoyl-CoA and octadecanoic acid. To facilitate the detection of metabolites in ToF-SIMS datasets, a series of metabolites standard spectra were acquired. Hypoxic metabolite markers detected in ToF-SIMS data of cell lysates included glycine, lactic acid and succinic acid, which were also shown to be metabolite markers in GC-MS metabolic data. Furthermore, MTS sections were imaged using ToF-SIMS to profile the chemical response to chemotherapy treatment within the oxygen gradient. Loadings from image PCA were explored to determine the metabolic response in the highly oxygenated outer region and hypoxic inner region of the MTS.

Conclusion: A multitude of analytical techniques were able to contribute to elucidating the metabolic mechanisms associated with hypoxia-induced chemoresistance. Metabolic profiling combined with a systems biology approach was further able to identify potential underlying metabolic regulation of resistance. Finally ToF-SIMS was developed as a tool for metabolite analysis in complex biological systems *in situ*.

Declaration

No portion of the work referred to in this thesis has been submitted in support of an application for another degree or qualification of this or any other university or other institute of learning.

Copyright Statement

i. The author of this thesis (including any appendices and/or schedules to this thesis) owns certain copyright or related rights in it (the "Copyright") and s/he has given The University of Manchester certain rights to use such Copyright, including for administrative purposes.

ii. Copies of this thesis, either in full or in extracts and whether in hard or electronic copy, may be made **only** in accordance with the Copyright, Designs and Patents Act 1988 (as amended) and regulations issued under it or, where appropriate, in accordance with licensing agreements which the University has from time to time. This page must form part of any such copies made.

iii. The ownership of certain Copyright, patents, designs, trademarks and other intellectual property (the "Intellectual Property") and any reproductions of copyright works in the thesis, for example graphs and tables ("Reproductions"), which may be described in this thesis, may not be owned by the author and may be owned by third parties. Such Intellectual Property and Reproductions cannot and must not be made available for use without the prior written permission of the owner(s) of the relevant Intellectual Property and/or Reproductions.

iv. Further information on the conditions under which disclosure, publication and commercialisation of this thesis, the Copyright and any Intellectual Property and/or Reproductions described in it may take place is available in the University IP Policy (see http://www.campus.manchester.ac.uk/medialibrary/policies/intellectual-property.pdf), in any relevant Thesis restriction declarations deposited in the University Library, The University Library's regulations (see http://www.manchester.ac.uk/library/aboutus/regulations) and in The University's policy on presentation of Theses.

Acknowledgements

Firstly, I would like to thank my supervisor Dr Nick Lockyer for his support of my research particularly in the area of ToF-SIMS. Secondly, I would like to thank my co-supervisors Prof. Hans Westerhoff, Prof. Roy Goodacre and Prof. Kaye Williams for their support in the areas of systems biology, metabolomics and cancer research respectively. Thirdly, I would like to thank key individuals for their support including Dr Adam McMahon, Dr John Fletcher (advice on ToF-SIMS), Prof. John Vickerman (advice on ToF-SIMS), Dr Alex Henderson (advice on data processing), Dr Graham Mullard and Dr Warwick Dunn for acquisition of UHPLC-MS data including processing of raw data and Dr William Allwood for the processing of raw GC-MS data. Additionally, I would like to acknowledge the collaboration with fellow PhD student Emily Armitage to develop methods including the preparation of multi-tumour spheroids, engineering of the hypoxybox and correlation network analysis. Dr John Fletcher, Emily Armitage and I have also worked closely together to develop a ToF-SIMS standards library of metabolites and my contribution is presented in this thesis. Finally, I would like to thank the doctoral training centre for systems biology and the BBSRC/EPSRC for funding this research.

Abbreviations

Analog to digital convertor	ADC
Adenosine triphosphate	ATP
Analysis of variance	ANOVA
Anoxia	A
Bis-N-oxide banoxantrone	AQ4N
Carbonic anhydrase IX	CAIX
Cholesterol ester	CE
Coefficient of variation	CV
Coenzyme A	CoA
Collision-induced dissociation	CID
Diacylglycerol	DAG
Deoxyribonucleic acid	DNA
Dimethyl sulphoxide	DMSO
Discriminant function analysis	DFA
Doubling time	DT
Edinburgh human metabolic network	EHMN
Electron ionisation	EI
Electrospray ionisation	ESI
Electrospray negative	ES-
Electrospray positive	ES+
False discovery rate	FDR
Fatty acid	FA
Foetal calf serum	FCS
Forward scatter	FSC
Fourier transform infra-red	FT-IR
Gas Chromatography-mass spectrometry	GC-MS
Glycerophosphoethanolamine	PE
Hexokinase	HK
Hypoxia	H
Hypoxia-inducible factors	HIFs
Human Metabolome Database	HMDB
Kyoto encyclopaedia of genes and genomes	KEGG
Lactate dehydrogenase	LDH
Limits of detection	LOD
liquid chromatography electrospray tandem mass spectrometry	LC-ESI-MS^2
Matrix assisted laser desorption ionisation	MALDI
Mass-to-charge	*m/z*
Matrix laboratory	MATLAB
Manchester Metabolomics Database	MMD
Mass spectrometry	MS
Monocarboxylate transporter 1	MCT 1
Monocarboxylate transporter 4	MCT 4
Multicellular tumour spheroids	MTS
Multivariate analysis	MVA
3-(4,5-Dimethylthiazol-2-yl)-2,5-diphenyltetrazolium bromide	MTT
Multidrug resistance 1	Mdr-1
Nicotinamide adenine dinucleotide	NAD^+
Nicotinamide adenine dinucleotide phosphate	NAD(P)
Normoxia	N
Not a number	NaN
Nucleotide-binding domain	NBD
Nuclear magnetic resonance	NMR
Passive lysis buffer	PLB
Phosphate buffered saline	PBS
Phosphoenolpyruvate	PEP
Phosphoenolpyruvate carboxykinase	PEPCK
Principal component	PC
Principal component analysis	PCA
P-glycoprotein	Pgp

Reactive oxygen species	ROS
Secondary ion mass spectrometry	SIMS
Side scatter	SSC
Signal-to-noise	S/N
Sphingomyelin	SM
Standard error	SE
Systems Biology Mark-up Language	SBML
Time-of-flight	ToF
Tirapazamine	TPZ
Total explained variance	TEV
Total ion current	TIC
Tricarboxylic acid cycle	TCA cycle
Trimethylsilylation	TMS
Ultra high performance liquid chromatography-mass spectrometry	UHPLC-MS

The Author

I obtained MChem (Hons.) Chemistry with Nanotechnology (2008) from The University of Hull. During my degree I had an industrial placement at Reckitt Benckiser (Hull) from 2006-2007 as an analytical chemist. I am an active member of The Royal Society of Chemistry, The British Association for Cancer Research and The Biochemical Society.

Publications in peer reviewed journals

H.L. Kotze, E.G. Armitage, J.S. Fletcher, A. Henderson, K.J. Williams, N.P. Lockyer, J.C. Vickerman (2012) ToF-SIMS as a tool for metabolic profiling small biomolecules in cancer systems. *Surface Interface Analysis* (available online).

E.G. Armitage, **H.L. Kotze**, J.S. Fletcher, A. Henderson, K.J. Williams, N.P. Lockyer, J.C. Vickerman (2012) ToF-SIMS as a novel approach to unlocking the hypoxic properties of cancer. *Surface Interface Analysis* (available online).

E.G. Armitage*, **H.L. Kotze***, N.P. Lockyer (2012) Imaging of metabolites using Secondary Ion Mass Spectrometry. *Metabolomics* (available online) *Authors contributed equally.

J.S. Fletcher[*], **H.L. Kotze**[*], E.G. Armitage*, N.P. Lockyer, J.C. Vickerman (2012) Evaluating the challenges associated with Time-of-Fight Secondary Ion Mass Spectrometry for metabolomics using pure and mixed Metabolites. *Metabolomics* (accepted) *Authors contributed equally.

H.L. Kotze, E.G. Armitage, K.J. Sharkey, J.W. Allwood, W.B. Dunn, K.J.Williams and R. Goodacre (2012) Network-based correlation analysis: a new systems biology approach to analysing metabolic profiling data. *BMC Systems Biology* (In preparation).

H.L. Kotze, E.G. Armitage, J.W. Allwood, R. Goodacre, and K.J. Williams (2013) Network-based correlation analysis of metabolic profiling data reveals pathway targets to overcome hypoxia-induced chemoresistance in cancer cells. *Molecular BioSystems* (In preparation).

E.G. Armitage, **H.L. Kotze**, J.W. Allwood, G. Mullard, W.B. Dunn, R. Goodacre, and K.J. Williams (2013) Metabolic profiling reveals potential metabolic markers associated with the role of HIF-1 in hypoxic cancer cells. *Metabolomics* (In preparation).

Furthermore, I have been approached by Springer (New York) with a proposal to write a Springer brief book covering correlation and network based modelling expected to be published in 2013.

Awards

Hopkins scholarship at the University of Hull for academic achievement (2005); Bursary to attend the International Course on Systems Biology of Metabolism, Sweden (2010); Bursary to attend Association for Radiation Research conference in Nottingham, UK (2011); Bursary to attend Metabolomics 2012 in Washington, USA (2012).

Presentations at conferences

Oral presentations

18th International conference on Secondary Ion Mass Spectrometry, September 2011, Riva del Garda, Italy; International Course on Systems Biology of Metabolism, May - June 2010, Gothenburg, Sweden

Poster presentations

13th International conference on Systems Biology, August 2012, Toronto, Canada; 12th International conference on Systems Biology, August-September 2011, Heidelberg/Mannheim, Germany; Association for Radiation Research/UK Environmental Mutagen Society joint meeting, June - July 2011, Nottingham, UK; Cancer and Metabolism: Pathways to the Future, September 2011, Edinburgh, UK; British Association for Cancer Research 50th anniversary meeting: Hallmarks of cancer- from mechanisms to therapies, June 2010, Edinburgh, UK**;** Metabolomics and More, March 2010, Freising-Weihenstephan, Germany; FEBS-SysBio2009: The 3rd FEBS Advanced Lecture Course on Systems Biology: From Molecular Biology to Biological Function, March 2009, Alpbach, Austria

Chapter 1

LITERATURE REVIEW

1.1 Introduction to cancer metabolism

In oncology, it is widely known that the metabolism of cancer cells differs from normal cells[1]. Leading this field was Otto Warburg who was awarded the Nobel Prize for his work in 1931[2]. Warburg reported that cancer cells prefer to undergo non-oxidative phosphorylation to facilitate rapid proliferation and maintain cellular bioenergetics. This is known as the Warburg effect and has been exploited for diagnostic purposes. For example, imaging the radioactive [^{18}F] glucose tracer uptake into glycolytic malignant cancer cells with positron emission tomography is used in cancer diagnosis[3]. With the advances in the area of genetics, much interest in oncology began focusing on the genetic origins of cancer[4]. More recently, cancer metabolism has become a renewed focal point of research[5].

1.2 The biology of tumour hypoxia

"Tumour" is a term used to describe an abnormal growth of neoplastic cells caused by genetic mutations; however only malignant tumours are considered as cancerous[6]. Genetic mutations can suppress or promote a gene to encourage a cancer cell's survival. Oncogenes are genes that promote cell growth and reproduction, whereas tumour suppressor genes cause a loss or reduction of gene function. Such genetic mutations enable cancerous tumours to promote survival mechanisms including angiogenesis, rapid proliferation and malignancy. Tumour hypoxia originates in tumour cells situated in poorly oxygenated environments. Tumour hypoxia is frequently found in solid tumours and occurs when the tumour outgrows its blood supply due to rapid proliferation. Rapidly proliferating tumours fail to form adequate blood vessels[6]. This causes part of the tumour have a poor blood supply and the cells become deprived of nutrients and oxygen. Cells located close to the blood vessels have an adequate supply of oxygen and nutrients and are labelled normoxic cells, which proliferate rapidly. As shown in Figure 1, cells (~100 µm) from the blood supply are considered hypoxic cells, which are cells that have rapidly outgrown the blood supply[7]. In these regions, where the oxygen concentration is significantly lowered, the metabolism is altered to promote cell survival through mechanisms including lowering extracellular pH and promoting angiogenesis[6]. Hypoxic tumour cells are often found to be resistant to radiotherapy and chemotherapy treatments[6, 8-11].

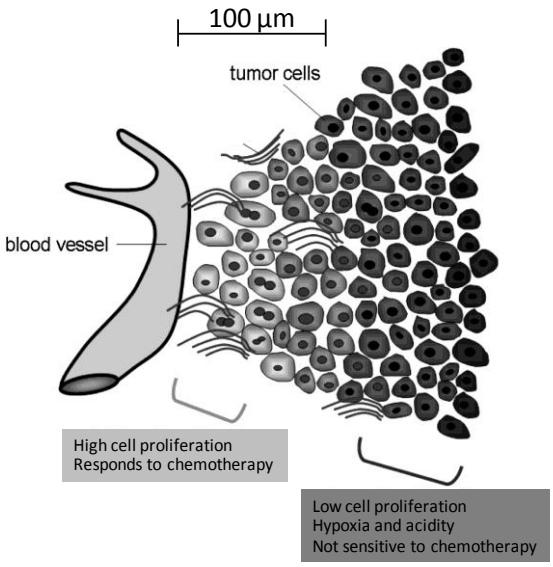

Figure 1: Structure of the solid tumour showing the location of the high and low oxygenated regions in relation to the blood vessel. Adapted from Trédan *et al*.[12]

Solid hypoxic tumours respond to changes in oxygen availability through the regulation of hypoxia-inducible factors (HIFs). These factors are responsible for the reprogramming of hypoxic tumour cells to facilitate cell survival in low oxygen tensions. HIFs are transcription factors that upregulate the expression of many genes in the presence of low oxygen environments. HIF were discovered by Semenza and Wang when investigating the effects of hypoxia on the erythropoietin gene[13]. HIFs are a family of heterodimer proteins and HIF-1 is a major focus for cancer, which has been shown to regulate many glycolytic enzymes in hypoxic tumours including hexokinase, phosphofructokinase, aldolase, triosephosphate isomerase, glyceraldehyde 3-phosphate dehydrogenase, pyruvate kinase, lactate dehydrogenase, glucose transporters, phosphoglycerate kinase and enolase[14]. Initially, glucose-related proteins were discovered to be directly affected by HIFs, however later it was found to be involved in the upregulation of many other genes as illustrated in Figure 2. HIF survival mechanisms include promoting angiogenesis, promoting proliferation, altering metabolism, promoting DNA repair and regulating pH[14] for growth and metastasis.

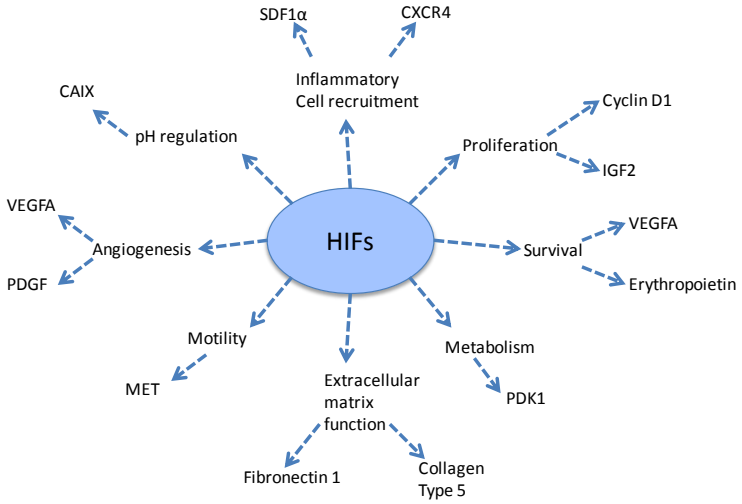

Figure 2: Genes encoding proteins regulated by hypoxia-inducible factors (HIF's) that promote tumour growth and metastasis where CAIX is carbonic anhydrase 9, CXCR4 is C-X-C chemokine receptor 4, IGF2 is insulin-like growth factor II, MET is met proto-oncogene (hepatocyte growth factor receptor), PDGF is platelet-derived growth factor B, PDK1 is pyruvate dehydrogenase kinase 1, SDF 1α is stromal cell-derived factor 1α and VEGFA is vascular endothelial growth factor A. Image adapted from Bertout *et al.*[14].

Ratcliffe and Maxwell later discovered the mechanism of HIF regulation[15]. The group discovered that the proline residues of the HIF-1α subunit are hydroxylated by prolyl hydroxylase when oxygen availability to cells is normal. This induces binding of the Von Hippel-Lindau tumour suppressor and ubiquitination labels HIF-1α for degradation by the proteasome. Hypoxia reduces the activity of prolyl hydroxylase, which prevents the degradation of HIF-1α. HIF-1α accumulates and is transported into the cell nucleus where it binds to HIF-1β and forms HIF-1. The HIF-1 complex binds to additional activators to upregulate several genes and thus promote cell survival[14] (Figure 2). Evidence has suggested that hypoxia-induced resistance to anti-cancer drugs, such as doxorubicin, is associated with a HIF-1α dependent decrease in senescence[10] and DNA damage[9].

1.3 Chemotherapy cancer treatments

Cancer can be treated by strategies including surgery, chemotherapy and radiotherapy[16]. Surgery removes the cancerous tumour and is often used in combination with radiotherapy or chemotherapy. Radiotherapy uses ionising radiation directed to kill cancer cells and is often applied to treat tumours localised to one area of the body. Furthermore, radiotherapy is used as a preventive tool to reduce the possibility of the tumour reoccurring. The ionising radiation damages DNA, which causes cell death[16].

Chemotherapy is the treatment of cancer with an anti-neoplastic therapeutic and can be administered as a combination of drugs. Chemotherapy is administered neoadjuvant

(preoperative) to shrink the primary tumour or adjuvant (postoperative) to prevent reoccurrence of the cancer and kill any cancer cells that may have metastasised to other areas of the body[16]. Many of these agents act by killing the fast-dividing cancer cells; however they also damage healthy proliferating cells in the bone marrow, digestive tract and hair follicles[16].

There are many types of chemotherapy therapeutics that can be defined based on the mode of actions. These can be categorised as alkylating agents, anti-metabolites, alkaloids and topoisomerase inhibitors[16]. Alkylating agents are so called because they alkylate nucleophilic functional groups[17] and includes melphalan and platinum-based chemotherapy such as cisplatin, carboplatin and oxaloplatin. The platinum-based compounds do not contain an alkyl group but act in an alkylating-like mechanism. The alkyl group is attached to guanine (DNA base), which facilitates cross linking of double stranded DNA preventing DNA replication. Additionally, these compounds covalently bond to amino, carboxyl, sulfhydryl, and phosphate groups to inhibit cell function. Antimetabolites are analogues of purine and pyrimidine compounds that imitate DNA building blocks. These compounds prevent purines and pyrimidines being included in DNA during synthesis (S) phase of the cell cycle thus impairing cell division[17]. Alkaloids, such as vincristine bind to tubilin to inhibit microtubule formation during the mitosis (M) phase of the cell cycle. Topoisomerase inhibitors interact with the topoisomerase enzymes used to maintain DNA. For example, doxorubicin is a topoisomerase II inhibitor that impairs the religation of DNA following DNA replication initiating double stranded DNA breaks leading to DNA damage and cell death[17].

1.3.1 Doxorubicin

The development of new cancer drugs has been driven at a rapid pace over the past decades; however a complete understanding of the mechanisms of action for existing, widely used, chemotherapy agents remains to be fully elucidated. Focusing research into exploring the mechanisms behind anti-tumour activity of gold standard chemotherapies is important to help identify where these drugs fail and guide the focus of new therapies. In this thesis the metabolic response of cancer cells to doxorubicin treatment was investigated to help ascertain why the drug is effective in treating oxygenated cancer cells but fails to be effective in treating solid hypoxic tumours.

Doxorubicin is a chemotherapy drug, which is known by the trade names Adriamycin® and Rubex®. The compound is an anthracycline antibiotic synthesised from daunorubicin, which is a natural occurring product of various wild type strains of *Streptomyces*. Figure 3 shows the chemical structure of doxorubicin, which has the systematic IUPAC name (8S,10S)-10-(4-amino-5-hydroxy-6-methyl-tetrahydro-2H-pyran-2-yloxy)-6,8,11-trihydroxy-8-(2-hydroxyacetyl)-1-methoxy-7,8,9,10-tetrahydrotetracene-5,12-dione.

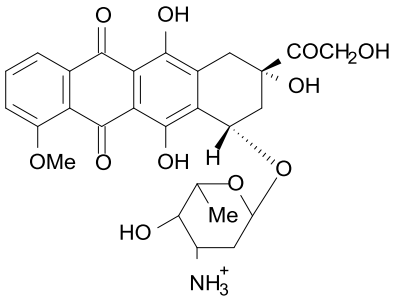

Figure 3: Chemical structure of doxorubicin, which has a molecular formula $C_{27}H_{29}NO_{11}$ and a molecular weight 543.52. Doxorubicin is an anti-neoplastic antibiotic synthesised from strains of *Streptomyces*.

Doxorubicin is transported through passive diffusion over the cell membrane[18]. A number of mechanisms for the mode of action of doxorubicin have been proposed. Firstly, the drug intercalates between the C and G DNA base pairs causing deformation of the DNA backbone[19]. Doxorubicin binds to DNA through non-covalent intercalation where the planar aromatic 4 membered ring system of doxorubicin inserts into the major groove of the DNA[17]. Doxorubicin is precise in its intercalation point between the terminal CpG, where the ring system inserts left to right head on into the major groove[19]. The chromophore inserts parallel and between the adjacent base pairs. This does not disrupt the stacking of the base pairs however the pairs must spread vertically along the DNA to allow the intercalation. Consequently, deformation of the DNA backbone occurs and the DNA adopts a long rigid structure. The sugar moiety bonds with the minor groove of the DNA and is vital for anti-tumour action as it has stronger DNA binding properties. The sugar moiety forms bonds to the sugar phosphate backbone and neighbouring proteins with the later forming the strongest bonds. If the sugar moiety was not present the chromophore would rapidly intercalate and deintercalate[20]. Intercalation disrupts replication and transcription processes.

Secondly, doxorubicin inhibits the topoisomerase II enzyme following cleavage of the DNA chain during the cell cycle. Both DNA strands are excised allowing DNA to pass through the gap, release tension on supercoiled DNA, unknotting DNA and decatenation.

Doxorubicin inhibits topoisomerase II from catalysing the ligation of double stranded DNA resulting in apoptosis and cell death[20].

Thirdly, doxorubicin generates free radicals in the presence of oxygen resulting in cellular damage and subsequently initiating apoptosis. Doxorubicin is catalysed by flavoproteins to produce a semiquinone free radical that can cause cellular damage[17]. Furthermore, redox cycling of the superoxide ion causes additional cellular damage. Doxorubicin undergoes a one electron reduction to form a free radical under aerobic conditions (Figure 4).

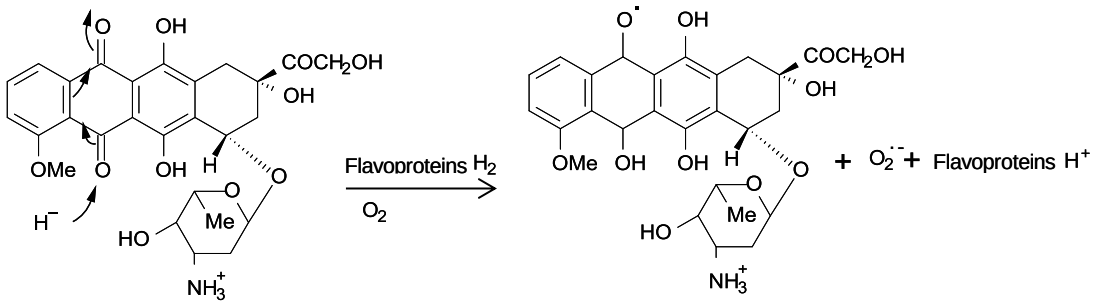

Figure 4: Reduction of doxorubicin catalysed by flavoproteins to form a semiquinone free radical and superoxide, which causes DNA damage.

Further, free radicals formed during oxidative phosphorylation metabolism interact with doxorubicin and generate the semiquinone compound. Doxorubicin forms the semiquinone intermediate with redox cycling transferring an electron onto oxygen allowing doxorubicin to reform[21]. In low oxygenated conditions this process cycles until oxygen depletes and subsequently doxorubicin is rapidly catalysed to 7-deoxyalglycone[21]. Doxorubicin may also form the semiquinone compound through reacting with superoxide generated during oxidative phosphorylation. The superoxide compound removes a proton from the phenol group to produce a phenolate anion[17]. The intermediate anion is oxidised and generates the semiquinone free radical structure. The semiquinone structure of doxorubicin can form hydroxyl radicals, which are catalysed by Fe(II), to oxidise polyunsaturated fatty acids, degrade deoxyribose and induce DNA double strand breaks[17]. Alternatively, doxorubicin and Fe(III)chloride may directly target lipid peroxidation. Figure 5 summarises the process that doxorubicin can use to cause cytotoxicity.

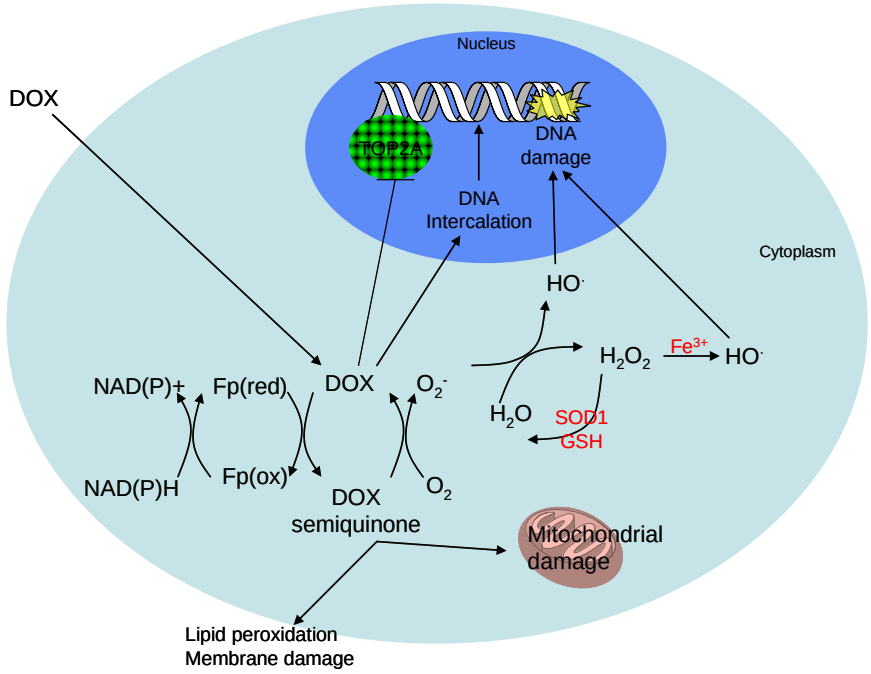

Figure 5: Summary of the anti-neoplastic mechanisms used by doxorubicin where Fp is flavoprotein. Doxorubicin (DOX) diffuses into the cell and, in the presence of oxygen, forms the semiquinone radical producing a superoxide molecule to damage DNA. Superoxide and doxorubicin enters the cell nucleus to intercalate into the DNA and inhibit topoisomerase II (TOP2A). Furthermore the doxorubicin semiquinone causes lipid peroxidation and mitochondrial damage.

The higher the dose of doxorubicin the greater tumour response; however clinically dose is restricted due to cardiotoxicity. When the dose reaches 550 mg/m², cardiac side effects occur, which can result in death and is characterised by a decrease in mitochondrial oxidative phosphorylation and reactive oxygen species (ROS) damage myocytes[22].

1.4 Tumour hypoxia: the impact on treatment

A great deal of research has been directed towards the effects of hypoxia in relation to cancer treatments. This field was driven in the 1950's by Gray who first confirmed the role of hypoxia in the development of radioresistance *in vivo*[14]. Resistance was shown to be at least three times higher in the anaerobic cells compared to aerobic cells, which became known as the oxygen enhancement effect[14]. Radiotherapy relies on oxygen to react with free-radical damage to generate ionising radiation in DNA leading to cell death[7]. Subsequently, hypoxic cells have also been reported to be resistant to many anti-cancer chemotherapy treatments[14, 23, 24].

1.4.1 Hypoxia and proliferation

The majority of chemotherapy compounds target proliferating cells however hypoxic cells have been reported to have slower proliferation rates compared to aerobic cells[25]. It has been shown that hypoxic cells undergo G1 arrest in the cell cycle resulting in an

accumulation of G_1 cells[7, 26]. Furthermore, it has been shown that S phase cells exposed to hypoxia arrest progression through the cell cycle following a few hours of treatment[26]. This suggests that cells in the S phase are more sensitive to hypoxia exposure than the other phases of the cell cycle. Additionally, it has been reported that HIF-1α inhibits Myc (an oncogene that drives proliferation in cancer cells) at the molecular level to prevent cell cycle progression[27].

1.4.2 Hypoxia and drug delivery

The vasculatures of solid tumours are often found to be insufficiently formed which impacts on the transportation of chemotherapeutics into the hypoxic regions of the tumour[6] (Figure 6). Consequently, cells within close proximity of blood vessels are exposed to the greatest dose of the drug[28]. Chemotherapy drugs fail to be transported into the hypoxic tumour cells that are located some distance from the blood capillaries. Additional features that inhibit the action of chemotherapy drugs include lymphatic deficiency that increases interstitial fluid pressure and modification to the extracellular matrix, which slows the movement of molecules in the tumour cells[6]. The accumulation and distribution of doxorubicin in multicellular tumour spheroids (MTSs) has been shown to be correlated with the efficacy of doxorubicin[29].

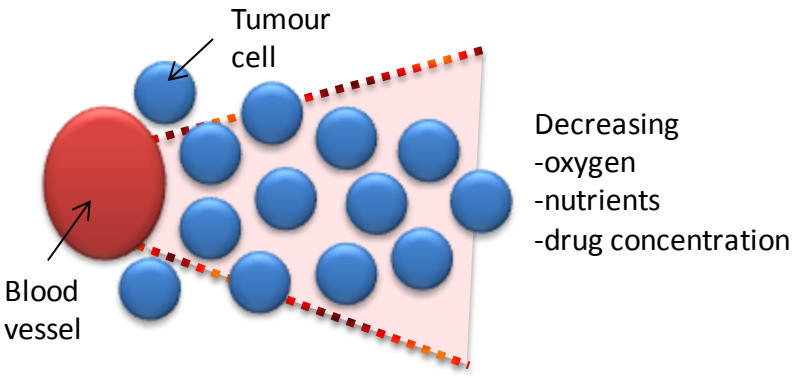

Figure 6: Illustration of drug penetration in solid tumours. The rapid growth of the tumour causes poor vasculature. This reduces the penetration for oxygen, nutrients and chemotherapy compounds into areas of the tumour with a poor blood supply. Image adapted from Minchinton and Tannock[6].

1.4.3 The influence of molecular oxygen in hypoxia

The mechanism of chemotherapy resistance originates in hypoxic tumours, in some instances, due to a lack of molecular oxygen that is required for the drug to become cytotoxic to the cells. For example, doxorubicin incites toxicity through initiating the formation of free radical molecules from oxygen to damage DNA, oxidise lipids and oxidise amino acids[19, 21]. Many chemotherapeutics, such as doxorubicin, use molecular

oxygen to produce a maximal cytotoxic effect. Anaerobic cells do not have the molecular oxygen required to produce this cytotoxic effect.

1.4.4 Hypoxia-induced acidosis

Non-cancerous tissue has an alkaline extracellular pH of approximately 7.4; however the pH decreases to around pH 6.5-6.8 malignant cells[30]. Increased acidity arises in hypoxic cells as a consequence of non-oxidative phosphorylation metabolism, which subsequently increases the efflux of lactate[30]. An insufficient oxygen supply causes a shift in metabolism as the oxidation of reduced nicotinamide adenine dinucleotide (NADH) to nicotinamide adenine dinucleotide (NAD^+) by the electron transport chain is unable to sustain glycolysis. As a result the NAD^+ is restored through reducing pyruvate to lactate. Acidity is generated due to excess protons produced as a consequence of ATP hydrolysis, which causes a reduction of intracellular pH. During glycolysis a net production of 2 ATP molecules can be used in cellular processes to release protons[30]. The cells transport protons out from the cancer cell via the ATPase pump or monocarboxylate transporter-1 and 4 to deacidify the cytosol[31]. Lactate and protons are expelled into the extracellular surrounding in order to maintain a neutral acidity within the intracellular environment. This action can protect the cancer cell from an immune system attack and overcome programmed cell death[32]. In addition, the acidic extracellular environment damages surrounding cells to facilitate metastasis[33]. Furthermore, the cell membrane transporter carbonic anhydrase IX (CA-IX) has been shown to be upregulated in hypoxia by HIF-1[34] to efflux HCO_3^-. Often an over expression of CA-IX is associated with a poor prognosis as these tumours tend to be highly metastatic and have poor vascularisation[35]. This multitude of cellular de-acidification mechanisms causes an increase in the extracellular acidity levels. Tumour acidity has been shown to prevent the uptake of doxorubicin into the tumour cells[36]. Low extracellular pH reduces the uptake of weakly basic compounds, such as doxorubicin, into the cytosol due to protonation of the drug, which reduces drug accumulation into the tumour. Additionally, weakly basic drugs can be protonated in the cytosol and subsequently diffuse into acidified endosomes reducing the accumulation into the cell nucleus and subsequently reducing cytotoxicity[30]. Preventing extracellular acidity has been reported to increase doxorubicin toxicity[30]. Greater uptake of doxorubicin has been shown at pH 7.4 compared to pH 6.6 suggesting uptake is pH dependent[37]. Approaches to overcome acidosis in cancer cells have been reported to help improve chemotherapy cytotoxicity. For example, Lu *et al.* have demonstrated the influx of doxorubicin is increased when the enzyme pyruvate dehydrogenase kinase-3 is inhibited[38]. Forced

expression of pyruvate dehydrogenase kinase-3 caused an increase in lactate accumulation and was correlated with drug resistance. Further, minimising the uptake of doxorubicin into acidic endosomes increase cytotoxicity through combination therapy with omeprazole[12]. Omeprazole is a proton pump inhibitor that acts to prevent drug uptake into the acidic endosomes[12]. Initial results showed improved doxorubicin penetration through multilayer cell culture[12].

1.4.5 Hypoxia-induced expression of P-glycoprotein

Many solid tumours express P-glycoprotein (Pgp) to aid their survival when exposed to chemotherapeutics[39]. Expression of Pgp has been shown to be correlated with tumour hypoxia[39]. Pgp was initially observed by Juliano *et al.* who discovered Chinese hamster plasma membranes expressed Pgp in the ovary cells[40]. Pgp is an ABC-transporter and is encoded by the multidrug resistant gene *Mdr-1*[41].

Structurally Pgps are inward facing transporters allowing drugs to enter in from the cytoplasm and inner leaflet of the lipid bilayer[42]. Pgps are mainly expressed in areas including the gut, the blood-brain barrier and the blood testes barrier to facilitate transport of potentially damaging substances[43]. The drug efflux pump can significantly reduce the intracellular concentration of xenobiotic compounds such as doxorubicin and hence contribute to drug resistance[44]. Doxorubicin enters the Pgp chamber on the plasma membrane and the nucleotide-binding domain (NBD) is phosphorylated. There are 12 transmembrane regions available for the drug to bind. To activate the pumping mechanism to export the chemotherapy drug located in the chamber, two ATP molecules attach to the ATP-binding cassettes causing dimerisation. Consequently, Pgp undergoes a conformational change at the NBD, initiating structural change in the transmembrane domain to facilitate the release of doxorubicin into the extracellular environment[42]. ATP hydrolysis releases the drug from the chamber through widening and motioning. Further ATP hydrolysis restores the Pgp to its original configuration releasing inorganic phosphate and ADP. The mechanism of transport is illustrated in Figure 7.

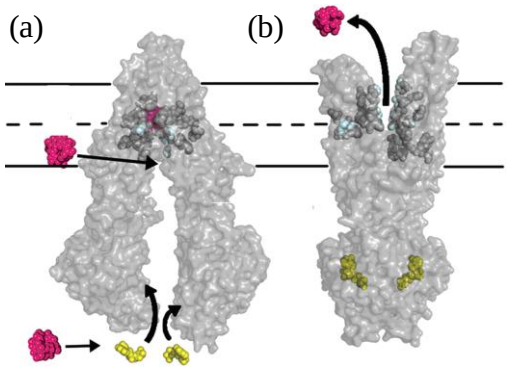

Figure 7: Mechanism of P-glycoprotein (Pgp) transporting a drug (magenta) to the extracellular environment where (a) the drug enters the chamber via the intracellular environment or the inner leaflet and (b) the ATP (yellow) binds to the nucleotide-binding domain (NBD) causing a conformational change allowing the release of the drug into the extracellular environment. Pgp returns to its original structure following hydrolysis and release of ATP. Image adapted from Aller[42].

Studies have suggested that the *Mdr-1* gene could be regulated by HIF-1α[11, 39]. Additionally, larger MTSs have an increased expression of HIF-1α and Pgp[11]. Furthermore, increasing ROS was reported to down-regulate the expression of HIF-1α and Pgp in large tumours[45]. Verapamil and cyclosporin A are inhibitors of the Pgp drug efflux pump[46] however the compounds developed to date to have neurotoxic side effects[46].

1.4.6 Hypoxia-induced inhibition of topoisomerase II expression

As described in section 1.3.1, doxorubicin is a topoisomerase II poison[20]. Topoisomerase II is responsible for ligating DNA double strand breaks following DNA replication. A decrease in the expression of topoisomerase II has been reported to be associated with a reduction in the sensitivity to chemotheraputics[47, 48]. The proteasome inhibitor lactacystin has been reported to avoid hypoxia resistance to topoisomerase II-directed therapeutics through preventing topoisomerase II depletion[47]. This enables the chemotherapeutics to have a greater cytotoxic effect to hypoxic tumours.

1.5 Strategies to overcome chemotherapy resistance in tumour hypoxia

Current strategies have been directed towards developing therapeutics that are toxic to hypoxic tumour cells through exploiting their unique properties. One strategy is to improve drug delivery thus increasing drug accumulation within tumours[49]. Erythropoietin, a glycoprotein hormone, is secreted in the kidneys during hypoxia to increase red blood cell production[49]. Enhancing haemoglobin levels has shown to improve the cytotoxicity of radiotherapy and chemotherapeutics in hypoxia cancer cells[49]. Alternatively, chemotherapies have been developed to specifically target hypoxia cells and are termed hypoxia activated prodrugs. These are often bioreductive compounds that are metabolised

specifically in low oxygen environments[12]. Killing hypoxic cells, rather than re-oxygenation, may be a smarter method of treatment as this may reduce the occurrence of metastasis[50]. Mitomycin C is a chemotherapy agent that uses reductive metabolism to promote toxicity. This mechanism is applicable to hypoxic cells that have limited oxygen available and it has been shown that the compound selectively kills hypoxic cells compared to normoxic cells *in vitro*[51]. Delayed bone marrow toxicity is a side effect of the drug, which prevents prolonged use of the compound. Tirapazamine (TPZ) is a bioreductive compound reported to have selectively toxicity to hypoxic cells[52]. Although TPZ has been reported to be toxic *in vitro*, studies *in vivo* have reported the drug alone cannot impact on tumour growth and it must be administered with other chemotherapeutics, such as cisplatin, to be effective[53]. Subsequent studies showed TPZ combined with cisplatin did not improve the toxicity towards advanced head and neck cancer[54]. Bis-N-oxide banoxantrone (AQ4N) is a bioreductive chemotherapy compound, which was developed as an analogue of mitoxantrone[55]. Similar to the other bioreductive compounds, AQ4N is reductively activated to AQ4, which binds with high affinity to DNA and acts as a topoisomerase II inhibitor[56]. This compound is one of the more successful hypoxia selective drugs developed as it remains active away from the hypoxic region. Furthermore, the drug has shown to have greater toxicity when applied in combination with other chemotherapeutics and to date is the most promising compound for treatment of hypoxia-induced chemoresistance[56].

1.6 Metabolomics and cancer research

The emerging field of metabolomics can offer both quantitative and qualitative measurement of metabolites present in a global biological process. The term ‘metabolomics’ was first introduced by Steve Oliver who used it to describe metabolites as low molecular weight intermediates[57]. The small molecules present in biochemical reactions are able to generate a large amount of information regarding the living system. Metabolites are the end products of cellular function and therefore the study of metabolism incorporates the overall response to a genetic or environmental perturbation. The metabolome is known to be more sensitive to perturbations within a global system in comparison to the transcriptome and proteome[58]. This arises as modification to the metabolic pathways rapidly induces changes to the concentrations of metabolites in comparison to the rate of enzymes (proteome level) and mRNA (transcription level)[58]. Metabolites are conserved in every organism and therefore metabolomics can be used to study a variety of biological organisms[58]. Monitoring these metabolite changes is a process

known as metabolic profiling. Metabolomic profiling can be carried out as metabolic fingerprinting to analyse the endometabolome (intercellular metabolism) or metabolic footprinting to analyse the exometabolome (extracellular fluid)[59].

There are two main platforms currently used in metabolomics, mass spectrometry (MS) and nuclear magnetic resonance (NMR) spectroscopy. NMR spectroscopy is a non-destructive technique, however MS is more sensitive and therefore requires a lower biomass of sample[60]. An overview of the advantages and disadvantages of the analytical approaches for metabolomics is available in the literature[60, 61] and summarised in Table 1.

Table 1: A comparison of the main analytical platforms used to acquire metabolomics datasets[60, 61].

Analytical platform	Strengths	Weaknesses
GC-MS	Robust High sensitivity Can analyse volatile and thermally stable polar and non-polar metabolites Electron impact provides reproducible gas phase fragmentation for chemical identification therefore mass spectral libraries are available	Destructive therefore sample cannot be recovered Dynamic range Chemical derivatisation needed to detect non-volatile metabolites.
UHLC-MS	Robust Sensitive detection Greater metabolome coverage High mass resolution (using FTICR or orbitrap mass analysers) Tandem mass spectrometry possible No chemical derivatisation needed	Destructive therefore sample cannot be recovered Commercial libraries are not available as retention indices are not transferable therefore difficult to identify metabolite
NMR	Non destructive therefore sample can be recovered Reproducible	Relatively insensitive compared to MS

There are two types of metabolic profiling that can be performed, targeted and non-targeted metabolomics[60]. For targeted metabolomics analyses, a small number of metabolites are preselected and quantified. The advantage of this method is the acquisition of quantitative data, which are useful to determine the extent a metabolite deviates from the normal level; however, extensive sample preparation and chromatographic separation is needed. Non targeted metabolomics, which is also known as metabolic fingerprinting, is

a method to semi-quantitatively measure metabolites (using an internal standard) to determine the metabolic changes in the whole metabolome. Non-targeted metabolic analysis is a useful rapid tool to screen the similarities and differences between different biological samples in metabolic pathways. Non-targeted metabolomics is usually most suitable for metabolite marker discovery and diagnostic analysis through determining the characteristic features of metabolism[62] and minimal sample preparation is needed. The number of metabolites within a eukaryotic cell has been suggested to be up to 20,000, therefore there is a need to develop mass spectrometric protocols to identify more metabolites than is currently possible[63]. The human metabolome project has identified and quantified greater than 6000 metabolites in human tissue[64]. Nevertheless, metabolic profiling of the metabolome gives a great insight into the regulation and function of metabolic pathways.

1.6.1 Metabolomics and cancer diagnosis

Metabolomics is proving to be a useful tool in cancer diagnostics to identify metabolite markers of specific cancers[65-67]. For example, the complexity of prostate cancer was characterised using metabolomics by identifying metabolite markers of cancer invasion and disease progression[66]. A study of clinical samples including tissue, urine and plasma were analysed using metabolic profiling with liquid chromatography mass spectrometry (LC-MS) and gas chromatography mass spectrometry (GC-MS). Metabolic profiles differentiated between benign prostate, localised prostate and metastatic samples.

Metabolomics can be applied to discover metabolite markers for cancer diagnosis, prognosis and therapeutic efficacy in samples ranging from preclinical or human cell cultures to biofluids and tumour tissue. Metabolomic studies in breast cancer diagnostics have revealed increased phosphocholine and decreased glycerophosphocholine and glucose levels in comparison to healthy tissue[68]. Metabolic phenotypes were discovered to predict histological grade, hormone status, and axillary lymphatic spread in breast cancer patients. Furthermore, a metabolomics study of metabolite markers in renal cell carcinoma in urine samples revealed a phenotype that can be used to diagnose the disease. Urine was analysed using three mass spectral platforms for a greater coverage of the metabolome to detect both lipophilic and hydrophilic metabolites[67]. Results revealed 30 potential metabolite markers that could potentially be used clinically to non-invasively diagnose renal cell carcinoma from urine[67]. This suggests metabolomics can contribute to clinical diagnosis and subsequently help determine the most effective treatment available thus leading to individualised treatment.

1.6.2 Metabolomics and tumour hypoxia

Metabolomics has previously been used to explore the metabolic response of hypoxic cancer cells. Troy *et al.* illustrated the effect of HIF-1β on tumour growth within the hypoxic region of tumours using NMR[69]. Data show a fivefold decrease in ATP, phosphocholine, choline, betaine and glycine and an increase in phosphodiester to phosphate ratio for HIF-1 deficient cells[69]. Results suggested HIF-1 increases choline metabolism, which is linked to an increase in lipid membrane synthesis. This study shows the potential of metabolomics to explore HIF-1 metabolism[69]. Furthermore, metabolic profiling of hypoxic cells has suggested catabolism is vital for cell survival. Frezza *et al.* suggested the catabolic process of autophagy in hypoxia sustained ATP level to maintain cell survival[70]. Subsequently, the group proposed inhibition of autophagy would be a hypoxia specific target to initiate cell death.

1.6.3 Metabolomics and cancer chemotherapy

In addition to tumour hypoxia, metabolomics has also been applied to the study of chemotherapy in cancer cells. A metabolomics study was undertaken to investigate the metabolic response of breast cancer cells to anti-cancer treatments including paclitaxel, vincristine, colchicine and nocodazole[71]. Results showed the anti-mitotic drugs reduced an increase in glycerophosphocholine, which increased further when cells were synchronised at the G_2/M phase of the cell cycle[71]. The study suggested a connection between microtubule status and cell phospholipids metabolism revealing a new mechanism of action of the anti-microtubule drugs. High-throughput metabolomics has also been applied to identify the metabolic response of B16 melanoma cells treated with doxorubicin. A number of metabolites associated with the action of doxorubicin were identified including lipids, lysine, glutamine and myo-insoitol highlighting the application of metabolomics as a useful tool to revealing the metabolic response to a drug. Metabolomics analysis of doxorubicin toxicity in rat urine samples was studied to identify metabolite markers related to doxorubicin toxicity[72]. The mechanisms of doxorubicin-induced toxicity remain to be fully identified and therefore studying the rat model was hoped to revealed metabolic changes relating to drug dose and duration after exposure[72]. Metabolites that differed as a consequence of doxorubicin toxicity included uric acid, tryptophan, phenylalanine, hippuric acid, 2,8-quinolinediol glucuronic acid and cholic acid[72]. This study may be useful for clinically detecting the early stages of doxorubicin-induced toxicity.

1.7 Systems biology as a tool for cancer research

Systems biology is the study of the function of molecules that arise from the whole biological system and how they interact together to animate life. Figure 8 shows the levels of complexity that interact within the biological system to give rise to a particular phenotype. The advent of powerful computers has allowed mathematical modelling of complex biological systems[73]. Modelling helps to generate an understanding of how the system functions as a result of its individual components. Such mathematical models aim to elucidate how and where the function of a system is regulated through the interactions of molecules.

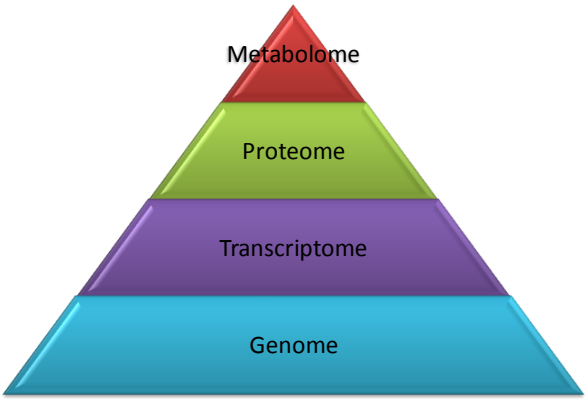

Figure 8: The holistic model depicting the complexity arising in biological systems. Interaction of the various 'omes' in the cell is a complex function of the other 'omes' (apart from genome) and the extent of this integration increases from the bottom of the triangle to the top. The phenotype of a cell is a consequence of the whole system process and can be directly studied in the metabolome, which represents the combined function of the other 'omes'.

Cancer is a robust disease that is able to adapt to and survive perturbations from anti-cancer strategies. Studying the mechanisms regulating cancer robustness could lead to the identification of therapeutic targets to prevent or inhibit further progression of the disease. Systems biology offers a framework to study the interconnected cancer systems' regulation to perturbations that are required to sustain cellular functions. Studying the intricate series of complex interactions can contribute towards the understanding of how cellular function is regulated in cancer. Furthermore, systems biology can offer a new approach to pharmaceutical research through developing individualised medicine to improve the effectiveness of therapeutics and minimising toxicity. Omics approaches could help to identify the most effective therapy for a patient, which would vary depending on the genetic makeup of the tumour and metabolism. One of the first examples of an individualised drug was Herceptin®, which is an antibody used to treat breast cancers that express HER2 receptors and has been shown to be a very effective treatement[74].

Mathematical models have been shown to be useful in explaining the mode of action of therapeutics. For example, mathematical models were able to elucidate the previously unknown mode of action of the cardio-protective drug Ranolazine[75]. There are many types of mathematical models that can be used to study metabolism including interaction based, constraint based and mechanism based models and the type of model to use depends upon the application and relevant experimental data available (Figure 9).

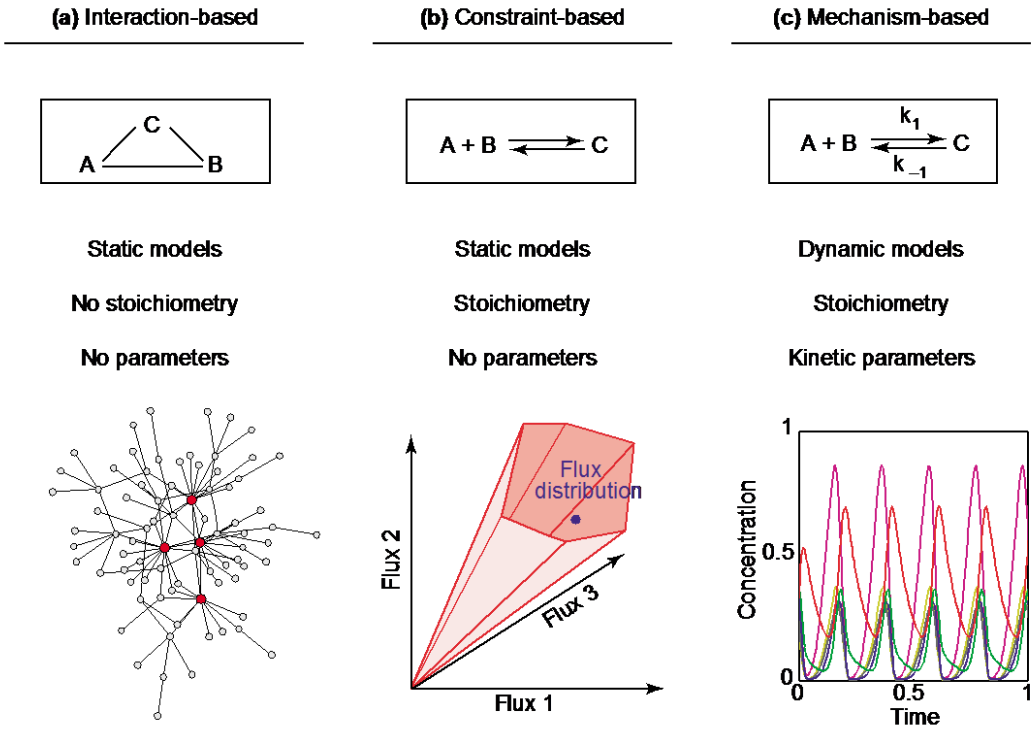

Figure 9: Comparison of the three types of metabolic network models and the data required to generate the model. Image adapted from Stelling[76].

Interaction based models are static models, which do not account for the element of time and are therefore ideal for exploring the network topology (patterns of interactions between substrates). These models do not require prior knowledge about the type of interaction, such as the stoichiometry. Often the model is large and used to describe metabolic or protein-protein interactions[77]. Graph theory can be applied to explore high connectivity in the components known as nodes (represented in Figure 9a as circles) and the interactions known as links. The robustness of the network to random node deletions can identify the essential genes within a network, although assumptions cannot be made about time or flux distribution within the network.

Constraint based models, similar to interaction based models, are static models and have no element of time[78]. Stoichiometry is incorporated into the model to account for

biological randomness in the system as stoichiometry is a quantitative relationship connecting substrates through the reaction. Given the initial set of parameters, values are calculated based upon probability distributions[78]. Prior knowledge of the metabolite concentration or enzyme kinetics is not needed for constraint based models. Constraint based modelling assumes the system is at steady state and uses the influx and efflux of a few metabolites to identify which fluxes in the pathway maximise the growth of an organism.

Mechanistic models are very detailed models often used to describe small networks. These are dynamic models and therefore include the element of time[79]. Greater detail is required to generate a mechanistic model. Developing a mechanistic model on the genome scale requires the inclusion of kinetic equations for each reaction in the metabolism. There is a lack of knowledge of the type of kinetic equation of every enzyme in metabolism. Furthermore, data such as metabolite concentration and rates that are also needed to construct mechanistic models is limited. In addition, the computational power needed to simulate a mechanistic genome scale model is greater than the power currently available. Teusink *et al.* applied mechanistic modelling to compare the behaviour of *in vitro* glycolytic kinetics of *Saccharomyces cerevisiae* to *in vivo* kinetics[79]. Comparisons revealed the activity of over half of the glycolytic enzymes in the *in vitro* model were able to describe the *in vivo* activity within a factor of two. This model contributed towards understanding the *in vivo* behaviour of glycolysis in *S. cerevisiae*.

1.7.1 Development of genome scale metabolic networks

Many large genome scale metabolic networks have been constructed for a range or organisms including *S. cerevisiae*[80] and *Escherichia coli*[81]. These are models of the cellular metabolism at the scale of the entire metabolic network and enable whole-network modelling of metabolism. One of the first mammalian metabolic models was constructed to study the human liver metabolism[82]. This was used to compare the flux distributions of fibrotic cells to healthy liver cells. A total of 125 reactions and 83 metabolites were included in the model, which mainly contained glycolysis, tricarboxylic acid (TCA) cycle and pentose phosphate pathways[82]. Results showed specific amino acids to have a limited production within the pathway and subsequently limit the production of other amino acids. This was proposed to be a factor contributing towards increasing collagen in fibrotic cells[82].

Subsequently, a reconstruction of the *Mus musculus* metabolic network was developed [83]. This was the first attempt to reconstruct a large mammalian metabolic network and compartmentalise the reactions into the cytosol, mitochondria and extracellular medium. The model contains 872 internal metabolites that undergo a total of 1220 reactions including 473 transport reactions[83]. Metabolic pathways included in the network were used to describe carbon and nitrogen metabolism[83].

A fundamental advance towards large-scale mammalian metabolic modelling came about with the simultaneous reconstruction of two independent genome scale human metabolic networks known as the Edinburgh human metabolic network (EHMN)[84] and Recon 1[85]. Both models were developed from human gene studies and extensive literature based searches. The level of detail within the models includes the stoichiometry of reactions, cofactors and conservation of metabolites at physiological pH[84, 85]. Both models are available as compartmentalised models, which contain exchange reactions between the compartments[85, 86], however the EHMN is also available as an uncompartmentalised model[87]. The potential application of genome scale modelling was demonstrated to predict alternative drug targets for treating hyperlipidemia[85]. In addition, the Recon 1 network was able to elucidate the role of the Warburg effect in cancer. The model suggested that the Warburg effect is a consequence of the metabolic adaption of cancer cells to increased biomass production rate[88]. Furthermore, a drug-reaction network was constructed from the Recon 1 model using drug target data and explored, using cell line specific gene expression data, to predict novel reactions and potential enzyme targets for cancer drugs[89]. Moreover, the Recon 1 has been adapted to create tissue specific *in silico* models through integrating the Recon 1 model with disease specific gene and protein expression data[90]. For example, a genome scale model of cancer metabolism was constructed and used to predict 52 cytostatic drug targets, some of which were already known and others a new area for research[89]. Of the 52 targets identified, there are currently non-cancer compounds available for 13 targets.The suitability of these compounds as anti-cancer agents is being investigated[91]. In a later study the cancer model was used to predict the synthetic lethality of haem oxygenase in the tumour suppressor fumarate hydratase[92]. It was not known how cancer cells survive without fumarate hydratase loss of which impairs the function of the TCA cycle. The model was used to demonstrate that the haem biosynthesis pathway facilitates fumarate hydratase deficient cancer cells in partial use of the TCA cycle to produce mitochondrial NADH[92]. Haem metabolism was targeted experimentally using genetically modified kidney mouse cells to confirm that the fumarate hydratase deficient

cells were no longer viable without this alternative pathway[92]. This suggested haem metabolism as a target to overcome hereditary leiomyomatosis and renal cell cancer.

1.7.2 Correlation analysis and network construction

Metabolomics studies generate large-scale datasets, due to the high-throughput nature of the approach, and are therefore complex to interpret with respect to providing an insight into cell physiology. Metabolomics is an important tool used in systems biology as it may be considered the ultimate response of gene expression[57]. Metabolites are produced from other metabolites and, as a consequence, this leads to interdependency between the concentrations[93]. Changes in metabolite concentrations are a systems property that can be influenced by both stress and genetic perturbations. The origin of a correlation is therefore a global system property of the network[93].

A simple interpretation of metabolite correlations would be to assume that pairs exhibiting strong correlations are neighbours in the metabolic network. In reality this is not always the case as many metabolites that are neighbours are not always strongly correlated while others that are spatially or temporally unconnected can be strongly correlated with one another. Computational analyses have indicated that correlations can be shaped by combinations of stoichiometric and kinetic effects[94]. Using metabolic control analysis, Camacho *et al.* investigated the origin of correlations in metabolomics data, which led to series of cases where high correlations were observed. This included chemical equilibrium, mass conservation, asymmetric control distribution and unusually high expression variance of a single gene[59]. Metabolites in chemical equilibrium will have a perfect positive correlation. Mass conservation generates a negative correlation and occurs when both metabolites correlated belong to a moiety-conserved cycle. Asymmetric control and high expression variance of a single gene arises when one parameter dominates the concentration of two metabolites due to a large concentration response to a common enzyme or an enzyme that carries unusually high variance. In the latter case high variance usually induces negative correlations between substrate and product metabolites. For both cases further data are needed to determine the enzyme responsible. Identifying metabolite correlations through repeat biological replicate measurements in identical experimental conditions is able to describe the interdependency between metabolites revealing the underlying system regulation.

To date, computational analysis on metabolomics data has been limited to statistical analyses such as univariate analysis (UVA) and multivariate analysis (MVA) to identify metabolite markers and phenotypes of disease[65-67]. Whilst it is useful to discover metabolite markers and phenotypes, these methods provide little information regarding the underlying metabolic system. Correlation analysis goes beyond the methods described above to bridge the gap between data and understanding the biological system. Correlation analysis has been used to study global metabolic datasets of plants[93-95]. For example, Morgenthal *et al.* successfully applied pair-wise correlation analysis to various plants, which have been subjected to different environmental conditions[96]. Metabolic profiles of plant leaves from *Arabidopsis thaliana*, *Nicotiana tabacum* and *Solanum tuberosum* and *S. tuberosum* tubers were extracted. The group identified metabolic differences in the four types of plant at a correlation level [96]. Some correlations were found to be preserved in all plant species such as glucose 6-phosphate and fructose 6-phosphate. Figure 10 shows the correlations between metabolites using a Pearson pair-wise correlation. The first and second column show pair-wise correlations that differ in the four samples. The third and fourth column shows those correlations, which are similar in the four samples, which are suggested to be robust correlations conserved over plant species.

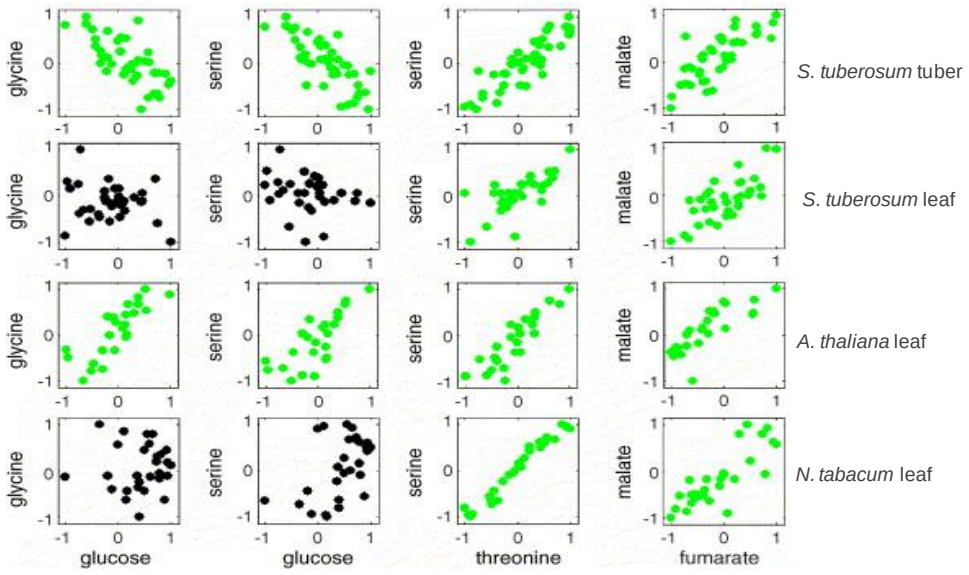

Figure 10: Adapted from Morgenthal *et al.* [96]. Pair-wise correlations identified in 3 plant species where green graphs represent correlations with a significance level of $p < 0.001$. The first two columns represent correlations that differed in the four samples and the last two columns represent correlations that were conserved in the four samples.

More recently, construction of differential correlation networks has produced a 'fingerprint' of the biological status of the system as a network response to biological perturbation[97]. Metabolic correlation networks have been constructed for both plant[98] and

mammalian[97] metabolomics datasets. Both examples created correlation networks from pair-wise correlations within the subject group and subsequently compared the topology of the correlation networks to identify differences. Correlations arising in three *A. thaliana* genotypes were constructed into networks to investigate the genotype dependent changes on metabolism. Results revealed network differences could be related to the genotype difference in known biochemical pathways of *Arabidopsis*[98]. Additionally, differential networks were constructed to study diabetes. Characteristic response with respect to lipoprotein metabolism was identified when comparing normal fasting glucose to impaired fasting glucose (prediabetic) subjects. Pair-wise correlations were generated within each group and the topological differences between the networks for the two subject types were able to identify the metabolic responses[97]. Whilst these networks are a snapshot of the system response, the underlying origin of the metabolic pathways connecting the correlations remains poorly understood.

1.8 Secondary ion mass spectrometry imaging of biological samples

Time-of-flight secondary ion mass spectrometry (ToF-SIMS) is a mass spectral imaging technique capable of mapping biological species to specific regions of a tissue or cell and can be applied to the study of disease progression and treatment. The theory of the technique is presented in section 2.9. Previously, SIMS was used as a surface science technique to study non-biological samples such as catalysts[99]. SIMS was developed for molecular analysis by Alfred Benninghoven at the University of Münster and John Vickerman at the University of Manchester Institute of Science and Technology. An early example of the analysis of biomolecules was the detection of immonium ions however analysis was limited by low sensitivity due to the atomic ion beams available[100]. Later, with the introduction of polyatomic primary ion beams and the introduction of ToF mass analysers (compared to a quadrupole), a greater range of biological compounds became possible[101]. ToF-SIMS has a typical mass range of 0-1500 Da; therefore the technique could be used to detect small molecules such as metabolites. The development of polyatomic primary beams such as the C_{60}^{+} primary ion beam[101] has facilitated molecular depth profiling beyond the sample surface in addition to increasing ionisation efficiency by several orders of magnitude[102-104]. Furthermore, ToF-SIMS is a label free imaging technique compared to other imaging mass spectrometry techniques such as matrix-assisted laser desorption/ionization mass spectrometry (MALDI-MS), which requires the application of a matrix to facilitate ionisation.

1.8.1 The study of lipid metabolism using secondary ion mass spectrometry

Imaging mass spectrometry has proved beneficial in the study of lipid metabolism. One example is the study the membrane fusion in *Tetrahymena* (a common fresh water protozoa)[105]. SIMS imaging illustrated phosphatidylcholine dissipates in the membrane regions during *Tetrahymena* fusion, which is associated with an increase in 2-aminoethylphosphonolipid. This study suggested the redistribution of lipids may be a feature of the fusion process. Furthermore, isotopic labelling has been implemented to study the spatial distribution of lipids in single cells[106]. Cells were cultured with isotopically labelled ^{13}C-oleic acid to investigate fatty acid pathways associated with fat storage in adipocyte cells. Using a Cs^+ primary ion beam (and microscope mode) both ^{13}C and ^{12}C were imaged simultaneously. The ^{13}C to ^{12}C ratio was determined for the intracellular lipids and in the extracellular region of specific adipocytes. Labelled lipids were in high abundance in the cytoplasm of the cell, which suggested free fatty acids are transported across the cell membrane against the electrochemical potential. This study also demonstrated the application of stable isotopic labels to study fatty acid distribution.

Moreover, ToF-SIMS has been applied to study the spatial distribution of lipids in a tissue samples. Lipid analysis in tissue was reported by Fletcher *et al.* who used ToF-SIMS to molecular depth profile an oocyte[107]. A *Xenopus laevis* oocyte was depth profiled to localise the chemical distributions of lipids such as phosphatidylcholine and cholesterol through the whole sample (Figure 11). This was one of the first 3D ToF-SIMS imaging examples in a biological system. More recently, a section of rodent brain was analysed using ToF-SIMS to demonstrate the lipid differences between the grey and white matter[108]. Chemical species detected in the initial tissue layer included cholesterol, dipalmitoyl phosphatidylcholine and phosphatidylcholine. Depth profiling (analysis beyond the surface layer) revealed a spatial relocation of phosphatidylcholine. The compound was initially detected in the grey matter, however in subsequent layers of the depth profile there was a location shift to the white matter. Further, an increase in phosphatidylcholine in the white matter was correlated with a reduction of cholesterol. This redistribution of chemistry within layers of tissue sections highlights the advantage of ToF-SIMS imaging beyond the surface.

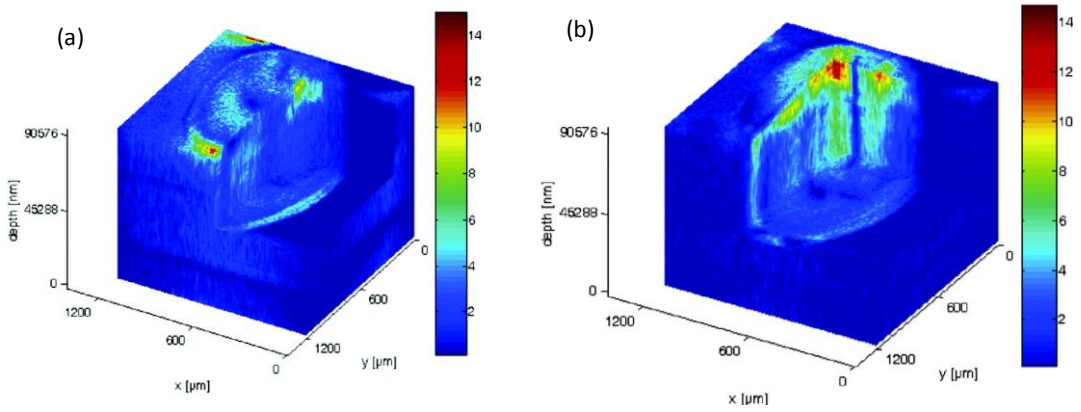

Figure 11: 3D ToF-SIMS imaging of a freeze-dried oocyte showing the distribution of (a) phosphocholine peaks *m/z* 58, 86, 166, and 184 and (b) cholesterol peak at *m/z* 369. Image adapted from by Fletcher *et al.* [107].

Lipids have also been identified as metabolic markers in human cardiovascular pathology where the lipid metabolism of atherosclerotic plaques was profiled[109]. Free fatty acids (C16 and C18), cholesterol, vitamin E, phosphatidic acid and sphingomyelin fragments were spatially localised within areas of the vasculature relating to plaque vulnerable sites. Results demonstrated that the free fatty acid lipid pathology in plaques is correlated with the presence of vitamin E (a redox marker) in areas of high cholesterol accumulation. ToF-SIMS was also reported as a tool for the study of Fabry disease, which is a disease that effects glycosphingolipid metabolism due to deficiency of the enzyme α-galactosidase A[110]. Tissue biopsies were analysed to spatially localise cholesterol, cholesterol sulphate and vitamin E. Cholesterol sulphate was suggested as a metabolite marker of the disease and suggested to be associated with the formation of the epidermal barrier during keratinocyte differentiation.

1.8.2 Cellular phenotyping using ToF-SIMS

ToF-SIMS has been demonstrated as a tool to phenotype the chemistry of the cell. Breast cancer cells were reported to have a different chemical phenotype across the various cell lines[111]. Kulp *et al.* analysed three human breast cancer cell lines (MCF-7, T47D and MDA-MB-231) and reported spectral differences that classified the three cancers types[111]. The characteristic mass spectra were determined using principal component analysis (PCA) to identify the spectral features that differed relating to the global activity of the cellular function. In addition, Baker *et al.* used discriminant function analysis (DFA) to classify the spectral features of prostate cancer cell lines[112]. The loading plots revealed lipid and amino acid spectral features were responsible for the cell line discrimination. These studies suggest ToF-SIMS, in combination with MVA techniques, is a potential tool to study cellular phenotypes.

High-throughput analysis using ToF-SIMS would allow the acquisition of mass spectra of more cellular biological replicates than is currently possible in a single analysis. A ToF-SIMS high-throughput surface characterisation approach has been shown to be a an effective tool to explore surface moieties, when combined with MVA, in the field of materials science[113]. Applying this approach to characterise the chemistry of cells through depositing samples in a microarray format (using robotic fluid handling system) would enable the simultaneous acquisition of more biological replicates than is currently possible, allowing the application of predictive MVA models that require multiple biological replicates.

1.8.3 Single cell analysis using ToF-SIMS

ToF-SIMS has the potential be a useful tool to analyse multiple metabolites within single cells. Single cell analysis cannot be performed using conventional metabolomics platforms due to sensitivity limitations of the concentrations of metabolites present in a single cell. The development of single cell analysis could prove to be a useful tool in cancer research to study the conversion of a normal cell into a neoplastic cancer cell. To date, ToF-SIMS molecular depth profiling of single cells has reported the localisation cellular components and organelles such as the intact cellular membrane, the cytosol or the cell nucleus. The 3D representation of a single HeLa-M cell is shown in Figure 12 where the green represents the membrane chemistry (*m/z* 184.1 identified as phosphocholine) and red represents the chemistry of the nucleus (*m/z* 136.1 identified as adenine) for HeLa-M cells[114]. Localisation of organelles within a cell could unlock ToF-SIMS as a tool to profile metabolic differences within organelle regions in a single cell, which is not possible with conventional metabolomics platforms.

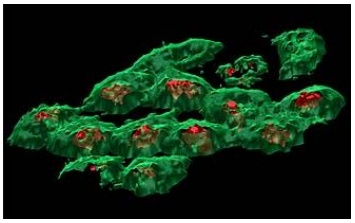

Figure 12: A 3D visualisation of frozen hydrated HeLa M cells revealing the localisation the green membrane and red nucleus that was generated from the spectral differences identified in the loadings plot of principal component analysis (PCA). Image adapted from Fletcher *et al.*[114].

1.8.4 ToF-SIMS and pharmaceutics

ToF-SIMS has been demonstrated as a tool to localise pharmaceuticals within biological samples. Studies (using dynamic SIMS where the sample is eroded by a high primary ion beam dose) by Chandra *et al.* detected boron containing anti-cancer compounds within the brain[115]. Furthermore, the doping of compounds into single cells have been detected using ToF-SIMS. Cocaine hydrochloride was doped into cells and detected suggesting that ToF-SIMS is capable of analysing pharmaceuticals at a sub-cellular resolution[116]. Although the doping of compounds into cells artificially could be detected by ToF-SIMS, the detection of drugs at physiological concentrations remains challenging.

1.9 Project aims

Solid tumours are associated with poor patient prognosis and are often difficult to treat as they are resistant to gold standard chemotherapy drugs. Understanding the resistant response of hypoxic tumours to chemotherapy remains to be fully elucidated. The aim of the project was to study the metabolic response of hypoxia-induced chemoresistance to identify the metabolic pathways differentially regulated by hypoxic cancer cells in response to doxorubicin treatment. This was investigated through:

1. Developing a metabolic profiling protocol that is suitable for the study of cancer cells cultures in normoxic, hypoxic and anoxic oxygen levels and subsequently treated with chemotherapy. (Chapter 3)
2. Comparing the metabolic profiles (acquired using GC-MS and UHPLC-MS) of MDA-MB-231 cell cultures to identify the metabolite markers of hypoxia-induced chemoresistance. Furthermore, the profiles were compared to ascertain the metabolite markers that are associated with overcoming hypoxia-induced chemoresistance. (Chapter 4)
3. Developing a novel computational approach to investigate the underlying biochemical pathways' response to hypoxia-induced chemoresistance. Metabolic networks were extracted from the GC-MS metabolic profiling data using pair-wise correlations. Metabolite pathways of the metabolic response to hypoxia-induced chemoresistance were deduced from the constructed network. (Chapter 5)
4. Developing ToF-SIMS as a tool for the study of metabolites in biological samples through initiating a ToF-SIMS metabolite database to interpret the spectra from biological samples. (Chapter 6)

5. Developing a protocol to prepare MTS for ToF-SIMS analysis to examine the *in situ* metabolite distribution in MTS treated with doxorubicin using image PCA to determine the metabolic response of hypoxic cells to chemotherapy treatment in 3D systems. (Chapter 6)

Chapter 2

MATERIALS AND METHODS

2.1 Cell culture

Human cell lines MDA-MB-231 breast adenocarcinoma and FaDu squamous cell carcinoma were obtained from the University of Manchester stocks. Cells were cultured, unless stated, as a monolayer in T75 or T175 flasks with a surface area of 75 and 175 cm^2 respectively. Cells were stored in a standard CO_2 incubator (5 % CO_2 and 95 % air at 37 ˚C) in RPMI 1640 (Invitrogen, UK) supplemented with 10 % heat inactivated fetal calf serum and 2 mM glutamine.

RPMI 1640 medium, L-glutamine and trypsin-ethylenediaminetetraacetic acid (EDTA) were purchased from Gibco BRL (Paisley, UK). Foetal calf serum (FCS) was purchased from Labtech International (Ringmer, UK). Dimethyl sulphoxide (DMSO) was supplied by Fisher (Leicestershire, UK). Phosphate buffered saline (PBS) was purchased from Oxoid (Hampshire, UK). Tissue culture dishes and flasks were purchased from Falcon (Runcorn, UK). HPLC grade methanol, water, doxorubicin hydrochloride and ammonium formate were obtained from Sigma (Dorset, UK).

Unless stated, for all experiments cells were seeded at a density of ~15,000 cells/cm^2 and always allowed to adhere for 24 h prior to experimental analysis. Normoxic oxygen levels were defined as ~21 % O_2, hypoxic levels as 1 % O_2 and anoxic levels 0 % O_2. Cells were cultured in specified oxygen conditions for 16 h followed by a 24 h drug exposure while cells remained in the specified oxygen condition. Doxorubicin was frozen in aliquots at a concentration of 1 mM, and only subjected to one freeze thaw cycle. Additionally, doxorubicin was spiked into the media at concentrations stated in each experiment. Cells exposed to hypoxic conditions were performed using a hypoxybox system, with a steady flow of 1 % O_2 and 5 % CO_2 mix in nitrogen (BOC, Manchester, UK) at 37˚C. The hypoxybox was developed in-house and comprised of an ADDIS® 5 litre air tight container (with removable clip lid) with a male BSPT- female BSPP reducer (RS Components Ltd, Stockport, UK) and male parallel straight adaptor (RS Components Ltd, Stockport, UK) to connect a 6 mm polytube (RS Components Ltd, Stockport, UK) to a 6 mm 2/2 finger tap (RS Components Ltd, Stockport, UK) at either side of the container

(Figure 13). Hypoxic gas was flowed into the container through the 6 mm polytube, which was connected to a 2/2 finger tap. To ensure gas was flowing through the container the 6 mm polytube connected to the opposite tap was placed into water to check for air bubbles in the outflow. The inlet and outlet valves of the sealed hypoxybox system were closed to maintain hypoxic conditions when the containers were transferred into the anoxic chamber for sample treatment or fixation. Cells exposed to anoxic conditions were introduced to into an anoxic chamber (Bactron anaerobic chamber, Sheldon Manufacturing, Cornelius, Oregon, USA) where 5 % CO_2, 5 % H_2 and 90 % N_2 (BOC, Manchester, UK) was flowed over a palladium catalyst to remove any remaining oxygen.

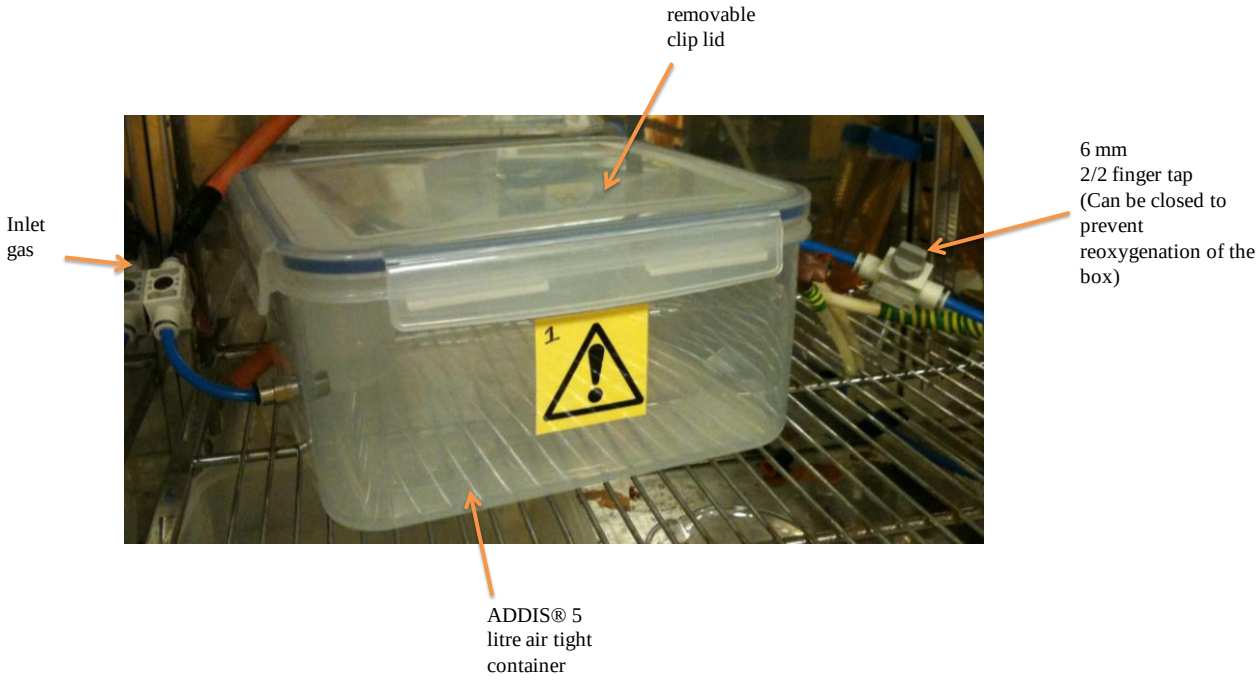

Figure 13: Image of the hypoxybox created from an ADDIS® 5 litre air tight container (with removable clip lid). Hypoxic gas is flowed into the container through 6 mm polytube, which is connected to a 2/2 finger tap.

2.1.1 Cell passage

Cells were cultured in 75 cm^2 tissue flasks and sub-cultivated every 2-3 d to maintain a cell confluency of 70-80 %. Extracellular medium was removed and cells were washed with PBS. Cells were detached from the flask using a trypsin-EDTA solution (500 mg/L trypsin and 200mg/L EDTA in sterile PBS) and incubated at 37 °C until detachment occurred. Following detachment, cells were resuspended in warmed medium and an aliquot was transferred into a new tissue culture flask containing warmed medium.

2.1.2 Freezing cell stocks

Cells were passaged following the procedure in section 2.1.1 to the resuspension stage. Resuspended cells were centrifuged at 212 × g for 5 min (Centaur-2, Sanyo, USA) to allow a pellet to form. Medium was removed and the pellet was resuspended in freeze medium containing 50 % RPMI, 40 % FCS and 10 % DMSO. Portions of the solution containing approximately 1×10^6 cells were distributed into cryotubes (Cellstar, Greiner Bio-one, UK). The cryotubes were frozen at -80˚C and subsequently transferred into liquid nitrogen (-196 ˚C) containers for long-term storage.

2.1.3 Culturing from frozen stocks

Cells were removed from the liquid nitrogen and warmed in an incubator at 37˚C. A warmed medium solution was added and centrifuged at 212 × g for 5 min. Medium was removed and the pellet was resuspended in fresh warmed medium, which was transferred into a T25 flask with a surface are of 25 cm^2. Medium was replenished daily and cells were passaged at least twice before being used experimentally.

2.1.4 Cell count

For experimental analysis, cells were counted prior to seeding into new flasks. For this, 13 µl of the cell solution obtained using the procedure outlined in section 2.1.1 were pipetted between a glass cover slip and haemocytometer. The solution is drawn under the cover slip due to capillary action. Cells were counted in each square using a light microscope where the volume of each square is 0.1 mm^3 and therefore the number of cells counted is multiplied by 10,000 to give the total number of cells per ml.

2.1.5 Growth analysis

A growth curve quantifies the growth of a cell specifically highlighting the lag time, doubling time (DT) (in exponential growth) and saturation density. The lag time is the length of time (in h) for the cells to recover from subculture and before entering into the exponential log phase. Once in log phase the cells multiply in population exponentially and the time taken for the population of cells to double can be quantified, which is known as the DT. Cells eventually reach a saturation density known as the plateau phase, whereby the culture achieves confluency and the growth rate either stops or considerably reduces.

Cells were seeded into 6 cm^2 Petri dishes, with a surface area of 9.5 cm^2, at a density 2,000 cells/cm^2. Cells were seeded to enable triplicate cell counts at 24, 48, 72, 96 and 168 h

intervals. After seeding, the remaining cell solution was counted to further ensure the accuracy of seeding. Where the variance was greater than 10 % the experiment was rejected. Cells were incubated under normoxia at 37 ºC and 5 % CO_2 for the duration of the experiment. At each time point the medium was aspirated, washed with PBS, trypsined from the Petri dish, fresh medium added to resuspend cells before cell count using a haemocytometer. Data were inputted into Graphpad® (Graphpad, CA, USA) where it was plotted and the DT calculated.

2.2 Seeding density analysis

Cells were seeded into 6 well plates (1.5 ml) at a total of 25,000, 50,000, 100,000, 150,000, 200,000 and 400,000 cells/ml. The volume of medium applied was selected based on the working medium volume suggested by the manufacturer. The analysis was repeated in triplicate. Cells were cultured in normoxic conditions to allow the cells to adhere. Subsequently, the cells were subjected to oxygen potentials of normoxia, hypoxia or anoxia for 16 h. After 16 h, cells were exposed to 1 µM of doxorubicin for a further 24 h. The extracellular solution was discarded and the intracellular metabolites were extracted following the procedure outlined section in 2.7.2. The extracted pellets were lyophilised (HETO VR MAXI with RVT 4104 refrigerated vapour trap; Thermo Life Sciences, Basingstoke, U.K) by freeze drying in a high vacuum and weighed on a balance (Mettler Toledo, Leicester, UK). Data were inputted into Graphpad® where it was plotted.

2.3 Determination cell viability by MTT analysis

An MTT (3-(4,5-dimethylthiazol-2-yl)-2,5-diphenyltetrazolium bromide) assay measures the cell proliferation through calculating the enzyme activity of metabolites such as NADH that reduce MTT[117]. MTT is a tetrazole that is reduced from a yellow solution to formazan, a purple solution[117]. A solution of DMSO is added to the MTT solution to dissolve the insoluble formazan crystals. The absorbance of formazan is read on a spectrophotometer at 565 nm. Reduction of MTT by living cells is dependent on exponential growth of viable cells, cell population, and growth conditions.

FaDu or MDA-MB-231 cells were seeded in 200 µl of media at a total of 1000 cells/ml in a 96 well plate and allowed to adhere for 24 h. Cells were cultured in normoxic, hypoxic or anoxic conditions for 16 h followed by a further 24 h of drug treatment. Doxorubicin was dosed over the range of 1.5-0.001 µM. The medium was replaced with fresh medium and cells were allowed to incubate in normal oxygen conditions for a further 5 d before

performing the MTT assay. Medium was aspirated before adding 200 µl of a solution containing 20 µl MTT (2.5 mg/ml in PBS) and 180 µl medium, which was incubated at 37 ºC for 4 h under dark conditions. The MTT solution was removed and 100 µl DMSO added to each well. Plates were placed on a plate shaker (Titramax 1000, Heidolph, Germany) for 5 min before being read on a microtiter plate reader (BioTek, Vermont, USA) at 565 nm using Gen5 software (BioTek, Vermont, USA). Data were exported into Graphpad® where it was plotted and the IC_{50} was calculated.

2.4 Determining HIF-1 activity

Cells were seeded in a 96 well plate, at a volume of 200 µl media and 150,000 cells/ml, which was allowed to adhere for 24 h. Prior to incubation in various oxygen conditions, cells were infected with an adenovirus containing a firefly luciferase reporter construct linked to the lactate dehydrogenase hypoxic response element sequence for 4 h [118]. The multiplicity of infection was 20 viral particles per cell. Cells were cultured in normoxia hypoxia or anoxia conditions for 5 h followed by a 12 h doxorubicin exposure at 0, 0.1 or 1 µM. Medium was removed from cells and were washed twice in PBS, before applying 50 µl of passive lysis buffer (PLB) (1 part PLB, four parts distilled water) (Promega UK Ltd, Hampshire, UK). Luciferase activity was analysed using a kit (Promega UK Ltd, Hampshire, UK). Optima software was used to operate a MicroLumat LB 96 luminometer (EG & G Berthold, UK) to measure the luminescence following a present protocol developed in-house[118]. Data were exported into Graphpad® where it was plotted.

2.5 Flow cytometry sample preparation

Cells were seeded into 10 cm Petri dishes and the experiment was carried out as outlined in section 2.1. Following treatment, metabolites were extracted whilst cells remained in the experimental oxygen level. Cells were trypsined from the culture dish surface before being fixed in 1 ml of (ice cold) 70 % ethanol whilst vortexing to prevent cells clumping. Cells were centrifuged, in 1.5 ml Eppendorf tubes, at 64 × g before being resuspended in staining buffer containing 50 µg/ml propidium iodide, 50 µg/ml ribonuclease A and 0.1 % v/v triton x-100 in PBS for 30 min. Samples were centrifuged and resuspended in PBS before being analysed by flow cytometry.

2.5.1 Flow cytometry analysis

All analysis was undertaken on a Partec CyFlow® ML (Paratec GmbH, Münster, Germany) Fluorescence-activated cell sorting bench top flow cytometer at a flow rate of

1 µl/sec. 100 µl of sample was diluted in 1 ml PBS prior to analysis. The gain of the forward scatter (FSC) was optimised (measured using a 488 nm laser) at 100 and side scatter (SSC) was 150 on the $\log_3$ scale so that the cells formed a cluster in the middle of the 3-log decade scale. The analysis was gated based on the FSC and SSC to ensure only cells were counted as events and omitting any cell debris as shown in Figure 14. Subsequently, cells were gated on the fluorescence of the area and width as shown in Figure 15. Fluorescence of PI was measured using a 488 nm excitation laser and a 536/40 nm emission filter. All samples were analysed prior to normalisation, where the smallest sample size detected (5000 cells) was selected and data were rerun from file to ensure all data represented the same number of cells. This was done using FloMax® v.2.7 (Quantum Analysis). Software and the gated data were exported from here to Microsoft Excel® for further data analysis.

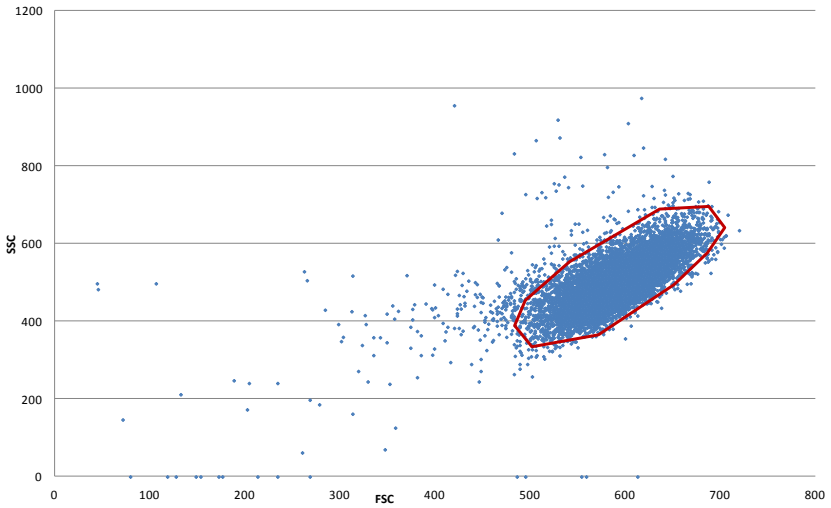

Figure 14: Forward scatter (FFC) *vs*. side scatter (SSC) events for MDA-MB-231 cells to demonstrate gated region 1 (shown in red). Gating based on the FSC and SSC ensured only cells were counted as events omitting cell debris.

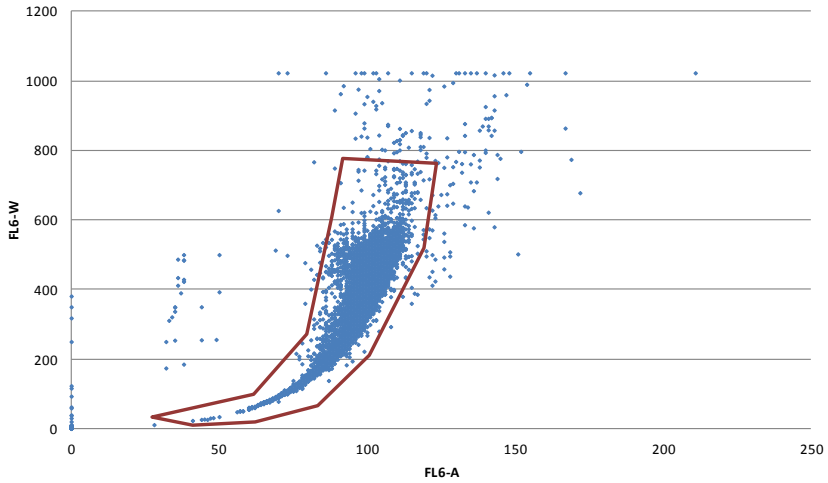

Figure 15: FL6-A (area) *vs*. FL6-W (width) demonstrating the area selected for gated region 2 (shown in red) for flow cytometry.

2.5.2 Flow cytometry data processing

Using Microsoft Excel®, a histogram of the events against fluorescent area was generated where phases of the cell cycle G_1 was present at ~200 and G_2/M at ~400. Here, G_1 is gap phase 1, S is DNA replication phase, and G_2/M is gap phase 2 mitosis in the cell cycle. A percentage of cells in each phase was calculated by summing the left half of the events of peak G_1 and the right half of G_2/M and multiplying each value by two. These areas are marked in Figure 16. S phase was calculated as the events of the area from the right of G_1 to the left of G_2/M minus half of that calculated for G_1 and G_2/M. Subsequently, each phase was converted into a percentage.

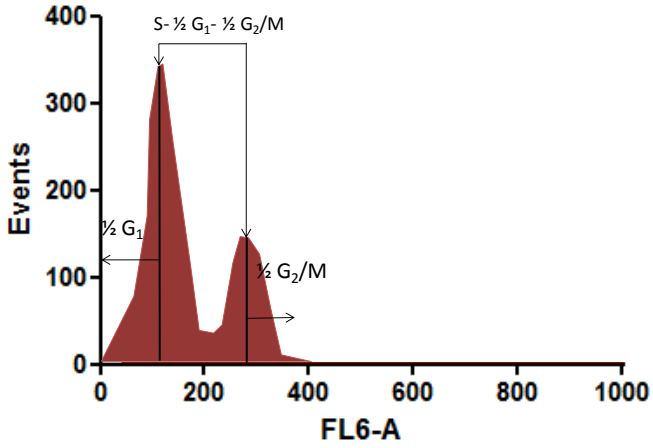

Figure 16: After all gating, a histogram of the fluorescent area was generated to determine the percentage of cells in the G_1, S and G_2/M phase of the cell cycle. Arrows indicate area used to calculate the percentages.

2.6 Measuring metabolite concentrations in the extracellular media

MDA-MB-231 cells were seeded into 10 cm Petri dishes and the experiment was carried out as outlined in section 2.1 with a doxorubicin treatment at the concentration 0, 0.1 or 1 µM. After this period, the medium was recovered each hour over a period of 6 h to determinate the glucose uptake, glutamine uptake and lactate efflux. For each time point 100 µl of medium was removed from the same Petri dish. The samples followed a linear trend over the 6 h and therefore the flux was calculated by taking the difference of the metabolites concentration in the starting medium to the 6 h point. Absorbance values of glutamine, lactate and glucose were converted into concentrations using a standard curve. All samples were analysed as three biological repeats and standards were analysed in triplicate. These concentrations were converted to rates by correcting for the weight of the dry pellet of cells in grams at the end of the assay and the length of the sampling in h.

2.6.1 Glucose uptake

A glucose assay kit (GAHK-20, Sigma Aldrich, UK) was used to measure the concentration of glucose present in the extracellular medium. The assay oxidises glucose and ATP to glucose-6-phosphate and ADP using the enzyme hexokinase (HK). Glucose 6-phosphate and NAD are converted to 6-phosphogluconate and NADH by the enzyme glucose-6-phosphate dehydrogenase (G6PDH). The absorption is measured at 340 nm is directly proportional to the concentration of glucose present in the sample[119].

To begin, a standard curve was generated from a 1 mg/ml glucose stock solution (provided by the kit). Serial dilutions of glucose were prepared at 0.5, 0.25, 0.125, 0.063, 0.031, 0.016, 0.068 and 0 mg/ml. The HK reagent provided was dissolved in 20 ml deionised water prior to use. A total of 20 µl of the serial dilutions were pipetted into a 96 well plate. Additionally, 5 µl of the extracellular samples and 15 µl of water were pipetted into other wells in the 96 well plate. To all wells containing sample or standard 100 µl of glucose assay was added. The plate was incubated at 37 ˚C for 15 min and read on a microtiter plate reader (BioTek, Vermont, USA) at 340 nm using Gen5 software. Data were exported into Graphpad® where it was plotted. An example of the glucose standard curve is shown in Figure 17 demonstrating the concentrations of glucose were in the linear range of the assay.

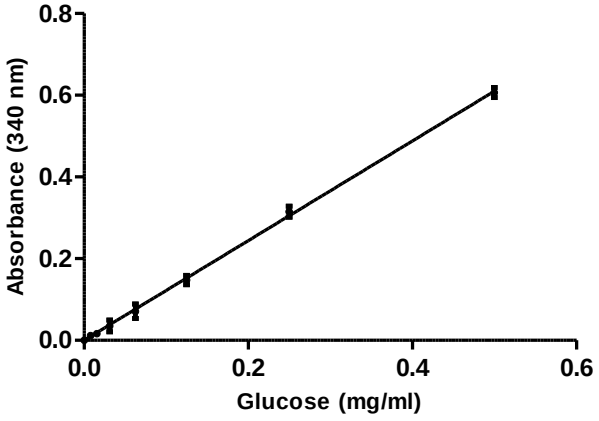

Figure 17: Glucose standard curve ranging from 0-0.5 mg/ml. Data are means ± s.d. (*n*=3) and R^2 = 0.9973.

2.6.2 Glutamine uptake

A glutamine assay kit (EGLN-100 BioAssay systems, Hayward, USA) was used to measure the concentration of glutamine present in extracellular medium. The assay converts glutamine to glutamate and ammonia using the enzyme glutaminase. Subsequently, glutamate and oxygen are converted to α-ketoglutarate, peroxide and

ammonia using the enzyme glutamate oxidase[120]. MTT is reduced from a yellow solution to formazan, a purple solution by peroxide, which is measured at 565 nm.

A standard curve was produced for a range of glutamine concentrations provided in the kit. Serial dilutions of glutamine were prepared from a 100 mM stock solution at 2, 1, 0.5, 0.25, 0.125, 0.063, 0.031 and 0 mM. A total of 20 µl of each of the glutamine standards were pipetted into a 96 well plate. Additionally, 5 µl of the extracellular samples were pipetted into additional wells of the 96 well plate to which 15 µl of deionised water was added. This was done twice to account for both glutamine and glutamate in the samples. The working solution was prepared through combining 65 µl assay buffer, 1 µl enzyme A, 1 µl enzyme B, 2.5 µl NAD, 14 µl MTT. The working blank was prepared through combining 65 µl assay buffer, 1 µl enzyme B, 2.5 µl NAD, and 14 µl MTT. For glutamine measurements of both the sample and glutamine standards, 80 µl of working solution was added. For glutamate measurements of the samples, 80 µl of working blank was added. After 40 min at room temperature 100 µl of stopping reagent was added to all samples and standards. The plate was read on a microtiter plate reader (BioTek, Vermont, USA) at 565 nm using Gen5 software. Data were exported into Graphpad® where it was plotted. An example of the glutamine standard curve is shown in Figure 18 demonstrating the concentrations of glutamine are in the linear range of the assay.

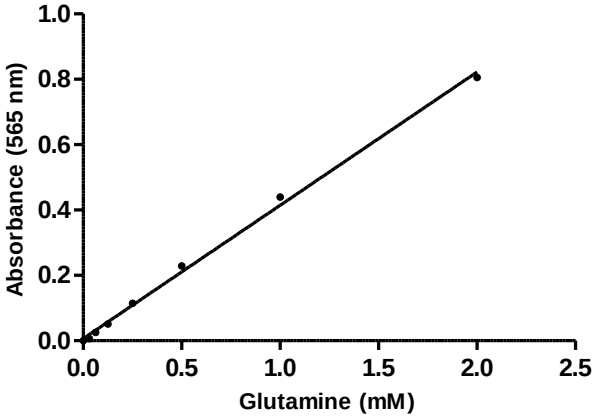

Figure 18: Glutamine standard curve ranging from 0-2 mM. Data are means ± s.d. (*n*=3) and R^2 = 0.9970.

2.6.3 Lactate efflux

A lactate assay kit (Trinity biotech, Bray, Ireland), was used to measure the concentration of lactate in extracellular medium. The assay converts lactic acid to pyruvate and H_2O_2 by the enzyme lactate oxidase. The peroxide formed in the reaction catalyses the oxidative condensation of chromogen precursors, which generates a purple coloured dye[121].

Absorption at 540 nm is directly proportional to the concentration of lactate present in the sample.

A standard curve was produced from a 1 mg/ml lactate stock solution. Serial dilutions of lactate were prepared at 0.094, 0.047, 0.023, 0.012, 0.059, 0.029 and 0 mg/ml. The lactate reagent provided was dissolved in 10 ml deionised water prior to use. A total of 20 µl of each of the serial dilutions were pipetted into a 96 well plate. Additionally, 2 µl of the extracellular samples and 18 µl of deionised water were pipetted into the 96 well. To all wells containing sample or standard 50 µl of lactate reagent was added. All samples were analysed as three biological replicates and the standard in triplicate. The plate was placed on a plate shaker (Titramax 1000, Heidolph, Germany) for 15 min and read on a microtiter plate reader (BioTek, Vermont, USA) at 540 nm using Gen5 software. Data were exported into Graphpad® where it was plotted. An example of the lactate standard curve is shown in Figure 19 demonstrating the concentrations of lactate are in the linear range of the assay.

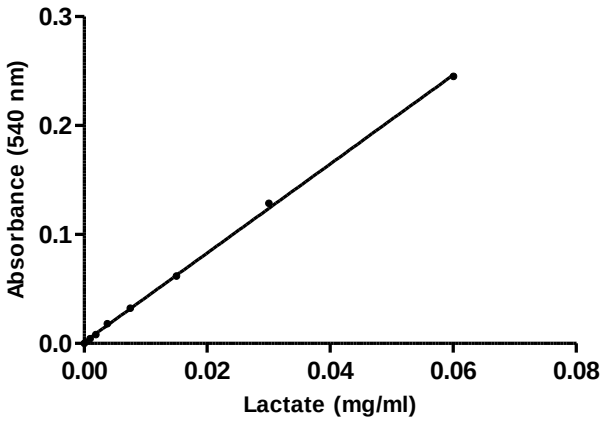

Figure 19: Lactate standard curve ranging from 0-0.094 mg/ml. Data are means ± s.d. (*n*=3) and R^2 = 0.9994.

2.7 Metabolomics

Metabolomics analysis was performed by GC-MS and ultra high performance liquid chromatography mass spectrometry (UHPLC-MS). This was to maximise the coverage of metabolites detected[67].

2.7.1 Metabolomics sample analysis

Complete medium was prepared with the same batch of FCS for all metabolomics experiments. FCS is an undefined solution and therefore different batches cannot be assumed to contain the same concentrations of biological compounds such as metabolites and proteins. MDA-MB-231 cells were seeded into 10 cm Petri dishes. Experimental

analysis followed that outlined in section 2.1. Cells were dosed with 0, 0.1 or 1 µM doxorubicin for 24 h. Control samples were not treated with doxorubicin. Following treatment, metabolites were extracted whilst remaining in the predefined oxygen condition.

2.7.2 Metabolite extraction

Extracellular medium was removed from the Petri dishes and 1 ml was aliquoted into an Eppendorf tube for extracellular metabolite analysis. Subsequently, cells were washed with three 1 ml aliquots of PBS. This was to remove remaining medium coating the cells that could result in the inaccurate quantification of intracellular metabolites. A total of 1 ml of methanol, at -48 ˚C, was added to each dish to quench the metabolism[122]. Methanol is an organic solvent that is used to fix cells whilst enabling the authentic state of the cell to be retained. Methanol dehydrates the cells and precipitates the proteins, which can be removed in the pellet. Usually trypsin is used in cell culture to detach adherent cells, however this method is time consuming compared to instantaneously quenching metabolism using methanol. Further the simple method of applying methanol to quench metabolism of adherent mammalian cells instantly has been shown to increase the number of metabolites detected by a factor of 50 compared to trypsin[122]. Cell scrappers were used to detach adherent cells from the Petri dish allowing the intracellular metabolites to be extracted into the methanol. The cell/methanol solution was transferred into a pre-weighed Eppendorf tube and subjected to three freeze thaw cycles. In this process samples were immersed in liquid nitrogen and thawed on dry ice. Subsequently, cells were centrifuged at 17000 × g for 15 min to separate the pellet from the supernatant. The supernatant was transferred into a fresh Eppendorf tube for analysis and the pellet was lyophilised and weighed. The volume of supernatant lyophilised was normalised according to the weight of the pellet for intracellular samples. When QCs were used, 150 µl of supernatant remaining after normalisation was pooled from each sample to generate a QC solution. Aliquots (1 ml) of the QC solution were placed into Eppendorf tubes. Subsequently, supernatant for both sample and QC was lyophilised.

2.7.3 Gas chromatography mass spectrometry (GC-MS)

GC-MS can detect a range of metabolites including amino acids, organic acids and sugars, and is therefore a popular choice for metabolomics studies [7, 8]. Furthermore, stable ionisation and reproducible fragmentation patterns that arise from using electron ionisation (EI) helps metabolite identification[123]. GC is typically used to analyse compounds that are volatile or compounds that can be made volatile by derivatisation[124].

GC is a front end separation technique for separating and analysing compounds that readily vaporise. Each compound interacts with the stationary phase, which in this case is the column, whilst being transported through the column by the mobile phase, which in this case is the carrier gas. For GC the mobile phase carrier gas is typically an inert gas such as helium. The stationary phase of the column is governed by the type of species in the sample, however the column generally comprises of a microscopic layer of polymer on an inert solid support. Approximately 5 µl of sample is injected into the pressurised injection port operated under high temperature. This causes the sample to vaporise and the analytes enter the column. Each analyte interacts differently with the column during transportation causing separation of the sample. The separated solution elutes from the column and enters the mass analyser. The mass spectrometer provides structural information enabling chemical identification[125].

After the compound is eluted from the column it passes into the mass spectrometer where it is ionised and fragmented by an ionisation source. The fragmented ions are subsequently detected in the mass analyser. Figure 20 is a diagram illustrating the process of ion generation through electron ionisation. Electrons are released from a heated filament and accelerated at 70 eV (the de Broglie wavelength) in the direction of the anode. Introduced perpendicular to the stream of electrons is a flow of gaseous molecules. At 70 eV the electrons energy matches the typical bond length of an organic molecule (~0.14 nm), which is the optimum energy for maximum ionisation efficiency [126]. Energy higher that 70 eV ionise fewer molecules as the wavelength of the electron becomes smaller than the bond length of organic species. The electrons collide with the gas phase molecules causing a large fluctuation in the electric energy field generating positively charged ion fragments. These ions are then directed into the mass analyser[126]. EI generates fragmentation patterns, which are characteristic of the molecule and reproducible, which reduces instrument-to-instrument variability. These spectra can be compared to spectral libraries to identify the compound present in the sample.

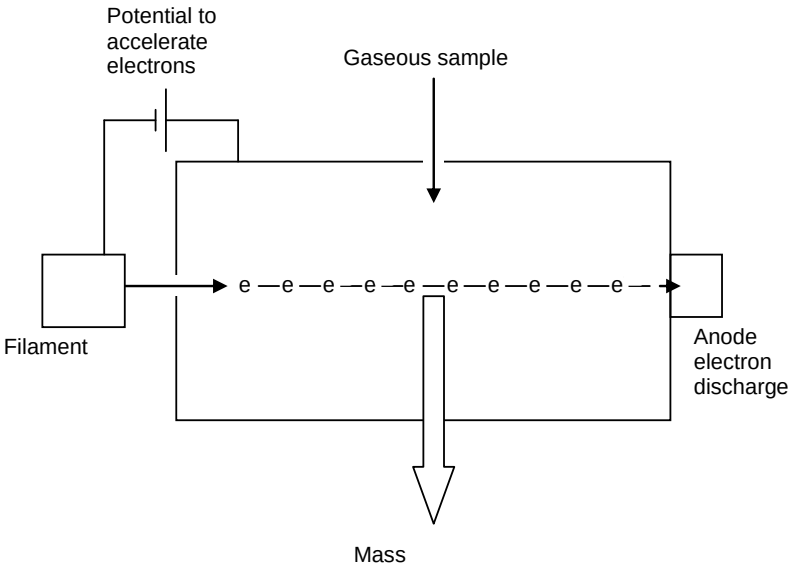

Figure 20: Diagram for the process of electron ionisation. The sample is introduced into the stream of electrons in the gas phase. The sample becomes ionised before entry into the mass spectrometer.

ToF is a method to determine the time taken for an ion to pass though the mass analyser and reach the detector (Figure 21). The ToF is a long straight tube with a source at one side of the mass analyser and a detector at the other. The ions are accelerated into the electric field of the ToF to the same kinetic energy; however the velocity of the ion varies depending on the mass-to-charge (*m/z*) ratio (therefore heavier particles have lower speeds). In theory all ions with the same *m/z* have the same kinetic energy as shown in Equation 1. As a result, ions with the same kinetic energy but a lighter mass will travel faster than those with a heavier mass[125].

$$KE = \frac{1}{2}mv^2$$

Equation 1: Kinetic energy (KE) where *m* is the mass and *v* is the velocity[125].

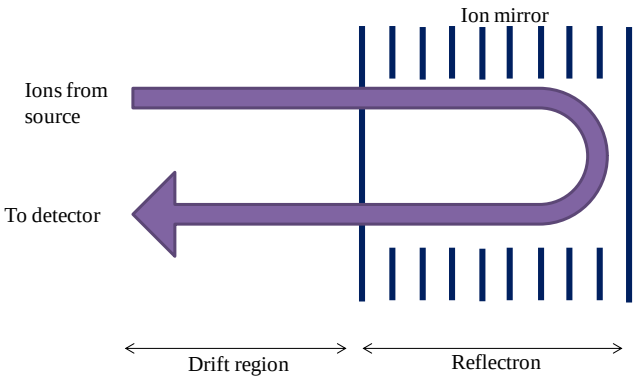

Figure 21: Schematic diagram of a time-of-flight (ToF) mass analyser. Ions are separated on their mass-to-charge (*m/z*) ratio. In reflectron mode ions are electrostatically reflected back through the mass analyser. This improves the mass resolution through minimising small variations in kinetic energy of ions.

Theoretically, for linear ToF the acceleration voltage is applied to ions with distinct initial velocities per *m/z.* In practice, however, a spread in kinetic energy can arise due to the vaporisation and ionisation. Using a reflectron ToF-MS, the spread of flight times of ions with the same *m/z* ratio are diminished through reversing their flight path, which improves the mass resolution. An ion mirror uses an electrostatic field to reflect the ions, changing their path towards the detector. Ions with the same *m/z* but more kinetic energy penetrate deeper into the reflectron creating a longer path length to reach the detector[125]. ToF mass analyzers are typically used in metabolomics studies, as they have high sensitivity, high acquisition rates and acquire accurate mass data[127].

2.7.4 Derivatisation of metabolites prior to GC-MS Analysis

Metabolites need to be chemically derivatised and this is used to decrease the boiling point enabling metabolites to be adequately volatile to pass through GC columns directly at temperatures reaching 350 ˚C[125]. The method transforms polar molecules into volatile compounds suitable for GC-MS through replacing polar groups such as N-H, O-H and S-H with bulky non-polar groups. The chemical derivatisation process varies depending on the polarity of the metabolite compound and can be done through alkylation, acylation or silylation[128]. In the current work silylation was used to replace polar groups with bulky methyl groups. This method derivatises a range of metabolites as it has been shown to alter many functional groups including many hydroxyls, ketones, carboxylic acids, thiols and amines[129]. Oximation converts ketones to oximes, which are subsequently derivatised by trimethylsilylation (TMS). TMS replaces the hydrogens with a trimethylsilyl group, which reduces the intra and inter-molecular hydrogen bonding and subsequently reduces the boiling point of the molecule[130].

A total of 100 µl internal standard solution (0.18mg/ml succinic d_4 acid in water) was added to each sample and subsequently lyophilised for 3 h. Chemical derivatisation was carried out in a two step procedure of Oximation and TMS. Firstly, 50 µl of 20 mg/ml O-methoxylamine hydrochloride in pyridine was added to resuspend the extract, followed by vortexing and incubation at 60 ˚C for 30 min in a dri-block heater. Secondly, 50 µl of N-methyl-N-trimethylsilyltrifluoroacetamide (MSTFA) was added to the extract followed by vortexing and incubated at 60˚C for 30 min. On completion, extracts were centrifuged at 17000 × g for 10 min and 20 µl of the retention index marker solution was added (0.3 mg/ml docosane, nonadecane, decane, dodecane and pentadecane in pyridine) and the supernatant transferred into GC-MS vials for analysis[127]. Where several batches were

analysed, a single randomised batch of samples including QCs and a blank were derivatised together and analysed each day.

2.7.5 GC-MS analysis of cell lysates

QC samples included in each batch of samples were prepared from pooling small aliquots of each biological sample. These QC samples had a composition closely related to the biological samples. For the large-scale metabolomics study, a total of 8 batches were analysed. 7 batches contained 40 samples and 9 QCs each and 1 batch contained 30 samples and 9 QCs. All samples were randomised prior to analysis to prevent bias statistical analysis that occurs due to analytical drift. For the small-scale metabolomics protocol development study a single batch of samples were analysed.

Samples were analysed on an Agilent 6890 GC (Agilent Technologies, Stockport, U.K.) coupled to a LECO Pegasus III (Leco Corp., St. Joseph, MO) EI-ToF-MS. The GC-MS instrument setup used has been previously described [127, 131]. QCs were used to condition the GC-MS before sample injection as it has previously been shown, for serum, the first four injections on GC-MS are not reproducible[127]. This arises as areas in the GC initially become blocked with sample matrix, which can be alleviated after multiple injections[130]. Additionally, QCs were used to calculate the reproducibility of the metabolites detected. A total of 5 injections of QC samples were performed prior to analysing samples to normalise the chromatographic conditions to the sample matrix. Every 5 sample injections were followed with a single QC injection. In addition three QC injections were made at the end of each analysis. These QC samples were compared to account for the system stability in each batch analysed. Briefly, the temperature was set at 70 °C for 4 min followed by a 20 °C increase every min until 300 °C was reached and stabilised for 4 min. Samples were injected (2 μl) onto the column. The mass spectrometer obtained a *m*/*z* range of 45-600 [127]. The total duration to analyse a single sample was 25 min.

2.7.6 Processing of raw GC-MS data

The processing of raw GC-MS data were performed following the methods described previously, using the LECO ChromaToF v3.25 software package to apply the chromatographic deconvolution algorithm[127, 131]. Chromatographic peaks from the QC samples (or experimental samples when QCs were not required for batch correction) were selected from each analytical block were manually integrated and added to a database, which included the peak the retention index and mass spectrum to compile a reference

database. This reference database was manually inspected to ensure the mass spectra had the required fragmentation patterns and met the criteria for signal-to-noise (S/N) ratio and chromatographic peak width. Metabolites with fewer than 50 % of features detected in the QC were removed[130]. The system stability is shown in Figure 22 where a tight cluster of QC samples in the PCA scores plot suggests minimal analytical variation in the dataset. Ideally the QC samples are expected to reside in the middle of the samples on the PCA scores plot. This does not occur in these QC samples as the pooled QC solution did not contain an equal quantity of each of the sample types due some having a biomass too low to enable a QC aliquot to be taken.

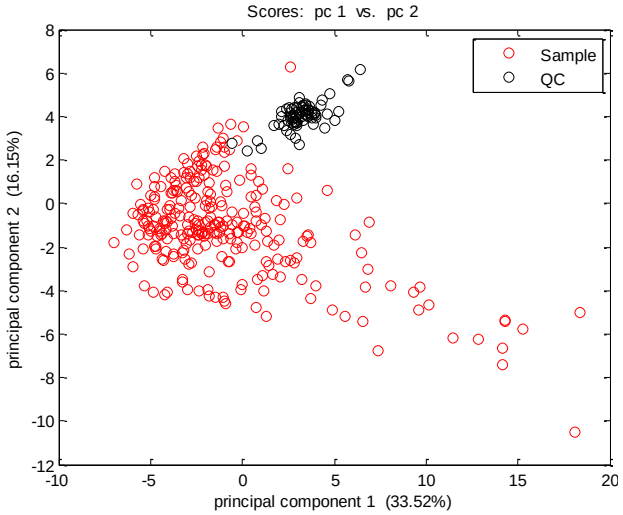

Figure 22: Principal component analysis (PCA) of 240 samples (red) and 75 QCs (black) to show the first two principal components (PC). The tight cluster of QC samples in the PCA scores plot suggests minimal analytical variation in the dataset.

Metabolites were identified by matching the mass spectrum and retention index of detected peaks to those present in an in house mass spectral library[132]. For a metabolite to be identified as having a high confidence match the chromatographic peak from the reference database was searched for in each of the sample where retention index deviation was less than ±30 and the mass spectral match was greater than 800. All other matches that did not meet this specification were not regarded as a high confidence match. The metabolite library was previously developed in-house from authentic standards at the University of Manchester. Metabolites that were not identified in the in-house database were searched against the Golm metabolome database[133], where a similar match score to the in-house database was applied[127]. The threshold used to identify metabolites is outlined by the metabolomics

standards initiative[134]. Chromatogram peaks areas were exported as an ASCII file into Microsoft Excel® before data analysis.

GC-MS was normalised to the internal standard succinic d_4 acid to account for the technical variability associated with chemical derivatisation and low sample injection volumes. For example, an error incurred by sample injection volumes can result in a different volume of sample being injected onto the column. Calculating the ratio of the peak area of the internal standard to metabolite compensates for this error.

Subsequently peak alignment and normalisation to succinic d_4 acid additional, pre-processing of the data were needed before analysis using algorithms such as PCA. The small-scale dataset comprised of cells cultured in normoxia, hypoxia or anoxia. In this dataset 163 peaks were integrated from the GC chromatogram of which 49 % were unidentified peaks. The large-scale dataset comprised cells cultured in normoxia, hypoxia or anoxia and treated with 0 µM, 0.1 µM or 1 µM doxorubicin. In this dataset 102 peaks were integrated from the GC chromatogram of which 45 % were unidentified peaks. Unidentified peaks were removed from the data matrix.

The coefficient of variation (CV) was calculated for metabolites detected in QC samples. Metabolites with a CV greater than 30 % were removed from the whole data matrix (including from the sample) as these were considered to have poor reproducibility[130]. A CV greater than 30 % could be caused during chemical derivatisation or due to the low sample injection volume[130]. A total of two metabolites had a CV > 30 % and were removed from the large-scale dataset.

An outlier is defined as a data point with values that are not in keeping with the majority of the other data points. A method to rapidly identify outliers is to determine the relative ratio of the median and mean of the distribution. When the ratio reveals the metabolite is more than three deviations away from the mean the outlying data point was replaced with an average from each group[135].

2.7.7 Missing values

A missing value is recorded when a peak is not detected for a metabolite in a sample. There are many options to overcome the issue of missing data points including replacing the value with the average or median from other samples or replacing the value with a

zero[94]. Simply removing those samples with missing values is another option however potentially valuable data values are also deleted. For statistical and correlation analysis, missing data remained in the matrix as not a number (NaN) as these algorithms can be performed on data that includes NaNs. For MVA the algorithm cannot be carried out on data containing missing values and therefore was replaced with a zero[94].

2.8 Ultra high performance liquid chromatography mass spectrometry (UHPLC-MS)

Analysis using both GC-MS and reversed-phase UHPLC-MS can detect a greater coverage of the metabolome. Furthermore, only a limited number of metabolites can be detected on both platforms such as tryptophan and phenylalanine[136]. Previously, it has been shown that combining the two techniques is able to detect 93 % of commercially obtainable metabolites of *Bacillus subtilis*[136]. GC-MS can detect metabolites including amino acids, fatty acids, carbohydrates, phosphorylated metabolites and cholesterol. Reversed-phase UHPLC-MS can detect higher molecular weight compounds of higher lipophilicity, such as lipids including glycerolipids, phospholipids, fatty acids, bile acids and sterols[130], but reversed-phase LC fails to retain polar metabolites on the column. UHPLC reduces the analytical run time compared to HPLC whilst maintaining the quality of separation[130]. UHPLC uses high pressure to pump a liquid solvent through a closed column to generate a high-resolution separation. The column is typically stainless steel and the stationary phase packed inside the column is typically bound to silica. The technique is selected when the analyte of interest is not sufficiently volatile for GC analysis. This includes analytes such as phospholipids, bile acids, glycosides, and sugars, which are typically greater than 600 Daltons. UHPLC can operate as normal-phase or reversed-phase chromatography. For metabolomics analysis, reversed-phase UHPLC was applied, which has a non-polar stationary phase and a polar mobile phase. This causes longer retention times for non-polar molecules and therefore is useful to separate non-polar metabolites[125]. This enables the separation non-polar metabolites detected in the range of 50-1,500 daltons[130]. The separated solution elutes from the column and enters the mass analyser.

Electrospray ionisation (ESI) is used to ionise the eluent from the UHPLC column[137]. The sample is initially dissolved in a volatile and polar solvent containing a trace of acid. The acid generates ions through protonating the Lewis base sites. The solution is pumped through a narrow stainless steel capillary and a high voltage is applied to the tip of the capillary generating a strong electric field. This causes the solution to spray from the tip of

the capillary to disperse into an aerosol of highly charged droplets. As the solvent evaporates the droplet contracts in size and this increases the charge concentration at the droplet surface. When the Rayleigh limit is reached the coulombic repulsion overcomes the droplet surface tension and the droplet bursts. The effect of the coulombic explosion generates a series of smaller lower charged particles. This process repeats until ions are formed[138]. Nitrogen gas is applied in the ionisation chamber to aid the direction of the spray from the capillary to the mass spectrometer, which is held under high vacuum[125].

The Orbitrap mass analyser used for these experiments consists of a barrel shaped electrode and a coaxial inner spindle electrode, which are used to generate an electrostatic field with quadrupole and logarithmic potential[139]. Ions orbit around the axial electrode and perform harmonic oscillations back and forth around the electrode. The frequencies of these harmonic oscillations are proportional to the square root of the *m/z*. Consequently, ions with a specific *m/z* oscillate along the spindle. Oscillations are detected using an image current detection and high mass accuracy (1-2 ppm) and high mass resolution resolving power (up to 150,000) have been demonstrated[139].

2.8.1 UHPLC analysis of cell lysates

Prior to analysis samples were reconstituted in 100µl water. Data were acquired as a single batch. Analysis was undertaken using an Accela UHPLC system coupled to an electrospray linear trap quadrupole Orbitrap Velos hybrid mass spectrometer (ThermoFisher Scientific, Hemel Hempstead, UK). The experimental setup for UHPLC-MS analysis has been previously described[130]. Both electrospray positive (ES+) and electrospray negative (ES-) ion modes were used to analyse the samples separately to increase the number of metabolites detected as some are only present in a single-ion mode, which is dependent on the acidity/basicity properties of the molecule. Solvent solutions (A; 0.1 % formic acid in water (vol/vol); B; 0.1 % formic acid in methanol (vol/vol)) were operated at a flow rate of 400 $\mu L.min^{-1}$ where 100 % A was held for 30 s followed by a 100 % increase in B for 4.5 min and subsequently held for 5.5 min. Subsequently, there was a switch to 100 % solvent A for 1.5 min. Eluting solution was transported to the orbitrap mass analyser (mass resolution 30,000 at *m/z* = 400) where a full scan profile was performed.

2.8.2 Processing of raw UHPLC-MS data

The UHPLC-MS raw data profiles were first converted into a netCDF format using the file converter programme in the Xcalibur software (ThermoFisher Scientific, Bremen, Germany). Peak deconvolution was performed using the freely available XCMS software as described previously[140]. Briefly, the data for each sample, which comprises the intensity, *m/z*, and time, were converted into a matrix of detected peaks against sample identification. Following the XCMS deconvolution, the matrix was exported to Microsoft Excel® for data processing. A total of 6183 metabolic features, with a retention time and unique accurate *m/z*, were detected for ES+ mode and 2284 for ES- mode. This related to metabolites and their related ions including the protonated ion, deprotonated ion, adduct ions (such as salts), isotopomers (such as ^{13}C and ^{34}S), fragment ions, dimmers and trimers[130, 141].

Metabolites with fewer than 50 % of features detected in the QC were removed. The CV was calculated for metabolites detected in QC samples only. Those metabolites with a CV greater than 20 % were removed from the whole data matrix (including sample) as these were considered to have poor reproducibility[130]. Following these steps 13 % of the peaks were removed for ES+ and 14 % for ES-.

Similar to GC-MS outliers were identified and replaced with an average. When the ratio reveals the metabolite is more than three standard deviations away from the mean the outlying data point was replaced with an average from each group[135].

Unlike GC-MS, UHPLC-MS data cannot be matched to mass spectral libraries due to the retention time not being reproducible between different systems. This is because different LC columns are used on different systems. Putative metabolite identification was carried out using PUTMEDID-LCMS workflows, which has been previously described[141].

2.8.3 Missing values

Missing values were treated in a similar manner to that described in GC-MS. For statistical change analysis, the algorithm could not be carried out on data containing missing values and therefore NaNs were replaced with zeros.

2.9 ToF- SIMS

Mass spectrometry came about in 1910 when J.J. Thomson measured the *m/z* of the electron[142]. His work led to the observation of emitted particles from sample surfaces

including positive ions, which is now known as sputtering and is the basis of secondary ion mass spectrometry (SIMS). Bombardment of the sample surface with primary ions, with energies in the range of tens of keV, causes collisions between the atoms, which sputter as fragments if the work function is overcome. A small proportion of the fragments sputtered are ionised and are detected by a mass spectrometer. If less than 1 % of the surface is impacted the technique is defined as static SIMS as statistically the point on the surface is only bombarded once [100]. Static SIMS with conventional monoatomic ion beams requires the primary ion dose to operate below 10^{12} ions/cm^2 to prevent the sample from undergoing chemical damage resulting in the loss of molecular information in the spectrum[100]. A ToF-SIMS image is generated by rastering the primary ion beam across the sample surface. A mass spectrum is acquired at each pixel and these are combined to generate the image[143]. Secondary ions are formed when primary ions bombard the sample surface transferring their energy in the process and as a result causes inter atomic collisions. Inter atomic collisions dissipate in all directions, some of which are directed towards the surface and emitted as secondary ions. The majority of the sputtered yield are emitted as neutrals, however a small proportion are ionised, which is a process dependent on the probability of ionisation of the chemical of interest in addition to the likelihood of de-excitation during release from the sample surface[143].

2.9.1 Primary ions options and secondary ion formation

Many primary ions beams have been developed each offering advantages and disadvantages, which can be optimised depending on the desired type of analysis. Many monoatomic primary ions have been developed that are widely used in the field of SIMS such as Ga^+ [144, 145]. These types of primary ions are particularly good for high spatial resolution imaging SIMS. Alternatively, cluster and polyatomic primary ion beams have been developed to increase the secondary ion yield compared to the monoatomic primary ions at a higher *m/z*. Cluster and polyatomic primary ions that are currently used includes Au_n^+, C_{60}^+, Bi_n^+ and SF_5^+ [145-148]. Polyatomic primary ions eject material in a nonlinear process known as mesoscale molecular motion rather than a collision cascade[149]. Moreover, the primary ion beam C_{60}^+ has an additional benefit over other polyatomic beams, such as Au_n^+, in that it is able to analyse beyond the static limit whilst preserving the initial spectrum, which is maintained throughout the depth profile[146]. This is explained by the difference in impact penetration of the polyatomic primary into the sample surface. Some polyatomic primary ions such as Au_n^+ penetrate deeper into the sample surface, whereas C_{60}^+ does not penetrate as deep due to the difference in the size and nuclearity of

the clusters that spreads the impact of the energy collision generating many collision cascades on the sample surface[150]. Deep primary ion penetration with Au_n^+ causes bombardment induced chemical damage and therefore is not used beyond the static limit[150].

The secondary ion current of the species of interest can be calculated using the basic SIMS equation as shown in Equation 2[143]. The basic SIMS equation states that the secondary ion current I_m is linearly dependent on the parameters $I_p.Y_m.\alpha^+.\theta_m.\eta$.

$$I_m = I_p.Y_m.\propto^+.\theta_m.\eta$$

Equation 2: The basic secondary ion mass spectrometry (SIMS) equation where I_m is the secondary ion current of the species m, I_p is the primary particle flux, Y_m is the total splutter yield, α^+ is the ionisation probability (in this case for positive ions), θ_m is the fractional concentration of the chemistry m in the surface layer (for a pure sample is 1) and η is the instrument transmission function[143].

The matrix effect occurs in a sample mixture where the presence of one species can enhance or prevent the ejection and/or ionisation of another species. The matrix effect is problematic when analysing biological species such as cells that contain many compounds. Sputter yield Y_m is defined as the number of species of component m ejected per primary ion, which is sample dependent and reliant on energy and type of primary ion beam. For example, as previously described, ion beams such as large clusters of C_{60}^+ penetrate into the sample to a lesser extent than Au_n^+ ion beams, which results in different sputter yields[151]. Ionisation probability is dependent on the species. The fractional concentration of the analyte of interest is influenced by the amount of species present therefore the more species the greater the secondary ion current. The transmission of conventional ToF-SIMS instruments are fixed, however the J105 3D chemical imager has a mass dependent transmission, which is influenced by the quadrupole and buncher (as described in section 2.9.2). The quadrupole radio frequency amplitude can be varied for low mass cut off and the buncher has low transmission for low mass therefore the transmission suffers when detecting very low mass species (<50 Da).

2.9.2 J105 3D Chemical Imager Instrument

The J105 3D Chemical Imager (Ionoptika Ltd, Southampton) has been developed at the University of Manchester to perform imaging ToF-SIMS. The instrument, shown in Figure 23, was developed within the Vickerman group in collaboration with Ionoptika Limited[152]. The J105 3D Chemical Imager is equipped with a Wien filtered 40 kV C_{60} primary ion gun and mounted at an angle of 45 °. Secondary ions are extracted when a voltage is applied to

the extraction optics. Extracted ions enter a quadrupole where they are collisionally cooled and focused. An electrostatic analyser filters out any uncooled ions and the remaining secondary ions pass into a buncher. As the mass spectrometry is de-coupled from the sputtering event, mass resolution is maintained regardless of the sample topography. Conventional ToF-SIMS instruments have a pulsed primary ion beam, which is created by moving the ion beam through an aperture. Short pulses produce good mass resolution, however spatial resolution is compromised and the small number of ions in each pulse increases the time required to acquire an image. The addition of a buncher allows the primary ions to bombard the sample in a continuous manner (direct current mode) whilst improving the mass resolution and increasing the duty cycle to allow imaging analysis to be carried out in a practical time frame. The buncher contains a series of plates and voltage is applied to the plates when the buncher 'fires'. The voltage applied to each plate is set so that the ions at the back of the buncher receive more energy than those closest to the exit of the buncher. Applying a distributed voltage to the ions acts to bunch the ions allowing them to be time focused into the ToF, which is important when the ions are to be separated purely on the time-of-flight. Ions accelerating from the buncher have more energy spread than those entering a conventional ToF, therefore a quadratic field along the ToF is needed and separation of the ions is dependent on simple harmonic oscillation where the flight time of the ions is due to the *m/z* and not the energy of the secondary ions. Primary ion sources can cause excess positive charge to accumulate on the sample surface. This often occurs in insulating biological samples, and is compensated by applying low energy electrons from an electron flood gun. High energy electrons can damage the sample surface and therefore only low energy electrons (<25 eV) are suitable. Additionally, the instrument has improved mass accuracy compared to other ToF-SIMS instruments available. Ions accelerated through the mass analyser at 20 keV are detected using a single microchannel plate attached to an analog to digital convertor (ADC) (Fast Flight, GmbH, Germany). The ADC detects ions arriving and reports this as a peak area, which is influenced by the size, speed and the number of ions simultaneously arriving at the detector with an identical mass. For all analyses undertaken in this thesis the duty cycle was 75 % and the data were down sampled to 0.05 Da bins due to file size limitations. For tandem mass spectrometry the precursor ion is selected and entered into the collision induced cell, where it fragmented by nitrogen gas. The parent ion and fragments then enter the ToF. Data were processed and analysed in MATLAB® version 7.8 (MathWorks Inc., Massachusetts, USA) using software developed in-house.

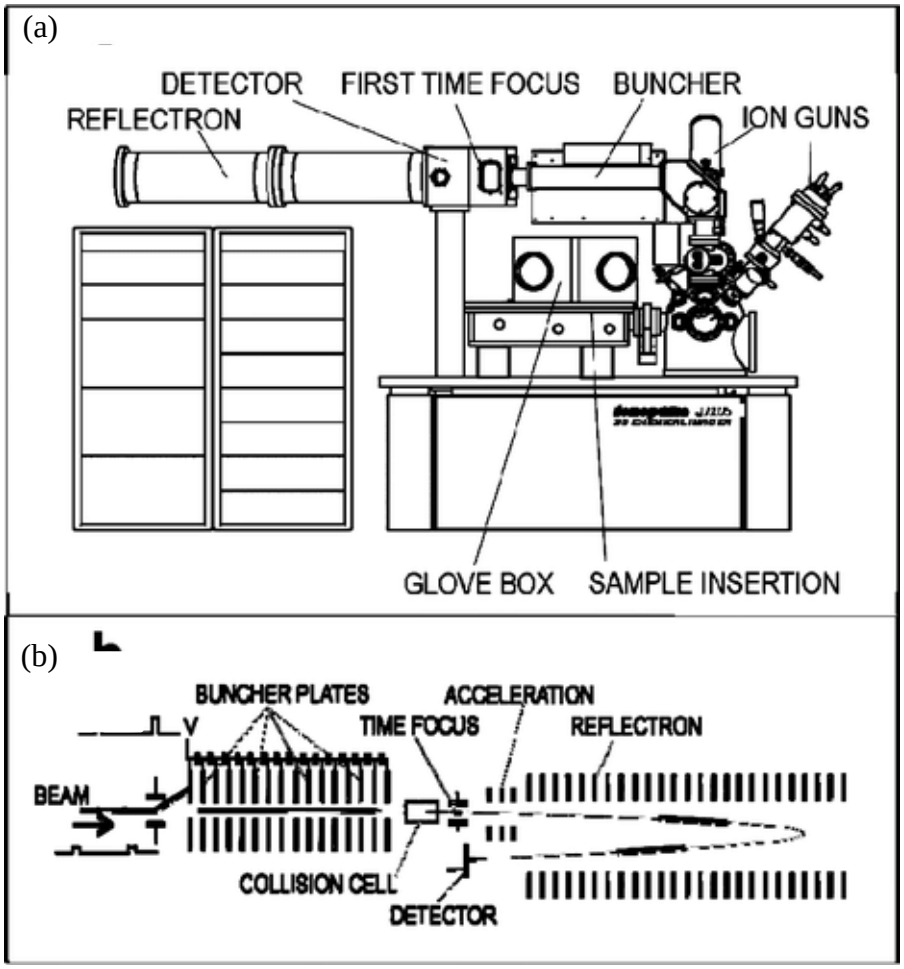

Figure 23: (a) A schematic of the J105 3D chemical imager developed by Ionoptika Ltd and SAI Ltd showing the location of features including sample insertion, ion guns, buncher and the reflectron. (b) An example of a section of the secondary ions bunched and introduced into the reflectron, where the collision cell is used for tandem mass spectrometry analysis. The J105 3D chemical imager has advantages over conventional SIMS instruments including the use of a continuous primary ion beam, minimised topography effects, increased the duty cycle, the ability to perform tandem mass spectrometry and improved mass resolution of biological imaging. (Image reproduced from reference[152]).

2.9.3 Preparation of silicon wafer

Silicon wafers were thoroughly washed in a range of solvents to ensure the samples were free from contamination. The silicon was washed in methanol, ethanol, chloroform and water to remove any surface contaminants prior to use.

2.9.4 Preparation of metabolite standards

Metabolites standards adenosine, carnitine, citric acid, citrulline, fructose, glutamine, glutathione, glutathione disulfide, lactic acid, methionine, myo-inositol, nicotinic acid, putrescine, succinic acid, thymine and uracil in addition to the therapeutic doxorubicin (Sigma Aldrich, UK) were prepared in water at a concentration of 1 mM before being spotted (2 µl) onto a clean 5 mm × 5 mm silicon wafer (Agar Scientific, Essex, U.K.). For all subsequent ToF-SIMS experiments, unless stated otherwise, a C_{60}^{+} primary ion beam was used operated at 40 keV (Ionoptika Ltd., UK) with a bombardment angle of 45 °.

Parameters specific to this experiment included operating the primary ion beam with 60 pA current, acquiring the image over a 300 × 300 μm^2 field of view using 16 × 16 dithered pixel accumulated in 200 shots per pixel, which provided a primary ion fluence of 1.6×10^{12} ions/cm^2. For tandem MS the same parameters were applied with the addition of the collision-induced dissociation (CID) gas volts being set to 50.

2.9.5 Sensitivity analysis

A 1 M stock solution of methionine was prepared by adding 0.149 g of methionine to 1 ml of water. Dilutions of the stock solution were prepared by diluting 1 µl into 1 ml of water to produce a 1 mM solution of methionine. This process was repeated to produce 1 µM, 1 nM and 1 pM solutions of methionine and 1 µl of each were spotted onto a cleaned 5 mm × 5 mm silicon wafer, which contained 1 pmol, 1 fmol and 1 amol of methionine respectively.

The primary ion beam operated with 178 pA current and 23 µm spot size. A 800 × 800 μm^2 field of view over 32 × 32 pixel accumulated in 500 shots per pixel, and 10 depth layers provided a primary ion fluence 6×10^{13} ions/cm^2. To ensure the entire spot was consumed, a series of 3×3 tiled images were acquired.

2.9.6 Cell lysate preparation

Cell lysates were prepared during metabolic profiling analysis as described in sections 2.7.1 and 2.7.2. After the supernatant was lyophilised each sample was reconstituted into 2 µl water and the whole sample was spotted onto cleaned 30 mm × 30 mm silicon wafer (Advent-rm, Oxford, UK). A total of 6 biological replicates were spotted for each sample type. Sample was dried and desiccated before being introduced into the J105 3D chemical imager.

Ziptips® (C18) (Millipore, MA, USA) are typically used as a single-step desalting method in protein studies. The Ziptip® is a pipette tip that contains a bed of chromatography resin bed at the end. When Ziptips® were used to prepare cell lysates the suggested manufacturer's directions were followed[153]. Lyophilised supernatants were reconstituted in 2 µl 0.1 % trifluoroacetic acid (TFA) (pH of <4). The Ziptips® was pre-wet in 50 % methanol and equilibrated using 0.1 % TFA solution. The column was loaded with sample through aspirating and dispensing the lysate solution for 10 cycles. The tip was washed with 0.1 % TFA solution for 3 cycles. 2 µl of 50 % methanol / 0.1 % TFA solution was

dispended into a clean Eppendorf tube (1.5 ml) and the sample on the column was removed through aspirating and dispending the eluent through the Ziptips® for 3 cycles. The eluent was lyophilised, reconstituted into 2 µl water and spotted onto cleaned 30 mm × 30 mm silicon wafer. Sample was dried and desiccated before being introduced into the J105 3D chemical imager.

The primary ion beam was operated with a current of 60 pA. Images were taken over an area of 500 × 500 μm^2 at 16 x 16 pixels and the C_{60}^+ was focused to a spot size of 10µm. One depth layer was acquired with 500 shots per pixel and primary ion fluence of 1.5×10^{12} ions/cm^2.

2.9.7 Multicellular tumour spheroid (MTS) preparation

FaDu cells were seeded into a T75 flask with 10^5 cells/ml and 30 ml RPMI1640 with 10 % FCS and 2 mM L-glutamine at 37 °C in water saturated 5 % CO_2/air. Flasks were positioned onto a microtitre plate shaker (Bibby Scientific Ltd., Staffordshire, UK) to prevent cells adhering to the culture flask and stimulate MTS formation. Flasks were continuously cultured and medium was replaced every 72 until the MTSs achieved ~500 µm diameter. MTSs were treated with doxorubicin at a concentration of 0 µM, 0.1 µM and 1 µM for 24 h. Subsequently, MTSs were stored in 3 % gelatine cubes at -80 ˚C. Sectioning was carried out on a cryostat-microtome (Bright, Starlet 2212, Instrument Company Ltd, Huntingdon, UK) under a temperature of -20 ˚C and 10 µm sections were thaw mounted onto cleaned 5 mm × 5 mm silicon wafer. Ammonium formate solution (0.15 M) (Sigma-Aldrich, Dorset, UK) was used to wash sections three times each for 1 min per wash before being dried on a spin caster (Laurell Technologies Corporation, Pennsylvania, USA) at 64 × g for 10 min to remove excess salts[154, 155]. Subsequently, samples were desiccated prior to ToF-SIMS analysis[156].

The primary ion beam was operated a 20 pA and focused to a spot size of 5 µm. Images were taken over an area of 1000 × 1000 μm^2 at 256 x 256 pixels with a total of 200 shots per pixel and primary ion fluence of 1.23×10^{13} ions/cm^2.

2.10 Fourier transform infra-red (FT-IR) spectroscopy

Fourier transform infra-red (FT-IR) spectroscopy was employed to develop a suitable protocol for the metabolic fingerprint analysis of MDA-MB-231 cells. Infrared is used to identify functional groups thus it is a suitable tool to determine the chemical fingerprint of

cells when coupled with chemometric analysis. The infrared (IR) region spans the electromagnetic spectrum from near-IR at 12500 cm^{-1} wavenumbers to far-IR at 10 cm^{-1} wavenumbers[125]. IR is passed through the sample and is absorbed; however some is transmitted to generate a spectrum of intensity (wavelength) *vs*. frequency (absorption intensity). Transmission is calculated as the ratio of the intensity of the radiant power from the sample (*I*) to the intensity to incident radiation I_0 and is related to absorbance (*A*) as shown in Equation 3.

$$A = \log_{10}(1/T) = -\log_{10}T = -\log_{10}I/I_0$$

Equation 3: Calculation of the transmission where the intensity of the radiant power from the sample is *I*, the intensity to incident radiation is I_0 and absorbance is *A*.

IR excites the atoms in molecules to vibrate as specific frequencies. A molecule that comprises of *N* atoms has *3N* degrees of freedom in the direction of the x, y and z axis. For linear molecules (such as CO_2) there are *3N*-5 degrees of freedom 2 are rotational and 1 is a translational vibrational mode. For non-linear molecules there are *3N*-6 degrees of freedom with 3 translational and 3 rotational vibrational modes. The various bending and stretching modes include asymmetric stretching, symmetric stretching, scissoring, rocking, wagging and twisting.

2.10.1 Sample preparation for FT-IR spectroscopy

MDA-MB-231 cells were seeded and cultured in normoxia prior to treatment. Subsequently, cells were cultured in normoxia, hypoxia or anoxia for 16 h followed by 0, 0.1 or 1 μM doxorubicin treatment for 24 h. Cells were washed three times with ice cold 0.85 % saline solution, resuspended in a 20 μl saline solution, and scraped into 1.5 ml Eppendorf tubes. Excess saline solution was removed from the pellet and the wet pellet weight was recorded. Cells were normalised to the wet pellet weight therefore the lowest mass was normalised to 20 μl of water. A 20 μl spot of pellet suspension was pipetted onto a silicon plate and dried at 37 ˚C for 20 min prior to FT-IR spectroscopy.

2.10.2 FT-IR spectroscopy

FT-IR spectroscopy was conducted on a Bruker Equinox 55 infrared spectrometer, operated using a motorised microplate module HTS-XT and a deuterated triglycine sulfate detector (Bruker Ltd.) as previously described[157]. Spectra were recorded from the dry pellet debris in transmission mode. A blank well on the silicon plate allowed the background reference spectra to be obtained before each measurement was collected. Each spectrum

was collected at a range 4000-600 cm^{-1} with a total of 64 scans at a 4 cm^{-1} resolution taking approximately 60 s per spectrum. Interpretation of the spectra acquired is shown in Figure 24 and breakdown of the groups responsible for the vibrations is shown in Table 2.

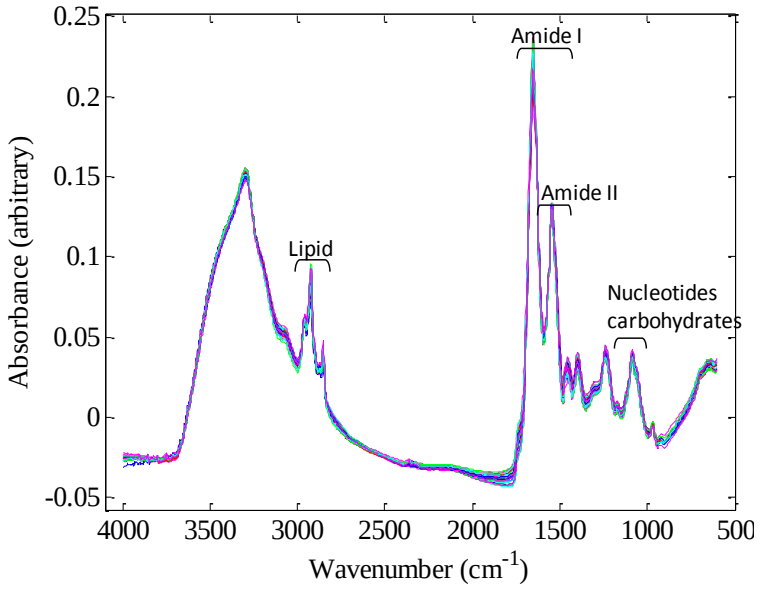

Figure 24: Fingerprint spectra produced by Fourier transform infra-red (FT-IR) spectroscopy of MDA-MB-231 cells exposed to various oxygen tensions and doxorubicin treatments. Spectra comprises of amides, nucleotides, carbohydrates and lipids. Cells were washed and extracted into saline solution and subsequent pellet normalisation accounted for the variation in cell biomass.

Table 2: Fourier transform infra-red FT-IR spectroscopy band assignment for intracellular and extracellular metabolism as identified in the literature [158].

Compound	Wavenumber (cm^{-1})	Assignment	FT-IR vibrational mode
Protein	~3400-3300	Amide A	Stretching mode of N-H
	~1690-1620	Amide I	N(C=O)
	~1590-1530	Amide II	Δ(N-H_ and ν(C-N)
Nucleotide	~1225		PO_2^- (asymmetric phosphate)
	~1080		PO_2^- (symmetric phosphate)
Lipid	~2924 and 2850	Membrane lipid	Symmetric CH2 stretch
	~2958 and 2873	Membrane lipid	Asymmetric CH3 stretch
	~1746		C=O
	~1463		CH2 bending
	~1165		Ester CO-O-C stretch
Carbohydrate	~1200-900		ν_s(C-O) coupled to the δ(C-O-H), ν_s(C-O-C), ν_s(C-O)
	~1030	Sugar(glycogen)	ν_s(C-O), ν_s(C-O-C)

2.10.3 FT-IR spectroscopy data pre-processing

The OPUS data files were extracted in MATLAB® using software developed in-house. The wavelengths corresponding to CO_2 were replaced with a trend of the spectrum. Data were scaled using extended multiplicative scatter correction[159].

2.11 Statistical analysis

Statistical analysis was performed on datasets acquired using GC-MS, UHPLC-MS, FT-IR and ToF-SIMS. A range of both UVA and MVA techniques were applied. All data analysis was undertaken using MATLAB®.

2.11.1 Data normalisation and data transformation

A univariate statistical test was selected based on the normalisation of the data. For each sample type a total of 30 biological replicates were analysed. This was not a sufficient number of data points for a histogram plot, which is the preferred option to determine the distribution of the data. As a result, a normality probability plot was used to assess whether each metabolite in each sample type could have originated from a normal distribution[160]. If the data followed a normal distribution the plot appears linear; however data that does not have a normal distribution does not follow a linear trend. For the GC-MS dataset, the addition of a constant and $\log_{10}$ scaling showed all metabolites followed a linear trend. Thus, GC-MS data were scaled and a parametric statistical test was used to analyse the data. Prior to analysis, GC-MS data were divide into groups of sample type and, for each metabolite, the outliers were detected when the distribution to the data were 3 standard deviations away from the mean. Subsequently, the data were transformed to have a normal distribution through adding 1.5 and $\log_{10}$ scaling. UHPLC-MS data did not follow a linear trend after scaling and therefore the data were analysed using a non-parametric statistical test.

2.11.2 Univariate analysis (UVA)

For GC-MS data, a parametric two-way analysis of variance (ANOVA) test of each metabolite was performed[161]. This test returned a *p*-value that relates to the mean difference in groups, variation in the data and the sample size. The *p*-value represents the likelihood of a metabolite having no real difference with respect to the various sample types, which is the null hypothesis. When a p-value < 0.05 is returned as there is a chance that there is a significant difference with respect to sample type. Although, this can also occur through random occurrence and there is no real difference known as the multiple testing problem[162]. For example, if a dataset containing 2000 biological samples was calculated to have a false discovery rate (FDR) of 10 % then 200 of the results would be false positives. If this test was performed on two independent metabolites the chance of them being a false positive is $1\text{-}0.90 \times 0.90 = 0.09$. To overcome this issue, the FDR was applied, which adjusted *p*-values for each test[163]. The *p*-value was adjusted by using a FDR

q-value (the confidence of the significant variable) of 0.1 to output the parametric *p*-value threshold[164, 165].

For UHPLC-MS data, Friedman analysis (a non-parametric statistical test) was used to compare the column effects in a two-way layout after adjusting for the row effects[161].When analysing the drug effect, for each metabolite, the column effect was dose of drug and the row effect was oxygen. Alternatively, when analysing the oxygen effect, for each metabolite, the column effect was oxygen and the row effect was dose of drug. Similar to two-way ANOVA the *p*-value was considered to be statistically significant when $p<0.05$. FDR was not applied to this dataset as the sample size was small (10 biological replicates). Alternatively a Bonferroni multi-comparison test could have been applied, however this only accounts for type I error (false positives) only and can increase the occurrence of type II errors (false negative)[166, 167]. Thus, there is a greater chance of ignoring a real relationship, which may be an important biological effect. To overcome false discovery, a box plot was outputted for each metabolite, which was observed manually to determine whether there was a difference in variance.

Statistically significant results from UVA were outputted as box and whisker plots. The top and bottom of each box represents the 25th and 75th percentiles of the feature, respectively. The central line in the box is the median value suggesting whether the feature exhibits skewness. The whiskers that expand above and below the box are the interquartile ranges to the furthest observation of the feature. Outliers, denoted by a red plus sign, are features that are 1.5 times the interquartile range from the top or bottom of the box.

2.11.3 Multivariate analysis (MVA)

MVA was used to identify metabolic differences associated with the sample condition and was undertaken using the MATLAB®. PCA is an unsupervised MVA technique, which was performed according to the singular value decomposition algorithm[168, 169]. This method is considered unsupervised as no prior knowledge regarding the sample groups is given in the analysis. PCA is a chemometric technique used to identify the combination of variables within the dataset to best describe the most significant trends. The technique can be used to compare similar samples to extrapolate peaks that cause a particular trend. This is a good method to identify metabolites with the greatest effect on inducing a particular separation. Outputted are a scores and loadings matrix where the scores represents the position of the sample and the loadings represents the input that each variable has for

causing configuration in the scores plot. The unsupervised technique reduces the dimensionality of the large dataset into a smaller set of non-correlated variables labelled principal components (PCs). The multidimensional data are projected into a lower dimensional space as a linear combination of variables labelled PC1, which contains the maximum variability about an axis of multidimensional space. Each variable is represented by an axis and it is the weighting of this that is described by the loadings. PC2 is the second largest variation, which is unrelated and orthogonal to PC1 and the percentage of the total explained variance (TEV) of PC2 is lower than for PC1. This process is repeated until the number of PC is equal to the number of variables.

MVA has a strong dependence on scaling as data dominated by a few intense variables has unequal weighting. There are many normalisation methods that can be used for MVA scaling, which includes taking the $\log_{10}$, square root, or quad root to reduce the dominating peaks in the dataset[170]. Prior to MVA both GC-MS and UHPLC-MS datasets were autoscaled so that the data were normalised to zero mean unit variance. This helps to ensure the MVA was not dominated by those variables with intense peak areas and therefore gives an equivalent weighting to low intensity peaks. Autoscale normalisation is particularly applicable when the peak area has been calculated compared to a spectra that includes noise as this will also be scaled and skew subsequent data analysis.

For ToF-SIMS, MVA methods such as PCA have been previously shown to be useful as a tool to classify a sample type or fragmentation patterns of biological samples and it has also been shown to be useful for improving image contrast[111, 171, 172]. Prior to MVA, the spectrum was normalised to total peak area and peak picked using an in-house reference library of metabolite standards. This list contained a total of 177 peaks relating to a range of metabolites including the molecular ion and related fragments and salt adducts. This reduced skewing of the PCA by non-biological spectral features such as silicon and other inorganic ions. PCA and image PCA were used to decrease the complexity of the data through distinguishing patterns of variables. The method was primarily used as a tool to determine which metabolite molecular ions and associated fragments were accountable for the difference. In-house scripts for MATLAB® were used to perform both PCA and image PCA where the Image Processing Toolbox was used to select a region of interest for image PCA. ToF-SIMS spectra are typically governed by a few intense peaks from secondary ions with high ionisation efficiency. In addition, there is a reduction in signal intensity with increased mass. As previously described, there are a variety of scaling methods that could

help to compensate for such spectral features For example, logarithmic scaling and autoscaling[172]. Both PCA and image PCA spectra were square root scaled to minimise the dynamic range of spectral intensity thus enabling separation to be influenced by less intense biological features[172].

DFA (also known as canonical variate analysis) is a supervised MVA approach and was used when the PCA did not display a clear separation of sample groups in the scores plot. As the method is supervised the test uses prior knowledge about the sample classes to perform the test. DFA was used to help distinguish groups through optimising the model by adjusting the number of PCs used to construct the model[173]. To prevent over fitting of the model, less than 95 % of the PC TEV was inputted into the algorithm[173]. The model was generated based on a training set, which was tested using a proportion of the data that was not selected in the training data. The test set is projected into the model space through measuring the Euclidean distance of the test data with regards to the training data and the accuracy of this projection is determined. The algorithm minimises the variation within a sample type (for each biological replicate) and maximises the variation between sample types through maximising the Fisher ratio. The Fisher ratio shown in Equation 4 is the class-to-class ratio variation divided by the sum of the within class variation. Similar to PCA, a scores and loadings plot is outputted.

$$((M_1 - M_2)^2)/(V_1 + V_2)$$

Equation 4: Fisher ratio where M_1 and M_2 are the mean of sample type 1 and 2 and V_1 and V_2 are the variance between the two sample types.

2.12 Network-based correlation analysis

The Pearson product-moment correlation coefficient was applied to the GC-MS data using the statistics toolbox in MATLAB®. The Pearson correlation coefficient of +1 describes a perfectly increasing linear relationship and -1 describes a decreasing anticorrelation[174]. Correlations close to zero are uncorrelated. A total of 30 biological replicates were extracted for each condition in order to minimise the biological variance in the dataset and to determine whether a correlation is statistically significant.

Biological replicates of the same state are required for correlation analysis as metabolite concentrations are expected to change with varying regulation. This perturbation from the mean state has been suggested to occur due to small differences in the parameters such as enzyme concentration, kinetic constants and the external environmental perturbations[93].

The number of biological replicates required to obtain a statistically significant correlation was calculated using Equation 5. Rearranging the standard error equation was able to determine the sample size needed to have a statistically significant correlation, as shown in Table 3. A standard error of 0.1 and a correlation of 0.70 can be inputted into Equation 5 to calculate the minimum sample size required is 27 (as highlighted in Table 3)[93]. This improved the statistical significance of the dataset, and minimised the error of observing false correlation.

$$SE = \frac{1-\rho^2}{\sqrt{n-1}}$$

Equation 5: Standard error (*SE*) equation where ρ is the correlation and *n* is the sample size [175].

Table 3: Application of the standard error equation (as given in Equation 5) to calculate the minimum number of samples required to accept a correlation ranging from 0.6-1 for a standard error values ranging from 0.01-0.12.

Standard error value	Correlation								
	0.60	0.65	0.70	0.75	0.80	0.85	0.90	0.95	1.00
0.01	4097	3336	2602	1915	1297	771	362	96	1
0.02	1025	835	651	480	325	194	91	25	1
0.03	456	372	290	214	145	87	41	12	1
0.04	257	209	164	121	82	49	24	7	1
0.05	165	134	105	78	53	32	15	5	1
0.06	115	94	73	54	37	22	11	4	1
0.07	85	69	54	40	27	17	8	3	1
0.08	65	53	42	31	21	13	7	2	1
0.09	52	42	33	25	17	11	5	2	1
0.10	42	34	27	20	14	9	5	2	1
0.11	35	29	22	17	12	7	4	2	1
0.12	29	24	19	14	10	6	4	2	1

Following Pearson's correlation, the difference between the pair-wise correlation coefficient for two sample types was calculated. To be considered a significant difference, one of the correlations must be greater than 0.7 and the difference between the correlations coefficients must be greater than 0.407. This was determined using the Fishers Z-transformation and permutation test as shown in Equation 6a and Equation 6b respectively.

$$\text{(a)}\quad Z_i = \frac{1}{2}\log\frac{1+C_i}{1-C_i} \qquad \text{(b)}\quad \hat{Z}^T = \frac{\left|z_1 - z_2\right|}{\sqrt{\frac{1}{N_1-3}+\frac{1}{N_2-3}}}$$

Equation 6: (a) Fishers Z-transformation where C_i is the Pearson's rank correlation coefficient For example, 0.7. (b) Permutation test for comparing correlations between metabolites, where $\hat{z}^T$ is a value that corresponds to the confidence of a correlation, z_1 and z_2 are the values calculated through equation 3a and N_1 and N_2 are the minimum sample sizes for each metabolite[176].

Table 4: The value for $\hat{z}^T$ with a significance of α[176].

Parameter	Significance (α)					
	10^{-6}	10^{-5}	10^{-4}	10^{-3}	0.01	0.05
$\hat{z}^T$	4.891638	4.4171173	3.890592	3.290527	2.575829	1.959964

Table 5: Application of the permutation test (Equation 6b) to calculate the significant correlation difference when $\hat{z}^T$ = 1.96. Correlation ranged from 0.6-1 and the sample size ranged from 15-30.

Sample number	Correlation difference							
	0.600	0.650	0.700	0.750	0.800	0.850	0.900	0.950
15	0.707	0.675	0.633	0.579	0.510	0.423	0.314	0.175
16	0.675	0.643	0.602	0.549	0.482	0.398	0.293	0.163
17	0.648	0.616	0.574	0.522	0.457	0.376	0.276	0.153
18	0.623	0.590	0.550	0.498	0.435	0.357	0.261	0.144
19	0.600	0.568	0.527	0.477	0.415	0.340	0.248	0.136
20	0.579	0.547	0.507	0.458	0.398	0.325	0.236	0.129
21	0.560	0.529	0.489	0.441	0.382	0.311	0.226	0.123
22	0.543	0.512	0.473	0.425	0.368	0.299	0.216	0.118
23	0.527	0.496	0.457	0.411	0.355	0.288	0.208	0.113
24	0.512	0.481	0.443	0.398	0.343	0.277	0.200	0.108
25	0.498	0.468	0.430	0.386	0.332	0.268	0.193	0.104
26	0.485	0.455	0.418	0.374	0.322	0.260	0.187	0.101
27	0.473	0.444	0.407	0.364	0.312	0.252	0.181	0.097
28	0.462	0.433	0.397	0.354	0.304	0.245	0.175	0.094
29	0.452	0.422	0.387	0.345	0.296	0.238	0.170	0.091
30	0.442	0.413	0.378	0.337	0.288	0.231	0.165	0.089

The Fishers Z-transformation approximately normalises the correlation coefficient to a Gaussian distribution for the correlation value. The normalised correlation coefficient was entered into a permutation test to calculate the difference between two correlations needed for the difference to be considered significant. The 95 % significance level was tested using Equation 6b to satisfy $\hat{z}^T$ = 1.96 shown in Table 4. For example, a correlation of 0.7 and a minimum of 27 samples must have a correlation difference of 0.407 to be statistically significant as highlighted in Table 5. Correlations were outputted as scatter plots and the correlation trends were observed.

Pair-wise correlations were mapped directly onto the uncompartmentalised EHMN[84]. The network was imported into MATLAB® using the SBML toolbox[177].Subsequently, the currency metabolites were removed. Currency metabolites are metabolites, such as water, that are present in scores of metabolic reactions. These compounds reduce the average path length connecting two metabolites and therefore the pathways extracted do not represent the connectivity of reactions. For example, water has 1083 metabolite connections and therefore needed to be omitted along with other highly connected energy and redox cofactors such as ATP, ADP, AMP, NAD, NADH, orthophosphate, hydrogen, carbon dioxide and oxygen[84]. Thus, currency metabolites were excluded from network analysis to allow elucidation of the main compounds in reactions linking the pair-wise correlation.

Subsequently, a stoichiometric matrix of the metabolic network was constructed using the SBML toolbox. This matrix was used to extract the two separate matrices of metabolites consumed and produced. The consumed network was multiplied by the transpose of the produced to construct a metabolite connectivity network. The matrix was symmetrised to account for reversibility in the network. Graph theory was implemented to calculate the shortest pathway between two metabolites using the bioinformatics toolbox included in MATLAB®. The shortest pathways were visually represented as a network using the software Cytoscape[178].

Chapter 3

DESIGN AND METHOD VALIDATION PROTOCOL FOR A METABOLIC PROFILING STUDY OF CELL LYSATES

3.1 Introduction

Metabolic profiling is able to identify metabolite differences in cells as a consequence of genetic or environmental perturbations[69, 179]. Monitoring the metabolic changes in a biological system is a process known as metabolic profiling[60].

The aim of this chapter was to develop a metabolic profiling protocol for the study of MDA-MB-231 cancer cells subjected to low oxygen tensions and chemotherapy treatments. Experimental design in metabolomics must be carefully planned to minimise bias and variance in the data, and to ensure the experiment suitably addresses the experimental hypothesis. It is also important to minimise factors that arise due to chance through determining the number of biological replicates to analyse[180]. Furthermore, cell line population effects can be accounted for by introducing biological replicates into the analysis; however the differences in sample yield must be normalised. Increasing the number of biological replicates helps to improve statistical accuracy when applying UVA. In addition, instrument drift can be accounted for by randomising sample analysis and introducing quality control samples[127, 180]. The aim of these preliminary studies was to gain a greater understanding of the biological system and ensure the method used to extract and detect metabolites using GC-MS or UHPLC-MS was robust. This included determining the duration of the experiment with respect to cell growth, the dose of drug and the biomass required.

3.2 Results and discussion

3.2.1 Cell growth

Growth characteristics are unique for each cell line and therefore a growth curve can be derived to determine the lag phase (time the cell requires to attach and spread), log phase (exponential increase in cell population) and stationary phase (cell culture becomes confluent and growth slows or stops). Cell growth transition from exponential to stationary phase has been reported to cause a major metabolic switch[181]. Consequently, it was

important that all analyses of cells were carried out when cells were in the exponential (growth) phase. Growth characteristics were calculated though constructing a growth curve. Thus the duration of time taken for cells to enter the exponential phase and the length of time cells remained in the exponential phase before reaching the stationary phase was calculated. Additionally, calculating the DT was used to approximate the expected biomass of cells over time. The lag phase was calculated through identifying the time the cells remained in the initial linear part of the graph. The DT was calculated from the point after the lag phase and determining the time taken for the cell population to double. MDA-MB-231 cells were found to have a lag phase of ~24 h and DT of ~26 h. Saturation density was not reached until after the experiment ended (168 h). Results show cells would not reach the stationary phase in the proposed period required for preparing cells for metabolic profiling. Furthermore, cells required 1 day to reach exponential phase therefore cells were left in normoxia to adhere to the Petri dish for 24 h prior to starting any experiment. FaDu cells had a similar lag phase of ~24 h and a DT ~26 h.

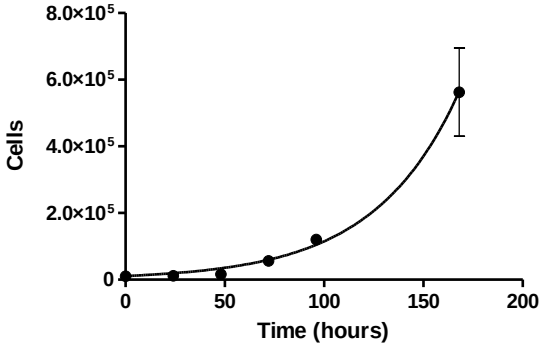

Figure 25: Growth curve for MDA-MB-231 cells over a period of 168 hours. Data are means ± s.d. (*n*=3).

Additionally, it is important for cells to not become over confluent over the course of the metabolic profiling experiment. As a result, a second experiment was conducted to optimise the extent of cell growth in relation to the initial seeding density. Maximising biomass is important for a strong signal during mass spectral metabolomics analysis. Cells were seeded ranging from 25,000 to 400,000 cells/ml and visually inspected at the end of the experiment to determine that the confluency did not exceed 70 %. A confluency greater than 70 % may cause cells to enter the stationary phase. Cells were seeded and remained in normoxia for 24 h prior to a 40 h exposure to either normoxic or anoxic conditions. Results, shown in Figure 26 suggests 100,000 cells/ml (with a cell density of approximately 15,000 cells/cm^2) maximises the biomass of cells cultured in normoxia or anoxia whilst confluency remained below 70 %. All subsequent experiments were designed based on this seeding validation test.

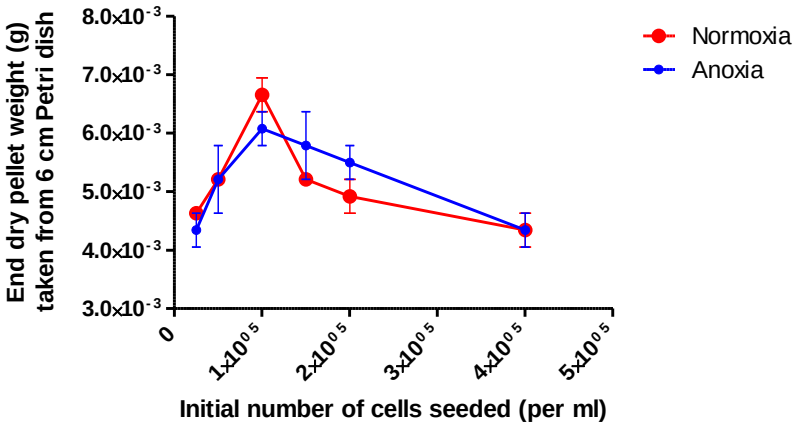

Figure 26: Result of cell seeding validation test to determine the optimum number of cells to seed to maximise biomass for MDA-MB-231 cells cultured in normoxia and hypoxia and treated with 1 µM doxorubicin. Data are means ± s.d. (*n*=3).

Whilst the growth curve was able to determine the growth of cells cultured in normoxia, over the course of the proposed experiment low oxygen conditions or drug treatment may decrease cell adhesion and increase cell death. Cells were subjected to three concentrations of doxorubicin after being cultured in normoxia, hypoxia or anoxia. Figure 27 shows the comparison of the dry weight of cells exposed to oxygen tension for 16 h followed by 24 h of drug treatment. The results suggest the oxygen tension had a greater effect on the biomass than drug treatment. Consequently, when designing subsequent metabolic profiling experiments the difference in biomass was accounted for through normalising the samples to the lowest pellet weight.

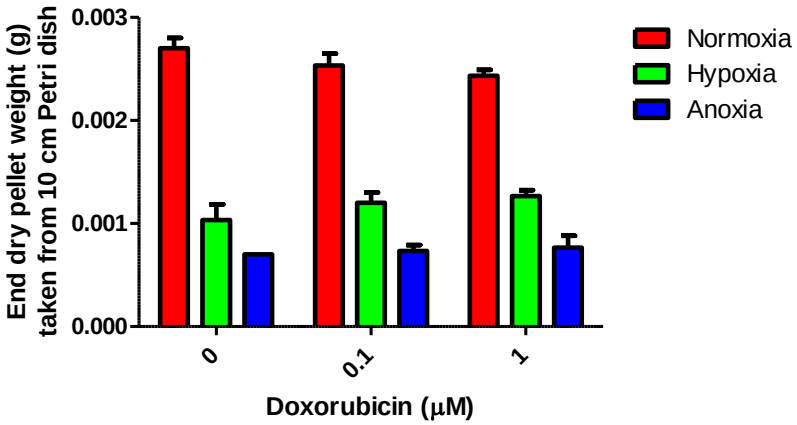

Figure 27: Comparing the biomass of MDA-MB-231 cells dosed with varying concentrations doxorubicin after being pre-exposed to specified oxygen tension normoxia, hypoxia or anoxia. Data are means ± s.d. (*n*=3).

3.2.2 Cell viability

Cancer cells pre-exposure to low oxygen levels has been reported to have a resistant phenotype to chemotherapy treatment[8-11]. To encapsulate the full extent of doxorubicin

resistance, MDA-MB-231 cells were pre-exposed to oxygen for 16 h before a 24 h drug treatment. The toxicity of doxorubicin was carried out under normoxic, hypoxic and anoxic oxygen tensions. The aim was to identify an IC_{50} value for each oxygen tension. The IC value is the concentration of the drug required to inhibit the cell growth by 50 % (IC_{50}). Results of the MTT analysis for MDA-MB-231 cells are shown in Figure 28, where the IC_{50} value for normoxia was 0.1 µM, hypoxia was 1 µM and anoxia was 1.4 µM. Results suggest oxygen tension is having an impact on the dose required to inhibit the growth of cells. Normoxia cells are the most responsive to treatment however hypoxic cells and anoxic cells require a greater dose to produce a similar response. The normoxia drug response may be related to the cytotoxic effect drug action mechanisms associated with oxygen availability such as ROS. Furthermore, anoxic cells appear to be more resistant than hypoxic cells and this may be due to different cellular mechanistic responses.

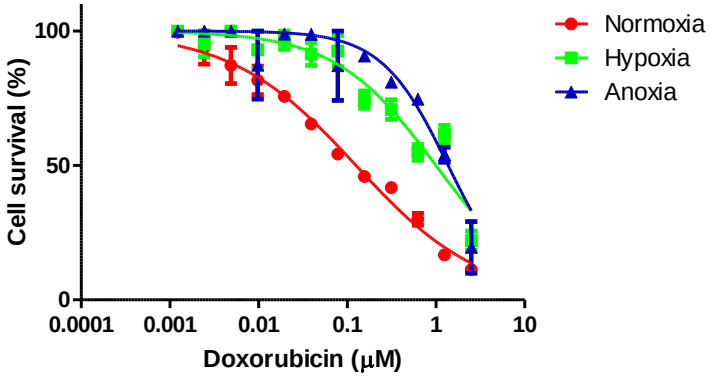

Figure 28: Result of MTT assay to determine the toxicity of doxorubicin for the MDA-MB-231 cell line when cells were cultured in normoxia, hypoxia or anoxia. The IC_{50} value for normoxia is 0.1 µM, hypoxia 1 µM and anoxia 1.4 µM. Data are means ± s.d. (*n*=3).

The IC_{50} for a 24 h doxorubicin exposure under normoxic conditions is consistent with that observed in the literature[182, 183]. IC_{50} for low oxygen levels cannot be found in the literature; however there are data for colony formation assays that show hypoxic cancer cells have a greater survival to doxorubicin treatment than normoxic cancer cells[9, 184]. As a result, two doses of doxorubicin (0.1 µM and 1 µM) were used in subsequent experimental analyses to account for the different cell responses with respect to oxygen tensions. Furthermore, the IC_{50} for FaDu cells cultured in normoxic and hypoxic conditions were 0.1 µM and 1.1 µM respectively.

3.2.3 Determining hypoxia using a firefly luciferase reporter construct linked to the HIF-1 responsive promoter region from gene encoding lactate dehydrogenase (LDH)

For each metabolic profiling experiment separate samples were collected from each batch to confirm the expression of hypoxic markers. This confirmed the hypoxybox and anoxic chamber were operating under low oxygen conditions, and samples were indeed subjected to appropriate hypoxic or anoxic conditions during the experiment. The activity of HIF-1 was measured using a firefly luciferase reporter construct linked to the HIF-1 responsive promoter region from gene encoding lactate dehydrogenase (LDH)[8]. Results show that luciferase expression driven by the LDH hypoxia response element increased in cells cultured in hypoxic and anoxic conditions. Interestingly, the higher drug dose, shown in section 3.2.2 to inhibit growth by ~50 % of MDA-MB-231 cells exposed to a low oxygen tension, reduced the expression of HIF compared to the lower drug dose and control in both hypoxic and anoxic oxygen tensions. It has been reported that disruption of HIF pathway can reverse the hypoxia-induced resistance to chemotherapy [10, 185, 186]. This data suggests high doses of doxorubicin that inhibit the growth of MDA-MB-231 cells by ~50 % has an impact on the activity of HIF-1 which may be a mechanism contributing to overcoming hypoxia-induced resistance. HIF activity has been reported to be inhibited by chemotherapy agents. For example, topotecan (a topoisomerase inhibitor) has been suggested to prevent HIF-1α activity [187, 188]. Furthermore, it has also been also been discovered that doxorubicin inhibits HIF-1 transcriptional activity by blocking its binding to DNA[189]. This study also validated the use of the hypoxybox, which was constructed in-house specifically to enable large-scale experiments to be undertaken as reported in Chapter 2.

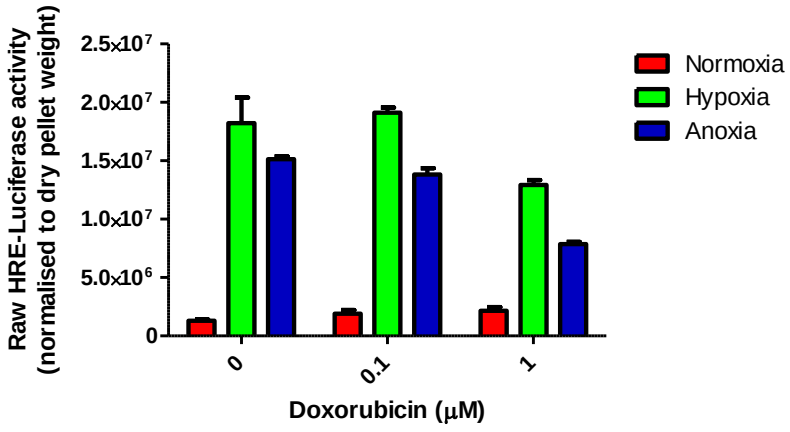

Figure 29: Expression of hypoxia-inducible factor 1 (HIF-1) activity for MDA-MB-231 cells following metabolic profiling analysis. Cells were infected with HIF reporter virus and exposed to various oxygen potentials. Luciferase activity is given as raw data. Data are means ± s.d. (*n*=3).

3.2.4 Cell cycle analysis using flow cytometry

The cell cycle is a succession of events that occur within a cell to enable cell replication, and is related to the rate of cell growth. The cell cycle was studied to determine the impact of low oxygen exposure and chemotherapy treatment on the growth of cells. Cells with a slower growth rate are expected to reprogram intracellular metabolic fluxes including energy metabolism, redox metabolism, oxidative pentose phosphate pathway and anaplerosis[181]. The cell cycle progression for low oxygen tensions has previously shown that hypoxia induces arrest of G_0/G_1 phase [26, 190]. Cell cycle division has also previously been shown to be a target of chemotherapy agents. For example, doxorubicin has demonstrated an induction of G_2/M arrest within cells, and in addition cells synchronized in the S and G_2/M phases were found to be more sensitive to doxorubicin treatment [190]. Hypoxia-induced cell cycle arrest in the G_0/G_1 phase may therefore be a factor contributing towards hypoxia-induced chemoresistance. A cell cycle study was conducted to investigate cell cycle regulation for MDA-MB-231 cells exposed to low oxygen potential and doxorubicin.

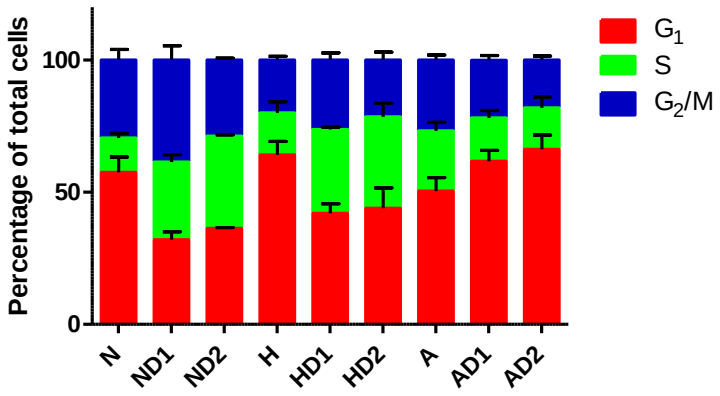

Figure 30: Cell cycle analysis of MDA-MB-231 cells cultured in normoxia (N), hypoxia (H), or anoxia (A) and treated with 0, 0.1 µM doxorubicin (D1) or 1 µM doxorubicin (D2). Data are means ± s.d. (*n*=3).

Figure 30 shows the cell cycle observed for normoxic, hypoxic and anoxic samples treated with three doxorubicin concentrations 0, 0.1 and 1 µM. Normoxic cells appear to reside ~55 % in the G_1 and S phase and ~45 % in the S and G_2/M phase. There is a clear shift towards S and G_2/M with the addition of 0.1 µM doxorubicin (ND1). A similar profile is observed for normoxic cells treated with1 µM doxorubicin (ND2). Hypoxic cells appear to have a greater proportion of cells in the G_1 phase compared to normoxic cells and fewer in the G_2/M phase. With the addition of 0.1 µM doxorubicin (HD1) or 1 µM doxorubicin (HD2) there is a shift towards S and G_2/M phases. Anoxic cells appear to have less cells in the G_1 phase similar to compared to normoxic and hypoxic cells. Anoxic cells appear to

show more S phase cells, which has previously been reported, however there is less G_2 as it has been suggested anoxic cell are unable to complete DNA synthesis[191]. Anoxic cells treated with 0.1 µM doxorubicin (AD1) or 1 µM doxorubicin (AD2) shows that there is a greater accumulation of cells in the G_1 phase. This suggests that drug response in anoxic conditions is different to the hypoxic or normoxic response with respect to the cell cycle and the origin may be explained by studying their metabolome.

3.2.5 Sample preparation and metabolite extraction for FT-IR spectroscopy of the intracellular metabolome

Before undertaking FT-IR spectroscopy, a preliminary experiment was performed to determine which solvent the intracellular metabolism should be extracted into and the biomass required to maximise the S/N ratio. A standard protocol previously optimised for the Bruker Equinox 55 infrared spectrometer in transmission-based FT-IR spectroscopy was applied to acquire spectra[157, 158]. The metabolism of MDA-MB-231 cells, seeded into a 6 well plate, was quenched by adding 100 % methanol (100 µl) and cells were harvested by detaching them from the culture surface using a cell scraper. Metabolites were extracted from the samples through snap freezing in liquid nitrogen and thawing on dry ice. This process was repeated three times to maximise extraction[192]. The samples were centrifuged (17000 × g for 15 min) and, following biomass normalisation, the supernatants were spotted (20 µl) into a 96 well silicon plate. The supernatant was difficult to spot onto the plate as methanol has poor surface tension properties which caused it to spread into neighbouring wells. Results, shown in Figure 31a, suggested samples lacked adequate biomass as shown by poorly defined peaks within the spectra and the inability to have biological intensity greater than the background absorbance (as shown by the horizontal vibrations at ~0 absorbance). To overcome the issue of surface tension a 0.85 % saline solution was chosen as an alternative solvent due to better surface tension properties easing the droplet spotting process of the supernatants. Figure 31b shows data from cells seeded into a 6 well plate that were prepared with saline solution (100 µl) and normalised to wet pellet weight. Normalisation was carried out based on the wet pellet weight and samples were spotted (20 µl) onto a silicon plate. Whilst biological peaks of interest appeared to be clearly defined, the sample signal intensity was below the background absorbance suggesting the biomass was too low. Subsequently, samples were prepared in 20 µl, rather than 100 µl, of saline solution to boost the concentration and samples were normalised to a maximum of 20 µl. Results showed the absorbance was above the background as shown in Figure 31c and biological peaks were clearly defined.

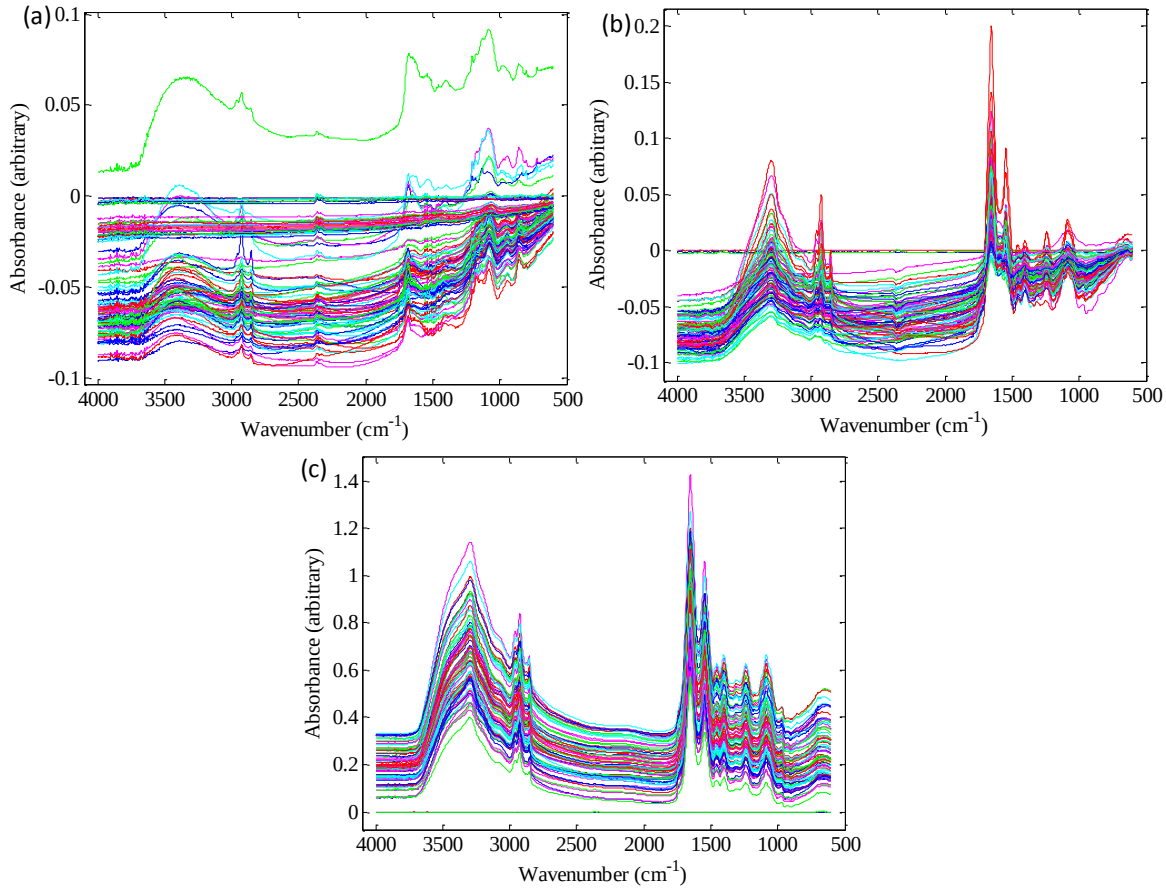

Figure 31: Fourier transform infra-red (FT-IR) spectroscopy of MDA-MB-231 cells where the intracellular metabolites for MDA-MB-231 cells were extracted in (a) 100 µl methanol (b) 100 µl saline and (c) 20 µl saline.

3.2.6 Phenotypic profiling of the cellular response to doxorubicin exposure of cells cultured in normoxic and anoxic conditions using FT-IR spectroscopy

FT-IR spectroscopy was used as a tool to investigate the duration of drug exposure required to induce a drug response in the global phenotype of MDA-MB-231 cells. The toxicity of doxorubicin is dose and time dependent therefore the global phenotype of cells was explored to determine the duration of time required to cause a biological response to doxorubicin[193]. Inhibition of the growth of cells by 50 % was calculated to be 0.1 µM for cells cultured in normoxic conditions and ~1 µM for cells cultured in low oxygen conditions when exposed over 24 h. FT-IR spectroscopy was used to confirm a global response occurred following the 24 h exposure. Figure 32 shows the PCA scores plots for MDA-MB-231 cells cultured in normoxia and exposed to 0.1 µM doxorubicin for 24 h (Figure 32a). Cells dosed with 0.1 µM for 24 h have drug response as shown in PC3. This separation suggests a 24 h drug exposure enables cells to have a response in the whole organism fingerprint[194].

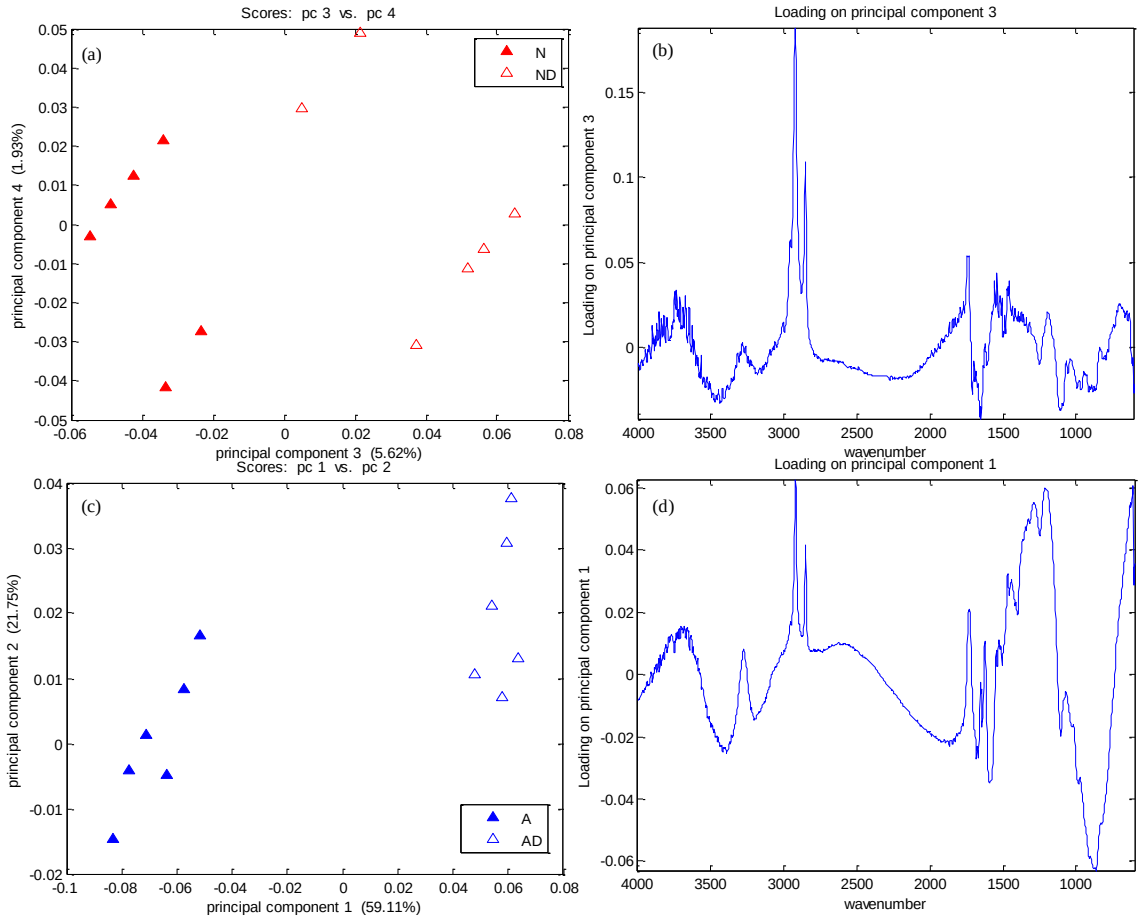

Figure 32: Principal component analysis (PCA) scores and loadings plots of Fourier transform infra-red (FT-IR) spectra for MDA-MB-231 cells cultured in (a) normoxia (N) and treated with 0.1 µM doxorubicin (ND) (c) anoxia (A) and treated with 0.1 µM doxorubicin (AD). For each sample type 6 biological replicates were analysed.

In the same experiment the metabolic drug response of anoxic cells were analysed to explore whether a 24 h doxorubicin exposure at of 0.1 µM doxorubicin produced a cellular response. Figure 32 shows the PCA scores plot for MDA-MB-231 cells cultured in anoxia and dosed with 0.1 µM doxorubicin for 24 h have a drug response as shown in PC1. This study shows FT-IR spectroscopy was a useful technique for monitoring phenotypic cellular changes in response to doxorubicin treatment. The loadings plots of the cellular response to doxorubicin treatment when cultured in normoxia or anoxia are shown in Figure 32b and Figure 32d respectively. Both loadings plots show a similar response to drug treatment where lipids are in the doxorubicin treated loadings and amides and carbohydrates/nucleotides are in the untreated loadings. Thus additional analytical platforms, such as GC-MS and UHPLC-MS are needed to elucidate normoxic drug action and anoxic drug resistant mechanisms.

The spectrum of doxorubicin was collected at a concentration of 1 mM (Figure 33). The maximum concentration used this study was 1 µM, which failed to generate an FT-IR

spectrum (data not shown). This suggests FT-IR spectra of cell lysates did not include spectral features directly due to doxorubicin, but rather the metabolic differences as a consequence of the action of the drug.

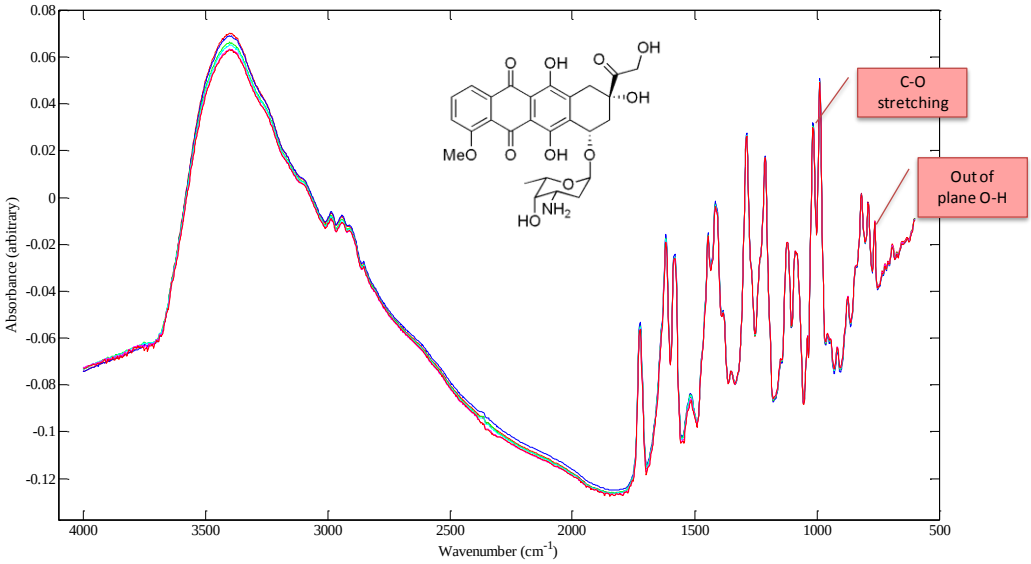

Figure 33: Typical Fourier transform infra-red (FT-IR) spectra for 1 mM doxorubicin, which is a thousand times more concentrated than the cells were treated with, and comprises of bands at 1000-1260 cm^{-1} (C-O stretching of alcohol), and 675-900 cm^{-1} (out of plane O-H bending) [195]. Additionally, the broad vibration at ~3500 cm^{-1} is due to O-H from H_2O.

3.2.7 Analysis of the intracellular metabolome of MDA-MB-231 cells using FT-IR spectroscopy to explore phenotypic response of cells cultured in several oxygen tensions

Metabolic profiling analysis was performed at three oxygen potentials, 21 %, 1 % and 0 %. Whilst studies of cells in normal oxygen condition are typically conducted at 21 %[10, 118], it has been shown that physiological concentration of oxygen *in vivo* is closer to 5 % [196]. FT-IR spectroscopy was used to determine the extent the global profile of the cells differ when exposed to 21 % oxygen and 5 % oxygen compared to 1 % and 0 %. Figure 34 shows the result of PCA of MDA-MB-231 cells cultured in four different oxygen levels 21 %, 5 %, 1 % and 0 % O_2. The scores plot presents a separation in PC1 between cells cultured in high oxygen levels (21 % and 5 %) on the left and low oxygen levels (1 % and 0 %) on the right. This suggests cells cultured in 21 % and 5 % O_2 have a similar phenotypic response which can be differentiated from those cultured in 1 % and 0 % O_2. Loadings for PC1 (Figure 34b) revealed high oxygen cells cluster in the scores plot due to the amide II band and low oxygen due to nucleotide or carbohydrates vibrations. Vibrations in low oxygen cells due to nucleotides and carbohydrates could arise as a result of a major shift from aerobic metabolism to anaerobic metabolism in the cells causing an

increase glucose uptake. Since FT-IR spectroscopy showed 21 % and 5 % have a similar phenotype, and it was not experimentally viable to conduct large-scale metabolic profiling studies for cells cultured in 5 % O_2, metabolic profiling of normoxia samples were conducted at 21 % O_2.

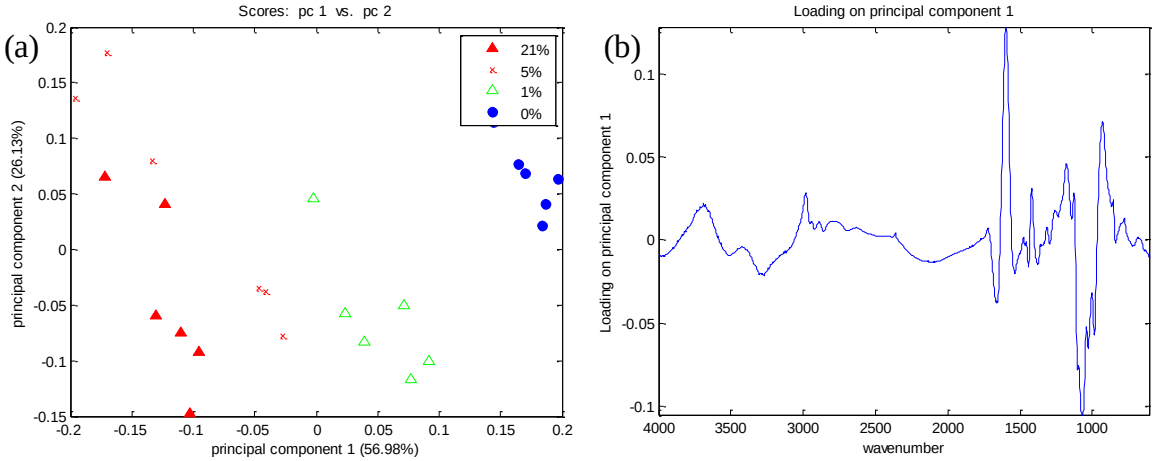

Figure 34: Principal component analysis (PCA) of the Fourier transform infra-red (FT-IR) spectroscopy data for the intracellular metabolism of MDA-MB-231 cells cultured in 21 %, 5 %, 1 % and 0 % oxygen where (a) is the scores plot and (b) is the loading plot. For each sample type 6 biological replicates were analysed.

3.2.8 A preliminary metabolic approach to explore the response of MDA-MB-231 cells exposed to three oxygen tensions

A preliminary study was used to validate the reproducibility of the metabolic profiling protocol. This protocol was tested in an initial small-scale metabolic profiling experiment. The small-scale experiment analysed four biological replicates acquired over a series of four passages to determine the robustness of the protocol, which was applied to subsequent experiments including the acquisition of a large GC-MS dataset (for correlation analysis) containing a minimum of 30 biological replicates per sample type. A limiting factor to this large-scale experiment is the ability to sample such a large number of replicates in a single analysis. In addition, the two hypoxyboxes can only contain 20 × 10 cm Petri dishes in each, thus future large-scale analyses would need to be acquired over four cellular passages in order to acquire an adequate number of samples. Biological replicates are necessary in the experimental design to eliminate biological variability from factors including the environment, cell cycle growth phase and cell passage number. Cell passage has been suggested to have an effect on the metabolome of cells in primary cell culture, however MDA-MB-231 cells are an immortal cell line[180]. A primary cell culture is directly extracted from a biological tissue and has a limited lifetime. Once the Hayflick limit (the number of times a cell population will divide before it stops) is reached cells no longer

divide (due to shortened telomeres) and may undergo senescence[197]. In comparison immortal cell lines are able to evade the Hayflick limit due to mutations enabling cells to be grown for a prolonged duration[198]. To overcome some of the variation caused through sampling over four cell passages, the same batch of FCS was employed to supplement the cell culture medium. FCS is a supplement required for growth containing embryonic promoting and survival enhancing factors. FCS is an undefined component therefore using different batches would increase variation in the datasets for samples acquired over a series of cell passages. As a result all datasets to be compared were cultured using the same batch of FCS. Metabolomic sampling was conducted following the schematic presented in Figure 35. A total of four biological replicates were taken during each analysis over a total of 4 cellular passages. This generated a total of 16 biological replicates for each sample type.

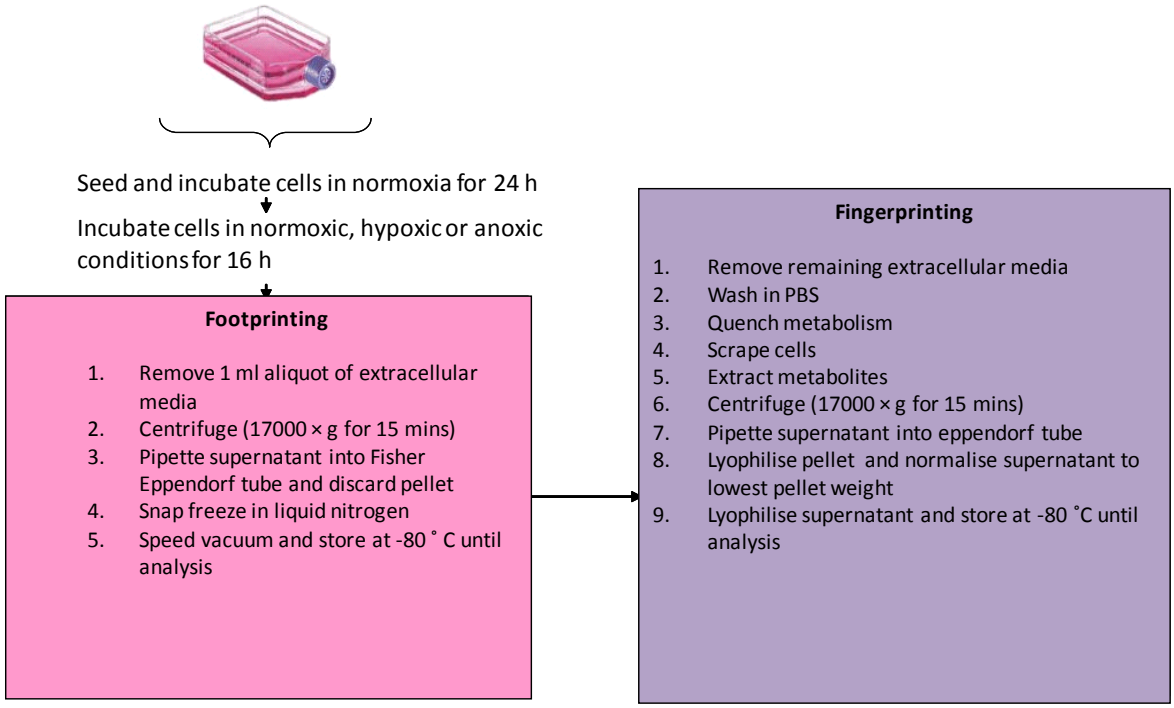

Figure 35: Workflow of the steps taken to extract intracellular and extracellular metabolites.

The aim of the initial metabolic profiling analysis was to determine whether the protocol was sufficiently robust to allow the separation of sample classes with respect to metabolism for both the intracellular and extracellular metabolomes. Furthermore, this preliminary study tested the reproducibility associated with sampling over a series of culture passages through applying chemometric analysis. Additionally, the study determined whether the metabolite extraction method was able to detect a range of metabolites for intracellular metabolism.

3.2.8.1 Biomass

Prior to acquiring metabolomic samples, it was important to determine the biomass of cells required to generate a high-quality chromatogram using GC-MS. 100,000 cells/ml were seeded into a 10 cm Petri dish at a total volume of 8 ml media. Cells were incubated for 48 h in normoxia after which the metabolism was quenched and metabolites were extracted as shown in Figure 35. Both extracellular and intracellular samples were extracted from the dish. The total ion current (TIC) chromatogram is shown in Figure 36 which revealed that the biomass for both the intracellular and extracellular metabolome were metabolite rich providing good signal intensity.

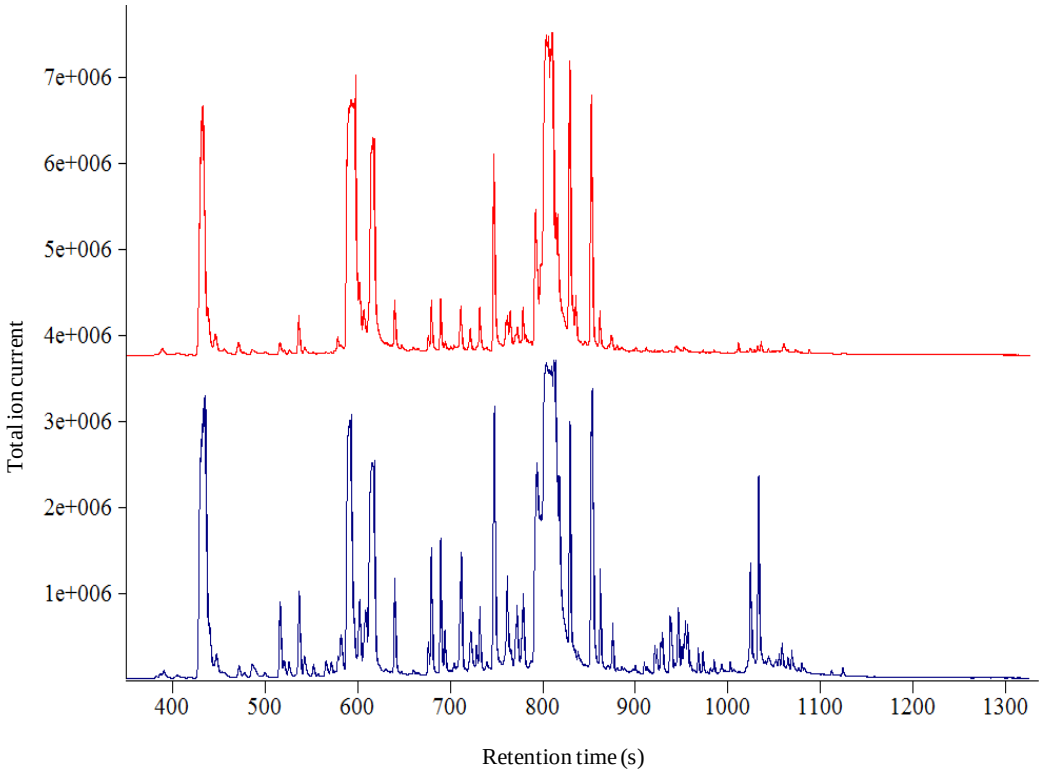

Figure 36: Typical total ion current (TIC) chromatogram of extracellular metabolites (blue) and intracellular metabolites (red) for MDA-MB-231 cells extracted from one 10 cm^2 Petri dish.

3.2.8.2 Extracellular metabolome

The extracellular metabolome contains the cellular response to environmental perturbations through changes to the uptake and efflux of metabolites. Analysing the extracellular metabolome can be useful as medium can be rapidly removed from the sample without the need for the time consuming process of metabolite extraction. Profiling both the intracellular and extracellular metabolome can offer a greater insight into the cellular metabolic response. A 'snapshot' of the extracellular metabolism was sampled to monitor differences arising from the rate of metabolite uptake and excretion.

The aim of analysing the extracellular metabolome was to determine whether it was possible to observe metabolic differences with respect to the different oxygen conditions. PCA of GC-MS data for MDA-MB-231 cells did not separate with respect to the oxygen culture conditions (Figure 37). The extracellular medium is a complex solution and metabolite rich, thus the small changes relating to oxygen tension are difficult to detect. Using other medium, such as minimal essential media, which also contains a complexity of metabolites required for cell growth would not help identify subtle extracellular metabolome differences. Additionally, cells may grow at a sub-optimum rate in minimal essential media altering cellular metabolism. The preliminary investigation suggested analysis of the extracellular metabolome could not phenotype the metabolic differences of cells cultured in various oxygen tensions. Consequently, future metabolomics experiments did not include the analysis of the extracellular metabolism.

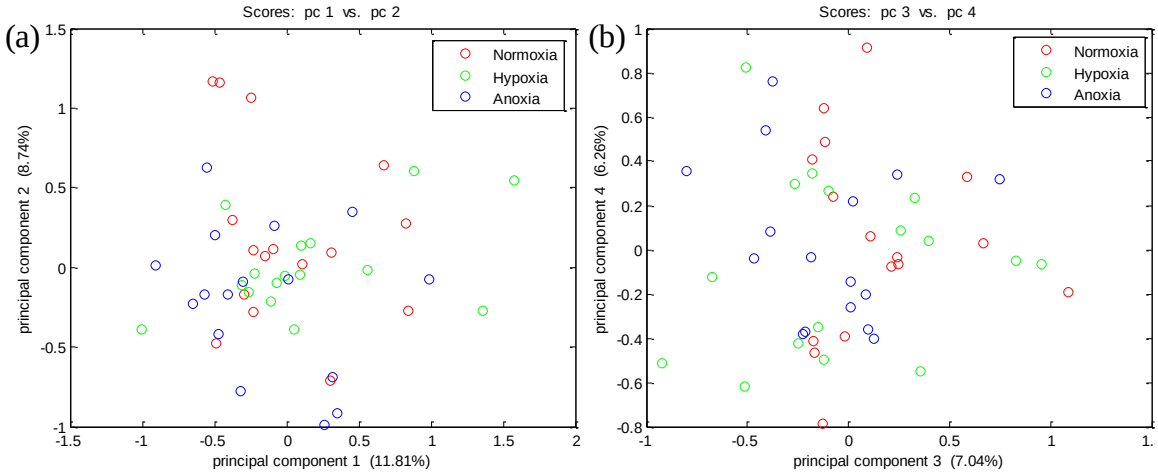

Figure 37: Principal component analysis (PCA) of gas chromatography mass spectrometry (GC-MS) data comparing extracellular metabolism of MDA-MB-231 cells cultured in normoxic, hypoxic or anoxic conditions. Cells were incubated for 24 h in normoxia followed by a 16 after which the extracellular metabolism was sampled. A total of 16 biological replicates were taken for each sample type.

3.2.8.3 Intracellular metabolome

Intracellular metabolites were quenched in methanol (1 ml) and extracted using the method of freezing (in liquid nitrogen) and thawing (at room temperature) over three cycles[192]. A total of 83 peaks were identified as metabolites in the chromatogram, and the coverage ranged from carbohydrates and amino acids to lipids. The aim was to determine whether a metabolic difference in the intracellular metabolome could be attributed to cells cultured in various oxygen conditions. Comparing the intracellular metabolites of all samples shows a clear difference with oxygen levels in PC2 (Figure 38). There is a clear separation between

normoxia and anoxia samples in PC2; however hypoxic samples did not separate from normoxia cells.

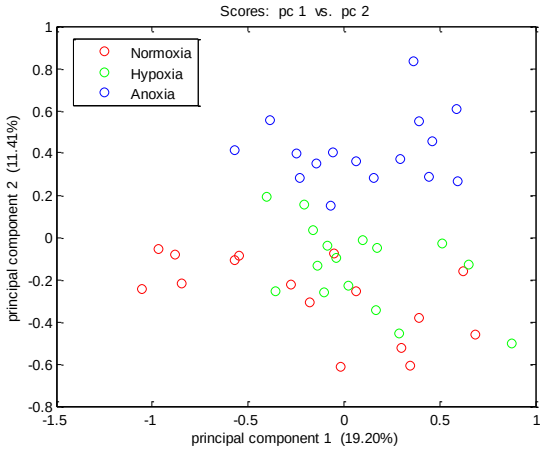

Figure 38: Principal component analysis (PCA) of gas chromatography mass spectrometry (GC-MS) data comparing the intracellular metabolism of MDA-MB-231 cells. Cells were cultured in normoxia for 24 h followed by 16. A total of 16 biological replicates were acquired for each sample type.

Further, the effect of cellular passages on the intracellular metabolome was explored. PCA of the intracellular metabolomesamples acquired over four passages is shown in Figure 39. Inspection of the scores plots suggests there is no pattern associated with a series of four cell passages, which suggests that the cells were suitably adapted to growth in *in vitro* conditions.

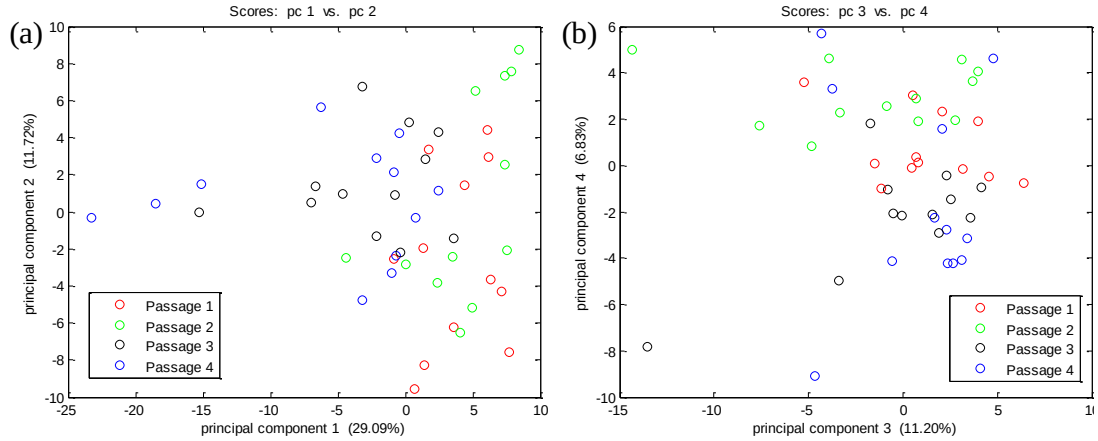

Figure 39: Principal component analysis (PCA) of gas chromatography mass spectrometry (GC-MS) data comparing the intracellular metabolism of MDA-MB-231 cells cultured in four cell passages labelled passage 1- 4. For each condition (normoxia, hypoxia and anoxia) 4 biological replicates were taken and therefore a total of 12 samples were taken for each passage.

3.3 Conclusion

The purpose of this work was to determine the experimental parameters required for all subsequent cellular analysis in this thesis. The growth of MDA-MB-231 cells was

determined, which was used to develop the length of future experiments. The IC_{50} values of MDA-MB-231 cells exposed to doxorubicin for 24 h was found to be 0.1 μM for cells cultured in normoxic conditions and >1 μM for cells cultured in low oxygen conditions. FT-IR spectroscopy was used as a tool to confirm that cells exhibited a global response to a 24 h doxorubicin exposure. Additionally, FT-IR spectroscopy was used as a tool to explore the global profile of cells exposed to a range of oxygen tensions and showed that cells exposed to the 5 % oxygen tension (physiologically relevant) had a similar phenotype to those exposed to 21 % oxygen. As large-scale metabolic profiling could not be carried out at 5 % oxygen, due to this not being experimentally possible due to the capacity of the incubator, it was encouraging that these cells exhibited a similar metabolic phenotype to those exposed to 21 % oxygen.

Following these preliminary experiments, a small-scale metabolic profiling study was carried out. Validation of a metabolic profiling protocol was necessary to determine whether metabolic effects due to cell passage exceed biological variation. Additionally, metabolic profiling was used to determine whether biological differences could be identified in both the intracellular and extracellular samples. Further, the extraction method was examined to determine whether it was suitable to detect a range of metabolites including amino acids and lipids. Data acquired for the extracellular metabolism did not present metabolic variation due to cell culture conditions. The medium is complex and contains high concentrations of metabolites that may mask the small changes caused by metabolite efflux and influx. Extracellular samples may be better suited towards targeted metabolic analysis to measure the changes in a few metabolites compared to the global metabolome. As a result the large-scale metabolic profiling analysis did not include the study of the extracellular metabolome. Intracellular samples were analysed using PCA, which showed separation could be attributed to biological variation however no separation could be assigned to cell passage. This suggested the protocol developed was suitable for sampling the intracellular metabolome over a series of 4 cell passages.

Chapter 4

METABOLIC PROFILING STUDY OF HYPOXIA-INDUCED CHEMOTHERAPY RESISTANCE USING GC-MS AND UHPLC-MS

4.1 Introduction

Targeting tumours is a major challenge for anti-cancer chemotherapeutics. Solid hypoxic tumours, both genetically and metabolically, adapt to facilitate their own survival[199]. These solid tumours contain a region of low oxygenated cells that exhibit a phenotype that is resistant to 'gold standard' chemotherapy treatments[30]. Potent chemotherapeutics, such as doxorubicin, lack specificity towards cancerous cells resulting in damage to normal cells[16]. Increasing the dose of the chemotherapeutic is often not possible due to the adverse side effects. For example, high doses of doxorubicin can cause cardiotoxicity[200].

Currently, little is known about the metabolic cellular response to hypoxia-induced chemoresistance. Metabolic profiling was used investigate the metabolic response of MDA-MB-231 cells to the adaptation of hypoxic environments and how this leads to the resistance of chemotherapy treatment. This was achieved through culturing cells at a variety of oxygen tensions and extracting the intracellular metabolites. To explore the underlying metabolic response to hypoxia-induced chemoresistance, a dose of 0.1 µM doxorubicin, shown in Chapter 3 to inhibit growth of normoxic MDA-MB-231 cells by ~50 % but which failed to inhibit the growth of hypoxic and anoxic cells, was used. Furthermore, to explore the mechanisms to overcome hypoxia-induced chemoresistance a higher dose of ~1 µM, shown in Chapter 3 to inhibit growth of hypoxic and anoxic MDA-MB-231 cells by ~50 % was used. The aim was to identify metabolite markers associated with hypoxia-induced chemoresistance and identify metabolite markers of the cellular response to overcome this resistance. This in turn could reveal potential metabolic pathways as targets for combination therapeutics.

4.2 Results

Samples for GC-MS, UHPLC-MS and ToF-SIMS were prepared simultaneously to enable cross comparison of the data. The protocol was designed as shown in Figure 40, and each

experiment took a total duration of 64 h to complete. For each batch of samples, cells were seeded into 90 x 10 cm Petri dishes and incubated for 24 h. Once cells adhered to the culture surface 90 samples were placed into 21 %, 1 % or 0 % oxygen tensions (30 samples in each condition) for a following 16 h. Samples were spiked with two concentrations of doxorubicin, 10 samples with 0.1 µM or 10 samples with 1 µM, and 10 control samples remained undosed for a further 24 h. A total of 270 samples were collected for GC-MS, therefore there were 30 biological replicates for each condition per instrument. This large dataset was required for correlation analysis. For UHPLC-MS, a total of 60 samples were analysed, therefore there were 10 biological replicates for each condition. A workflow of the data processing for each metabolomics platform is shown in Figure 41. Sample labels were assigned as shown in Table 6. For each metabolic profiling experiment separate samples were collected from each batch to confirm the expression of a hypoxic marker as described in Chapter 3 through the use of a firefly luciferase reporter construct linked to the HIF-1 responsive promoter region from gene encoding LDH. This confirmed the hypoxybox and anoxic chambers were operating under low oxygen conditions, and samples were subjected to appropriate levels of hypoxia or anoxia.

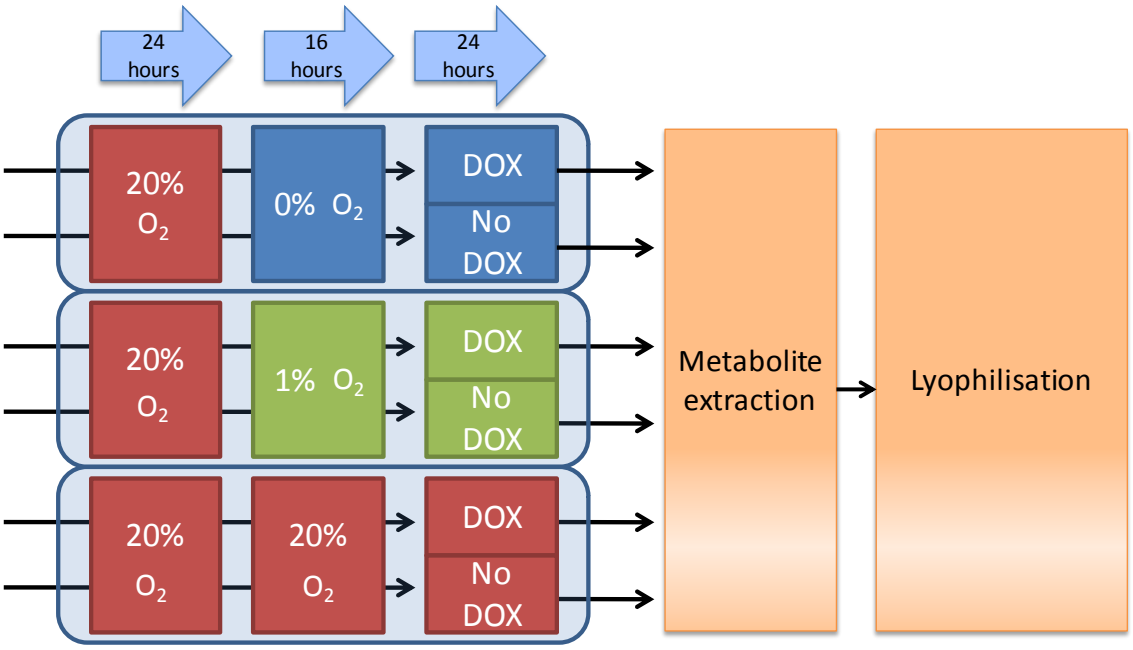

Figure 40: A schematic diagram outlining the method of sample preparation for metabolic profiling analysis. MDA-MB-231 cells were seed into 10 cm Petri dishes and allowed to adhere for 24 h. Samples were placed into oxygen potentials 21 %, 1 % and 0 % for a following 16 h. Samples were spiked with two concentrations of doxorubicin (0.1 µM and1 µM) and control samples remained untreated for a further 24 h. Subsequently, metabolites were extracted and lyophilised.

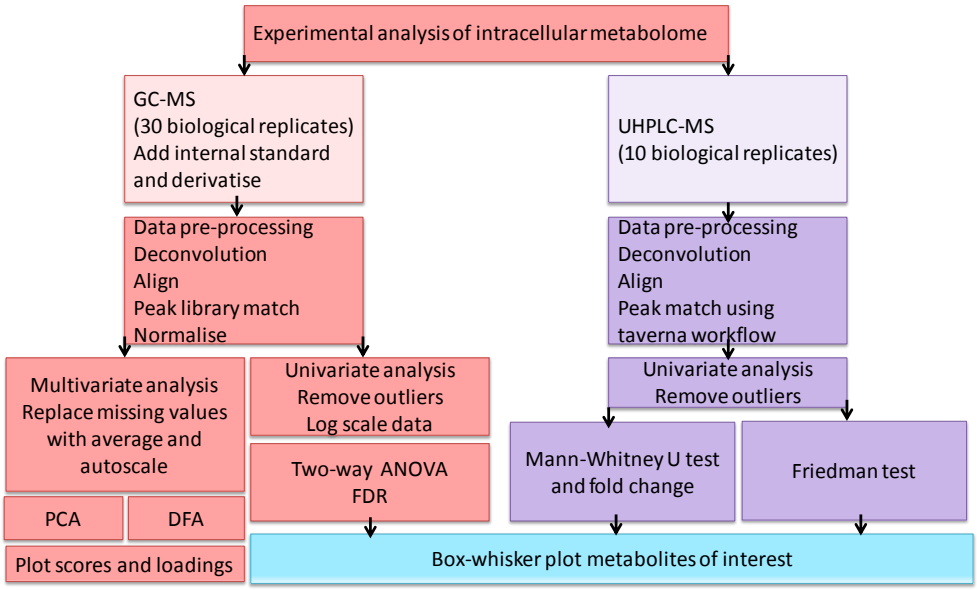

Figure 41: Workflow of the data processing that followed sample collection for both gas chromatography mass spectrometry (GC-MS) and ultra high performance liquid chromatography (UHPLC-MS).

Table 6: Samples treatments were assigned with a sample ID.

Sample ID	Sample treatment
N	Normoxia
ND1	Normoxia + 0.1 µM doxorubicin
ND2	Normoxia + 1 µM doxorubicin
H	Hypoxia
HD1	Hypoxia + 0.1 µM doxorubicin
HD2	Hypoxia + 1 µM doxorubicin
A	Anoxia
AD1	Anoxia + 0.1 µM doxorubicin
AD2	Anoxia + 1 µM doxorubicin

4.2.1 The metabolic response of MDA-MB-231 breast cancer cells in low oxygen tensions

Intracellular metabolic extracts were analysed using GC-MS which, after data pre-processing, generated a total of 52 metabolite features in each of the 270 samples. To determine the variability in the dataset with respects to the low oxygen phenotype both UVA and MVA was applied. A total of nine samples types were analysed including three oxygen tensions and two drug treatments cultured as 30 biological replicates over a series of 1.5 weeks. Table 7 contains a list of metabolites detected in the GC-MS including whether the metabolite identification was with high confidence[134]. For a metabolite to be identified as having a high confidence match the chromatographic peak from the reference database was searched for in each of the sample where retention index deviation was less than ±30 and the mass spectral match was greater than 800 (as described in section 2.7.6). Spectral matches are calculated by a forward and reverse match. The forward match determines the number of spectral features in the sample that match the standard mass

spectra and the reverse match determines the extra peaks that are in the sample , which are not in the standard. Those not identified with high confidence resulted fromlow match to the score in either the reference mass spectrum or retention index. This is often due to the high-throughput nature of method where some metabolites with a similar chemical structure cannot be detected accurately.

Table 7: 52 metabolites peaks detected using gas chromatography mass spectrometry (GC-MS) including corresponding KEGG ID or associated pathway[201]. High confidence matches were assigned when the metabolite peak matched the retention index and mass spectrum of the chemical standard.

ID	Metabolite name	KEGG ID	High confidence match	Pathway
1	Glycine	C00037	Yes	Amino acid metabolism
2	Lactic acid	C00186	Yes	Glycolysis pathway
3	Pyruvic acid	C00022	Yes	Glycolysis pathway
4	Valine	C00183	Yes	Amino acid metabolism
5	Leucine	C00123	Yes	Amino acid metabolism
6	Glycerol	C00116	Yes	Glycerolipid Metabolism
7	Isoleucine	C00407	Yes	Amino acid metabolism
8	Leucine	C00123	Yes	Amino acid metabolism
9	Malonic acid	C00383	Yes	Pyrimidine metabolism
10	Glycine	C00037	Yes	Amino acid metabolism
11	Phosphate	C00009	Yes	Osmolyte, enzyme cofactor, signalling
12	Threonine	C00188	No	Amino acid metabolism
13	Alanine	C00041	Yes	Amino acid metabolism
14	Threonine	C00188	Yes	Amino acid metabolism
15	Succinic acid	C00042	No	TCA cycle
16	Benzoic acid	C00180	No	Unknown
17	Threitol/erythritol	C00503	No	Unknown
18	Malic acid	C00149	No	TCA cycle
19	4-hydroxyproline	C01157	No	Amino acid metabolism
20	Aspartic acid	C00049	Yes	Amino acid metabolism
21	4-aminobutyric acid	C00334	Yes	Amino acid metabolism
22	Aspartic acid	C00049	No	Amino acid metabolism
23	4-hydroxyproline	C01157	Yes	Amino acid metabolism
24	Xylitol	C00379	No	Pentose and glucuronate interconversion metabolism
25	2-hydroxyglutaric acid	C03196	No	Butanoate metabolism
26	4-hydroxybenzoic acid	C00156	Yes	Carbohydrate metabolism
27	Methionine	C00073	Yes	Amino acid metabolism
28	Creatinine	C00791	No	Amino acid metabolism
29	Putrescine	C00134	Yes	Amino acid metabolism
30	Hypotaurine	C00519	Yes	Amino acid metabolism
31	Glutamic acid	C00025	Yes	Amino acid metabolism
32	2-ketoglutaric acid	C00026	No	TCA cycle
33	Fructose	C02336	No	Carbohydrate metabolism
34	Sorbose/fructose	-	No	Carbohydrate metabolism
35	Sorbitol/galactose /glucose	-	No	Carbohydrate metabolism
36	Sorbose/fructose	-	No	Carbohydrate metabolism
37	Glycerol 3-phosphate	C00093	No	Glycolysis pathway
38	Galactose/glucose	-	No	Carbohydrate metabolism
39	Galactose/glucose	-	No	Carbohydrate metabolism
40	Galactose/glucose	-	No	Carbohydrate metabolism
41	Citric acid	C00158	No	TCA cycle
42	N-acetylaspartic acid	C01042	Yes	Amino acid metabolism
43	Glucose	C00031	No	Carbohydrate metabolism
44	Scyllo-inositol	C06153	No	Carbohydrate metabolism
45	Lysine	C00047	No	Amino acid metabolism
46	Scyllo-inositol/myo-inositol/inositol	-	No	Carbohydrate metabolism
47	Pantothenic acid	C00864	Yes	Pantothenate and CoA biosynthesis
48	Tyramin/tyrosine	-	No	Amino acid metabolism
49	Hexadecanoic acid	C00249	Yes	Fatty acid metabolism
50	Octadecanoic acid	C01530	No	Fatty acid metabolism
51	Myo-inositol 1-phosphate	C01177	No	Carbohydrate metabolism
52	Lactose/maltose/cellobiose	-	No	Carbohydrate metabolism

To assess the metabolic phenotype of MDA-MB-231 cells cultured in low oxygen tension, 30 biological replicates of cells cultured in 21 %, 1 % and 0 % oxygen were analysed by GC-MS. The unsupervised method of PCA was used for pattern recognition in the GC-MS data. PCA identifies clusters of metabolites that most strongly represent the variation in the data. Results from the PCA for the three oxygen tensions are shown in Figure 42 where PC1 accounts for 33.10 % of the TEV and PC2 accounts for 12.59 % of the TEV. The scores plot shows normoxia and anoxia samples separate in PC2, however hypoxia samples localise centrally between these two groups. Inspection of the loadings plot was able to reveal the chemical compounds that are responsible for the separation between the normoxic and anoxic samples. The loadings plot of PC2, where the separation between the two groups occurs, was studied to determine the metabolites that greatly differentiate the two groups. The loadings plot shows the metabolite ID number, which relates to the metabolite ID given in Table 7. The loadings plot revealed the most intense variable peaks, which are the main features responsible for the separation. Metabolite IDs strongly correlated in the positive loadings, and therefore attributed to anoxia, were metabolic features 19, 26, 50 and 51 relating to 4-hydroxyproline, 4-hydroxybenzoic acid, octadecanoic acid and myo-inositol 1-phosphate respectively. Normoxic samples correlated in the negative region of the loadings and the strongly separating variables were 18, 32, 33, 42, 43 and 48 relating to malic acid, 2-ketoglutaric acid, fructose, N-acetylaspartic acid, glucose and tyramin/tyrosine respectively.

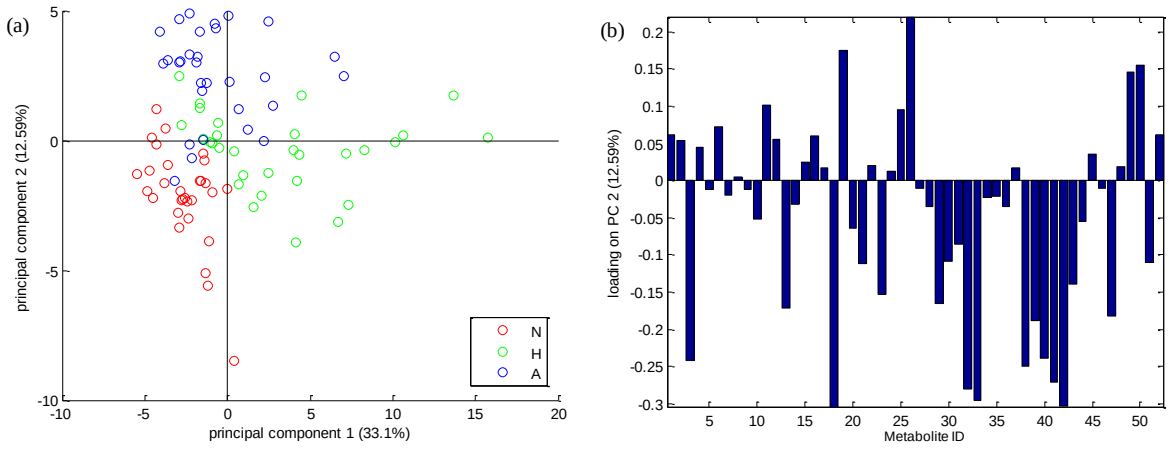

Figure 42: Principal component analysis (PCA) (a) scores and (b) loadings plot of gas chromatography mass spectrometry (GC-MS) data for MDA-MB-231 cells cultured in normoxia (N), hypoxia (H) or anoxia (A).

Subsequently, the supervised method, DFA was applied using the PCs from PCA of GC-MS data. DFA was used to determine the metabolic features that contributed to hypoxia metabolism, which could not be identified using PCA alone. Results are shown in Figure

43. To prevent over fitting of the DFA model, less than 95 % of the PC TEV was inputted into the algorithm. A total of 12 PCs were used to generate the model in Figure 43 accounting for 83.27 % of the TEV. The scores plot shows the hypoxia group cluster in DF2 whereas the normoxia and anoxia groups separate in DF1. The hypoxia group appear situated towards the anoxia region of DF1, suggesting the metabolism of hypoxic cells is more similar to anoxic cells. Similar to PCA, the loadings plot for DFA shows the metabolites that are causing the separation observed in the scores plot where the variables furthest from zero have a more significant contribution than those close to the zero. The loadings for DF1 (Figure 43b) described the metabolic difference with respect to normoxia and anoxia samples, which were found to be similar to PCA loadings plots. Metabolites similar in both analyses were malic acid, 2-ketoglutaric acid, fructose, N-acetylaspartic acid, glucose and tyramin/tyrosine in normoxia and 4-hydroxyproline, 4-hydroxybenzoic acid, octadecanoic acid and myo-inositol 1-phosphate in anoxia. DFA loadings also showed pyruvic acid, alanine and putrescine separated in normoxia and 2-hydroxyglutaric acid and hexadecanoic acid in anoxia. Furthermore, DFA was able to separate the hypoxic group; therefore metabolites could be interpreted from the loadings plot. Metabolite IDs in the positive loadings of DF2 (Figure 43c) that had the greatest variation in the hypoxic samples and included 4, 9, 10, 11, 14, 21, 31, 37, 41, and 51, which related to metabolites leucine, malonic acid, glycine, phosphate, threonine, 4-aminobutyric acid, glutamic acid, glycerol 3-phosphate, citric acid and myo-inositol 1-phosphate.

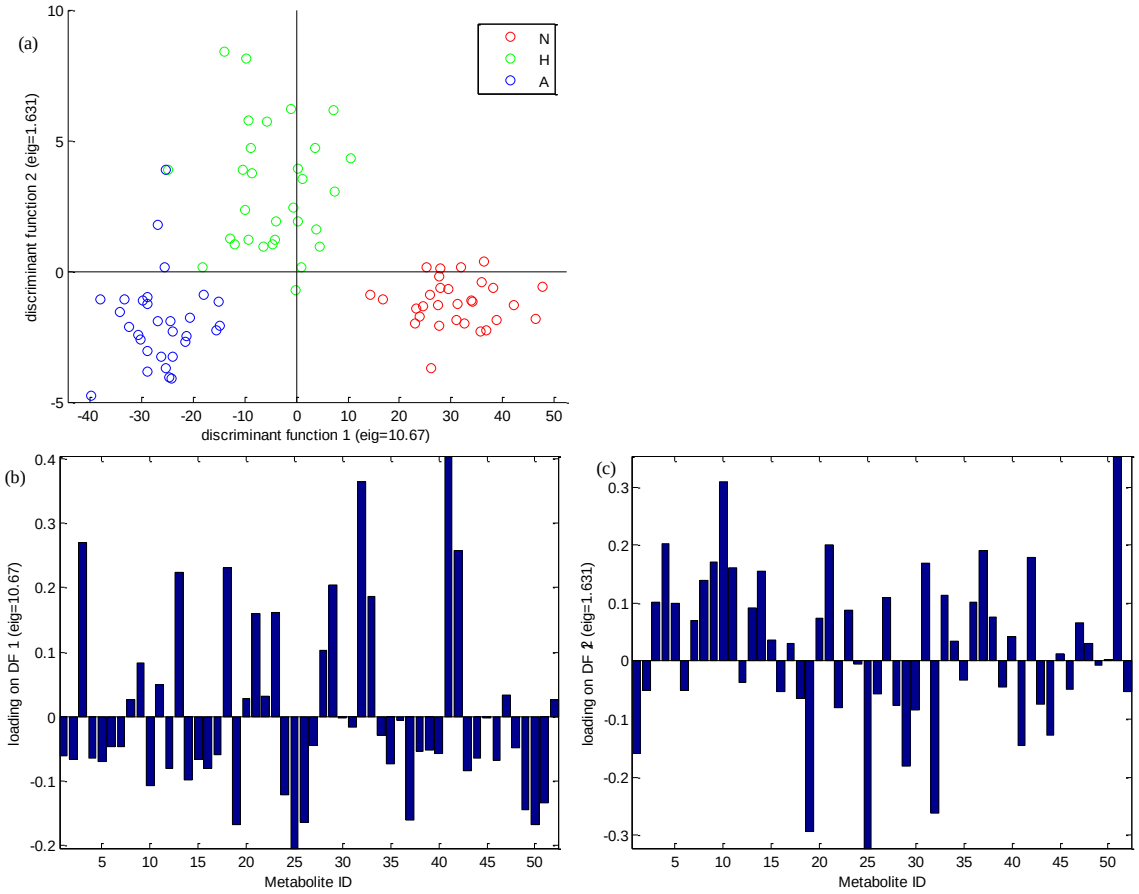

Figure 43: Discriminant function analysis (DFA) (a) scores plot (b) loadings on discriminant function 1 (DF 1) and (c) loadings on discriminant function 2 (DF 2) of gas chromatography mass spectrometry (GC-MS) data of MDA-MB-231 cells cultured in normoxia (N), hypoxia (H) or anoxia (A).

UVA was applied to the GC-MS data for the discovery of metabolite markers of hypoxia-induced doxorubicin resistance in the breast cancer cells MDA-MB-231. The *p*-value is a measure of the probability that the result observed could have occurred by chance and is associated with a test statistic. A *p*-value < 0.05 suggests the metabolite was significantly different across the sample groups and the null hypothesis is rejected. The null hypothesis tested here is that a metabolite does not differ with respect to lowering the oxygen tension. Since the dataset has two characteristics (oxygen and drug treatment) a two-way ANOVA statistical test was applied. The overall metabolites differences with respect to either oxygen or drug treatment are additive effects. Interaction effects arise from both oxygen level and drug treatment over multiple observations. Additive effects of oxygen on the cancer cells identified 20 metabolites shown in Table 8.

Table 8: Metabolites identified, using gas chromatography mass spectrometry (GC-MS), to be statistically different in MDA-MB-231 cells cultured in normoxia, hypoxia or anoxia. Low oxygen indicates where the change in metabolite concentration occurred in both the hypoxia and anoxia samples. The direction of the metabolite concentration change is given relative to normoxia. *P*-values, calculated using a two-way analysis of variance (ANOVA), were corrected for a false discovery rate (FDR) *q*-value = 0.1.

Interaction	*p*-value	Metabolite	Pathway	Direction of metabolite difference with respect to normoxia
Hypoxic	0	Glycine	Amino acid metabolism	Increase
	9.88×10^{-15}	Myo-inositol 1-phosphate	Carbohydrate metabolism	Increase
Anoxic	0	Pyruvic acid	Glycolysis pathway	Decrease
	0	2-hydroxyglutaric acid	Butanoate metabolism	Increase
Low oxygen	0	2-ketoglutaric acid	TCA cycle	Decrease
	0	Glycerol 3-phosphate	Glycolysis pathway	Increase
	0	Citric acid	TCA cycle	Decrease
	0	N-acetylaspartic acid	Amino acid metabolism	Decrease
	8.88×10^{-16}	Sorbose/ Fructose	Carbohydrate metabolism	Increase
	2.00×10^{-15}	Sorbitol/ Galactose / Glucose	Carbohydrate metabolism	Increase
	7.66×10^{-15}	Xylitol	Pentose and glucuronate interconversion metabolism	Increase
	4.05×10^{-13}	Leucine	Amino acid metabolism	Increase
	3.26×10^{-12}	Threitol/Erythritol	Unknown	Increase
	2.05×10^{-10}	Hexadecanoic acid	Fatty acid metabolism	Increase
	2.07×10^{-10}	Lactic acid	Glycolysis pathway	Increase
	2.59×10^{-10}	Succinic acid	TCA cycle	Increase
	1.42×10^{-9}	Isoleucine	Amino acid metabolism	Increase
	2.36×10^{-9}	Glycerol	Glycerolipid Metabolism	Increase
	5.94×10^{-6}	Methionine	Amino acid metabolism	Increase
	2.27×10^{-5}	Valine	Amino acid metabolism	Increase

Some of the metabolites markers are represented as box-whisker plots shown in Figure 44.

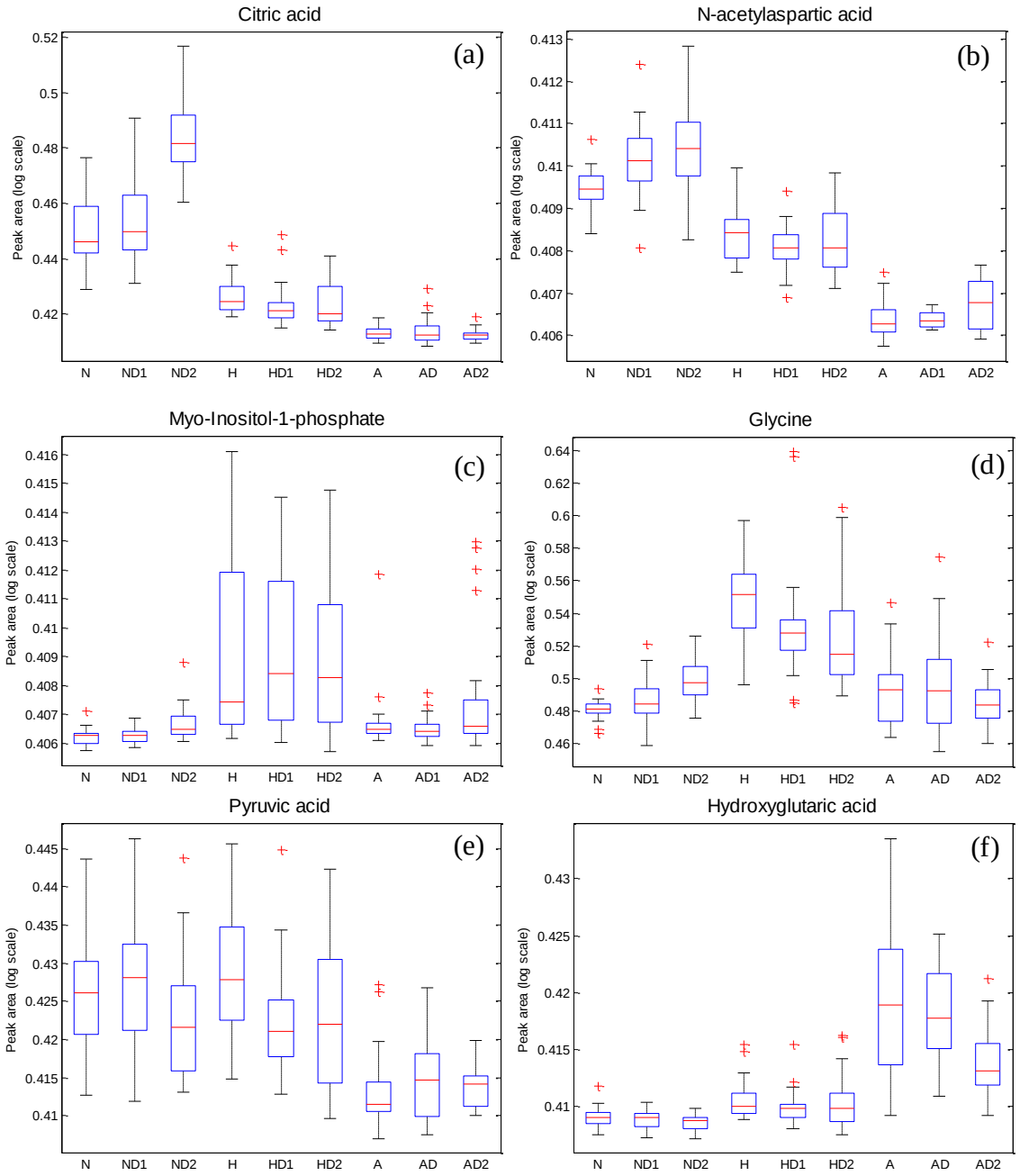

Figure 44: Box–whisker plots showing the difference in the expression of intracellular metabolites (a) citric acid, (b) N-acetylaspartic acid, (c) myo-inositol, (d) glycine, (e) pyruvic acid and (f) 2-hydroxyglutaric acid acquired using gas chromatography mass spectrometry (GC-MS). MDA-MB-231 cells were cultured in normoxia (N), hypoxia (H) or anoxia (A). Subsequently cells were untreated, or treated with either 0.1 (D1) or 1 µM (D2) doxorubicin. The lower and upper limits of the blue box are the 25th and 75th percentiles respectively, the red line in the box is the median of the peak area and the lower and upper whiskers are the 5th and 95th percentiles respectively. A cross represent an outliers when value is more than 1.5 times the interquartile range away from the top or bottom of the box.

In addition to GC-MS, intracellular metabolic extracts of MDA-MB-231 cells were analysed using UHPLC-MS and, after data pre-processing, 6183 chromatographic features were detected in positive ion mode and 2284 in negative ion mode for 60 samples. Two oxygen tensions (normoxia and hypoxia), three drug treatments (0, 0.1 and 1 µM doxorubicin), and 10 biological replicates for each group were analysed. UHPLC-MS chromatographic features were putatively identified using Taverna workflows to match the

accurate mass of the fragment[141]. A larger number of biological replicates were analysed by GC-MS compared to UHPLC-MS as, in addition to metabolite marker discovery, correlation analysis of GC-MS data performed in Chapter 5, required a greater number of biological replicates. To determine the variability in the dataset with respects to the low oxygen phenotype both UVA and MVA were applied. The unsupervised method of PCA was used to explore the variability in the data. PCA was able to identify the greatest variability within the data, which could be attributed to the two oxygen levels. Results from the PCA for the two oxygen tensions are shown in Figure 45a for positive ion mode and Figure 45b for negative ion mode. This confirms there is a clear cellular metabolic response to the two oxygen types in the UHPLC-MS data. Interpretation of the loadings for each of these PCA scores plots was too complex (data not shown) as positive ion mode contained 6183 features and negative ion mode contained 2284 features.

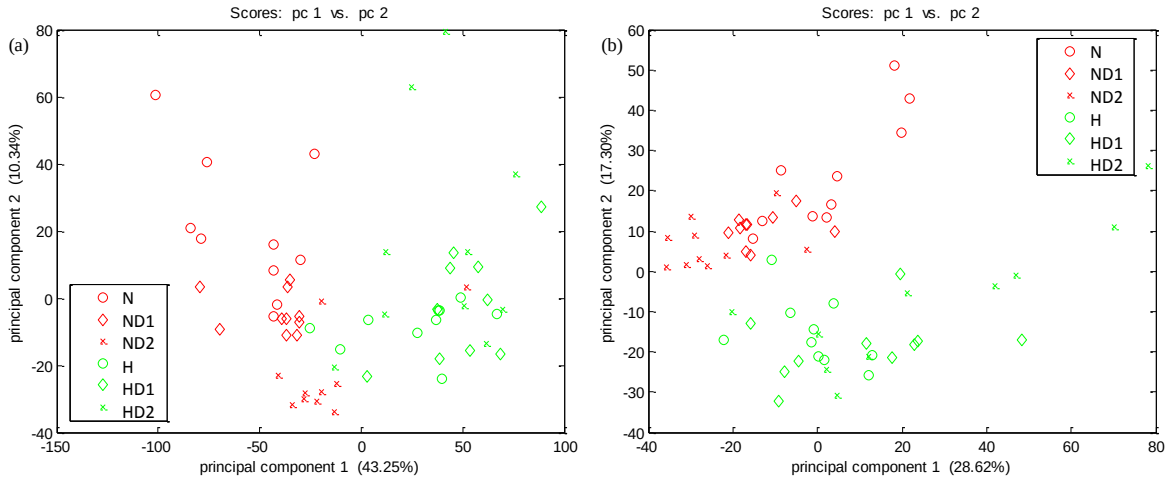

Figure 45: Principal component analysis (PCA) on ultra high performance liquid chromatography mass spectrometry (UHPLC-MS) data for (a) positive ion mode and (b) negative ion mode. MDA-MB-231 cells were cultured in normoxia (N), or hypoxia (H). Subsequently cells were untreated, or treated with either 0.1 (D1) or 1 µM (D2) doxorubicin.

Since the magnitude of the UHPLC-MS data were too great to interpret the loadings from PCA, UVA was applied. A Friedman test, which is a non-parametric statistical test, was applied to the UHPLC-MS data to determine the effect of oxygen after adjusting for possible drug effects. FDR was not applied to this dataset as there were too few biological replicates for the test to be useful. Alternatively a Bonferroni multi-comparison test could have been applied, however this only accounts for type I error (false positives) and can inflate the occurrence of type II errors (false negative)[166, 167]. Thus, there is a greater chance of ignoring a real relationship, which may be an important biological effect. Furthermore, the Friedman test is a non-parametric test and therefore more conservative than parametric methods. Consequently, manual inspections of the box plots were

conducted to confirm that the result observed was true, thus minimising false discovery. The top 10 identified metabolites were outputted for positive ion mode and negative ion mode as shown in Table 9 and Table 10 respectively. These metabolites are markers of the cellular response to low oxygen environments.

Table 9: Metabolites detected by ultra high performance liquid chromatography mass (UHPLC-MS) in positive ion mode that were observed to be statistically different for MDA-MB-231 cells cultured in normoxia and hypoxia. *P*-values were calculated using Freidman analysis.

***p*-value**	**Metabolite ID**	**Direction of metabolite difference with respect to normoxia**
5.89×10^{-11}	Dodecatrienol	Decrease
7.88×10^{-11}	Proline	Decrease
7.88×10^{-11}	Amino-octanoic acid or ethyl-hexenoic acid or methyl-heptenoic acid or Octenoic acid	Decrease
1.40×10^{-10}	Hydroxy-undecanoic acid	Decrease
1.40×10^{-10}	LysoPC(14:0) or PC(O-12:0/2:0) or 1alpha,25-dihydroxy-24-oxo-23-azavitamin D2	Increase
1.87×10^{-10}	L-Carnitine or (5-L-Glutamyl)-L-glutamine	Decrease
2.48×10^{-10}	13-hydroxy-tridecanoic acid or 2-hydroxytridecanoate or 3-hydroxy-tridecanoic acid or 3R-hydroxy-tridecanoic acid or 4-hydroxy-tridecanoic acid	Decrease
2.48×10^{-10}	8-hydroxydeoxyguanosine 5-triphosphate or GTP or Guanosine-3-Monophosphate-5-Diphosphate	Increase
3.29×10^{-10}	N-palmitoyl taurine	Increase
3.29×10^{-10}	Hydroxy-tridecanoic acid	Increase

Table 10: Metabolites detected by ultra high performance liquid chromatography mass (UHPLC-MS) in negative ion mode that were observed to be statistically different for MDA-MB-231 cells cultured in normoxia and hypoxia. *P*-values were calculated using Freidman analysis.

***p*-value**	**Metabolite ID**	**Direction of metabolite difference with respect to normoxia**
5.89×10^{-11}	(4R,5S)-4,5,6-Trihydroxy-2,3-dioxohexanoate or 2,3-Dioxo-L-gulonate or ",5-Didehydro-D-gluconate or 4,5-Dehydro-D-Glucuronic Acid or 5-Dehydro-4-deoxy-D-glucarate or 5-keto-4-deoxy-D-glucarate or Carboxymethyloxysuccinate or Citrate or Isocitrate	Decrease
7.88×10^{-11}	(2S, 3S)-3-methylaspartate or Isoglutamate or Glutamate or threo-Methylaspartate or N-Acetylserine or O-Acetyl-L-serine	Decrease
3.29×10^{-10}	LysoPC(18:0) or PC(O-16:0/2:0)	Increase
4.35×10^{-10}	N-Acetyl-L-Citrulline	Decrease
2.48×10^{-10}	3-Dehydro-L-threonate or Malic acid	Decrease
5.89×10^{-11}	Aconitate or Dehydroascorbic acid	Decrease
3.29×10^{-10}	AminoDAHP or S-Acetyldihydrolipoamide or 5-Hydroxyindolepyruvic acid or 8-Methoxykynurenate or N2-acetyl-alpha-aminoadipate	Decrease
1.40×10^{-10}	Indolepyruvic acid or AminoDHQ or Glutarylglycine or L-2-Amino-6-oxoheptanedioate or N-Acetylglutamic acid or N-Carbamoylputrescine	Decrease
9.96×10^{-10}	Gamma-L-Glutamyl-L-cysteinyl-beta-alanine or S-Methyl GSH	Decrease
2.48×10^{-10}	Choline stearate	Increase

4.2.2 Metabolic response of hypoxia-induced chemotherapy resistance

To explore the underlying metabolic response to hypoxia-induced chemoresistance a dose of 0.1 µM doxorubicin, shown in Chapter 3 to inhibit growth of normoxic MDA-MB-231 cells by ~50 % but to have no effects in low oxygenated cells, was used to treat cells pre-exposed to normoxia, hypoxia or anoxia. MVA was used to classify the metabolic phenotype of hypoxia-induced chemotherapy resistance for GC-MS data. Six groups, normoxia, hypoxia and anoxia samples with and without a 24 h treatment of 0.1 µM doxorubicin were included in the DFA. A total of 12 PCs were used to generate the model in Figure 46 accounting for 81.67 % of the TEV. Results shown in Figure 46 illustrate drug treated samples cannot be separated from the oxygen tension as the variation with respect to oxygen is too great.

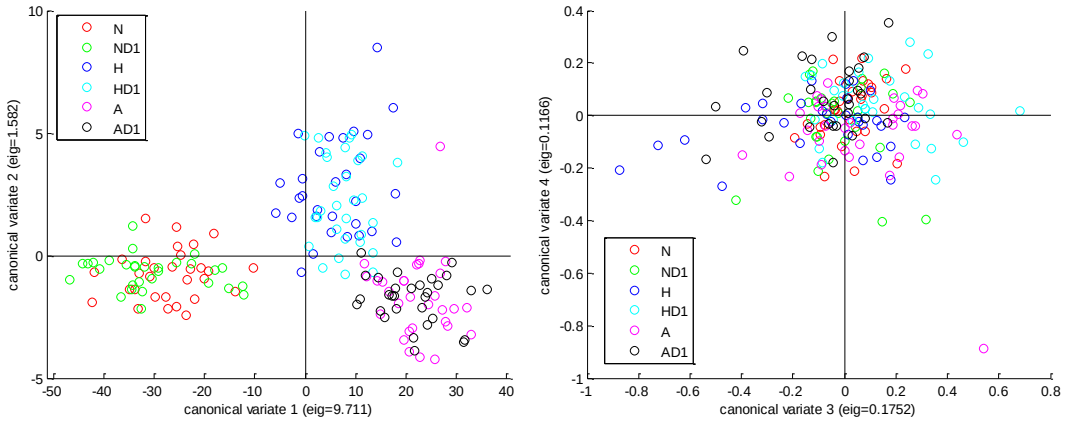

Figure 46: Discriminant function analysis (DFA) scores plots (a) 1 *vs.* 2 and (b) 3 *vs.* 4 of gas chromatography mass spectrometry (GC-MS) data for MDA-MB-231 cells cultured in normoxia (N), hypoxia (H) and anoxia (A). Subsequently cells were untreated, or treated with 0.1 µM (D1) doxorubicin.

Subsequently, the data were divided into smaller groups to investigate the metabolic response of drug treatment in individual oxygen tensions. The aim was to explore the metabolic response of drug toxicity in normoxic cells and drug resistance in hypoxic cells. Figure 47 illustrates the results of DFA for normoxia samples with and without doxorubicin 0.1 µM treatment. A total of 18 PCs were used to generate the model in Figure 47 accounting for 89.91 % of the TEV. Figure 48 and Figure 49 show the result of DFA for hypoxia and anoxia, respectively, treated with and without 0.1 µM doxorubicin. A total of 18 PCs were used to generate the model in Figure 48 accounting for 93.32 % of the TEV. A total of 18 PCs were used to generate the model in Figure 49 accounting for 94.03 % of the TEV. Inspection of the loadings revealed the normoxic metabolites IDs that differ with respect to the presence of doxorubicin were 32, 41, 42 and 46 relating to the metabolites 2-ketoglutaric acid, citric acid, N-acetylaspartic acid and scyllo-inositol/myo-inositol/inositol. Inspection of the hypoxic loadings showed metabolites IDs that differ

with respect to the presence of doxorubicin were 1, 2, 16, and 24 relating to the metabolites glycine, lactic acid, benzoic acid and xylitol. Inspection of the anoxic loadings showed metabolites IDs that differ with respect to the presence of doxorubicin were 10, 18, 19, 27 and 30 relating to the metabolites glycine, malic acid, 4-hydroxyproline, methionine and hypotaurine.

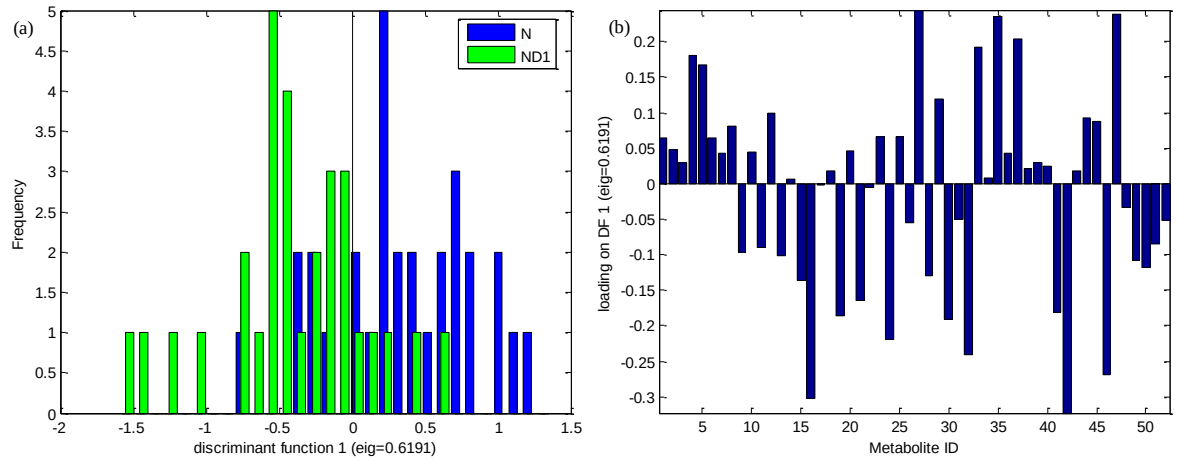

Figure 47: Discriminant function analysis (DFA) (a) frequency plot and (b) loadings plot of gas chromatography mass spectrometry (GC-MS) data for MDA-MB-231 cells cultured in normoxia (N) or cultured in normoxia and treated with 0.1 µM doxorubicin (ND1).

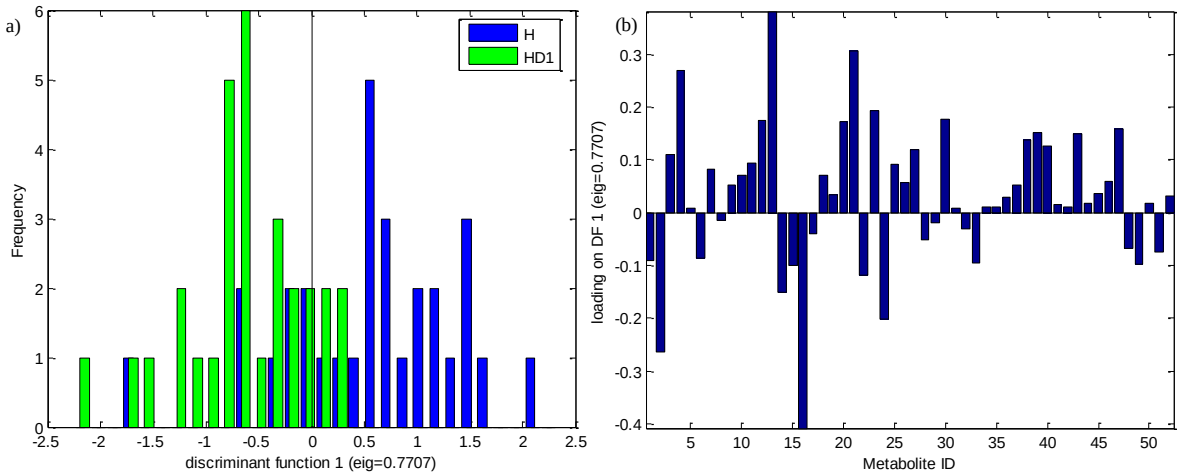

Figure 48: Discriminant function analysis (DFA) (a) frequency plot and (b) loadings plot of gas chromatography mass spectrometry (GC-MS) data for MDA-MB-231 cells cultured in hypoxia (H) or cultured in hypoxia and treated with 0.1 µM doxorubicin (HD1).

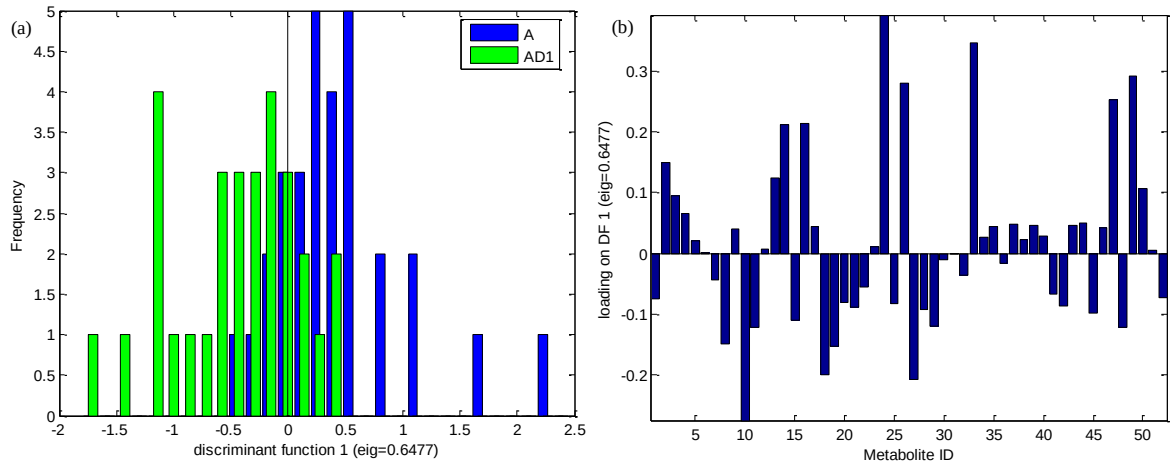

Figure 49: Discriminant function analysis (DFA) (a) frequency plot and (b) loadings plot of gas chromatography mass spectrometry (GC-MS) data for MDA-MB-231 cells cultured in anoxia (A) or cultured in anoxia and treated with 0.1 µM doxorubicin (AD1).

UVA was performed using a two-way ANOVA to discover the interaction of metabolites over the three oxygen tensions with respect to drug treatment. More specifically, the interaction was used to reveal metabolite markers of hypoxia-induced drug resistance. Interaction effects of doxorubicin treatment on the cancer cells exposed to various oxygen tensions identified 11 metabolites and are shown in Table 11.

Table 11: Metabolites observed in gas chromatography mass spectrometry (GC-MS) data to be statistically different for MDA-MB-231 cells cultured in normoxia, hypoxia or anoxia and untreated or treated with 0.1 µM doxorubicin. The direction of the metabolite concentration change is given relative to the non-drugged oxygen tension. *P*-values were calculated using a two-way analysis of variance (ANOVA), were corrected for a false discovery rate (FDR) *q*-value = 0.1.

Interaction	*p*-value	Metabolite	Direction of change relative to non-drugged oxygen tension
Normoxic	0	N-acetylaspartic acid	Increase
Hypoxic	0	Glycine	Decrease
	7.66×10^{-11}	Pyruvic acid	Decrease
	3.47×10^{-9}	Xylitol	Decrease
	1.92×10^{-6}	Glutamic acid	Decrease
	1.84×10^{-5}	Methionine	Decrease
	2.97×10^{-3}	Malonic acid	Decrease
	3.71×10^{-3}	Scyllo-inositol / myo-inositol/ inositol	Decrease
Anoxic	4.68×10^{-7}	Threonine	Decrease
	1.25×10^{-6}	Hypotaurine	Decrease
	1.93×10^{-4}	Benzoic acid	Decrease

Some of the metabolites markers are represented as box-whisker plots shown in Figure 50.

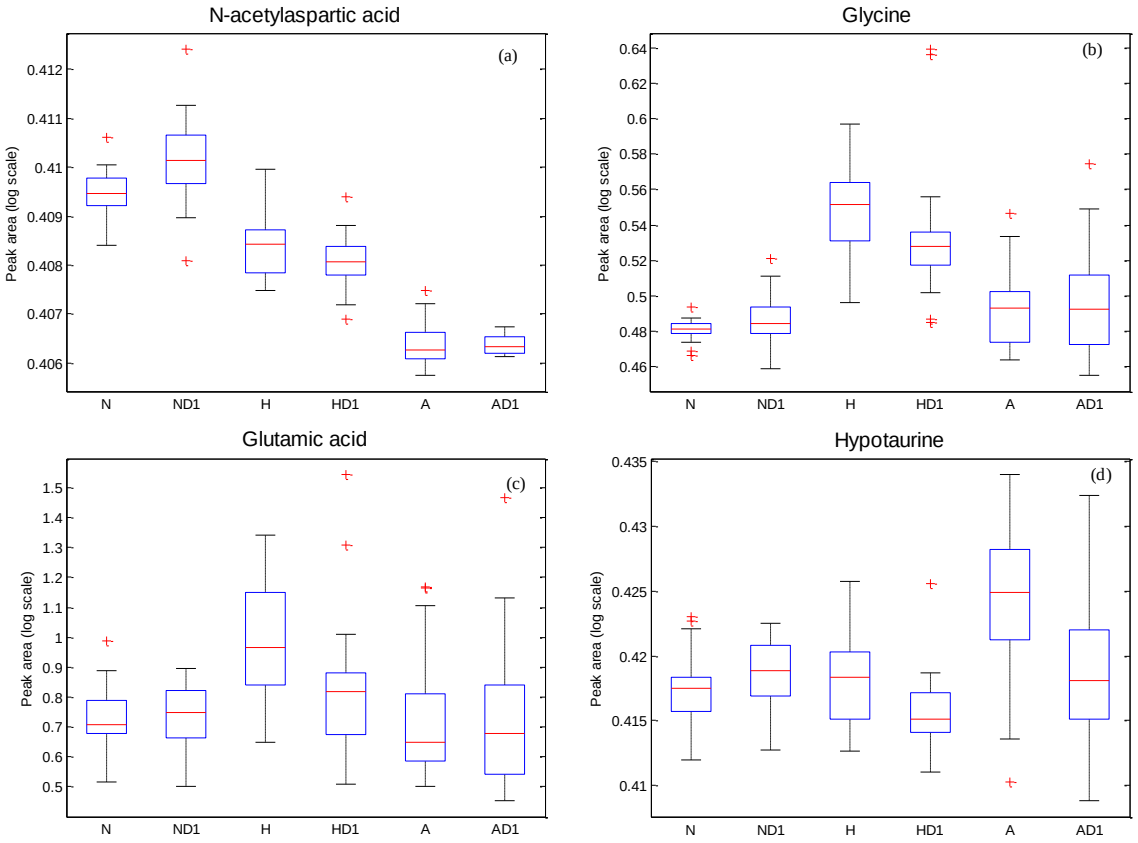

Figure 50: Box–whisker plots showing the difference in the expression of intracellular metabolites (a) N-acetylaspartic acid, (b) glycine, (c) glutamic acid and (d) hypotaurine acquired using gas chromatography mass spectrometry (GC-MS).). MDA-MB-231 cells were cultured in normoxia (N), hypoxia (H) or anoxia (A). Subsequently cells were untreated, or treated with 0.1 µM doxorubicin (D1).

Metabolite markers of hypoxia-induced drug resistance were detected in UHPLC-MS data through applying a Friedman test to observe the drug resistant response after adjusting for possible oxygen effects. Normoxia and hypoxia drug responses, when treated with 0.1 µM doxorubicin, were compared to untreated samples to explore the metabolites contributing to drug resistance. The 14 most significantly identified metabolite markers in positive ion mode are shown in Table 12 and negative ion mode in Table 13.

Table 12: Metabolites observed, using ultra high performance liquid chromatography mass spectrometry (UHPLC-MS) in positive ion mode, to be statistically different for MDA-MB-231 cells cultured in normoxia or hypoxia and untreated or treated with 0.1 µM doxorubicin. The direction of the metabolite concentration change is given relative to the non-drugged oxygen tension. *P*-values were calculated using Freidman analysis.

***p*-value**	**Metabolite ID**	**Direction of difference relative to non-drugged oxygen tension**
2.41×10^{-5}	Thymidine	Hypoxia increase
6.24×10^{-4}	LysoPC(15:0) or LysoPE(0:0/18:0) or LysoPE(18:0/0:0) or PC(14:0/O-1:0) or PC(15:0/0:0)[U] or PC(7:0/O-8:0)	Normoxia decrease
6.24×10^{-4}	1-O-Hexadecyl-lyso-sn-glycero-3-phosphocholine or PC(O-15:0/O-1:0) or PC(O-16:0/0:0) or PC(O-8:0/O-8:0)	Normoxia decrease
1.11×10^{-3}	N-Alpha-Acetyl-3,5-Diiodotyrosylglycine	Hypoxia Increase
1.34×10^{-3}	Eicosenol, eicosanal or thromboxane	Normoxia decrease
1.34×10^{-3}	2-Octaprenyl-3-methyl-6-methoxy-1,4-benzoquinone or DG(39:3)	Normoxia decrease
1.61×10^{-3}	PC(35:3) or PE(38:3)	Normoxia decrease
1.93×10^{-3}	DG(44:7)	Normoxia decrease
1.93×10^{-3}	PE(40:8)	Normoxia decrease

Table 13: Metabolites observed, using ultra high performance liquid chromatography mass spectrometry (UHPLC-MS) in negative ion mode, to be statistically different for MDA-MB-231 cells cultured in normoxia or hypoxia and untreated or treated with 0.1 µM doxorubicin. The direction of the metabolite concentration change is given relative to the non-drugged oxygen tension. *P*-values were calculated using Freidman analysis.

***p*-value**	**Metabolite ID**	**Direction of difference relative to non-drugged oxygen tension**
2.78×10^{-4}	DG(38:3)	Normoxia decrease
4.19×10^{-4}	SM(d18:1/16:0)	Normoxia decrease
7.59×10^{-4}	PG(38:4) or PC(33:0) or PE(36:0) or PC(35:3) or PE(38:3)	Normoxia decrease
7.59×10^{-4}	PC(38:5)	Normoxia decrease
9.20×10^{-4}	PE(20:5/dm18:1) or PE(22:6/dm16:0) or PE(O-16:1/22:6) or PC(32:1) or PE(35:0) or PE-NMe(34:1) or PE(18:2/dm18:1) or PE(18:3/dm18:0) or PE(20:3/dm16:0) or PE(O-16:0/20:4)	Normoxia decrease
9.20×10^{-4}	PC(16:0/dm18:0) or PC(18:0/dm16:0) or PC(O-16:0/18:1) or PC(O-16:0/18:1) or PC(O-18:0/16:1) or PC(O-18:1/16:0)	Normoxia decrease
9.20×10^{-4}	PT(36:1) or PC(34:2) or PE(37:2) or PE-NMe(36:2)	Normoxia decrease
1.11×10^{-3}	PC(22:5/dm18:1) or PC(22:6/dm18:0) or PC(P-18:0/22:6)	Normoxia decrease
1.34×10^{-3}	PC(38:4)	Normoxia decrease
1.34×10^{-3}	GlcCer(d18:0/22:0) or PC(O-14:0/22:0) or PC(O-16:0/20:0) or PC(O-18:0/18:0) or PC(O-20:0/16:0)	Normoxia decrease

4.2.3 Metabolic response to overcome hypoxia-induced chemotherapy resistance

To explore the underlying metabolic response required to overcome hypoxia-induced chemoresistance, a dose of 1 µM doxorubicin, shown in Chapter 3 to inhibit growth of hypoxic or anoxic MDA-MB-231 cells by ~50 %, was used to treat cells pre-exposed to hypoxia or anoxia. This dose is higher than the dose required to inhibited growth in ~50 % of cells cultured in normoxia. MVA was applied to examine the metabolic response of the drug in samples exposed to the same oxygen tension. For example, hypoxia untreated samples to hypoxia drug treated samples.

DFA was applied to the GC-MS data to identify the metabolic effect of a cytotoxic drug treatment on hypoxic cells. Figure 51 shows the DFA scores and loadings plot where a difference in DF1 can be observed. A total of 18 PCs were used to generate the model in Figure 51 accounting for 92.83 % of the TEV. Inspection of the loadings revealed the hypoxic metabolites IDs that differ with respect to the doxorubicin treatment were 1, 8, 15, 16, 19, 28, 42 and 50 relating to the metabolites glycine, leucine, succinic acid, benzoic acid, 4-hydroxyproline, creatinine, N-acetylaspartic acid and octadecanoic acid. Figure 52 shows the DFA of the metabolic effect of doxorubicin treatment on anoxic cells. A total of 18 PCs were used to generate the model in Figure 52 accounting for 91.47 % of the TEV. Inspection of the anoxic loadings showed metabolites IDs that differ with respect to the presence of cytotoxic doxorubicin were 9, 28, 50, 51, and 52 relating to the metabolites malonic acid, creatinine, octadecanoic acid, myo-inositol 1-phosphate and lactose/maltose/cellobiose.

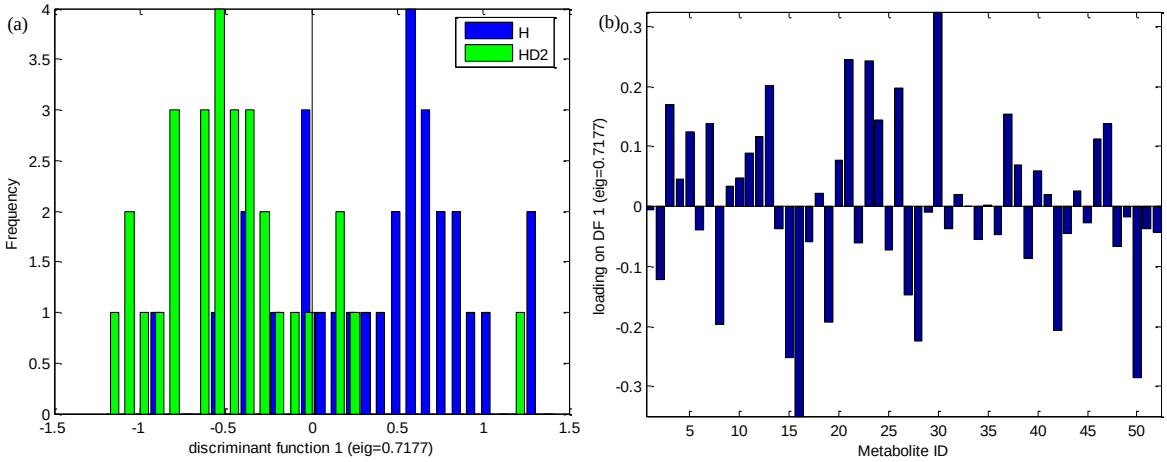

Figure 51: Discriminant function analysis (DFA) (a) frequency plot and (b) loadings plot of gas chromatography mass spectrometry (GC-MS) data for MDA-MB-231 cells cultured in hypoxia (H) or cultured in hypoxia and treated with 1 µM doxorubicin (HD2).

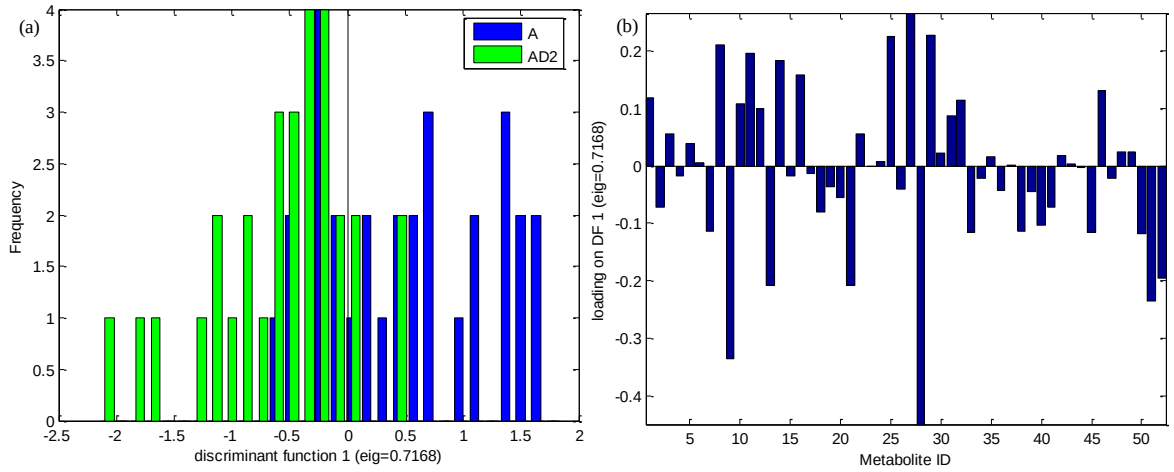

Figure 52: Discriminant function analysis (DFA) (a) frequency plot and (b) loadings plot of gas chromatography mass spectrometry (GC-MS) data for MDA-MB-231 cells cultured in anoxia (A) or cultured in anoxia and treated with 1 µM doxorubicin (AD2).

UVA using a two-way ANOVA was used to identify the interaction of metabolites over the three oxygen tensions with respect to a cytotoxic dose of doxorubicin. Interaction effects of a doxorubicin treatment on the cancer cells cultured in various oxygen tensions identified 6 metabolites and are shown in Table 14.

Table 14: Metabolites observed in gas chromatography mass spectrometry (GC-MS) data to be statistically different for MDA-MB-231 cells cultured in normoxia, hypoxia or anoxia and untreated or treated with 0.1 µM doxorubicin in normoxia or 1 µM doxorubicin in hypoxia or anoxia. The direction of the metabolite concentration change is given relative to the non-drugged oxygen tension. *P*-values were calculated using a two-way analysis of variance (ANOVA), were corrected for a false discovery rate (FDR) *q*-value = 0.1.

Interaction	*p*-value	Metabolite	Direction of difference relative to non-drugged oxygen tension
Normoxic	0	N-acetylaspartic acid	Increase
Hypoxic	0	Glycine	Decrease
	6.80×10^{-2}	Scyllo-inositol / myo-inositol/ Inositol	Decrease
Anoxic	0	2-hydroxyglutaric acid	Decrease
	1.30×10^{-6}	Hypotaurine	Decrease
	5.45×10^{-4}	Benzoic acid	Decrease

Some of the metabolites markers are represented as box-whisker plots shown in Figure 53.

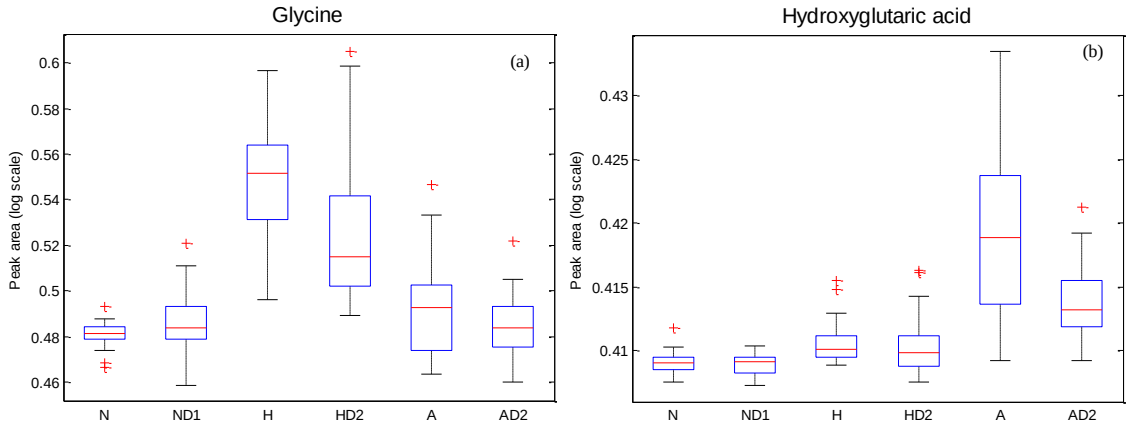

Figure 53: Box–whisker plots showing the difference in the expression of intracellular metabolites for (a) glycine and (b) hydroxyglutaric acid acquired using gas chromatography mass spectrometry (GC-MS). MDA-MB-231 cells were cultured in normoxia (N), hypoxia (H) or anoxia (A). Subsequently cells were untreated, or treated with 0.1 µM doxorubicin (D1) or 1 µM doxorubicin (D2).

Metabolite markers that represented the metabolic response to overcome hypoxia-induced drug resistance were detected in UHPLC-MS data using a Friedman test to observe the drug treatment response after adjusting for possible oxygen effects. Normoxia and hypoxia drug responses, when treated with 0.1 or 1 µM doxorubicin, respectively, were compared to untreated samples to investigate the metabolites contributing to overcome drug resistance. Metabolite markers identified for positive ion mode are shown in Table 15 and negative ion mode in Table 16.

Table 15: Metabolites observed, using ultra high performance liquid chromatography mass spectrometry (UHPLC-MS) in positive ion mode, to be statistically different for MDA-MB-231 cells cultured in normoxia (N) or hypoxia (H). Subsequently normoxia cells were treated with 0.1 µM doxorubicin and hypoxia cells were treated with 1 µm doxorubicin. The direction of the metabolite concentration change is given relative to the non-drugged oxygen tension. *P*-values were calculated using Freidman analysis.

***p*-value**	**Metabolite ID**	**Direction of change relative to non-drugged oxygen tension**
1.61×10^{-3}	Acetylspermidine	Hypoxia increase
3.88×10^{-3}	PE(36:7);PE(34:4) or PE(14:1/dm18:1)	Hypoxia increase
4.61×10^{-3}	Phosphoenolpyruvic acid	Hypoxia decrease
8.82×10^{-3}	PC(O-14:0/15:0) or PE(O-16:0/16:0)	Hypoxia increase
8.82×10^{-3}	3-Hydroxypropionyl-CoA or Lactyl-CoA/Lactoyl-coenzyme A	Normoxia increase
1.20×10^{-2}	D-Urobilinogen or I-Urobilin	Hypoxia increase
1.20×10^{-2}	CE(10:0)	Hypoxia increase

Table 16: Metabolites observed, using ultra high performance liquid chromatography mass spectrometry (UHPLC-MS) in negative ion mode, to be statistically different for MDA-MB-231 cells cultured in normoxia (N) or hypoxia (H). Subsequently normoxia cells were treated with 0.1 µM doxorubicin and hypoxia cells were treated with 1 µm doxorubicin. The direction of the metabolite concentration change is given relative to the non-drugged oxygen tension. *P*-values were calculated using Freidman analysis.

***p*-value**	**Metabolite ID**	**Direction of change relative to non-drugged oxygen tension**
1.20×10^{-4}	3-Dehydro-L-threonate or Malic acid	Hypoxia decrease
2.26×10^{-4}	3-UMP or Pseudouridine 5-phosphate or UMP or Uridine 2-phosphate or uridine 3-monophosphate	Hypoxia increase
3.42×10^{-4}	L-Acetylcarnitine	Hypoxia decrease
4.19×10^{-4}	N-Acetyl-L-citrulline	Normoxia decrease
7.59×10^{-4}	GDP-D-mannose or GDP-glucose or GDPhexose or GDP-L-galactose or GDP-L-gulose or GDP-mannose	Normoxia decrease
1.34×10^{-3}	Alpha-D-Glutamyl phosphate or alpha-L-glutamyl phosphate or L-Glutamyl 1-phosphate or L-Glutamyl 5-phosphate	Normoxia decrease
1.61×10^{-3}	PG(34:4) or PC(29:0) or PE(32:0) or PE(34:3)	Normoxia decrease
1.93×10^{-3}	Glutamylalanine	Normoxia decrease
3.28×10^{-3}	Octadienoic acid	Hypoxia increase
4.61×10^{-3}	AminoDAHP or S-Acetyldihydrolipoamide or 5-Hydroxyindolepyruvic acid or 8-Methoxykynurenate or N2-acetyl-alpha-aminoadipate	Normoxia increase

4.2.4 Quantification of the uptake of carbon sources glutamine, glucose and the excretion of lactic acid

Metabolic footprinting analysis was found to be too complex for metabolic profiling analysis, as shown in Chapter 3. The media is metabolite rich and contains undefined FCS, a supplement required for growth containing embryonic promoting and survival enhancing factors, prevent the subtle metabolic differences from being detected by metabolic profiling analysis. Thus, three assays were used to quantify the uptake of glucose, uptake of glutamine and the efflux of lactic acid. Flux data were used in combination with intracellular metabolic profiling data to support the experimental outcome. Results for the uptake of carbon sources glucose and glutamine are shown in Figure 54 and Figure 55 respectively. Results revealed anoxic cells rely on an increase consumption of both carbon sources to maintain survival under the low oxygen tension when compared to normoxic cells. An increased uptake of glucose may be a metabolic survival response to generate more ATP (through non-oxidative phosphorylation metabolism) required for bioenergetic processes such as DNA repair pathways and drug efflux via Pgp[202]. Furthermore, increased glutamine uptake may be used to supplement the TCA cycle to synthesise metabolic precursors for cell growth as a result of non oxidative phosphorylation metabolism. Non-oxidative phosphorylation metabolism drives glycolysis for energy production therefore glutaminolysis maintains the TCA cycle to produce metabolic precursors such as 2-ketoglutaric acid for cell growth[203]. A significant decrease in glutamine uptake was observed between anoxic cells and anoxic cells treated with 1 µM doxorubicin. This was

not observed in normoxia cells treated with doxorubicin. Thus, anoxic cells treated with 1 µM doxorubicin may be using alternative metabolic pathways to overcome chemoresistance.

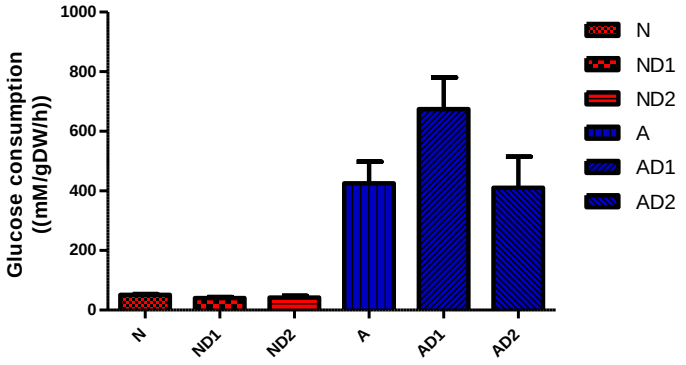

Figure 54: Uptake of glucose (mM/gDW/h) from the extracellular media for MDA-MB-231 cells cultured in normoxia (N), hypoxia (H) or anoxia (A). Subsequently cells were untreated, or treated with 0.1 µM doxorubicin (D1) or 1 µM doxorubicin (D2). One-way analysis of variance (ANOVA) and subsequent Tukey revealed N and A are significantly different (p<0.05). Data are means ± s.d. (n=3).

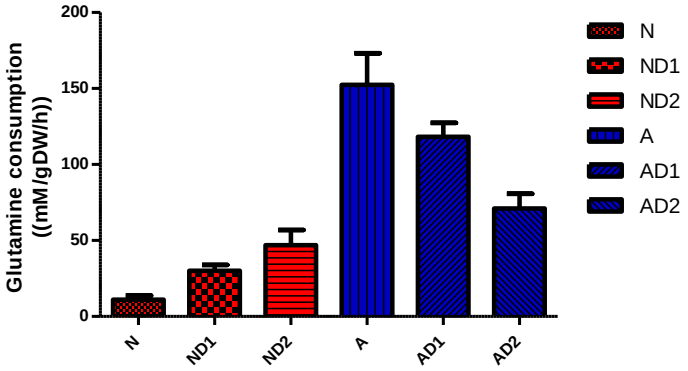

Figure 55: Uptake of glutamine(mM/gDW/h) from the extracellular media for MDA-MB-231 cells cultured in normoxia (N), hypoxia (H) or anoxia (A). Subsequently cells were untreated, or treated with 0.1 µM doxorubicin (D1) or 1 µM doxorubicin (D2). One-way analysis of variance (ANOVA) and subsequent Tukey revealed N and A are significantly different (p<0.05). Additionally, A and AD2 are significantly different (p<0.05). Data are means ± s.d. (n=3).

Lactate efflux approximately doubled in anoxic cells compared to normoxic cells, which confirmed anoxic cells are undergoing non-oxidative phosphorylation metabolism (Figure 56). Lactate is the end product of non-oxidative phosphorylation metabolism, which under physiological pH exists in its protonated form. Lactate diffuses across cell membranes and into the extracellular environment contributing to acidosis, which has been shown to prevent the uptake of doxorubicin[204].

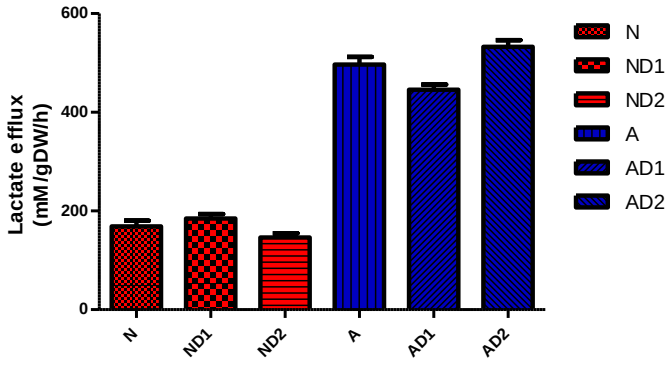

Figure 56: Efflux of lactate (mM/gDW/h) from the extracellular media for MDA-MB-231 cells cultured in normoxia (N), hypoxia (H) or anoxia (A). Subsequently cells were untreated, or treated with 0.1 µM doxorubicin (D1) or 1 µM doxorubicin (D2). One-way analysis of variance (ANOVA) and subsequent Tukey revealed N and A are significantly different ($p<0.05$). Data are means ± s.d. ($n=3$).

4.3 Discussion

Metabolomics has contributed towards understanding the metabolic response of numerous diseases including the complexity of cancer[62, 65, 67]. Metabolomics analysis of both hypoxia[69] and the chemotherapeutic doxorubicin[72, 205] have previously been studied however, there are currently no studies of hypoxia-induced chemoresistance using a metabolomics approach, particularly with respect to the MDA-MB-231 breast carcinoma cell model. Previous studies have shown MDA-MB-231 cells cultured in hypoxia results in chemoresistance[184, 206]. Furthermore, the MDA-MB-231 breast carcinoma model cultured in 1 % oxygen was shown in section 2.3 to induce doxorubicin resistance. Consequently, the MDA-MB-231 breast carcinoma model was selected to study hypoxia-induced resistance to doxorubicin. Metabolomics was able to identify novel metabolite markers, which could be used to predict the phenotype of hypoxia-induced chemotherapy resistance. Monitoring the metabolite marker changes to overcome hypoxia-induced chemoresistance contributed towards understanding why commonly used chemotherapeutics fail in treating hypoxic tumours, thus unravelling promising new drug targets and combination therapies (as will be shown in the next paragraph).

The first aim was to determine whether the metabolite profile in normoxic cells differ from those exposed to a low oxygen tension. Subsequently, the metabolic response of cells cultured in normoxia and treated with a cytotoxic dose of doxorubicin was compared to low oxygen cells treated with the same dose known not to be cytotoxic. Data were then examined to investigate the metabolic response of low oxygen cells treated with a higher dose of drug, which has been shown to induce toxicity.

4.3.1 Cellular metabolism in a low oxygen environment

Tumour cells can regulate the cellular response to overcome the toxic effects of chemotherapeutic treatment in each level of the cell from the genome, transcriptome, proteome and metabolome[207]. The metabolic responses to the low oxygen environments were determined to ascertain the survival mechanism and may also contribute to cells acquiring a chemoresistance phenotype prior to treatment. Uptake of the metabolites glutamine and glucose and the efflux of lactic acid, determined using biochemical assays, suggested cells cultured in anoxia undergo non-oxidative phosphorylation metabolism. Increased uptake of the carbon source glucose correlated with an increase in lactic acid efflux suggests anoxic cells are relying on non-oxidative phosphorylation metabolism to maintain ATP production, which is vital for many cellular processes[208]. Non-oxidative phosphorylation metabolism causes acidosis in the extracellular environment, which has previously been linked a reduction of doxorubicin uptake[12, 209]. Doxorubicin diffuses passively across the cell membrane, which occurs most readily when the molecule is in an uncharged state[37]. Lowering the extracellular pH causes doxorubicin, a weakly basic compound, to become protonated and subsequently reduces drug uptake. Non-oxidative phosphorylation metabolism may predispose cells to decrease doxorubicin uptake and thus reduce cytotoxicity. In addition, an increase in glutamine uptake for anoxic cells suggests utilisation of the glutaminolysis pathway to produce biomass precursors for growth and energy production (described in more detail below).

PCA of GC-MS data revealed metabolic differences with respect to normoxia and anoxia (but not for hypoxia as the samples were distributed over the scores origin). The loadings for normoxic metabolites were mapped onto metabolic pathways including TCA cycle, carbohydrate metabolism, and amino acid metabolism. Loadings for anoxic metabolites were mapped onto pathways such as carbohydrate metabolism, fatty acid metabolism, and amino acid metabolism. Comparing the unique pathway differences between the samples types suggests anoxic samples differ with respect to fatty acid metabolism whereas normoxic samples differ with respect to the TCA cycle. Cells cultured in normoxia may use the TCA cycle for energy maintenance and to produce metabolic precursors for biomass and cell growth. Cells cultured in anoxia may rely on fatty acid metabolism for survival. Anabolism of fatty acids is initiated in the TCA cycle from citrate. Citrate is transported into the cytosol where it is converted to acetyl-CoA and subsequently malonyl-CoA. Malonyl-CoA is converted to palmitate by fatty acid synthase[208] (Figure 57). Free

fatty acids are stored as triacylglycerols by adipose cells (in mammalian systems) or are used to generate phospholipids, which are used in the cell membrane.

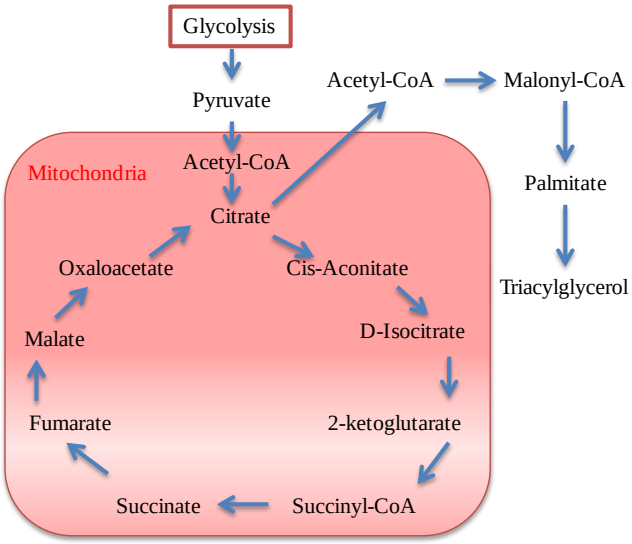

Figure 57: Mechanism of fatty acid metabolism in the cytosol and mitochondria.

Fatty acid synthase has been shown to be associated with cancer and inhibition of this enzyme has been associated with apoptosis210. Furthermore, the gene that encodes the enzyme has been proposed as an oncogene[211] and an indicator of poor prognosis[212]. Also, the over expression of fatty acid synthase has been reported to be associated with chemoresistance[213]. Anaerobic cancer cells may upregulate fatty acid synthesis to promote survival, which may precondition cells to have a chemo-resistant phenotype prior to drug treatment. Additionally, fatty acid synthesis may be a mechanism to maintain redox balance similar to the reason for increasing non-oxidative phosphorylation metabolism. For example, for each molecule of glucose approximately 10 NADH and 2 $FADH_2$ compounds are generated by the TCA cycle[208]. Restricting oxygen availability limits the flux through the mitochondrial electron transport chain, which produces a redox imbalance and consequently NADH and $FADH_2$ remain in a reduced state. Generation of palmitate requires approximately 14 NADPH, which contributes to stabilising the redox imbalance[214].

DFA showed similar metabolite differences in GC-MS data with respect to the separation between normoxia and anoxia samples; however, hypoxia samples, which were previously residing on the origin of the scores plot in PCA, separated in DF2 offering an insight into hypoxia metabolism. Many of the metabolism differences exist in amino acid metabolism; however the glycolytic and pyrimidine metabolic pathway also differed. Amino acids

including leucine, glycine, threonine and glutamic acid differed with respect to hypoxia metabolism. Hypoxic cells may increase amino acid uptake for catabolism to help maintain intracellular ATP and biomass precursors for growth.

Statistical analysis of GC-MS data using a two-way ANOVA highlighted 20 metabolites that differ significantly with respect to lowering the oxygen tension. Glycine and myo-inositol 1-phosphate were hypoxia specific metabolite markers, which were also identified using DFA. Glycine is a non-essential amino acid and can be synthesised from the glycolysis metabolite 3-phosphoglycerate. Additionally, glycine can be generated from choline in the glycine-betanine pathway[215]. Glycine has a role in nucleotide and protein synthesis[179]. It has previously been reported that high glycine levels in malignant breast cancer tumours was associated with poor patient prognosis[179]. An elevated level of glycine in the hypoxic samples is possibly a consequence of the altered regulation of the glycolysis pathway or the glycine-betaine pathway. The hypoxia metabolite marker myo-inositol 1-phosphate is a carbohydrate that resides in the inositol phosphate pathway. This metabolite increased in hypoxic samples in comparison to normoxia and anoxia samples. Myo-inositol 1-phosphate is a cyclohexane alcohol and, in addition to formation in the inositol phosphate pathway, it can be produced from glucose 6-phosphate through the enzyme inositol 3-phosphate synthase 1[216]. Myo-inositol 1-phosphate is also a member of the phosphatidylinositol signalling system. The inositol phosphate pathway is involved in a number of cellular processes including cell growth, apoptosis, cell migration, endocytosis and cell differentiation[216]. Myo-inositol 1-phosphate is therefore a unique metabolite marker of hypoxia metabolism.

Pyruvic acid and 2-hydroxyglutaric were anoxia specific metabolite markers. These metabolites were also identified using DFA. Pyruvic acid decreases relative to normoxic and hypoxic samples. Pyruvic acid is an intermediate compound for the generation of carbohydrates, proteins and fatty acids through decarboxylation to acetyl-CoA, carboxylation to oxaloacetic acid, transamination to alanine, and reduction to lactic acid[201]. Since lactic acid efflux was shown to significantly increase with respect to low oxygen availability, pyruvic acid as a metabolite marker is more likely to be related to non-oxidative phosphorylation metabolism. The anoxic metabolite marker 2-hydroxyglutaric acid increased compared to hypoxia and normoxia samples. 2-hydroxyglutaric acid is formed from 3-hydroxybutanoate by the enzyme hydroxyacid-oxoacid transhydrogenase and can be converted to 2-ketoglutaric acid by the enzyme 2-hydroxyglutarate

dehydrogenase. 2-ketoglutaric acid is a metabolite in the TCA cycle. The metabolite may be used to supplement the TCA cycle in a similar fashion to glutamine[217].

Metabolites including 2-ketoglutaric acid, glycerol 3-phosphate, citric acid, N-acetylaspartic acid, leucine and hexadecanoic acid were found to be both hypoxic and anoxic metabolite markers and therefore represent low oxygen metabolism. These metabolite markers were also identified using DFA. A decrease in citric acid and 2-ketoglutaric acid may be connected through the TCA cycle. These TCA cycle intermediates may be a consequence of the shift from oxidative phosphorylation metabolism to non-oxidative phosphorylation metabolism, which would reduce the metabolic flux through the TCA cycle. Furthermore, succinic acid, another TCA cycle intermediate, increased with respect to diminishing oxygen availability, which suggests cells are undergoing an alternative mechanism to non-oxidative phosphorylation metabolism. Results may be suggesting the presence of a truncated TCA cycle similar to hypoglycaemia studies[218]. Acetyl-CoA is converted to citrate; however the conversion of citrate to isocitrate by the enzyme aconitase is inhibited by high concentrations of ROS[219]. Glutamine is converted to glutamate and subsequently to 2-ketoglutaric acid caused by an over expression of glutaminase[220]. 2-ketoglutaric acid is converted in the TCA cycle to malic acid. The enzyme NAD(P)-dependent malic acid decarboxylase is over expressed, which converts malic acid to pyruvic acid and subsequently to lactic acid for energy production[221]. This mechanism has been suggested to support cellular growth and viability[217, 222] and is shown in Figure 58.

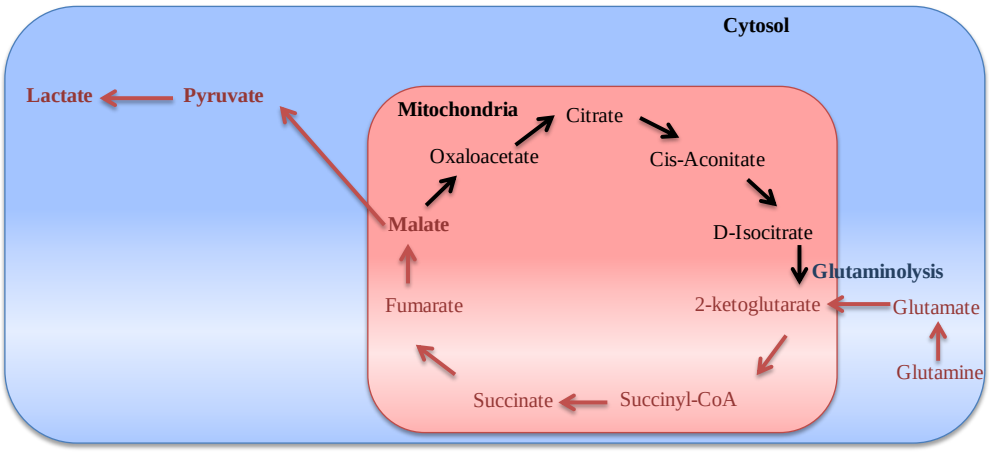

Figure 58: Schematic of the metabolites, highlighted in red, involved in glutaminolysis pathway, which occurs in the mitochondria and cytosol.

Low oxygen metabolite markers included an increase in amino acids leucine, isoleucine, methionine and valine. Autophagic degradation of proteins may be occurring in oxygen

limited samples for energy production, which would result in an increase in free amino acids[208]. Glycolytic cells requiring excess glucose may reprogram metabolic pathways for energy producing processes crucial for cell survival. Autophagy has previously been reported to promote the survival of hypoxic colon cancer cells[223]. In low oxygen environments cells may adapt and use this mechanism to feed amino acids back into central carbon metabolism to maintain cellular energy.

Overall these results have suggested that low oxygen cancer cells may promote their survival through exploiting metabolic mechanisms including anaerobic respiration, fatty acid synthesis, glutaminolysis, autophagy and truncation of the TCA cycle as shown in Figure 59. Some of these metabolic pathways such as non-oxidative phosphorylation metabolism predispose cells to a more chemotherapeutic resistant phenotype prior to treatment.

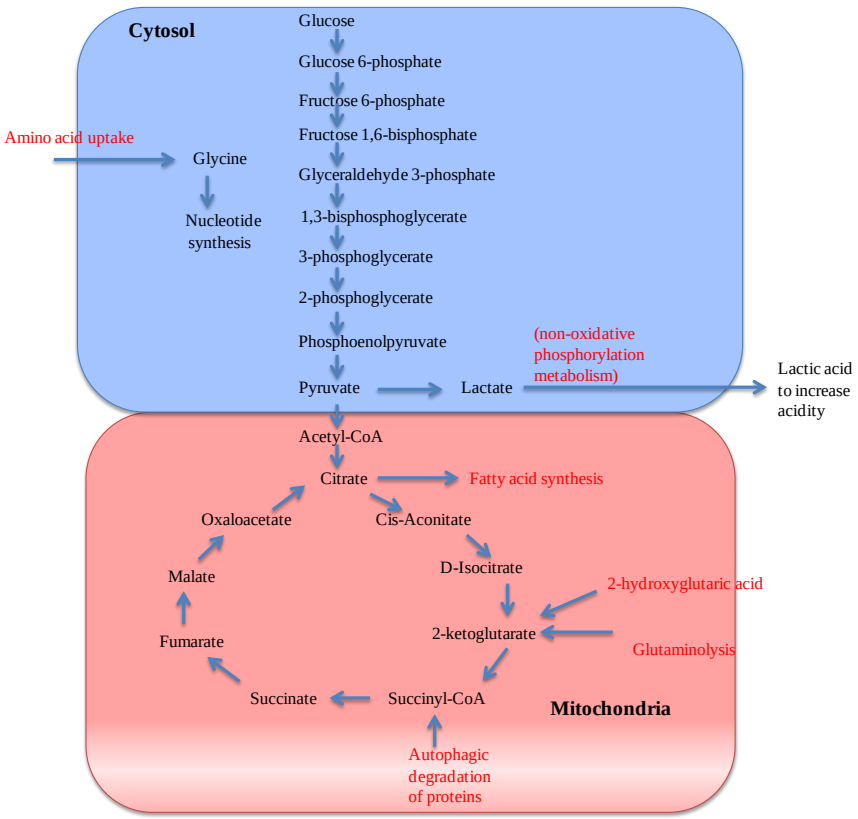

Figure 59: Summary of the pathways differentially regulated in high and low oxygenated cells.

4.3.2 Effect of doxorubicin treatment on cellular metabolism in normal oxygen environments

Doxorubicin is a valuable chemotherapeutic compound used to treat a wide variety of cancers including non-Hodgkin's and Hodgkin's lymphoma, multiple myeloma, lung,

ovarian, gastric, thyroid, breast, sarcoma and paediatric cancers[200]. Drug resistance in hypoxic cancer cells is dose dependent and can be overcome though increasing the drug dose; however, clinically, the dose of doxorubicin that can be used is restricted by dose-dependent cardiotoxicity. Whilst higher doses of doxorubicin are toxic towards hypoxic tumours, clinically a high dose produces too many side effects in patients[193]. In addition to cardiotoxicity, high doses of doxorubicin can also cause hepatic lipid peroxidation[224]. The cellular metabolic response to clinical doses of doxorubicin is not fully known or understood, however some metabolic pathways have been suggested to be targeted by the drug including inhibition of nucleic acid synthesis[225], inhibition of protein synthesis[225], and differential regulation of prostaglandins[193]. Further doxorubicin is known to have anti-tumour activity through intercalating into the DNA inhibiting synthesis, poisoning the topoisomerase II enzyme and generating free radicals that cause cell membrane damage[19].

The cellular metabolic response to a cytotoxic dose of doxorubicin was investigated in cells cultured in normoxia compared to cells cultured in normoxia and treated with 0.1 µM doxorubicin. DFA was able to classify the sample types in GC-MS data with respect to doxorubicin treatment. Loadings revealed metabolites associated with drug treatment to included 2-ketoglutaric acid, citric acid, N-acetylaspartic acid and scyllo-inositol/myo-inositol/inositol. Inositol is associated with cell detoxification processes, which may be a mechanism upregulated during doxorubicin treatment in an unsuccessful attempt to overcome the ROS (generated by doxorubicin)[205]. Citrate has been suggested to inhibit glycolysis through feedback inhibition of the glycolytic enzyme phoshofructokinase[208]. Doxorubicin treatment may cause the cytosolic levels of citrate to increase, thus decreasing the glycolytic flux and reducing energy metabolism and energy dependent drug resistance processes such as Pgp efflux[226] and DNA repair[9].

The interaction between oxygen level and drug treatment was examined using a two-way ANOVA of GC-MS data and Friedman analysis of UHPLC-MS data. GC-MS data were $\log_{10}$ scaled resulting in the data exhibiting a parametric profile, thus a two-way ANOVA parametric statistical test was used[161]. UHPLC-MS did not have a parametric profile (following scaling) and therefore the Friedman non-parametric statistical test was used[227]. Box plots of the most significant interactions showed the direction of the difference between the oxygen and drug effects. A relative increase in N-acetylaspartic acid was found to be significantly different in normoxia samples with respect to drug treatment. In addition N-acetylaspartic acid was found by DFA to be a metabolite contributing to the

separation of normoxic drug treated samples. N-acetylaspartic acid is a novel metabolite marker of doxorubicin toxicity. N-acetylaspartatic acid is found in the alanine, aspartate and glutamate metabolism of the Kyoto encyclopaedia of genes and genomes (KEGG) database[201] and is converted to L-aspartic acid through the enzyme aspartoacylase. N-acetylaspartic acid has been reported as one of the highest concentrated free amino acids synthesised and stored in the brains neurons[228]. Not a great deal is known about the synthesis and use of this metabolite other than in the brain; however there has been some research describing the presence of N-acetylaspartic acid in the lens of the eye[229]. More recently, N-acetylaspartic acid was discovered as a metabolite marker in the benign serous fluid of ovarian tumours [230, 231]. It has been proposed that N-acetylaspartic acid plays a role as a molecular water pump in the central nervous system[228]. Furthermore, Friedman analysis of UHPLC-MS data revealed additional metabolite markers of normoxic drug action. Metabolite markers that decrease in normoxic drug treated samples, but did not respond in hypoxic drug treated samples, included diacyglycerol (DAG(44:7)), DAG(38:3), glycerophosphoethanolamine (PE(40:8)), sphingomyelin (SM(d18:1/16:0)), glycerophosphocholine (PC(38:5)), PC(38:4), N-acetyl-L-citrulline and glutamylalanine. DAG(44:7), DAG(38:3), PE(40:8), SM(d18:1/16:0), PC(38:5) and PC(38:4) are unsaturated lipids that decrease with drug treatment suggesting a lipid response. In the presence of oxygen, the doxorubicin-semiquinone radical is re-oxidised back to doxorubicin resulting in the formation of ROS and hydrogen peroxide. ROS can cause membrane damage through lipid peroxidation[232], which is known to target fatty acids[208]. Polyunsaturated fatty acids contain multiple double bonds therefore there are many methylene groups that contain reactive hydrogens for peroxidation[208]. Glutamylalanine was shown to decrease in doxorubicin treated cells, which may be related to the metabolite being used to synthesise glutamate[64]. Glutamylalanine may be used to produce glutamate thus reducing glutamate uptake from the extracellular environment. Inhibition of glutamate uptake (using dihydrokainate a glutamate transporter inhibitor) has been suggested to decrease the efflux of doxorubicin[233]. A reduction of glutamate uptake in drug treated cells may reduce doxorubicin efflux thus increasing cytotoxicity.

Overall these results suggest drug action in normoxic cancer cell may promote toxicity through exploiting known mechanisms such as lipid peroxidation and unknown mechanisms such as increasing N-acetylaspartic acid and targeting the synthesis of glutamylalanine to glutamate (Figure 60). These metabolite markers suggest the metabolic mechanisms doxorubicin induces in normoxic cells to promote toxicity.

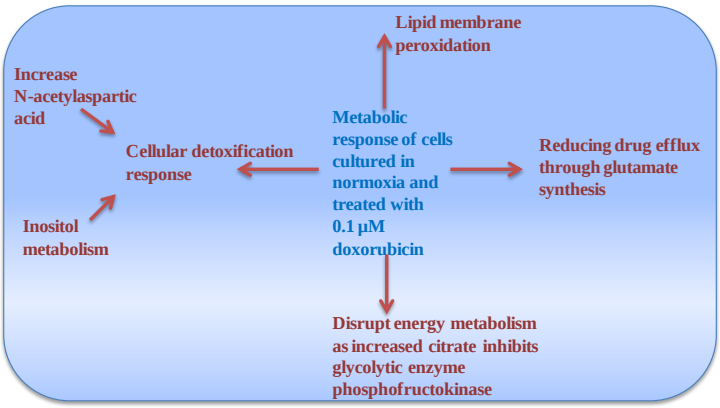

Figure 60: Summary of the metabolic response of MDA-MB-231 cells cultured in normoxia and dosed with 0.1 µM doxorubicin.

4.3.3 Metabolism and hypoxia-induced chemotherapy resistance

Two-way ANOVA of GC-MS data generated metabolite markers of low oxygen induced chemotherapy resistance and metabolite markers associated with overcoming low oxygen induced chemotherapy resistance. These two lists of metabolites were compared to identify the common metabolites of drug response in low oxygen environments. Common metabolites of a cellular response to doxorubicin, irrespective of dose, in low oxygenated environments included glycine and scyllo-inositol/myo-inositol/inositol for hypoxic samples and hypotaurine and benzoic acid for anoxic samples, some of which were also identified using DFA. These metabolites represent the cellular response of cells cultured in low oxygen environments to doxorubicin treatment regardless of the dose thus these metabolites are not metabolite markers of resistance or response. While these metabolites are not markers, viewing them in combination with other resistance or response metabolite markers may reveal a more comprehensive overview of the metabolic pathway responses.

Metabolite markers of hypoxia-induced chemotherapy resistance, determined through applying a two-way ANOVA to GC-MS data, included pyruvic acid, xylitol, glutamic acid, methionine, malonic acid, glycine and scyllo-inositol/myo-inositol/inositol. Furthermore, DFA identified glycine and xylitol to contribute to the separation of hypoxic drug treated samples. Metabolite markers discovered by Friedman analysis (with a single metabolite identification) of UHPLC-MS data (positive and negative ion mode) included thymidine and N-alpha-acetyl-3,5-diiodotyrosylglycine. A decrease in glutamic acid, a non-essential amino acid, and methionine, an essential amino acid were metabolite markers contributing to chemoresistance. Chemotherapy efficacy in tumours has been suggested to be decreased by ATP-dependent drug efflux pumps[226] and drug detoxification by glutathione[234].

Methionine has been suggested to be used for ATP production and to increase cellular detoxifying glutathione pools[235]. Decreasing methionine in the diet of rats has been shown to increase tumour sensitivity to the treatment of doxorubicin inhibiting tumour survival[235]. A mechanism of hypoxic cellular response to doxorubicin may be to use methionine for ATP production to drive ATP-dependent drug efflux pumps (such as Pgp) and drug detoxification through glutathione production. Furthermore, folate can be used to synthesise methionine; however increased methionine uptake would enable cells to use folate to synthesis thymidine and uracil thus promoting DNA repair and DNA replication mechanisms[236]. The metabolite marker malonic acid decreased in hypoxic drug treated cells. Malonic acid is involved in pyrimidine and fatty acid synthesis and is a competitive inhibitor of succinate dehydrogenase, which is located in the TCA cycle and the respiratory electron transport chain[237]. Decreasing malonic acid may reduce the inhibition of succinate dehydrogenase in the TCA cycle to enable the production of NADH and NADPH. NADPH is required for anabolic reactions such nucleic acid synthesis. Glycine is a metabolic precursor of nucleic acid synthesis, which decreases with drug treatment. In addition, there is an increase in the pyrimidine metabolite thymidine. Doxorubicin has been reported to damage DNA thus the upregulation of DNA synthesis pathways may be in response to repair DNA damage[193]. DNA synthesis rather than DNA repair may be a more successful target for drug resistant samples in combination with doxorubicin treatment.

Results suggest two metabolic mechanisms are contributing towards hypoxia-induced chemoresistance. Pathway targets to overcome chemoresistance include inhibiting methionine uptake and inhibiting DNA synthesis in hypoxic cells in combination with doxorubicin treatment. Combination cancer therapy may be useful to target the DNA synthesis pathways. This would improve the toxicity of doxorubicin towards hypoxic cells thorough a combination with another chemotherapeutic to target alternative metabolic pathways. The anti-metabolite 5-fluorouracil is clinically used to treat cancer through inhibiting the thymidylate synthase enzyme in the DNA synthesis pathway[16]. A combination of doxorubicin treatment and a DNA synthesis inhibitor (such as 5-fluorouracil) may be a lethal combination to hypoxic tumours.

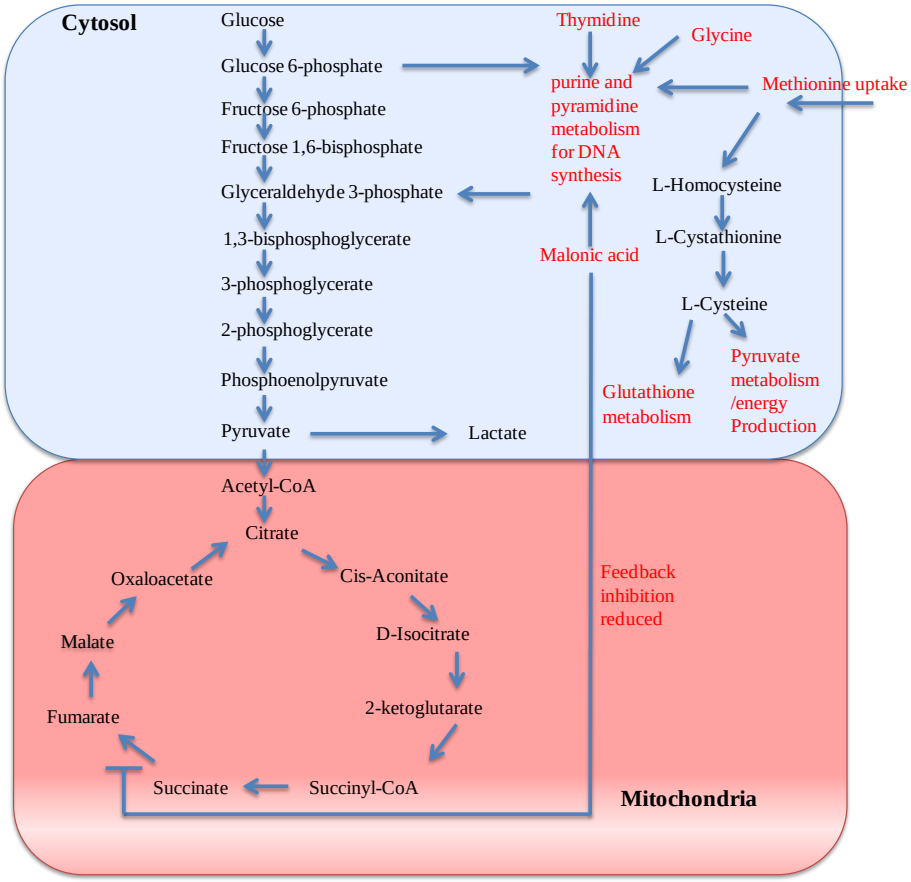

Figure 61: Summary of the metabolic response of MDA-MB-231 cells cultured in hypoxia and dosed with 0.1 µM doxorubicin. Mechanisms represent hypoxia-induced chemoresistance.

Two-way ANOVA of GC-MS data revealed metabolite markers associated with overcoming hypoxia-induced chemoresistance including glycine and scyllo-inositol/myo-inositol/inositol. Further interaction determined by Friedman analysis for UHPLC-MS data (for positive and negative ion mode) revealed metabolite markers overcoming resistance included acetylspermidine, phosphoenolpyruvic acid, cholesterol ester (CE(10:0)), L-acetylcarnitine and octadienoic acid. DFA identified octadecanoic acid to contribute to the separation of hypoxic drug treated samples. For hypoxia, glycine was discovered to be a common metabolite of drug response regardless of the dose. A major role of glycine in mammalian metabolism is to provide the central C_2N subunit of all nucleotide metabolism[208]. Purine ribonucleotides generate adenine and guanine used for DNA and RNA suggesting the drug is acting on purine metabolism in hypoxic cells. Hypoxic cells may use glycine for purine synthesis, and subsequently DNA repair mechanisms to overcome chemoresistance in the lower dose samples[9]. The extent of DNA damage may be too great for the high dosed samples to overcome through DNA repair. L-acetylcarnitine may be suggesting the regulation of fatty acid synthesis pathways to overcome hypoxia-induced chemoresistance. L-acetylcarnitine is produced from carnitine and acetyl-CoA in the mitochondria. L-acetylcarnitine is transported into the cytosol where it is converted

back to L-carnitine and acetyl-CoA[238]. L-carnitine is cycled back into the mitochondria with acyl groups for fatty acid synthesis[238]. Subsequently, acetyl-CoA may be directed towards fatty acid synthesis to synthesise CE(10:0), octadecanoic acid and octadienoic acid (an unsaturated fatty acid). The detection of a single unsaturated fatty acid metabolite marker is unlikely to be the result of lipid peroxidation as peroxidation would affect many lipids. Cell membranes of mammals have a higher composition of polyunsaturated fatty acids and highly unsaturated membranes have been shown to help maintain membrane fluidity[239]. This mechanism may allow larger quantities of the drug to be diffused into the cells. In the presence of toxic concentrations of drug, hypoxic cells may alter the membrane to enable a higher membrane fluidity to increase the uptake of components from the extracellular environment, such as essential amino acids, in an attempt to detoxify the effects of doxorubicin. Increasing membrane fluidity may also facilitate the diffusion of doxorubicin into the cell raising the concentration of doxorubicin thus increasing cytotoxicity. Phosphoenolpyruvic acid (PEP) is a product of glycolysis but also a product of a gluconeogenesis reaction[208]. Oxaloacetate is converted to PEP and carbon dioxide by the enzyme pyruvic acid carboxylase or phosphoenolpyruvate carboxykinase (PEPCK). It has been reported that the DNA cross-linking agent mitomycin C prevents the translation and transcription of PEPCK through cross-linking close to the promoter region of the DNA[240]. A reduction of PEP may be due to doxorubicin intercalating into the promoter region of *PEPCK* preventing expression of this anaplerotic enzyme. Additionally, mitomycin C has been reported to affect the protein expression of Pgp (a cell membrane protein) as the drug cross-links DNA in the *MDR1* promoter region[241]. Thus doxorubicin may intercalate DNA at in *MDR1* promoter region and inhibit translation, transcription and protein expression of Pgp leading to the reorganisation of the cell membrane and resulting fatty acid synthesis.

Results suggest two metabolic mechanisms are contributing towards overcoming hypoxia-induced chemoresistance (Figure 62). A drug target to overcome chemoresistance may be to feed cells unsaturated fatty acids in combination with a low dose of doxorubicin to increase cell membrane fluidity. Additionally, results implied that doxorubicin may intercalate into the DNA at the promoter region of *MDR*, which leads to the reduction of Pgp expression. This suggests Pgp is a drug target to overcome hypoxia-induced chemoresistance. Verapamil and cyclosporin A are inhibitors of the Pgp drug efflux pump[46]. The drugs have been shown to improve the toxic effects of cytotoxic chemotherapy compounds for cell lines expressing Pgp[46]. Unfortunately, the compounds

developed to date to inhibit Pgp also induce neurotoxic side effects[46]. This occurs as Pgp transporters in the blood-brain barrier are vital to protect the brain from compounds such as xenobiotics.

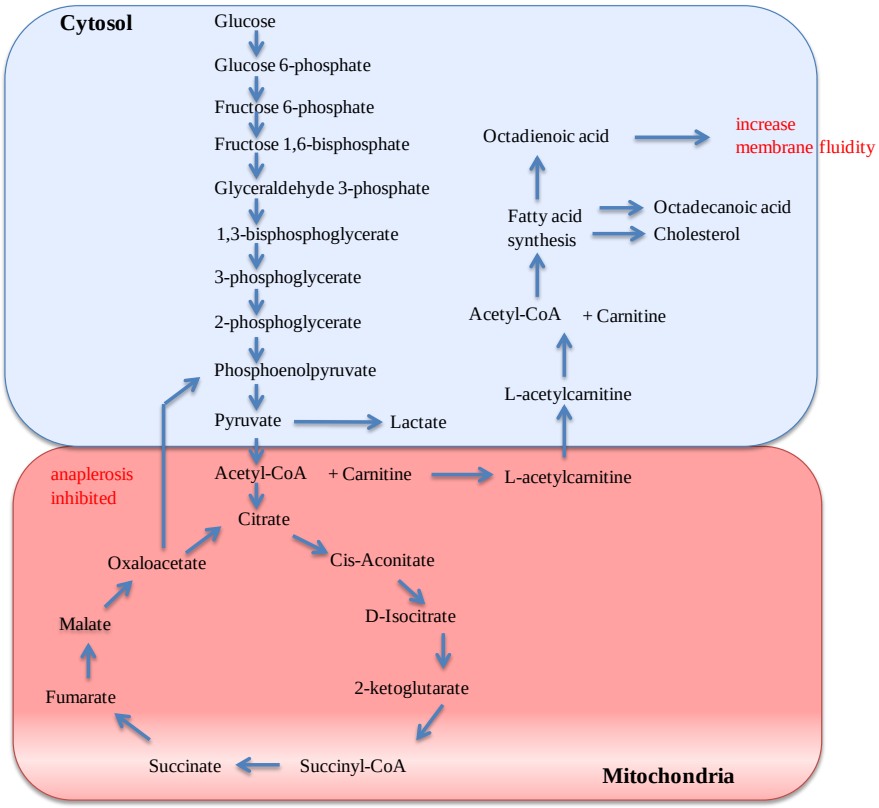

Figure 62: Summary of the metabolic response of MDA-MB-231 cells cultured in hypoxia and dosed with 1 µM doxorubicin. Mechanisms represent overcoming hypoxia-induced chemoresistance.

4.3.4 Metabolism and anoxia induced chemotherapy resistance

Anoxia-induced chemoresistance metabolite markers, identified using two-way ANOVA of GC-MS data, included threoinine, hypotaurine and benzoic acid. Metabolite markers relating to overcoming resistance included 2-hydroxyglutaric acid, hypotaurine and benzoic acid. In addition, DFA identified benzoic acid to contribute to the separation of hypoxic cells for both drug doses. Hypotaurine and benzoic acid represent the response of anoxic cells regardless of the drug dose therefore the metabolite marker of resistance is threonine and response is 2-hydroxyglutaric acid. Hypotaurine is located in the taurine and hypotaurine metabolic pathway and is produced from the enzyme cysteamine dioxygenase[201]. The metabolite has been suggested to have antioxidant properties as it scavenges for hydroxyl radicals and hypochlorous acid. This suggests hypotaurine is acting as an antioxidant agent against reactive oxidative species[242] that may contribute towards the resistant phenotype. The concentration of ROS in the higher drug dosed low oxygenated samples may be too high for hypotaurine to detoxify, thus the mechanism is

only effective to detoxify low drug doses. Benzoic acid has been shown to be a product of β-oxidation of odd-chain fatty acids[208]. Doxorubicin may be involved in inhibiting the oxidation of odd-chain fatty acids. A product of odd-chain fatty acid β-oxidation is succinyl-CoA, a TCA cycle intermediate, and cells may be using this mechanism to regenerate the TCA cycle for bioenergetics production and growth[208]. In the presence of doxorubicin, benzoic acid decreases with drug treatment suggesting a reduction of β-oxidation of odd-chain fatty acids. In drug resistant samples glutaminolysis may be helping the cells to overcome this doxorubicin induced mechanism. Although, at higher doses glutamine uptake decreases suggesting the cells can no longer replenish the TCA cycle and therefore drug induced reduction of fatty acid oxidation may be contributing to drug toxicity.

A metabolite marker unique to anoxia-induced drug resistance was reduced threonine. Threonine, an essential amino acid, may be metabolised to overcome toxicity. Threonine is can be converted to pyruvic acid or converted to glycine for purine biosynthesis by the enzyme threoinine dehydrogenase[208]. Mouse embryonic stem cells that highly express the threoinine dehydrogenase gene have been reported to deplete threoinine for DNA synthesis[243]. The anoxia-induced chemo resistant response may be to direct threoinine towards purine biosynthesis to repair the DNA damage caused by doxorubicin intercalation into DNA and inhibition of the topoisomerase II enzyme[19] (Figure 63).

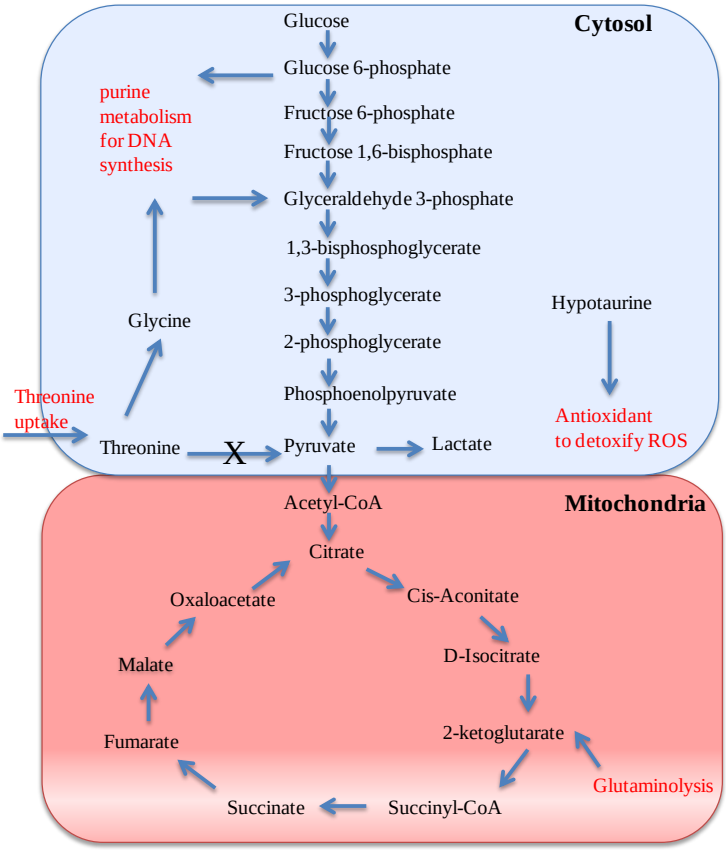

Figure 63: Summary of the metabolic response of MDA-MB-231 cells cultured in anoxia and dosed with 0.1 µM doxorubicin. Mechanisms represent anoxia-induced chemoresistance.

A metabolite marker unique to overcoming anoxia induced drug resistance was a reduced level of 2-hydroxyglutaric acid. Furthermore, glutamine uptake is significantly reduced in the anoxic samples treated with a higher dose of doxorubicin. It has previously been suggested that some hypoxic cells use glutamine for citrate production to support cytosolic macromolecular synthesis when glucose availability is limited[217]. Glutamine enters the TCA cycle and is enzymatically converted to glutamate and subsequently to 2-ketoglutaric acid. In hypoxia, it has been suggested that 2-ketoglutaric acid is catalysed by isocitrate-dehydrogenase to synthesise isocitrate and subsequently citrate, which has been proposed as a HIF-1 mediated mechanism[217]. This hypoxia related increase in citrate has been associated with a simultaneous increase in 2-hydroxyglutarate[217]. Reduction of 2-hydroxyglutarate and a significant reduction of glutamine uptake suggest anoxic cells treated with high doses of doxorubicin may be no longer be supporting cell growth through this mechanism, which contributes to drug toxicity.

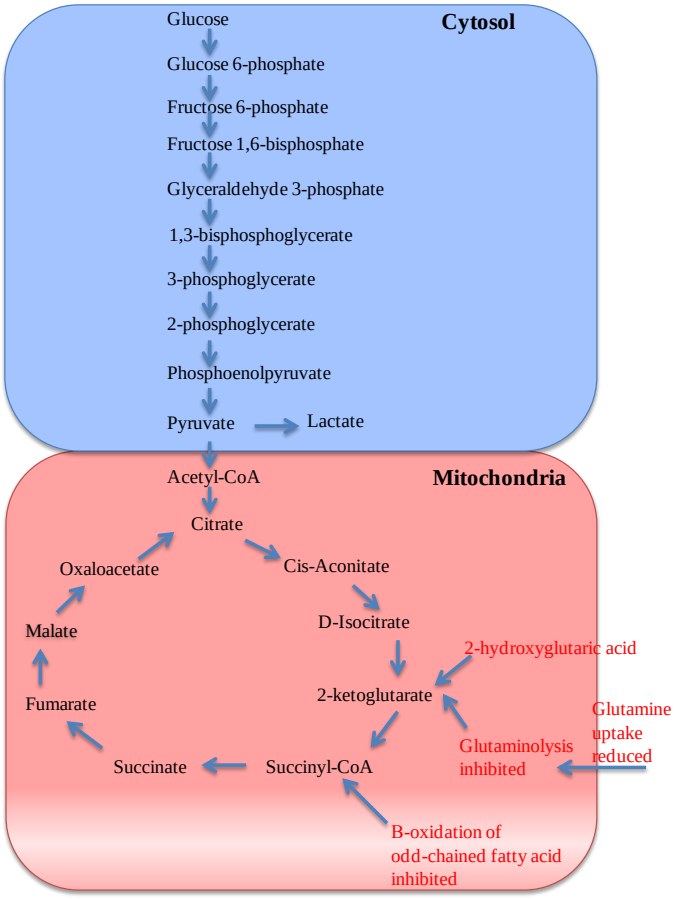

Figure 64: Summary of the metabolic response of MDA-MB-231 cells cultured in anoxia and dosed with 1 µM doxorubicin. Mechanisms represent overcoming anoxia-induced chemoresistance.

Results suggest overcoming anoxia-induced chemoresistance is mediated by inhibition of β-oxidation of odd-chain fatty acids in combination with reduced glutaminolysis (Figure 64). Glutamine uptake is significantly reduced in anoxic cells treated with a toxic concentration of doxorubicin, which further confirms the metabolite marker as a potential drug target for resistance. Additionally, DNA synthesis pathways may play a role in drug resistance. Targeting purine synthesis would prevent cells from being able to repair the DNA damage caused by low doses of doxorubicin (Figure 63).

4.4 Conclusions

Metabolic fingerprinting analysis was able to characterise a snapshot of cells exposed to various environmental perturbations. 270 intracellular samples were analysed by GC-MS and 60 intracellular samples by UHPLC-MS. MVA determined the metabolic patterns that characterise a particular sample type and statistical analysis identified several metabolite markers. Both methods were applied to detect a range of metabolites over various metabolic classes such as lipids to amino acids to encompass as much of the metabolism as possible. Metabolism was studied to gain an insight into the metabolic pathway response to

hypoxia-induced chemotherapy resistance. Additionally, the method offered potential mechanisms of metabolism differentially regulated to overcome hypoxia-induced chemoresistance. Results suggested that cancer cells exposed to a low oxygen tensions promoted survival through exploiting metabolic pathways including anaerobic respiration, truncation of the TCA cycle, glutaminolysis and autophagy (Figure 59). Doxorubicin treatment in normal oxygen levels identified metabolic responses of drug action including promoting toxicity through lipid peroxidation, targeting N-acetylaspartic acid and decreasing doxorubicin efflux through reducing the uptake of glutamate. Low oxygen chemoresistance was promoted through DNA synthesis and overcoming chemoresistance was mediated by fatty acid pathways targets.

An outcome of this metabolomics study was to determine metabolic pathways that may be suitable targets to overcome hypoxia-induced chemoresistance. Future work may be to validate the metabolite markers as drug targets through generating knockout models. Although metabolic metabolite markers were identified a network-based approach may be more useful to understand fully the relationship between metabolites with respect to the metabolic interactions. Subsequently, a systems biology approach of network-based correlation analysis was undertaken in Chapter 5 for a greater understanding of the mechanistic relationship of metabolism that may lead to improving the toxicity of chemotherapy treatments in hypoxic tumours.

Chapter 5

APPLICATION OF NETWORK-BASED CORRELATION ANALYSIS TO THE STUDY OF HYPOXIA-INDUCED CHEMORESISTANCE

5.1 Introduction

Systems biology is the study of the complex interactions within a biological system to determine the emergent properties arising from the interaction of the genes, proteins and metabolites. This can be considered as a holistic approach and presents an understanding into how interactions give rise to a systems function and behaviour. Cancer is a complex disease that arises due to a series of mutations, not a single gene effect, and it is the combination of these gene mutations that give rise to cancer as an emergent property of the cellular system that it interacts with. Hanahan and Weinburg proposed six biological hallmarks of cancer that arise as a result of genome instability highlighting the complexity of the disease[244]. The proposed hallmarks of cancer includes sustaining proliferative signalling, avoiding growth suppressors, opposing cell death, replicating indefinitely, angiogenesis and the ability to metastasise into previously non-cancerous regions. An additional two hallmarks of cancer have recently been recognised, which includes evading immune destruction and, importantly, reprogramming of energy metabolism[245]. Applying systems biology to cancer research offers a new perspective and has the potential to unveil the emergent properties of cancer metabolism.

Chemotherapy resistance in hypoxic cancer cells was studied using metabolic profiling to investigate resistance at the metabolome level. Camacho *et al.* have proposed mechanisms that cause high correlations between two metabolites[93]. A high correlation between two metabolites may be assumed to arise as a result of the metabolites being neighbours in the biochemical network; however this has been shown not to be the case[95]. Steuer *et al.* demonstrated that neighbouring metabolites in a network are not correlated whilst others that are spatially unconnected have a strong correlation with one another and suggest this to be the result of the amalgamation between stoichiometry and kinetic influences[95]. A correlation 'origin' is therefore a global system property of the metabolic network where the possibility of two metabolites being highly correlated is the result of the combination of all reactions in the system.

The aim was to identify strongly correlated metabolites within MDA-MB-231 breast cancer cells exposed to a low oxygen environment and during treatment with doxorubicin. Correlation differences were interpreted from isolating the interconnecting metabolites in the human metabolic network to construct a metabolic network of chemoresistance. Subsequently, novel chemotherapeutic strategies were interpreted from the constructed networks.

5.2 Results

Metabolomics data were acquired using GC-MS as outlined in Chapter 4. This dataset comprised of 3 oxygen sample types and 3 doxorubicin treatments giving a total of 9 sample types. For each sample type 30 biological replicates were acquired.

The EHMN[84] was developed by the Goryanin group and contains 2715 metabolites and 2824 reactions, which were constructed from human gene annotations obtained from a variety of databases in addition to a literature based search. Another high quality human metabolic network is the Recon 1 developed by the Palsson group and contains 2766 metabolites and 3742 reactions[85]. This model was curated using gene annotations in addition to an in-depth literature search. The main difference between the two models is compartmentalisation of metabolic pathways to specific organelle regions. The EHMN is an uncompartmentalised model and therefore transport reactions and subcellular localisation of metabolites are not considered; consequently, the EHMN has fewer reactions than the Recon 1 as transport and exchange reactions have not been included. More recently a compartmentalised version of the EHMN has become available[86] however an uncompartmentalised model is more suitable for metabolomics data. This is because metabolomics data of cell lysates cannot identify the organelle the metabolite was extracted from.

5.2.1 Correlation and network analysis of the metabolic response of MDA-MB-231 breast cancer cells to low oxygen tensions

Correlations between metabolites in cells exposed to normoxia were compared to those in cells exposed to hypoxia to determine the metabolic reprogramming that occurs during hypoxia and to explore the hypoxic metabolic response in cancer cells. A total of 30 biological replicates were analysed for each sample type and therefore, due to this high number of biological replicates, it is assumed that the variation in semi-quantitative

concentrations of metabolites is due to biological variation. Furthermore, it is assumed that the metabolite differences are caused by the interconnectivity of metabolism and not an independent observation[246]. Cellular metabolism is a complex dynamic system, and fluctuations evolving due to environmental factors such as lowering oxygen availability and drug treatment give rise to the emergent formation of correlations[95]. A total of eight correlations differed between normoxic and hypoxic samples as shown in Table 17.

Table 17: Pearson's pair-wise correlation of metabolites that were significantly different for MDA-MB-231 cells cultured in normoxia compared to hypoxia. Data were acquired using gas chromatography mass spectrometry (GC-MS) and 30 biological replicates were analysed for each sample treatment.

Metabolite A	Metabolite B	Correlation coefficient in normoxic samples	Correlation coefficient in hypoxic samples	Correlation coefficient difference
Glucose	Malic acid	0.70	-0.42	1.13
Galactose / Glucose	Malic acid	0.71	-0.26	0.98
Malic acid	Pyruvic acid	-0.14	0.72	0.87
Octadecanoic acid	Glutamic acid	-0.07	0.72	0.79
Glucose	Galactose / Glucose	0.92	0.29	0.62
Hexadecanoic acid	Glycerol 3-phosphate	0.11	0.73	0.61
Pyruvic acid	Lactic acid	0.86	0.33	0.54

Figure 65 shows a visual example of the metabolite scatter plot for the difference between metabolites glycerol 3-phosphate and hexadecanoic acid for normoxia (red) and hypoxia samples (blue). Here, the metabolites were positively correlated in hypoxia (correlation value of 0.73) but not in normoxia (correlation value of 0.11).

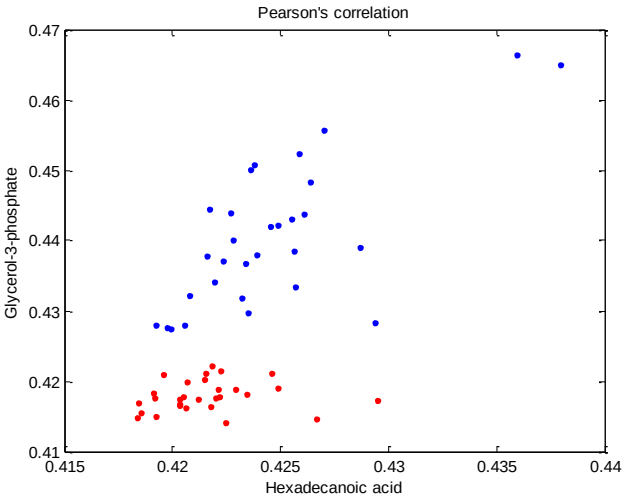

Figure 65: Pearson's pair-wise correlation of metabolites glycerol 3-phosphate and hexadecanoic acid where normoxia samples are shown in red and hypoxic samples are shown in blue.

Figure 66 shows the construction of the correlations as a network. This figure shows some metabolites appear to have more than one correlation. For example, malic acid is shown to be correlated with three other metabolites two of which, glucose and pyruvic acid, can be specifically localised to energy metabolism. Multiple metabolites assignments shown in the network are due to the high-throughput nature of metabolic profiling analysis, which can result in some metabolites not being detected accurately often due to metabolites having a similar chemical structure (as discussed in Chapter 4). Metabolites were mapped directly onto the EHMN metabolic network and shortest pathway connecting the pair-wise correlation was recovered. Some metabolites identified, such as glucose, were found to have more than one isoform in the EHMN. In this case, all isoform pathways were calculated and used to construct a metabolic network of low oxygen metabolism. For example, glucose, correlated with malic acid, has two isoforms in the EHMN which are α-D-glucose and β-D-glucose. Thus both metabolite pathways were extracted.

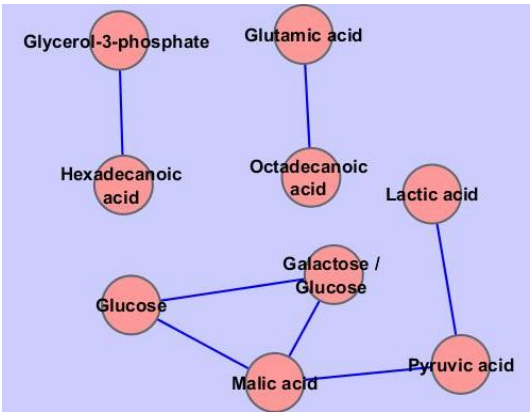

Figure 66: Correlation network of the metabolites that significantly differed in MDA-MB-231 cells cultured in normoxia compared to hypoxia.

Subsequently, the correlations between normoxic and anoxic samples were calculated. A total of 11 correlations were identified that differed between normoxic and anoxic samples as shown in Table 18.

Table 18: Pearson's pair-wise correlation of metabolites that were significantly different for MDA-MB-231 cells cultured in normoxia compared to anoxia. Data were acquired using gas chromatography mass spectrometry (GC-MS) and 30 biological replicates were analysed for each sample treatment.

Metabolite A	Metabolite B	Correlation coefficient		
		Normoxic	Anoxic	Difference
Xylitol	Lactic acid	0.73	-0.05	0.79
Benzoic acid	Isoleucine	0.71	-0.03	0.78
Threitol/erythritol	Lactic acid	0.85	0.16	0.76
Glycerol	Lactic acid	0.86	0.20	0.71
Isoleucine	Lactic acid	0.74	0.19	0.60
Citric acid	Lactic acid	0.77	0.22	0.59
Sorbitol/ Galactose / Glucose	Lactic acid	0.77	0.23	0.58
Sorbose/ Fructose	Lactic acid	0.76	0.24	0.57
Scyllo-inositol / myo-inositol/ Inositol	Xylitol	0.74	0.22	0.53
Glucose	Malic acid	0.70	0.19	0.51
Galactose / Glucose	Malic acid	0.71	0.22	0.48

A network of these correlations is shown in Figure 67. For anoxia, lactic acid appears to be the most highly correlated metabolite. Comparing hypoxic and anoxic results revealed three similar correlations, which were galactose / glucose with malic acid, benzoic acid with iosleucine and glucose with malic acid.

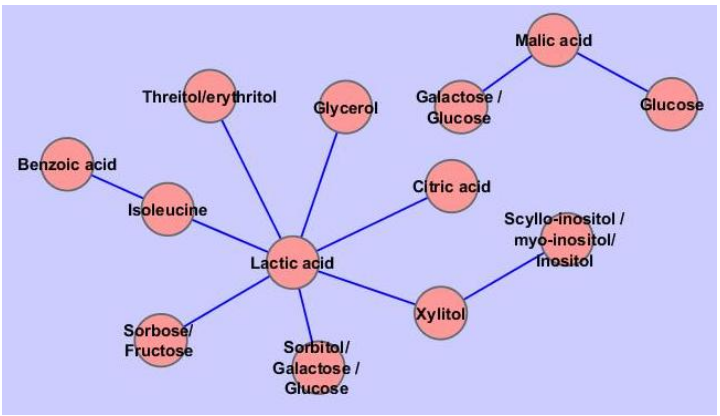

Figure 67: Correlation network of the metabolites that significantly differed in MDA-MB-231 cells cultured in normoxia compared to anoxia.

Correlated metabolites relating to the anoxic metabolic response were mapped directly onto the EHMN metabolic network and the shortest pathway connecting two correlated metabolites was identified. Pathways for both oxygen tensions were combined to generate a single model of low oxygen metabolic response (Figure 68). This model can be used to determine which metabolic pathways are differentially regulated in low oxygen. Shared

components between both oxygen tensions in the network are displayed as green nodes. Three pathways are common between the two oxygen tensions. Additionally, hypoxic only pathways are shown as blue nodes and anoxic only are yellow nodes. A sub-network connecting hexadecanoic acid and glycerol 3-phosphate is exclusive to hypoxic metabolism. This sub-network may be the result of biological regulation from the main network in the form of a feedback loop or oscillation[247].

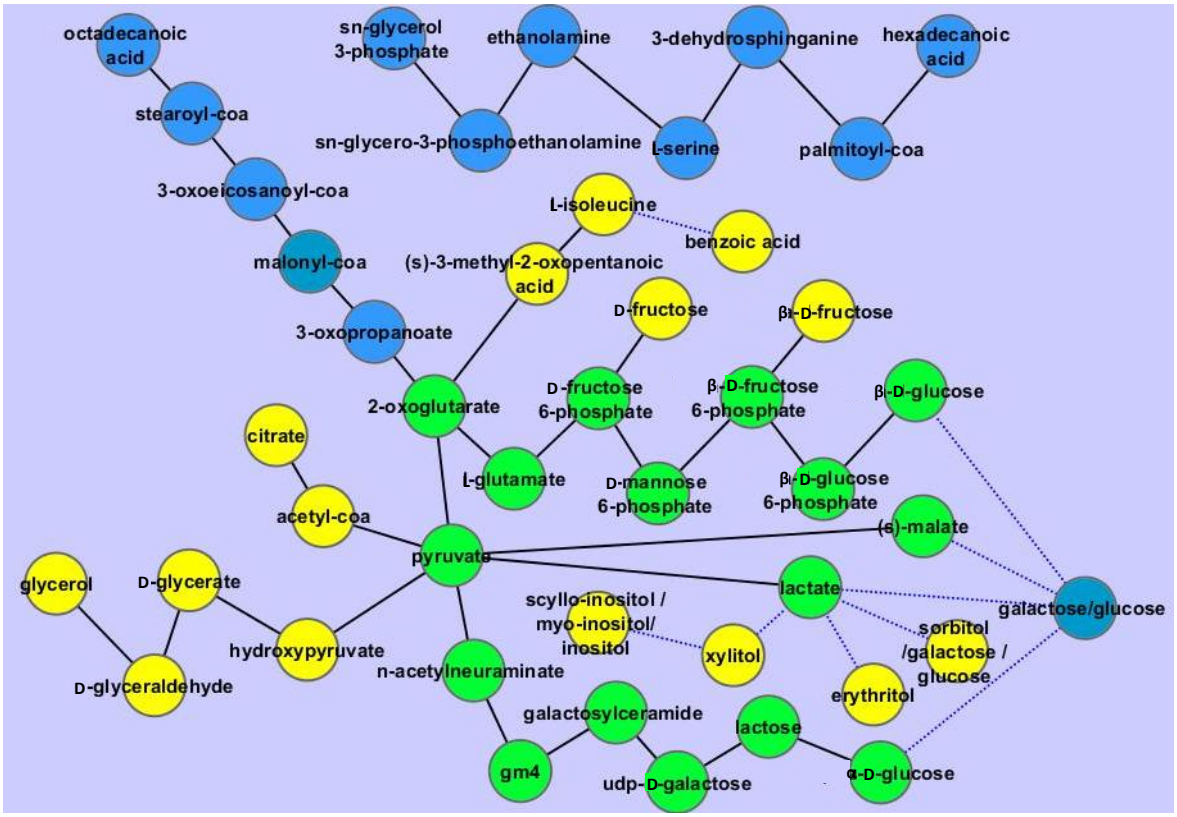

Figure 68: Network of the shortest path connecting pair-wise correlations of metabolites that significantly differed for MDA-MB-231 cells cultured in normoxia compared to hypoxia or anoxia. Shortest pathways connecting two metabolites were determined using Edinburgh human metabolic network (EHMN). The blue nodes represent metabolites present in hypoxia pathways, yellow represents metabolites present in anoxia pathways and green are the metabolites present in both hypoxia and anoxia pathways. Solid black lines connect metabolites through from EHMN pathways and the dotted blue lines connect correlated metabolites (as metabolites were not connected in the EHMN).

5.2.2 Correlation and networks analysis of the metabolic response to chemotherapy treatment in cells under a normal oxygen tension

To explore the underlying metabolic response to hypoxia-induced chemoresistance a dose of 0.1 µM doxorubicin, shown in Chapter 3 to inhibit growth of normoxic MDA-MB-231 cells by ~50 % but to have no effects in low oxygenated cells, was used to treat cells pre-exposed to normoxia, hypoxia or anoxia. Furthermore, to explore the mechanisms to overcome hypoxia-induced chemoresistance a higher dose of ~1 µM, shown in Chapter 3 to inhibit growth of low oxygenated MDA-MB-231 cells by~50 % was used to treat cells

pre-exposed to normoxia, hypoxia or anoxia. Correlation analysis between normoxia and normoxia samples treated with 0.1 µM doxorubicin yielded a single metabolic correlation (Table 19), when adhering to the criteria that the correlation must be greater than 0.7 and the difference between the correlations must be 0.407(these parameters were selected based on the sample size as described in section 2.12). This may be due to the action of the drug on the cancer cells under normoxic levels not having a significantly large influence on these metabolites detected by GC-MS. This may be overcome through employing other analytical platforms such as UHPLC-MS, which is able to detect a greater number of metabolites including a larger range of lipids which were reported in Chapter 4 to have a large metabolic response to drug action.

Table 19: Pearson's pair-wise correlation of metabolites that were significantly different for MDA-MB-231 cells cultured in normoxia and subsequently untreated or treated with 0.1 µM doxorubicin. Data were acquired using gas chromatography mass spectrometry (GC-MS) and 30 biological replicates were analysed for each sample treatment.

Metabolite A	**Metabolite B**	**Correlation coefficient**		
		Normoxia	Normoxia treated with 0.1 µM doxorubicin	Difference
Fructose	Glutamic acid	-0.27	0.73	0.46

Correlation analysis was conducted to compare normoxia and normoxia samples treated with 1 µM doxorubicin and yielded 10 correlations (Table 20). This dose of doxorubicin was shown to be highly toxic to the cells in normoxic conditions and therefore these correlations represent high toxicity in the cells. These mechanisms do not reflect the clinical response to doxorubicin; however, they do provide information regarding the potential mechanisms of drug action.

Table 20: Pearson's pair-wise correlation of metabolites that were significantly different for MDA-MB-231 cells cultured in normoxia and subsequently untreated or treated with 1 µM doxorubicin. Data were acquired using gas chromatography mass spectrometry (GC-MS) and 30 biological replicates were analysed for each sample treatment.

Metabolite A	Metabolite B	Correlation coefficient		
		Normoxia	Normoxia treated with 1 µM doxorubicin	Difference
Malic acid	Lactic acid	-0.20	0.84	1.04
Malic acid	Pyruvic acid	-0.14	0.82	0.96
Benzoic acid	Isoleucine	0.73	-0.16	0.90
Malic acid	Threitol/erythritol	0.14	0.88	0.74
Xylitol	Malic acid	0.21	0.90	0.69
Hypotaurine	Glycerol	0.23	0.77	0.54
Glutamic acid	Malic acid	0.40	0.89	0.49
Sorbose/ Fructose	Malic acid	0.23	0.70	0.47
Scyllo-inositol / myo-inositol/ Inositol	Malic acid	0.40	0.82	0.42
Galactose / Glucose	Malic acid	0.72	0.30	0.42

A network of the correlations is shown in Figure 69, which reveals malic acid (located in the TCA cycle) as a hub metabolite.

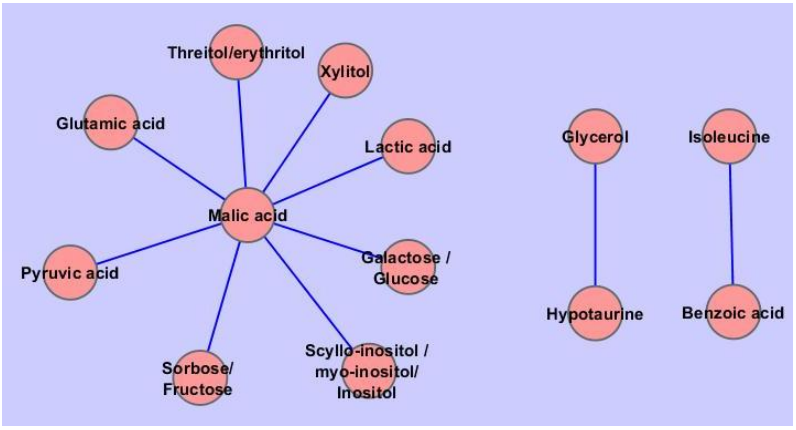

Figure 69: Correlation network of the metabolites that significantly differed in MDA-MB-231 cells cultured in normoxia and subsequently untreated or treated with 1 µM doxorubicin.

Pathways of drug action in normoxic samples were combined to generate a single model of drug metabolic response as shown in Figure 70. This is a network of all the potential mechanisms of drug action with respect to metabolism for cells exposed to a normal oxygen tension. A sub-network connecting glycerol and hypotaurine may be the result of biological regulation from the main network.

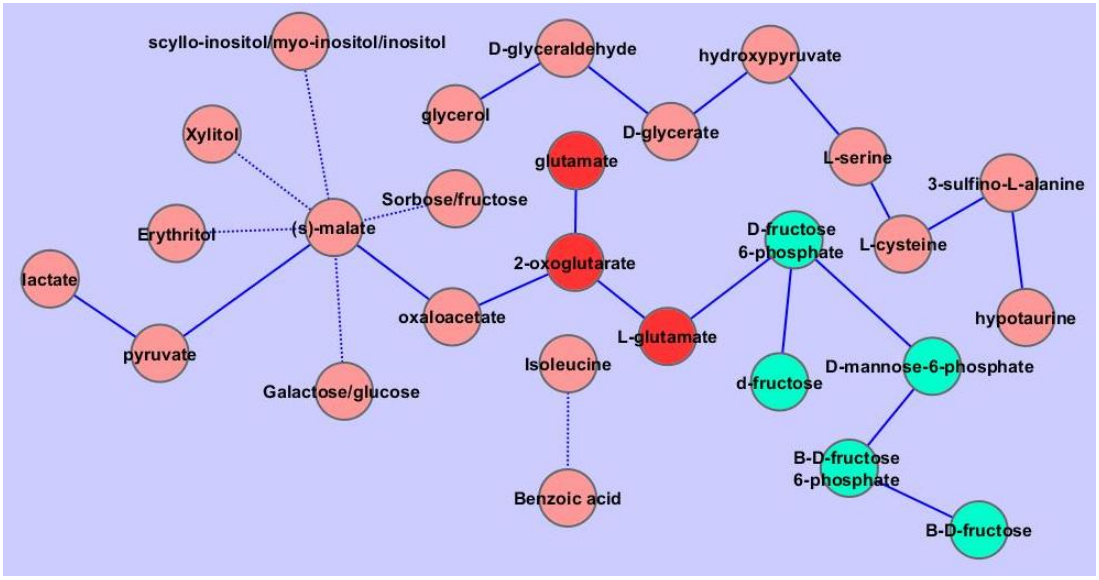

Figure 70: Network of the shortest path connecting pair-wise correlations of metabolites that significantly differed for MDA-MB-231 cells cultured in normoxia compared to normoxia dosed with 0.1 µM or 1 µM doxorubicin. Shortest pathways connecting two metabolites were determined using Edinburgh human metabolic network (EHMN). The turquoise nodes represent pathways of metabolites present in the lower drug dose, orange represents pathways of metabolites present in higher drug dose and red are the pathways of metabolites present in both doses of doxorubicin. Solid blue lines connect metabolites through from EHMN pathways and the dotted blue lines connect correlated metabolites (as metabolites were not connected in the EHMN).

5.2.3 Correlation and network analysis of the metabolic response of chemotherapy resistance in low oxygen tensions.

Three correlations of hypoxia-induced chemoresistance between hypoxia and hypoxia samples treated with 0.1 µM doxorubicin were identified (Table 21). All of the correlations were uncorrelated in hypoxic samples and became positively correlated in response to drug treatment. A network of these correlations is shown in Figure 71.

Table 21: Pearson's pair-wise correlation of metabolites that were significantly different for MDA-MB-231 cells cultured in hypoxia and subsequently untreated or treated with 0.1 µM doxorubicin. Data were acquired using gas chromatography mass spectrometry (GC-MS) and 30 biological replicates were analysed for each sample treatment.

Metabolite A	Metabolite B	Correlation coefficient		
		Hypoxia	Hypoxia treated with 0.1 µM doxorubicin	Difference
Benzoic acid	Lactic acid	0.27	0.74	0.47
Sorbose/ Fructose	Benzoic acid	0.25	0.71	0.46
Glutamic acid	Lactic acid	0.40	0.84	0.44

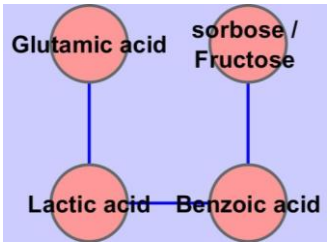

Figure 71: Correlation network of the metabolites that significantly differed in MDA-MB-231 cells cultured in hypoxia and subsequently untreated or treated with 0.1 µM doxorubicin.

Correlations of anoxia induced chemoresistance were determined between anoxia and anoxia samples treated with 0.1 µM doxorubicin, which generated 10 correlations (Table 22). The network of these correlations is shown in Figure 72 where octadecanoic acid appears to be a highly connected hub.

Table 22: Pearson's pair-wise correlation of metabolites that were significantly different for MDA-MB-231 cells cultured in anoxia and subsequently untreated or treated with 0.1 µM doxorubicin. Data were acquired using gas chromatography mass spectrometry (GC-MS) and 30 biological replicates were analysed for each sample treatment.

Metabolite A	**Metabolite B**	**Correlation coefficient**		
		Anoxia	Anoxia treated with 0.1 µM doxorubicin	Difference
Octadecanoic acid	Glutamic acid	-0.03	0.77	0.80
Octadecanoic acid	Isoleucine	0.01	0.80	0.79
Octadecanoic acid	Threonine	-0.01	0.74	0.75
Octadecanoic acid	Threitol/erythritol	0.16	0.81	0.65
Glutamic acid	4-hydroxyproline	0.16	0.78	0.62
Octadecanoic acid	Sorbitol/ Galactose / Glucose	0.14	0.75	0.61
Octadecanoic acid	Glycerol	0.18	0.75	0.58
Octadecanoic acid	Sorbose/ Fructose	0.21	0.76	0.55
4-hydroxyproline	Isoleucine	0.28	0.76	0.48
Octadecanoic acid	Aspartic acid	0.25	0.73	0.48

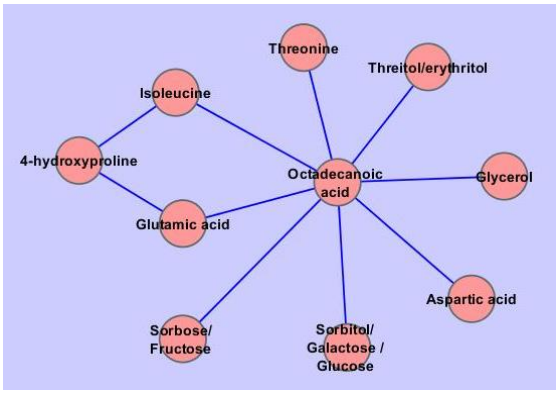

Figure 72: Correlation network of the metabolites that significantly differed in MDA-MB-231 cells cultured in anoxia and subsequently untreated or treated with 0.1 µM doxorubicin.

Pair-wise correlations representing low oxygen induced chemoresistance were mapped directly onto the EHMN metabolic network to obtain the shortest pathways connecting two correlated metabolites. These pathways were combined to generate a single model of chemoresistance as shown in Figure 73. This model can be used to determine which metabolic mechanisms are responsible for chemotherapy resistance. Shared components between both oxygen tensions in the network are displayed as blue nodes. Three nodes common between the two oxygen tensions were L-glutamate, octadecanoic acid and sorbose/fructose. Additionally, hypoxic only pathways are shown as green nodes and anoxic only are red nodes.

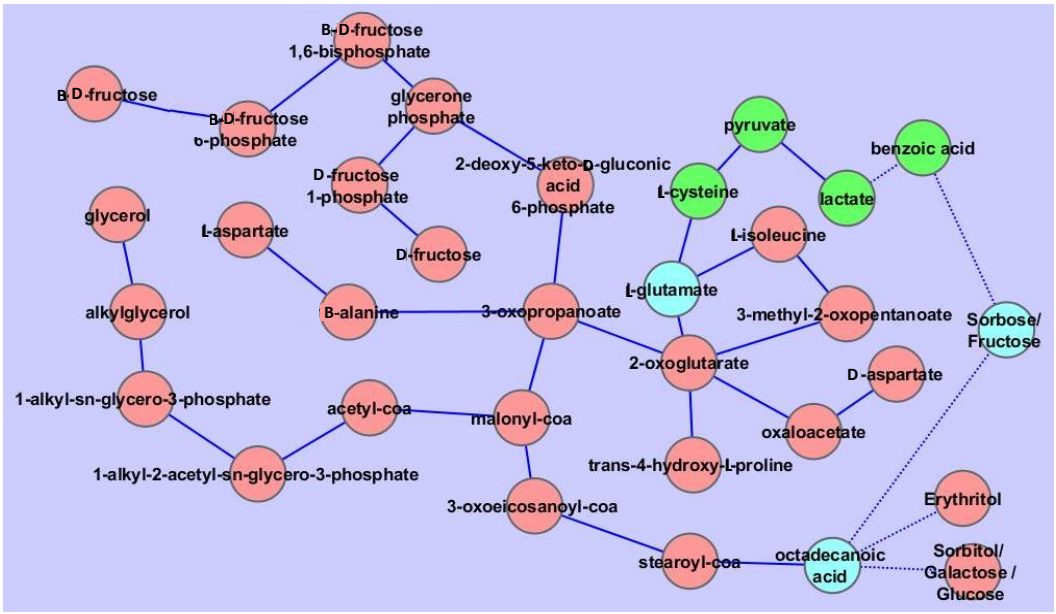

Figure 73: Network of the shortest path connecting pair-wise correlations of metabolites that significantly differed for MDA-MB-231 cells cultured in hypoxia compared to hypoxia treated with 0.1 µM and comparing cells cultured in anoxia to anoxia treated with 0.1 µM. Shortest pathways connecting two metabolites were determined using Edinburgh human metabolic network (EHMN). The green nodes represent pathways of metabolites present in the hypoxia drug treated cells, pink represents pathways of metabolites present in anoxia drug treated cells and blue are the pathways of metabolites present in both oxygen conditions dosed with drug. Solid blue lines connect metabolites through from EHMN pathways and the dotted blue lines connect correlated metabolites (as metabolites were not connected in the EHMN).

5.2.4 Correlation and network analysis of the metabolic response to overcome chemotherapy resistance in low oxygen tensions.

To explore the mechanisms to overcome hypoxia-induced chemoresistance a higher dose of ~1 µM, shown in Chapter 3 to inhibit growth of low oxygenated MDA-MB-231 cells by ~50 % was used to treat cells pre-exposed to hypoxia or anoxia. This is a high dose of doxorubicin, which has been shown (in Chapter 3) to be toxic to low oxygenated cells. Correlations of hypoxia and hypoxia samples treated with 1 µM doxorubicin produced 13 correlations shown in Table 23. Whilst this dose is not clinically viable, the potential mechanisms to overcome hypoxia-induced chemoresistance can be elucidated.

Table 23: Pearson's pair-wise correlation of metabolites that were significantly different for MDA-MB-231 cells cultured in hypoxia and subsequently untreated or treated with 1 µM doxorubicin. Data were acquired using gas chromatography mass spectrometry (GC-MS) and 30 biological replicates were analysed for each sample treatment.

Metabolite A	**Metabolite B**	**Correlation coefficient**		
		Hypoxia	Hypoxia treated with 1 µM doxorubicin	Difference
Pyruvic acid	Lactic acid	0.31	0.92	0.61
Sorbose/ Fructose	Benzoic acid	0.25	0.86	0.61
Citric acid	Benzoic acid	0.21	0.78	0.57
Benzoic acid	Threonine	0.22	0.79	0.57
Benzoic acid	Lactic acid	0.27	0.83	0.56
Glutamic acid	Lactic acid	0.40	0.93	0.53
Hexadecanoic acid	Pantothenic acid	0.18	0.70	0.52
Threitol/erythritol	Benzoic acid	0.30	0.82	0.52
Scyllo-inositol / myo-inositol/ Inositol	Benzoic acid	0.31	0.80	0.49
Pantothenic acid	Threonine	0.24	0.72	0.47
Sorbitol/ Galactose / Glucose	Benzoic acid	0.37	0.84	0.47
Benzoic acid	Glycerol	0.32	0.78	0.46
Benzoic acid	Isoleucine	0.38	0.83	0.45

The network of these correlations is shown in Figure 74. Benzoic acid to be a highly connected node suggesting it is a hub metabolite.

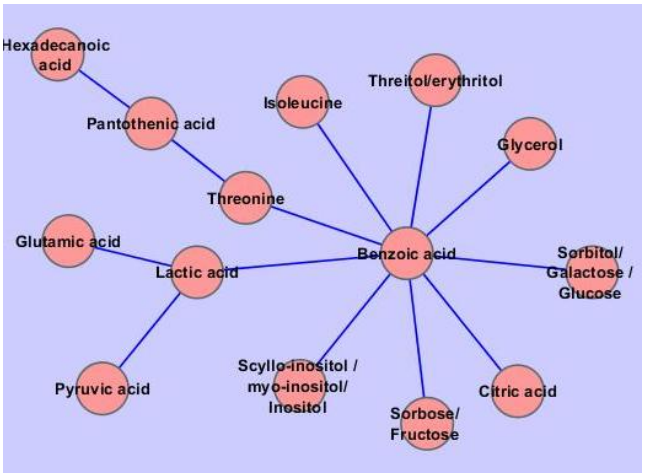

Figure 74: Correlation network of the metabolites that significantly differed in MDA-MB-231 cells cultured in hypoxia and subsequently untreated or treated with 1 µM doxorubicin.

Correlations between anoxia and anoxia samples treated with 1 µM doxorubicin produced six correlations shown in Table 24.

Table 24: Pearson's pair-wise correlation of metabolites that were significantly different for MDA-MB-231 cells cultured in anoxia and subsequently untreated or treated with 1 µM doxorubicin. Data were acquired using gas chromatography mass spectrometry (GC-MS) and 30 biological replicates were analysed for each sample treatment.

Metabolite A	**Metabolite B**	**Correlation coefficient**		
		Anoxia	Anoxia treated with 1 µM doxorubicin	Difference
Tyramin/Tyrosine	Lactic acid	0.01	0.76	0.75
Threitol/erythritol	Lactic acid	0.08	0.83	0.75
Glycerol	Lactic acid	0.13	0.85	0.72
Aspartic acid	Lactic acid	0.07	0.76	0.70
Sorbose/ Fructose	Lactic acid	0.17	0.79	0.62
Isoleucine	Lactic acid	0.17	0.77	0.60

The network of these correlations is shown in Figure 75, which shows lactic acid to be a highly connected node suggesting it is a hub metabolite. Lactic acid was also a hub metabolite in the correlation network comparing normoxic and anoxic metabolism.

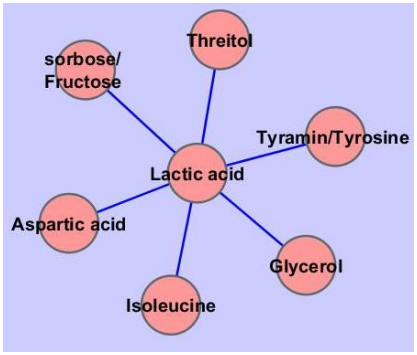

Figure 75: Correlation network of the metabolites that significantly differed in MDA-MB-231 cells cultured in anoxia and subsequently untreated or treated with 1 µM doxorubicin.

Pair-wise metabolite correlations that represented the metabolic response to overcoming low oxygen induced chemoresistance were isolated in EHMN metabolic network and the shortest pathway connecting two correlated metabolites was calculated. These pathways were combined to generate a single model as shown in Figure 76. Shared components between both oxygen tensions are displayed as blue nodes in the network. A single pathway common between the oxygen tensions is shown in blue that connects lactate, pyruvate, 2-oxoglutarare and glutamate. Additionally, hypoxic only pathways are shown as green nodes and anoxic only are red nodes. Furthermore, the network has a sub-network that connects hexadecanoic acid to pantothenate.

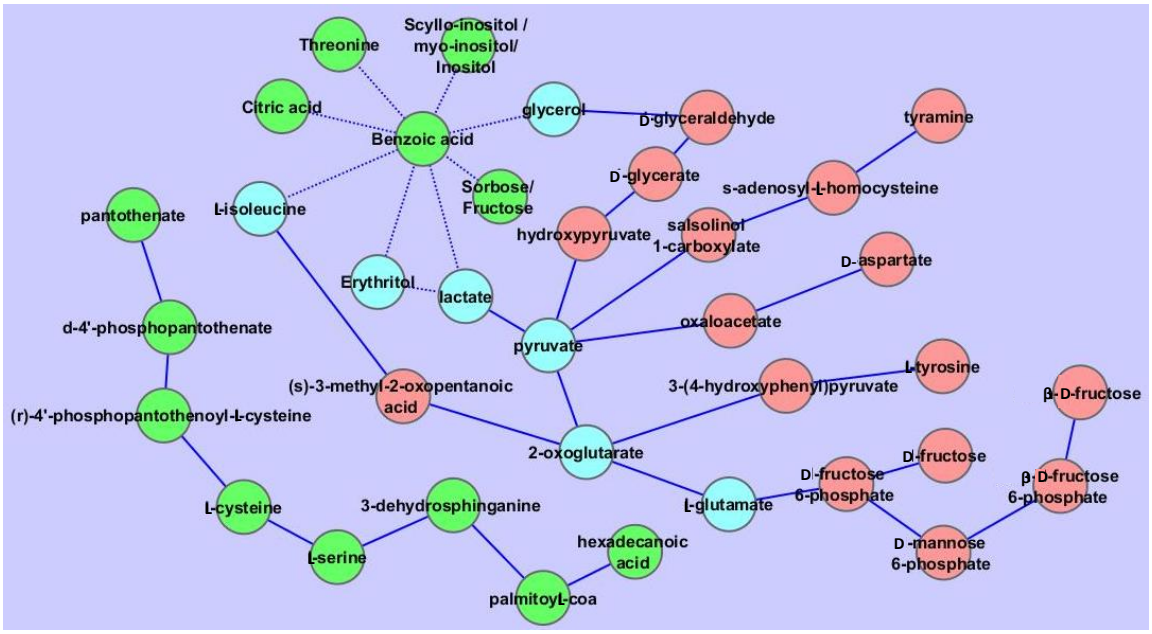

Figure 76: Network of the shortest path connecting pair-wise correlations of metabolites that significantly differed for MDA-MB-231 cells cultured in hypoxia compared to hypoxia treated with 1 µM and comparing cells cultured in anoxia to anoxia treated with 1 µM. Shortest pathways connecting two metabolites were determined using Edinburgh human metabolic network (EHMN). The green nodes represent pathways of metabolites present in the hypoxia drug treated cells, pink represents pathways of metabolites present in anoxia drug treated cells and blue are the pathways of metabolites present in both oxygen conditions dosed with drug. Solid blue lines connect metabolites through from EHMN pathways and the dotted blue lines connect correlated metabolites (as metabolites were not connected in the EHMN).

5.3 Discussion

Analysis of metabolic profiling data in Chapter 4 was able to identify metabolite markers of hypoxia-induced chemoresistance and metabolite markers indicative of the metabolic response to overcome resistance. Whilst the analysis was able to suggest many metabolites associated with resistance, incorporating knowledge of the underlying metabolic system required an alternative approach. Using a systems biology approach, the metabolic network of chemotherapy resistance was identified using network-based correlation analysis. Construction of metabolic networks, through compiling all relevant pathway responses, enables a greater insight into the network mechanisms. Thus, the topology and dynamics (fluctuations) of the metabolic responses can be explored. Furthermore, these networks can be compared to understand the pathway responses that overcome chemoresistance.

Network approaches to biological systems can be useful for the visual representation of complex patterns provided they do not contain too many connections. Proteomics have explored the use of network-based approaches to biological systems. Protein-protein interaction maps have been generated from high-throughput proteomics experiments. For example, a protein interaction network for adenocarcinoma of the breast was constructed and used to predict patient breast cancer outcomes[77]. Valcárcel *et al.* explored the application of correlation analysis to develop networks of the metabolic differences between individuals with normal fasting glucose and prediabetes[97]. Individual networks of partial correlations were constructed and cross compared to reveal differences in lipoprotein metabolism relating to diabetic dyslipidemias[97]. Genome scale human metabolic networks such as the EHMN[84] can be used with metabolomics data to generate an interaction-based metabolic network. The aim in this study was to construct metabolic networks that connect the pair-wise correlations to explore the metabolic response in the context of the entire metabolic network. Pair-wise correlation analysis identified many metabolite connections that differed with respect to sample treatment and from this a metabolic network describing the cellular response to metabolic perturbations in biological systems was constructed. Four metabolic networks were created to describe the cellular response of MDA-MB-231 cancer cells cultured in low oxygen levels, treated with a cytotoxic dose of doxorubicin in high oxygen levels, treated with a non-cytotoxic dose of doxorubicin in low oxygen levels and treated with a cytotoxic dose of doxorubicin in low oxygen levels. These networks offer an insight into how cells respond, metabolically, to environmental perturbations and further reveal metabolic pathways as potential targets to help overcome hypoxia-induced chemotherapy resistance. Observing the relationship

between the resistance and overcoming resistance by treating with a higher drug dose was able to identify novel targets that could improve toxicity in resistant cells.

There were some aspects arising from the metabolomics data and the human metabolic network that limit network-based correlation analysis. For example, some metabolites were not definitively identified as a single species in the GC-MS data. Reasons behind this were discussed in Chapter 4. Thus, these multiple identifications cannot be mapped onto the metabolic network. Furthermore, the genome-scale network reconstructions contain many metabolic reactions; however these models, whilst being the most comprehensive available, are incomplete due to limitations in current knowledge regarding the complexity of the human genome. Future releases of human metabolic models may address this limitation through applying better reconstruction algorithms and a more extensive search of the literature. For example, benzoic acid is an important hub in the correlation network, however there are two reactions associated with this metabolite in the EHMN connecting benzoic acid to benzamide and benzoyl phosphate, neither of which are involved in successive reactions thus connectivity within the network was not possible. Whilst this was a limiting factor, the network was able to map the connectivity of many other metabolites generating comprehensive networks.

Creating networks of the shortest pathway that connect two pair-wise correlated metabolites produced connections between metabolites that may not have previously been considered. These pathways represent the minimum number of reactions needed to convert one metabolite into the other. This method uncovered novel pathway responses to an environmental perturbation as a combination of known reference pathways, as shown in Table 25 for the correlation of octadecanoic acid and glutamate. Thus correlations revealed connectivity between metabolites that were seemingly unconnected with respect to sub-networks. These novel pathways can generate hypotheses that can be subsequently verified experimentally.

Table 25: Shortest pathway calculated using in the Edinburgh human metabolic network (EHMN) that connects the metabolites octadecanoic acid and glutamate. These metabolites were found to have significantly different pair-wise correlations for MDA-MB-231 cells cultured in normoxia compared to hypoxia.

Metabolic pathway	KEGG ID	Reference pathway
Octadecanoic acid → Stearoyl-CoA	C01530 → C00412	De novo fatty acid biosynthesis
Stearoyl-CoA → 3-oxoeicosanoyl-CoA	C00412 → CE2251	De novo fatty acid biosynthesis
3-oxoeicosanoyl-CoA → Malonyl-CoA	CE2251 → C00083	De novo fatty acid biosynthesis
Malonyl-CoA → 3-oxopropanoate	C00083 → C00222	Propanoate metabolism
3-oxopropanoate → 2-oxoglutarate	C00222 → C00026	Histidine metabolism
2-oxoglutarate → L-glutamate/glutamate	C00026 → C00025/ C00302	Lysine metabolism/ Tryptophan metabolism/ Tyrosine metabolism/ Urea cycle and metabolism of arginine, proline, glutamate, aspartate and asparagine

Furthermore, the networks created are relatively small-scale and only include the pathways that are necessary to describe the perturbation. Thus, these models are more useful to identify the essential responses to a perturbation, whereas a complete representation would prove to be much more difficult to interpret. Reactions in the network were not annotated with the enzyme as many of the reactions could be catalysed by more than one enzyme or isoform. For example, the reaction connecting L-glutamate to 2-oxoglutarate can be catalysed by enzymes including a class of oxidoreductases (EC number (representing the catalytic function of the enzyme[201]) 1.4.1.2, 1.4.1.3, 1.4.1.4) and a class of transferases (2.6.1.1, 2.6.1.2, 2.6.1.5, 2.6.1.7, 2.6.1.9, 2.6.1.19, 2.6.1.39, 2.6.1.40, 2.6.1.52, 2.6.1.55 and 2.6.1.57). Isoforms increase the robustness of the system and each has a different kinetic rate and regulatory property[248]. Thus annotating reactions in the network would not have provided any additional information about the impact of the pathway on the system.

The origins of metabolite correlations can arise as a consequence of metabolic regulation, post-translational regulation, and transcriptional regulation. The rate of a reaction is dependent on the catalytic activity of the enzyme. Enzymes can be allosterically affected by the presence of a metabolite (other than the enzyme substrate) to inhibit or activate activity. Thus, allosteric regulators vary the substrate-binding affinity. A negative correlation may arise in a pair of metabolites as one metabolite is an allosteric inhibitor of the enzyme that produces the other metabolite. A positive correlation may arise in a pair of metabolites as one metabolite is an allosteric activator of the enzyme to increase the generation of the other metabolite. Results did not identify any negative correlations that

were significantly different as a result of decreasing oxygen availability. Thus all correlations that differed significantly were positive correlations hence the presence of one metabolite could have had an effect on the activity of an enzyme in other metabolic pathways, resulting in a change in the flux through the shortest pathway given in the constructed network. Furthermore, the metabolome can be regulated by transcriptional control of an enzyme, such as an increase or decrease in enzyme expression. Additionally, post-translational modification can change the activity of an enzyme through mechanisms including phosphorylation[208]. An overview of mechanisms of regulation in cellular metabolism is shown in Figure 77.

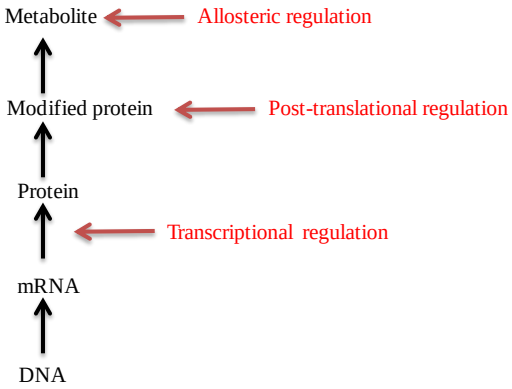

Figure 77: An overview of regulation in cellular metabolism. Metabolism can be regulated by concentrations of metabolites or by down-stream effects such as post-translational regulation and transcriptional regulation.

5.3.1 Low oxygen metabolism

Correlations were examined prior to the construction of metabolic networks to investigate the specific patterns exhibited in each oxygen tension (normoxia, hypoxia and anoxia). The aim was to explore correlations between two metabolites that differ with respect to oxygen tension. As shown in Table 17, the pair-wise interaction between pyruvic acid and lactate in normoxic samples is positively correlated; however there is a shift in hypoxic samples and this pair becomes poorly correlated. Biological interpretation suggests the glycolytic pathway was involved in a metabolic shift. Thus, this may be the result of the metabolic shift from oxidative phosphorylation metabolism to non-oxidative phosphorylation metabolism with respect to lowering the oxygen tension. Pyruvate is a branch point in glycolysis and is involved in numerous reactions including being transported into the mitochondria where it can enter the TCA cycle for oxidative phosphorylation. Under aerobic conditions the pair-wise correlation suggests the concentration of lactate increases as pyruvate increases. This correlation may be a result of the 'Warburg effect'[249] where cancer cells in highly oxygenated environments reprogramme central carbon metabolism to

produce energy by a high rate of glycolysis. Under anaerobic conditions cells have been shown to increase the uptake of glucose through accelerating the flux through the glycolysis pathway to maintain cellular energy. As oxygen is limited the cells no longer rely on the TCA cycle and oxidative phosphorylation for the generation of ATP and therefore the majority of pyruvate will be converted to lactate. Consequently, hypoxic tumour microenvironments are often acidic inhibiting the uptake of some pH sensitive chemotherapeutics such as doxorubicin[37]. One would expect a correlation between pyruvate and lactic acid due to non-oxidative phosphorylation metabolism; however these metabolites were uncorrelated in low oxygenated samples. This may be due to the upregulation of the monocarboxylate transporter 1 and 4 (MCT1 and MCT4) in low oxygenated samples to increase the efflux of lactate[250]. As a result, for hypoxic cells, the lactate generated is rapidly effluxed compared to normoxic cells. Furthermore, the metabolic correlation network comparing normoxia and anoxia metabolism (Figure 67) suggests lactic acid is an important hub with high connectivity.

Comparing correlations offers an additional level of data interpretation compared to univariate statistical analysis; however, mapping the pathways connecting correlated metabolites onto a human metabolic network can be used to construct a network of the response. Thus the pathway connectivity of the metabolite correlations that differed in cells cultured in low oxygen levels compared to high oxygen was used to construct an interaction network as shown in Figure 68. Closer inspection of this network revealed three pathways (green nodes) that were present both hypoxia and anoxia correlations. Two of these pathways originated from the correlation between glucose and malate. Glucose has two isoforms α-D-glucose and β-D-glucose thus it is not possible ascertain which of these pathways contributed to the correlation. Consequently, pathways of both isoforms were included in the network. This central pathway was linked with other pathways in the remainder of the network that were exclusive to hypoxia (blue nodes) and anoxia (yellow nodes) metabolism. Hypoxia regulated two additional pathways from this central pathway towards glucose/galactose and octadecanoic acid whereas anoxia regulated more pathways including towards glycerol, citrate and L-isoleucine. Lipid metabolism was also positively regulated in a separate sub-network of hypoxia connecting hexadecanoic to glycerol 3-phosphate. It was previously suggested in Chapter 4 that fatty acid metabolism promotes cell survival in low oxygenated environments to maintain the redox balance[214]. The network further suggested fatty acid metabolism was a hypoxia specific response. This may be supported by glutaminolysis shown in Figure 78.

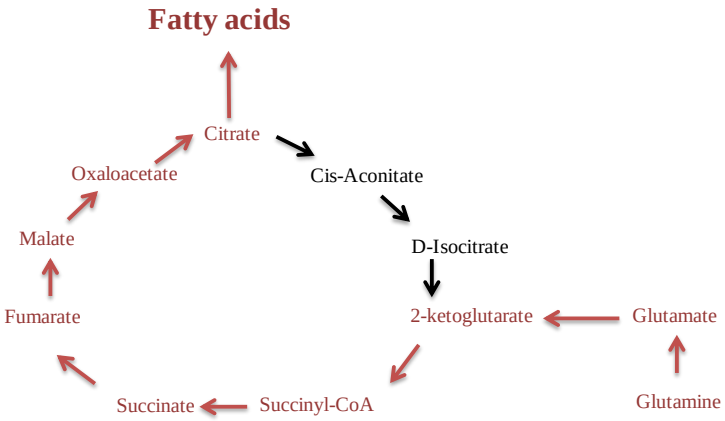

Figure 78: Uptake of glutamine to support the synthesis of fatty acids.

Furthermore, a pathway connecting the positive correlation between pyruvate and malate was found for hypoxic cells, which may be in response to glutaminolysis replenishing glycolytic pathways [208] shown in Figure 58.

5.3.2 Chemotherapy response in a normal oxygen tension.

Correlations between normoxia and normoxia samples treated with a cytotoxic dose of doxorubicin (0.1 µM) revealed a single correlation between fructose and glutamic acid. Metabolic correlations between samples treated in normoxia with and without 1 µM doxorubicin revealed a greater number of correlations in response to drug treatment. The higher dose is not clinically viable and was shown, in Chapter 3, to inhibit cell growth by 70 %. Thus these correlations represent high cytotoxicity.

The limited metabolic response of cells cultured in 0.1 µM doxorubicin may be due to the drugs effect on a portion of the metabolism that is not represented by the 52 metabolites detected by GC-MS. For example, metabolite markers detected by UHPLC-MS (in Chapter 4) suggested doxorubicin caused lipid peroxidation; however a limited number of lipids can be detected by GC-MS and therefore the network regulation of lipid peroxidation was beyond the scope of this study. Wang *et al.* studied the systems toxicology of doxorubicin in rat urine and suggested uric acid, tryptophan, phenylalanine, hippuric acid and cholic acid to be metabolite markers of doxorubicin toxicity[72]. These metabolites were not detected directly in the GC-MS dataset however related metabolites such as benzoic acid were identified. In rats the toxic metabolite marker hippurate is synthesised from benzoic acid. Thus metabolites detected in the GC-MS dataset, such as benzoic acid, may be associated with pathways of toxicity. A network of drug toxicity was

constructed for normoxic cells representing both doses of drug treatment, low and high, to visualise the drug dose response pathways. Including both doses into a single network enabled more cytotoxic pathways to be identified.

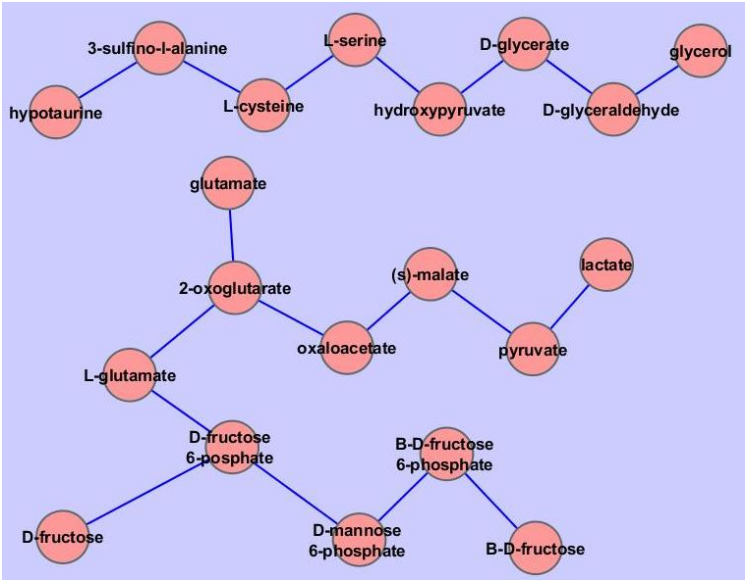

Figure 79: Sub-section of the network in Figure 70 describing the pathway response of MDA-MB-231 cells dosed with 0.1 µM or 1 µM doxorubicin.

Pathways of drug action in normoxic cells discussed below are shown in Figure 79. A lactic acid response to drug toxicity occurs in high doses of doxorubicin. It has been suggested that LDH is a clinical parameter of doxorubicin induced toxicity [72] and therefore lactic acid is considered to be a metabolite marker of doxorubicin toxicity. Lactic acid was positively correlated with malate, in cells treated with doxorubicin, and is connected by pyruvate in the network. Cellular response to cytotoxicity may therefore be related to gluconeogenesis. The pathway connecting glutamate to 2-oxoglutatate, shown in Figure 79, is a common in both drug doses. Cells treated with a lower dose of doxorubicin regulate these metabolites through a positive correlation with β-D-fructose/D-fructose. Cellular response to doxorubicin may increase fructose uptake to generate glutamate, which was suggested in Chapter 4 as a mechanism of normoxic drug action. The network suggests glutamate is synthesised from fructose, which would reduce the cells need to influx glutamate from the extracellular environment. Reducing glutamate uptake has been suggested to reduce doxorubicin efflux, thus a greater concentration of the drug is retained. There are many isoforms of glutamate that interact with transport inhibitors with different affinities[233]. In addition, some glutamate isoform inhibitors increased the uptake of glutamate[233]. The network suggests rather than inhibiting the many complex glutamate isoforms, cells should be encouraged to synthesise glutamate from fructose to increase

cytotoxicity of doxorubicin. Furthermore, for high drug doses, glutamate has a positive correlation with malate suggesting use of the malate-aspartate shuttle (a mitochondrial shuttle for the transport of reducing agents, such as NADH that cannot cross the mitochondrial membrane, through reducing molecules that can cross the membrane) to generate glutamate reducing glutamate uptake[208]. The network also showed a pathway connecting glycerol and hypotaurine, which is related to a high drug dose. Hypotaurine and metabolic precursors in the pathway such as cysteine have been suggested to act as antioxidants. Cells may upregulate this pathway in response to drug induced ROS to minimise the cytotoxic effects[242]. Furthermore, the correlation network, shown in Figure 69, suggested malate as a hub in the network. The activity of succinate dehydrogenase and malate dehydrogenase have been shown to decrease in rats treated with doxorubicin[251], which would impact on energy metabolism. This suggests cytotoxicity of doxorubicin may have an impact on intermediates in the TCA cycle.

5.3.3 Low oxygen metabolism and chemotherapy resistance

The low oxygen induced chemoresistance was investigated by comparing drug treated cells to non drug treated cells cultured in similar oxygen levels. This approach revealed metabolic correlations (at each oxygen level) relating to cells treated with 0.1 µM doxorubicin, which has previously been shown, in Chapter 3, to have poor efficacy towards hypoxic cells. Pair-wise correlations representing low oxygen induced chemoresistance were mapped onto the EHMN and the shortest pathway connecting the metabolites was used to construct the metabolic network shown in Figure 73. All the pair-wise correlations shown in the network were highly correlated in the drug treated samples. Exploration of the topological properties of the network revealed pathways of metabolism contributing to chemoresistance. A network of chemoresistance in both hypoxic and anoxic samples was constructed to visualise the characteristic mechanisms of low oxygen resistance. A greater number of correlations were identified for resistance compared to drug action. Furthermore, more metabolite markers of resistance were identified using statistical analysis shown in Chapter 4. This suggests hypoxia-induced chemoresistance has a greater metabolic response than the normoxic model of drug action.

Comparing the resistant (Figure 73) and toxic (Figure 70) networks suggests resistance cells use β-D-fructose for octadecanoic acid synthesis rather than for glutamate production. Octadecanoic acid is a saturated fatty acid and has been suggested by Zeng *et al.* to modulate cell responses to DNA damage[252]. Octadecanoic acid promotes the expression of

DNA damage signalling pathways p21 and Bax when the cells have double-stranded DNA breaks[252]. Doxorubicin initiates double-stranded DNA damage through inhibiting topoisomerase II from ligating DNA following replication. Resistant cells may synthesis octadecanoic acid to mediate DNA repair mechanisms to overcome the DNA damage[19] (Figure 80).

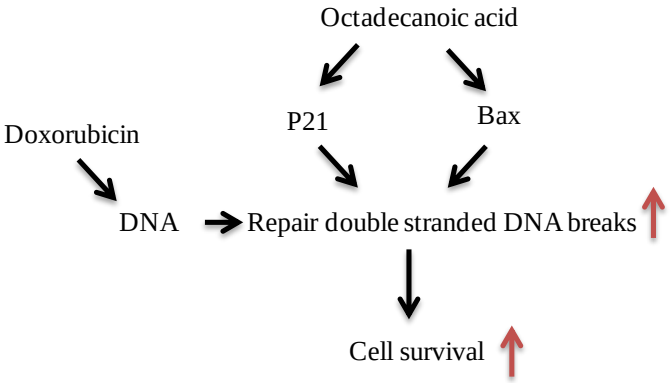

Figure 80: Overview of a proposed hypoxia-induced chemo-resistant mechanism. Octadecanoic acid promotes the expression of DNA damage signalling pathways p21 and Bax to repair double-stranded DNA breaks.

Furthermore, correlations suggest octadecanoic acid is synthesised from many other metabolites including glutamic acid, L-isoleucine, threitol/erythritol, sorbitol/galactose/glucose and aspartate (Figure 81). A closer network inspection reveals the targets to inhibit octadecanoic acid synthesis are malonyl-CoA, 3-oxoeicosanoyl-CoA, stearoyl-CoA and octadecanoic acid as all pathways in this network that synthesise octadecanoic acid filter into these four metabolites.

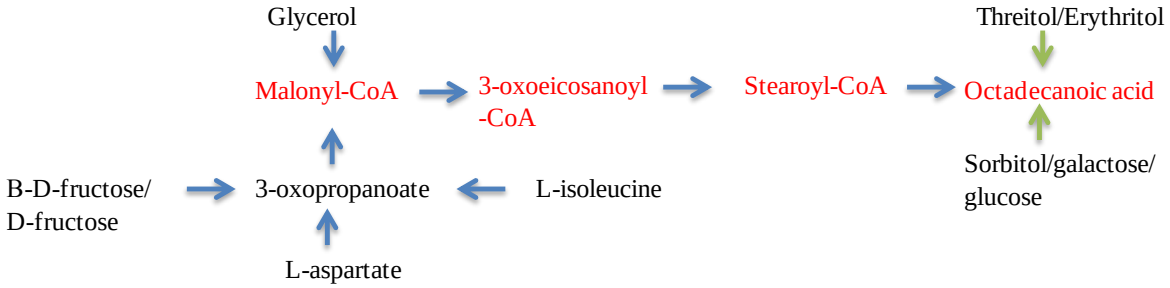

Figure 81: Summary of the proposed pathway low oxygenated cells regulate to promote the synthesis of octadecanoic acid for DNA repair mechanisms. Metabolites shown in red are the potential drug targets in this pathway. Green arrows represent correlations and blue arrows represent the pathway that connects correlations calculated using the Edinburgh human metabolic network (EHMN).

An additional pathway of chemoresistance links 4-hydroxy-L-proline, 2-oxoglutarate, L-glutamate and L-isoleucine. Doxorubicin has been shown to inhibit prolyl hydroxylase and consequently inhibit collagen synthesis, which reduces cell proliferation and growth[253]. In anoxic cells, doxorubicin may be prevented from inhibiting prolyl hydroxylase resulting in

an increase in 4-hydroxylproline and subsequently mediating resistance through collagen synthesis[254]. An aggressive cancer phenotype in pancreatic and non-small cell lung cancers have been associated with high levels of collagen[255]. Spivey *et al*. suggested aggressive cancers have increased collagen XXIII to control metastasis through cell–cell and cell–matrix adhesion in addition to anchorage-independent cell growth[255]. Furthermore, L-isoleucine, an essential amino acid, may be more readily taken up in anoxic cells to facilitate chemoresistance as it is also a component of collagen.

5.3.4 Low oxygen metabolism and strategies to overcome chemotherapy chemoresistance

The hypoxic tumour metabolism is robust and can counteract single metabolic targets. The resistant network suggested a multitude of mechanisms are employed to overcome the toxic effects of doxorubicin. The metabolic response to overcome resistance can be explored in the network constructed of cells cultured in low oxygen levels and treated with a cytotoxic dose of doxorubicin to determine the multitude of drug response pathways. Metabolic correlations (at each oxygen level) relating to cells treated with 1 µM doxorubicin, which has previously been shown, in Chapter 3, to have good efficacy towards hypoxic cells were calculated. Pair-wise correlations representing the metabolic response to overcome low oxygen induced chemoresistance were mapped onto the EHMN and the shortest pathway connecting the metabolites was used to construct the metabolic network shown (Figure 76). Comparing the networks of doxorubicin toxicity of cells cultured in normal oxygen levels (Figure 70) to low oxygen levels (Figure 76) showed some similar metabolic mechanisms of cytotoxicity. The pathway connecting the positive correlation between β-D-fructose/D-fructose correlated with glutamate in both networks suggested the uptake of fructose may be a key player in regulating glutamate synthesis. Reducing glutamate uptake has been reported to prevent the efflux of doxorubicin maintaining the drug concentration in the cell and thus increasing toxicity[233].

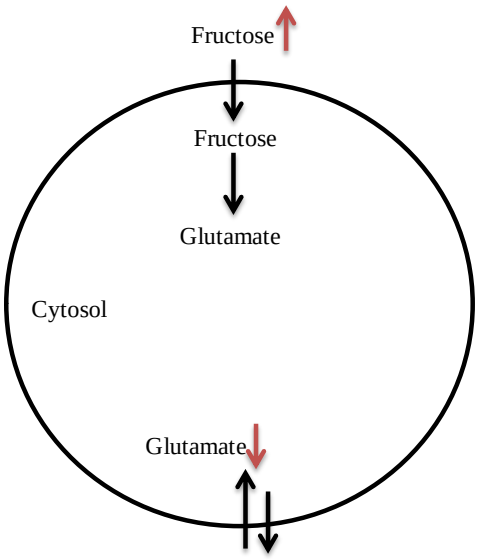

Figure 82: Overview of a proposed mechanism to overcome hypoxia-induced chemoresistance. Fructose synthesises glutamate therefore the uptake of glutamate is reduced, which is related to a decrease in the efflux of doxorubicin.

The networks suggest glutamate synthesis is an important mechanism for drug toxicity regardless of oxygen tension. Furthermore, in the normoxic network glutamate has a positive correlation with malate suggesting use of the malate-aspartate shuttle to cytosolic malate from the mitochondria to synthesise glutamate in the cytosol and thus reduce glutamate uptake[208]. The anoxic network does not have this pathway suggesting, the fructose mechanism to be more effective target to overcome resistance. Although the fructose mechanism appears to evoke toxicity in the cells, the robustness of cancer to low dose doxorubicin treatment in hypoxic cells may overcome a single pathway target. Thus targeting both pathways may be more effective.

Unique pathways in the network to overcome low oxygen-induced chemoresistance were further explored in the network (Figure 76). Benzoic acid was found to be a highly connected hub and was also reported as a metabolite marker of anoxia drug toxicity in Chapter 4. Benzoic acid was correlated to a single metabolite in the normoxic drug action and drug resistance networks; however in the low oxygenated drug action network benzoic acid was correlated with seven metabolites. High connectivity suggests benzoic acid is an important low oxygen response mechanism to drug toxicity. Many of the metabolites correlated with benzoic acid, are TCA cycle intermediates and related amino acids. Doxorubicin may be involved in inhibiting the β-oxidation of odd-chain fatty acids[208] leading to cellular toxicity, as suggested in Chapter 4. A product of odd-chain fatty acid oxidation is succinyl-CoA, a TCA cycle intermediate, and resistant hypoxic cells may require this mechanism to regenerate the TCA cycle for bioenergetics production and

growth[208]. Inhibiting β-oxidation of odd chain fatty acid synthesis may reduce the cells ability to maintain ATP required for drug resistant mechanisms, such as DNA repair and drug efflux through the TCA cycle. Furthermore, benzoic acid has been suggested to inhibit MCT1, which transports lactate from the cytosol to the extracellular environment[256]. Lactate was shown to be a hub in the network, which may be a result of MCT1 inhibition. Majumdar *et al.* used the human retinal pigmented epithelium cell line, ARPE-19, to study lactate uptake in combination with monocarboxylic acid treatments[256]. Benzoic acid was found to inhibit lactate transport through inhibiting the MCT1[256]. Tumour hypoxia has been shown to regulate the expression of MCT1 suggesting it is an important mechanism for cell survival in low oxygen environments[31]. Inhibition of MCT1 would reduce the glycolytic flux through preventing the efflux of lactate leading to a reduction of intracellular pH and reduction of ATP, which would subsequently reduce tumour growth and induce cell death[31] (Figure 83).

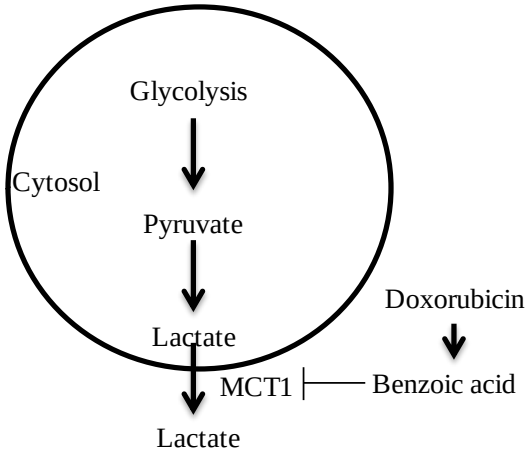

Figure 83: Overview of the proposed mechanism to overcome hypoxia-induced chemoresistance. Benzoic acid inhibits monocarboxylate transporter 1 (MCT1) to reduce lactate efflux and reduce intracellular pH leading to cell death.

In addition, Sonveaux *et al.* used MCT1 inhibitors α-cyano-4-hydroxycinnamate and siRNA to effectively treat tumour bearing mice[257]. This research suggested MCT1 was involved in a metabolic symbiosis between normoxic and hypoxic cancer cells. Lactate produced by hypoxic cells is taken up by normoxic cells for oxidative phosphorylation[257]. The MCT1 inhibitors disrupted this metabolic symbiosis leading to hypoxic cell death. Additionally, the study showed enhanced growth delay when the inhibitors were used in combination with radiotherapy[257]. A combination of doxorubicin treatment and an MCT1 inhibitor may be a lethal combination to hypoxic tumours.

Another unique pathway that may contribute to overcoming chemotherapy resistance in low oxygen environments is the correlation between hexadecanoic acid and pantothenate. This lipid response pathway is a hypoxia specific response to drug treatment. Doxorubicin liposomes loaded with ascorbyl palmitate were shown to improve drug targeting, which was linked with improving cell membrane permeability[258]. Low oxygen cells may induce hexadecanoic acid synthesis causing enhanced permeation properties of the cell membrane.

5.4 Conclusions

Network-based correlation analysis was a useful tool to explore the metabolic pathways of hypoxia-induced chemoresistance in the GC-MS dataset. The networks were explored to help understand why hypoxia cells are resistant to chemotherapy treatment and how resistance may be overcome from a metabolic perspective. Some of the mechanisms associated with low oxygen metabolism were consistent with existing knowledge; however since knowledge of the metabolic regulation of hypoxia-induced chemoresistance is limited, many of the mechanisms proposed are novel.

Network analysis presented a complementary approach to the metabolite marker analysis performed in Chapter 4. Some of these metabolite markers were present in the networks thus potential metabolic pathways associated with the metabolite markers were identified. Similarities between metabolite marker analysis and network analysis included cells cultured in low oxygen levels regulate fatty acid synthesis to promote cell survival, normoxic cells treated with doxorubicin synthesise glutamate to minimise drug efflux and benzoic acid suggests inhibition of β-oxidation of odd chain fatty acids in low oxygenated cells treated with high drug doses. In contrast, some metabolic pathways were not previously elucidated though metabolite marker discovery. For example, low oxygenated cells treated with a lower dose of doxorubicin synthesised the fatty acid octadecanoic acid to signal DNA repair mechanisms, whereas metabolic markers suggested metabolic precursors of DNA repair such as purines and pyrimidines were fundamental to resistance. Both of these mechanisms are likely to be factors involved in chemoresistance, however only by applying metabolite marker and network analysis could both pathways were revealed. A combination of analyses is therefore important to fully interpret metabolic mechanisms of disease. Furthermore, building metabolic networks was useful to pinpoint specific reactions within a pathway as potential drug targets. For example, synthesis of octadecanoic acid involved many pathways that all filtered into four reactions producing malonyl-CoA, 3-oxoeicosanoyl-CoA, stearoyl-CoA and octadecanoic acid suggesting this

section of the pathway is the most suitable target to inhibit octadecanoic acid production. Furthermore, network-based correlation analysis can be readily applied to metabolomics data of other disease states to explore the topology and dynamics (fluctuations) of the metabolic responses.

Biochemical control of regulatory pathways is not solely regulated by metabolism; it is also regulated by hierarchical control. Future analysis to develop network-based correlation analysis of metabolomic and proteomic datasets would offer a novel strategy to explore the regulatory pathways in biological systems. Modelling these datasets would help to determine regulation in the network with respect to allosteric (metabolic), post-transcriptional and transcriptional regulators.

Chapter 6

THE DEVELOPMENT OF SECONDARY ION MASS SPECTROMETRY AS A TOOL FOR SPATIALLY IMAGING METABOLITES

6.1 Introduction

ToF-SIMS is an imaging surface analysis technique that enables the chemistry of a sample surface to be analysed. Secondary ions are extracted into a ToF mass analyser to generate an image of the sample surface with spectra contained within each pixel making up the image. In comparison to other imaging mass spectral analysis techniques, such as Matrix-Assisted Laser Desorption Ionisation Mass Spectrometry (MALDI-MS), ToF-SIMS offers high spatial resolution imaging and the ability to perform molecular depth profiling analysis beyond the surface layer[114]. Additionally, ToF-SIMS does not require a matrix to be applied to enable ionisation as MALDI-MS does. ToF-SIMS is able to detect species up to several thousand Da, but in imaging mode where the small area of the pixel can limit sensitivity, masses up to 1 kDa are normally reported. The technique is potentially well-suited to the analysis of small molecules such as metabolites. Mass spectral instruments typically used in metabolomics studies, such as GC-MS and LC-MS, require metabolite extraction of the sample and therefore there is a loss of spatial localisation of the metabolites. In contrast, ToF-SIMS offers spatial localisation of molecule allowing the direct study of a disease process. Furthermore, development of mass spectral imaging tools could advance towards *in situ* metabolite analysis of a sample such as *in vitro* single cells or *ex vivo* tissue imaging. The aim of this project was to unlock ToF-SIMS to the application of *in situ* metabolite analysis. Further, ToF-SIMS was used as a tool to investigate the underlying metabolic mechanisms related to hypoxia-induced chemotherapy resistance in cancer cells and 3D tumour models (MTSs).

Metabolite standards were prepared in 1 mM solutions and spotted onto silicon wafer prior to analysis. Analysis was performed on the J105 chemical imager and spectra were annotated. Fragmentation patterns were compiled into a table to enable subsequent spectral interpretation of metabolites in biological samples. MTSs were cultured from FaDu cells and treated with various doses of doxorubicin to explore the metabolic response to hypoxia-induced chemoresistance *in-situ*.

6.2 Results

6.2.1 The development of a ToF-SIMS metabolite database for metabolite analysis studies

ToF-SIMS has been applied and developed considerably in the area of inorganic analysis including fields such as semiconductors[259] and polymers[260]. More recently the field has progressed towards the biosciences[105, 114, 261]. ToF-SIMS analyses of biological samples have shown the potential to identify lipids[262] such as phosphocholine, cholesterol and some other small molecules including DNA bases such as adenine[114]. Whilst ToF-SIMS has been demonstrated as a tool for analysing lipids, very few metabolite examples can be found in the literature or the SIMS library[263]. Identifying peaks in ToF-SIMS spectra that relate to metabolites is challenging due to the lack of metabolite reference standards available from the literature. To overcome this issue, a series of metabolite standard spectra were acquired using ToF-SIMS. The aim was to use the mass spectra patterns to annotate the ToF-SIMS spectra of biological samples with metabolite fragments. Metabolic profiling analysis (described in Chapter 4) detected a range of metabolites. A proportion of these metabolites were obtained and analysed using ToF-SIMS to identify the molecular ion and related fragments as shown in Table 26. For all metabolites analysed the molecular ion and most intense fragments in the mass spectra and tandem mass spectra are presented. Improved mass resolution increases confidence in assigning chemical species in ToF-SIMS spectra. Currently, the J105 3D chemical imager is only able to acquire positive ion spectra. Consequently, all analysis undertaken in this Chapter acquired data in positive ion mode only.

Table 26: Metabolite standards acquired on the J105 3D chemical imager. For all metabolites the molecular ion ($[M+H]^+$) and most intense fragments in the mass spectra and tandem mass spectra are presented. The *m/z* values are presented to closest 0.05 for MS and 0.1 for MS^2. Database MS^2 fragments (from MassBank or Metlin) common with time-of-flight secondary ion mass spectrometry (ToF-SIMS) spectrum presented.

Metabolite	Molecular ion; $[M+H]^+$	ToF-SIMS Fragments	MS^2 fragments from CID of $[M+H]^+$ ion in ToF-SIMS	ToF-SIMS fragments common with MassBank MS^2 spectrum	Database spectrum used (MassBank unless stated)
Adenosine	268.10	178.10, 136.10, 119.05, 109.05, 94.05	136.2	136.06, 119.04, 109.05, 94.04	Adenosine; LC-ESI-QToF; MS^2; MERGED;$[M+H]^+$
Carnitine	162.10	118.10, 103.05, 102.10, 100.10, 85.0, 74.10, 60.10, 58.05	103.1, 102.1, 100.2, 85.1, 60.1, 59.1, 58.1, 43.0, 42.1	103.04, 102.09, 85.03, 60.08, 58.07	Carnitine; LC-ESI-QToF; MS^2; MERGED;$[M+H]^+$
Citric acid	193.05	175.05,139.00, 129.00, 111.00, 87.00	175.1, 139.1, 129.1, 87.1, 69.1, 43.0	-	$[M+H]^+$ ion data not currently in MassBank or Metlin.$[M+Na]^+$ MS in Metlin
Citrulline	176.10	159.10, 113.10, 70.05	159.1, 113.1, 70.1	159.08, 113.07, 70.07	L-Citrulline; LC-ESI-QToF; MS^2; MERGED; $[M+H]^+$
Doxorubicin	544.25	379.10, 361.10, 337.10, 321.10, 306.05	-	554.18, 379.08, 361.07, 321.08	Doxorubicin; LC-ESI-QToF; MS^2; MERGED; $[M+H]^+$
Fructose	181.05	171.00, 163.05, 145.05, 127.05, 115.05, 111.00, 99.00, 97.05, 85.05, 73.05	-	-	Positive ion data not currently in MassBank or Metlin
Glutamine	147.10	130.05, 84.05, 56.05	130.1, 84.1	130.05, 84.05, 56.05	Glutamine; LC-ESI-QToF; MS^2; CE:20 eV; $[M+H]^+$
Glutathione	308.10	233.05, 179.05, 162.0, 130.05, 84.05, 76.05	179.1, 130.14, 84.1, 76.1	233.07, 179.97, 162.04,130.05	L-Glutathione (reduced form); LC-ESI-ITFT; MS^2
Glutathione disulfide	613.05	595.05, 538.05, 484.05, 308.00, 130.00, 84.00, 56.00	-	595.15, 538.13, 484.12, 130.05	L-Glutathione (oxidized form); LC-ESI-QToF; MS^2;MERGED;$[M+H]^+$
Lactic acid	91.05	89.05, 73.05, 55.05, 45.05	63.12, 45.0	-	Positive ion data not currently in MassBank or Metlin
Methionine	150.05	133.05, 104.05, 102.05	133.1, 104.1, 102.1, 61.0	133.03, 104.05, 102.06	L-Methionine; LC-ESI-QToF; MS^2; MERGED;$[M+H]^+$
Myo-inositol	181.10	163.05, 150.10, 145.05, 127.05, 116.05, 109.05, 102.05, 85.05, 81.05, 73.05	163.1, 127.1, 109.1, 85.1, 81.1, 73.1, 69.1, 43.0	-	Data not in available MassBank or Metlin.
Nicotinic acid	124.05	106.05, 80.05, 78.05	106.1,79.1, 78.1, 51.0	106.03, 80.05, 78.03	Nicotinic acid; LC-ESI-QToF; MS^2; MERGED; $[M+H]^+$
Putrescine	89.10	72.10	72.1	72.08	Putrescine; LC-ESI-QToF; MS^2; MERGED; $[M+H]^+$

Succinate	119.05	101.00, 95.10, 73.05, 55.05	101.0	-	Data not available in MassBank or Metlin
Thymine	127.05	110.00, 84.05, 82.00	110.1	110.02, 84.04, 82.03	Thymine; LC-ESI-QToF; MS^2; MERGED;$[M+H]^+$
Uracil	113.05	96.05, 70.05	-	96.01, 70.03	Uracil; MS^2 10 V; Metlin $[M+H]^+$

An example of a metabolite ToF-SIMS spectrum is shown in Figure 84, which is a spectrum of methionine. The spectrum comprises of a quasi-molecular ion peak at *m/z* 150.05 and additional fragments *m/z* 133.05, 104.05 and 102.05. Metabolite spectra obtained by ToF-SIMS were compared to LC-MS fragments found in the online MassBank database[264]. The metabolite spectra acquired using ToF-SIMS were found to have a similar fragmentation pattern to merged liquid chromatography electrospray tandem mass spectrometry (LC-ESI-MS^2). Merged spectra are a unique entity of the MassBank database and are a single artificial spectrum created through overlaying LC-ESI-MS^2 spectra for range of collision energies[264]. The common fragments between the ToF-SIMS spectrum and the MassBank merged spectrum of methionine have been annotated with a star, as shown in Figure 84.

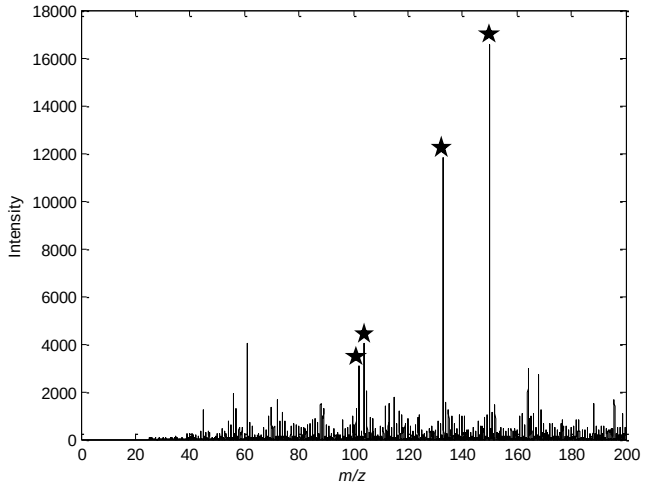

Figure 84: Time-of-flight secondary ion mass spectrometry (ToF-SIMS) spectrum of methionine for positive ion mode displaying the molecular ions can be identified at *m/z* 150.05. Peaks labelled with a star are common between the merged liquid chromatography electrospray tandem mass spectrometry (LC-ESI-MS^2) spectrum of methionine in the MassBank database[264] and the ToF-SIMS spectrum.

6.2.2 Metabolite quantification and matrix effects limitations in ToF-SIMS

Ionisation probability has been suggested to be a limiting factor of ToF-SIMS in the analysis of biomolecules. Methods to increase the ionisation of molecular species would help to improve the secondary ion yields and improve the sensitivity of the technique. It was unknown whether the J105 3D chemical imager was capable of detecting metabolites at physiologically relevant levels. To investigate this methionine was spotted onto silicon

wafer so that the total number of molecules present was 1 pmol, 1 fmol and 1 amol. The whole sample spot was bombarded during the SIMS analysis using an ion beam fluence to ensure all the molecules on the sample surface were consumed.

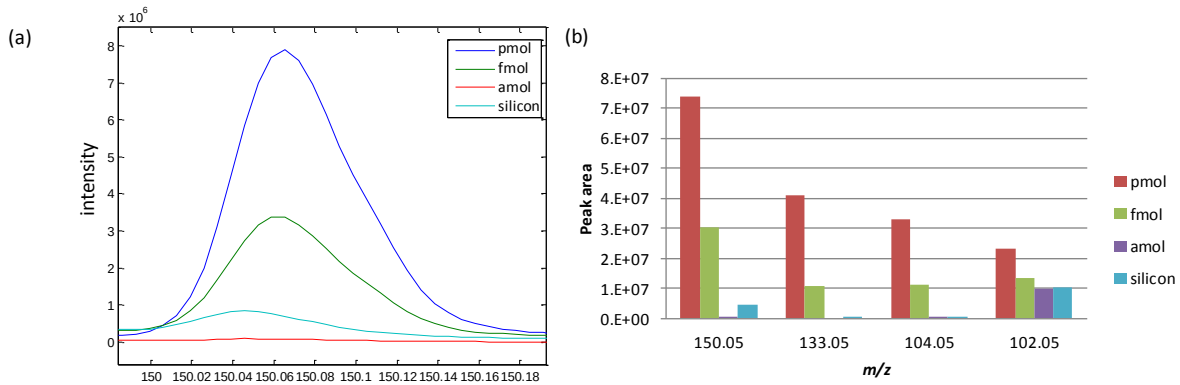

Figure 85: Analysis of methionine at 1 pmol, 1 fmol and 1 amol and silicon using the J105 3D chemical where (a) shows the spectrum of the intensity of the *m/z* 150.05 (b) shows the graph of the spectral peak area of the molecular ion and related fragments of methionine.

The peak area of the methionine molecular ion and related fragments were calculated as shown in Figure 85b. The peak areas, displayed in Figure 85b, suggest the S/N limits of methionine is in the region of 1 fmol, as shown by peak intensities of the molecular ion and fragments being greater than the silicon substrate. Furthermore, Figure 85a visually illustrates the molecular ion at *m/z* 150.05 has a higher peak area in the silicon substrate compared to the 1 amol methionine sample. It is expected that the 1 amol sample would have a similar peak area to silicon if the S/N of the compound was too low. The substrate may have a greater peak area than the 1 amol sample as the analyte of methionine present in the sample sputtering from the surface prevents the detection of substrate whilst the yield of the analyte sputtered is too low to detect. Detection of these metabolites as a heterogeneous mixture is more complex due to the introduction of the matrix effect.

ToF-SIMS, along with other mass spectrometry platforms, encounter ionisation suppression or enhancement known as the matrix effect. The chemical matrix of the complex biological sample can affect the ionisation probability and detection sensitivity of a compound for ToF. The matrix effect has been reported for lipid species but not for metabolites[265]. A cholesterol and phosphocholine mixture demonstrated cholesterol promoted protonation, whereas phosphocholine suppressed protonation during ionisation[265]. When imaging a heterogeneous sample the interpretation of the distribution of biomolecules needs to be undertaken with caution. Normalisation of ToF-SIMS data prior to interpretation has been suggested to be an important tool for deconvoluting the

matrix effect[172]. To normalise a spectrum each pixel is divided by the total ion counts. The matrix effect of metabolite mixtures was investigated using two of the metabolites in Table 26. The spectrum of citric acid and methionine analysed individually and subsequently overlaid is shown in Figure 86a. The overlaid spectrum showed citric acid ionises well compared to methionine where the quasi-molecular ion was double the intensity of methionine. A 50:50 mixture of methionine and citric acid was analysed and the spectrum is shown in Figure 86b and Figure 86c. The predicted overlay, that assumes no matrix effect, suggested citric acid would be the more readily ionising species (Figure 86a) however the mixture spectrum showed the ionisation of methionine exceeded citric acid. Taking the mixture spectrum and removing the predicted spectrum shows the metabolite fragments that were suppressed and those that were enhanced (Figure 86d). The spectrum revealed methionine was enhanced in the mixture and citric acid was suppressed. Both of these compounds are polyprotic acids and therefore they can lose more than one proton. The K_a acid dissociation constants for citric acid are 7.4×10^{-4}, 1.7×10^{-5} and 4.0×10^{-7}, whereas the K_a acid dissociation constants for methionine are $6.3 \times 10^{-3}$and 8.9×10^{-10} [125]. Given the dissociation constants expected for the first dissociation, the pH for 1 mM citric acid and 1 mM methionine were calculated as 2.62 and 3.05 respectively. This shows citric acid has a lower (more acidic) pH, which may promote the ionisation of methionine through proton donation. These results show that despite the matrix effect the suppressed fragments remain present in the spectrum however not all fragments are affected by the matrix effect equally. Consequently, the most useful method to identify metabolites in biological spectra is through locating the multiple fragment ions in the spectra rather than matching the relative intensity of the peaks.

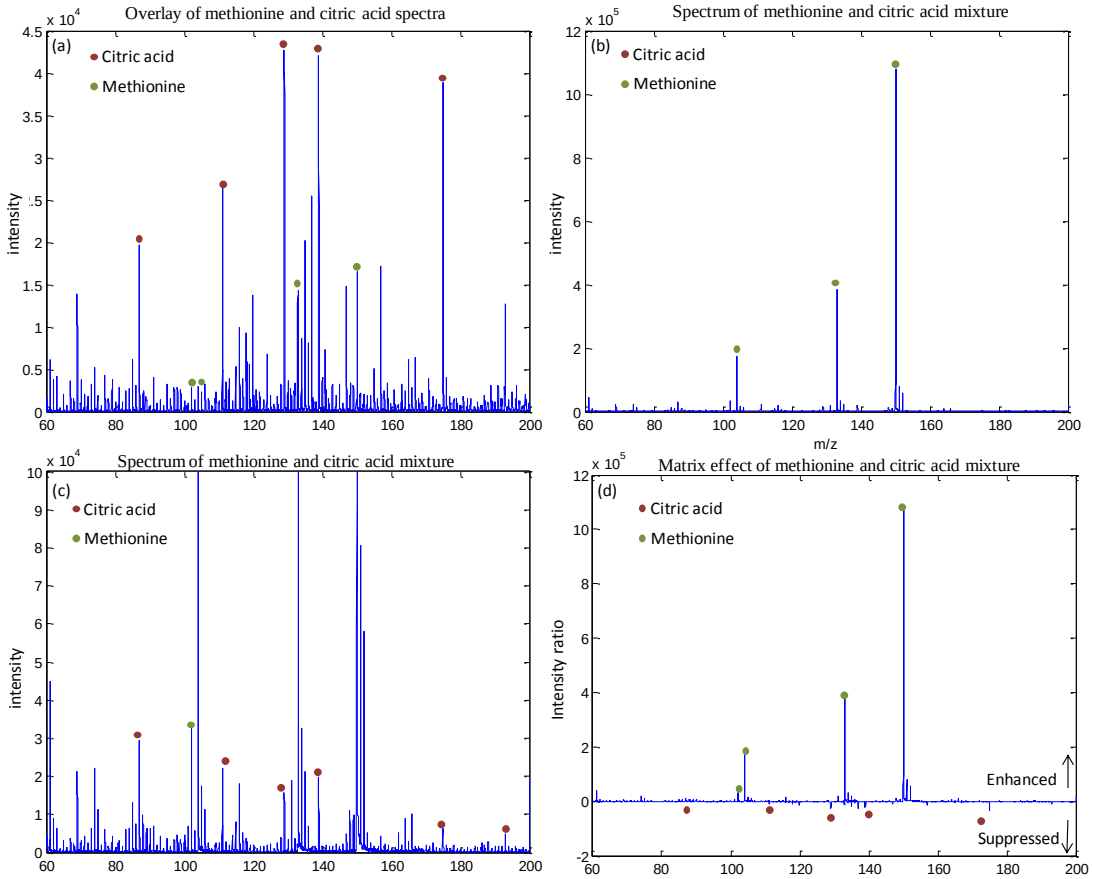

Figure 86: Matrix effect for methionine and citric acid analysed using time-of-flight secondary ion mass spectrometry (ToF-SIMS) where (a) is an overlay of the two standards analysed separately (b) is the spectrum of a 50:50 methionine and citric acid mixture (c) is the methionine and citric acid mixture where the window of intensity has been reduced to show less intense fragments and (d) is the spectrum of the mixture minus the individual standard spectra to show that the ionisation of methionine is enhanced and citric acid is suppressed.

6.2.3 Peak picking metabolite molecular ion and fragments in ToF-SIMS spectra

ToF-SIMS spectra are complex, hundreds of peaks are simultaneously detected in a single pixel, and many features in the biological spectra can be unrelated to the component of interest. Often spectra contain features attributed to the substrate (such as silicon) or biological salt. Figure 87 shows an example of PCA of MTSs images. The MTS has been preselected in the image prior to analysis to omit substrate spectral features however interpretation of the loadings shows substrate peaks were present, as indicated by the green triangles. The loadings plot was dominated by substrate features; however biological fragments were also present in the loadings. Using the ToF-SIMS metabolite fragments shown in Table 26 and ToF-SIMS spectra reported in the literature, a reference list of metabolite and lipid peaks was compiled[262, 266]. Included in this list was the sodium and potassium adducts of the metabolite and lipid molecular ions. This accounted for salt adducts expected in biological samples as the samples contain salts. Prior to PCA the spectra were preselected for peaks in the compiled list to minimise affect of intense

inorganic peaks from skewing PCA. Furthermore, the peak picking method speeded up the process of manually interpreting the loading to identify metabolite and lipid peaks.

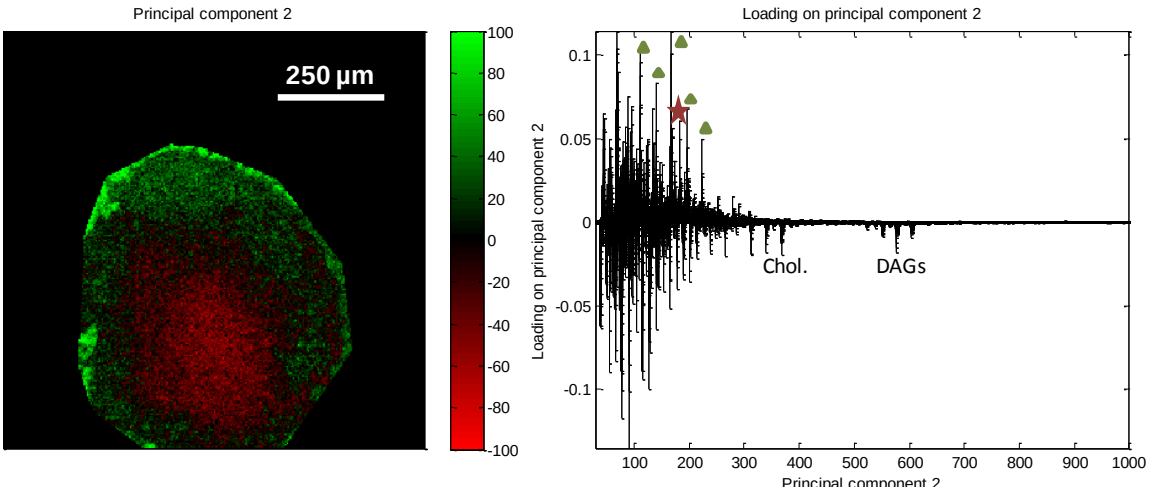

Figure 87: Scores and loading plots of principal component analysis (PCA) for FaDu multicellular tumour spheroid (MTS) treated with 1 mM doxorubicin. The variation represented is 45.68 %. Loadings are annotated with phosphocholine (star), substrate (triangle), cholesterol (Chol.) and diacylglycerol (DAGs)[156]. Image taken from Kotze *et al.*[156].

6.2.4 ToF-SIMS as a tool for high-throughput metabolite detection of MDA-MB-231 cell lysates

ToF-SIMS has been shown to be useful for phenotyping cancer cell lines[111, 112, 267], however identifying specific features within the spectrum, such as metabolites, has been challenging due to the limited availability of metabolite ToF-SIMS spectra. Compiling a small-scale ToF-SIMS metabolite library has enabled metabolite detection in ToF-SIMS spectra of cell lysates[266]. Cell lysates were generated during the large-scale metabolic profiling experiment discussed in Chapter 4 where the metabolism was quenched in ice cold methanol and the metabolites were extracted in a series of three freeze thaw cycles. Initial results suggested the spectra of lysates was dominated by inorganic peaks (Figure 88a) at *m/z* 80.9, 112.9 and 186.9, which may be related to salt adducts. Thus Ziptips® were used to desalt the biological samples. These comprise of a small column positioned in the pipette tip, and have previously been reported to be useful to desalt biological samples prior to mass spectrometric analysis [268, 269]. Mass spectral data acquired following desalting suggested fewer ion species reached the detector, likely to be due to the removal of the readily ionising salt adducts. An inorganic species *m/z* 64.9 dominated the spectra; however organic compounds *m/z* 381.2 and 409.2 also featured to a greater extent, assigned as fatty amides $C_{23}H_{43}NO_3$ and $C_{26}H_{51}NO_2$ respectively (Figure 88b).

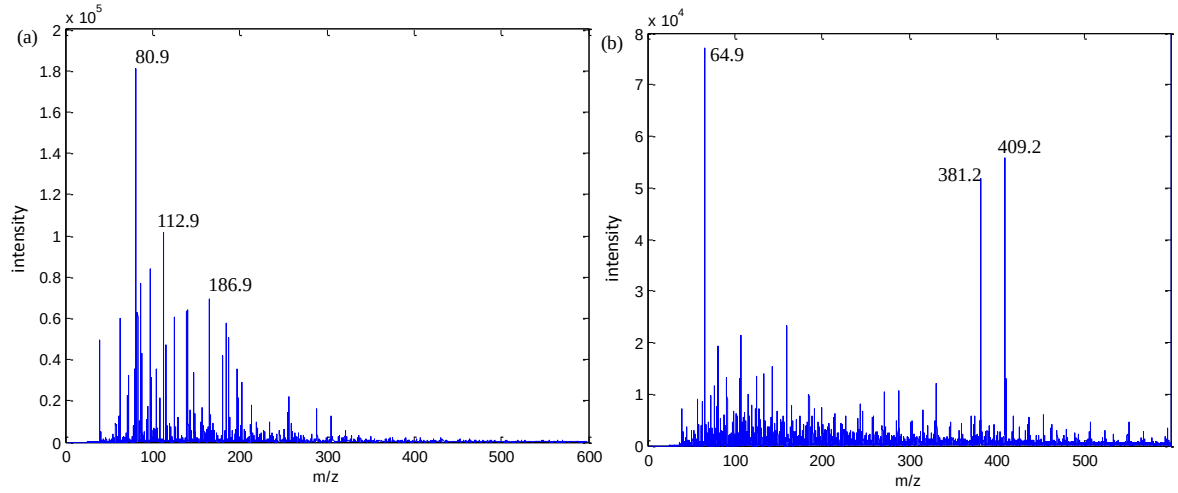

Figure 88: Total ion spectrum of MDA-MB-231 cell lysate extracts analysed using time-of-flight secondary ion mass spectrometry (ToF-SIMS) where samples were prepared (a) without Ziptip® and (b) with Ziptips®.

A closer spectral comparison of the Ziptips® spectra compared to non-Ziptip® spectra is shown in Figure 89. As previously stated, the inorganic peaks are more intense in the lysate sample without the use of a Ziptip® (Figure 89a *m/z* 112.9 (K_2Cl)), however the organic part of the peak at *m/z* 113.01 is more intense in the lysate analysed without a Ziptip®. Additionally, Ziptips® appear to remove some peaks. For example, *m/z* 184, suggested to be a phosphocholine head group[262], appears less intense in Ziptip® samples. This may be owing to the structure being a quaternary ammonium ion that is pre-charged and likely to be retained on the Ziptips® along with other pre-formed ions. Whilst the Ziptips® do appear to remove salt from the sample, the full extent of which other species are removed is uncertain. Thus, while Ziptips® appear to reduce inorganic peaks in ToF-SIMS spectra, Ziptips® were not used in subsequent analyses of lysates. To overcome intense inorganic peaks from dominating the ToF-SIMS spectra, peak picking was used as suggested in section 6.2.4 prior to analysis. Peak picking the spectrum removed inorganics and unknown peaks and therefore reduced the effects of inorganic peaks from skewing PCA.

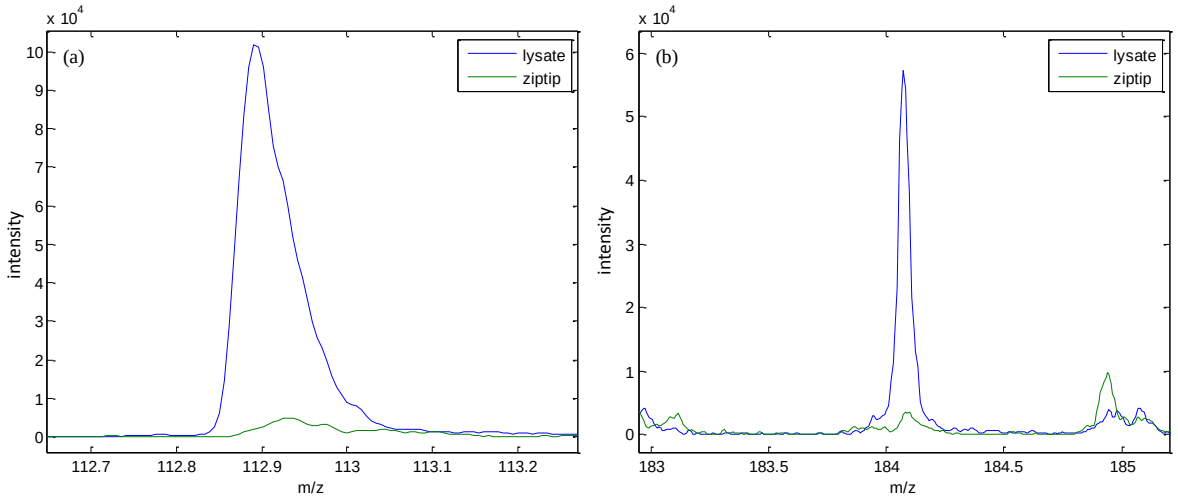

Figure 89: Examples of lysate spectra of MDA-MB-231 cells prepared without a Ziptip® (blue) and with a Ziptip® (green). Spectra shown are *m/z* 113 and 184 acquired using time-of-flight secondary ion mass spectrometry (ToF-SIMS).

A total of 36 samples were analysed using ToF-SIMS. Samples were acquired in the same experiment for metabolic profiling described in Chapter 4. Six biological replicates were acquired for cells cultured in 21 %, 1 % or 0 % O_2 prior to being treated with 0, 0.1 or 1 µM doxorubicin. The aim of the analysis was to determine whether ToF-SIMS can phenotype the sample types based on known metabolite and lipid species, and to determine whether the phenotype was due to metabolites that were also discovered to be significantly different in the data acquired using GC-MS. This would confirm whether ToF-SIMS analysis of metabolites is a complementary tool to the standard platforms currently used to acquire metabolomics data. Subsequently, the discovery of metabolite similarities when comparing ToF-SIMS data to conventional metabolomics data would validate ToF-SIMS as a mass spectral imaging tool for the detection of metabolites *in situ*. Results from PCA of all sample types are displayed in Figure 90, which shows samples separated with respect to the cellular oxygen tension. The normoxic samples are predominantly on the left of PC1 and the low oxygenated samples are on the right. Examination of the loadings revealed the metabolites accountable for this separation. GC-MS metabolite markers of low oxygenated samples included citric acid, glycine, lactic acid, methionine, succinic acid and valine (Chapter 4). All of these metabolites increased relative to the normoxia samples except for citric acid, which decreased. The GC-MS metabolite markers were also metabolites acquired as spectral standards using ToF-SIMS[266]. The loadings of the PCA of ToF-SIMS data were explored to ascertain whether these metabolite markers were correlated in the regions relating to the separation between normoxia and hypoxia. Interpretation of the loadings showed glycine (*m/z* 76), lactic acid (*m/z* 89.05, 73.05, 45.05) and succinic acid (*m/z* 119.05, 101.00, 73.05) contribute to the low oxygenated sample separation. Since GC-

MS data suggested these three metabolites increase in low oxygenated samples they would be expected to be in residing in the positive loadings corresponding to the low oxygenated samples. Methionine, citric acid and valine fragments were not consistently located in either the positive or the negative loadings. In GC-MS analysis the metabolites are separated by the chromatography column and therefore ionisation suppression is reduced. SIMS ionisation is a competitive process as there is no prior separation.

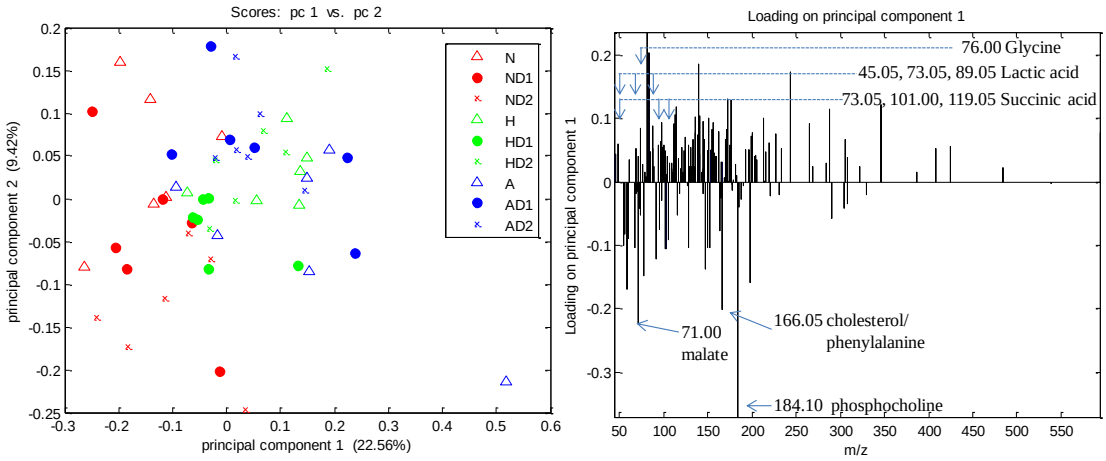

Figure 90: Principal component analysis (PCA) (a) scores plot and (b) loadings plot of time-of-flight secondary ion mass spectrometry (ToF-SIMS) data for MDA-MB-231 cells cultured in normoxia (N), hypoxia (H) and anoxia (A). Subsequently cells were untreated or treated with 0.1 µM doxorubicin (D1) or 1 µM doxorubicin (D2). Intense loadings peaks have been annotated with the *m/z* values and corresponding metabolite.

6.2.5 Sample preparation of MTS

MTSs are often used as a model to study the formation of hypoxia *in vitro*[11, 45, 270, 271]. MTSs are formed from single cells, growing into a ball, with a depleting oxygen gradient from the central to outer regions in a similar manner to solid tumours *in vivo*. These three dimensional models provide an insight into the origin of hypoxia-induced chemoresistance that develops in solid tumours. MTSs form from single cells and express regions of necrosis in the core, quiescence, and proliferation in the outer region[271]. Cells in the central regions experience a similar environment to solid tumours with limited oxygen, limited glucose and varying acidity levels.

Mass spectral imaging was used to investigate the metabolite differences between the hypoxic and normoxic region of MTSs relating to the metabolic mechanisms associated with hypoxia-induced chemoresistance. MTS sections were prepared as described in section 2.9.7.ToF-SIMS analysis can be sensitive to sample preparation methods used to prepare the biological sample therefore steps were taken to identify the optimum method of preparing MTSs. ToF-SIMS is operated under high vacuum and therefore there is often a

compromise between the preservation of tissue and analysis under high vacuum. Furthermore, as shown for lysates, excess salt in the sample can generate a matrix effect reducing the secondary ion yields. To overcome these issues biological samples are often washed prior to analysis to reduce the effects of salt suppression[272]. Common washing solutions for preparing cell for ToF-SIMS include ammonium formate and ammonium acetate, which have been reported to remove salts without compromising the cellular osmosis [154, 273, 274]. MTSs were washed with ammonium formate to determine whether reducing salt suppression improved secondary ion yields whilst the spatial localisation of metabolites was maintained[272]. Prior to analysis, the sections were washed with 0.15 M ammonium formate and desiccated [154]. Washed MTSs were compared to unwashed desiccated MTSs. Analysing biological samples in vacuum can be a challenge in ToF-SIMS. To maintain sample integrity in vacuum MTSs were dried prior to analysis to preserve the localisation of the metabolites (after the removal of salts). The total ion image and spectrum of the unwashed and washed MTS sections are shown in Figure 91 and Figure 92 respectively.

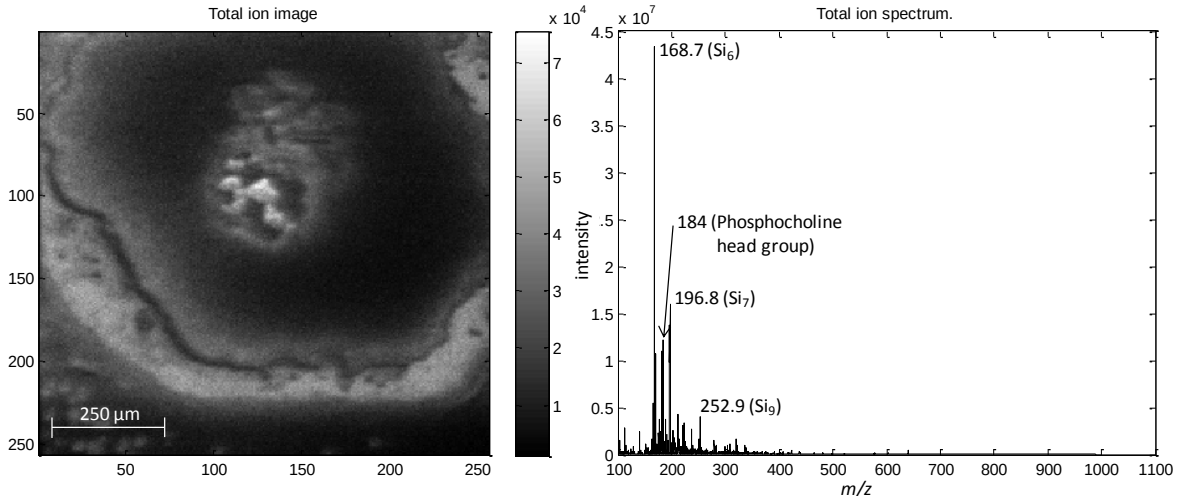

Figure 91: Time-of-flight secondary ion mass spectrometry (ToF-SIMS) data of a multicellular tumour spheroid (MTS) section where (a) is the total ion image and (b) is the total ion spectrum of the unwashed section.

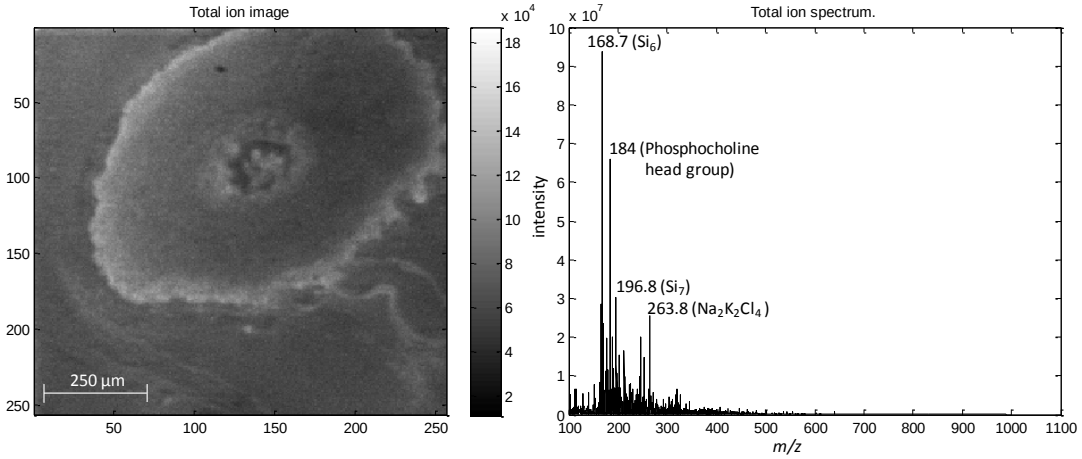

Figure 92: Time-of-flight secondary ion mass spectrometry (ToF-SIMS) data of a multicellular tumour spheroid (MTS) section where (a) is the total ion image and (b) is the total ion spectrum of the ammonium formate washed section.

The most intense peak present in both spectra was a silicon substrate cluster Si_6 (*m/z* 168.7). This silicon cluster was much more intense in the washed MTS section, which may be due to the MTS being slightly smaller revealing more silicon substrate. Furthermore, washing the MTS resulted in the detachment of gelatine (used to embed the MTSs); therefore more silicon substrate was revealed, which may contribute to a more intense silicon peak in the spectra. Additional intense silicon peaks in both spectra included Si_7 (*m/z* 196.6) and Si_9 (*m/z* 252.8) for the unwashed and Si_7 for the washed. The spatial distribution of Si_6, shown in Figure 93, revealed the silicon cluster was localised to the substrate region of the sample and clarifies silicon is present over a greater area in the washed sample.

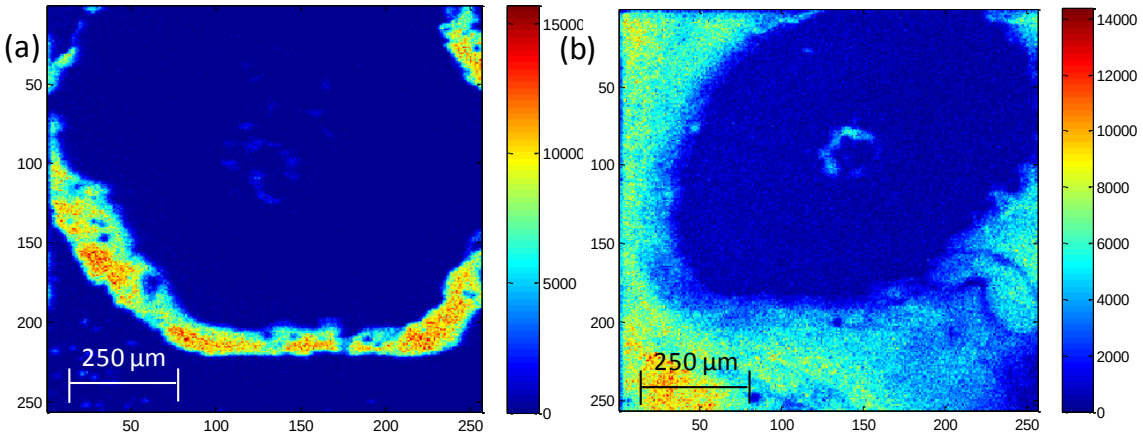

Figure 93: Distribution of silicon *m/z* 168.7 (Si_6) for (a) unwashed and (b) washed for multicellular tumour spheroid (MTS) sections acquired using time-of-flight secondary ion mass spectrometry (ToF-SIMS).

Further exploration of the spectra revealed the washed MTS, which is a smaller of the two MTSs, peak at *m/z* 184 (a phosphocholine head group fragment) was more intense. As the

washed sample was the smaller MTS it would be expected that the biologically related peaks were less intense compared to the bigger unwashed MTS. Furthermore, DAG related fragment (*m/z* 607) was also discovered to be more intense in the washed MTS (Figure 94). Metabolically, DAG is synthesised from dihydroxyacetone phosphate, which is a product of the glycolysis pathway that forms glycerol 3-phosphate. Glycerol 3-phosphate is acylated with acyl-CoA to form lysophosphatidic acid and is subsequently acylated again with acyl-CoA generating phosphatidic acid, which is dephosphorylated to form DAG[208]. This pathway appears to be differentially regulated in low oxygen regions of the MTS. The distribution of DAG for unwashed spheroids was mainly localised in the necrotic inner region of the section (Figure 94a). Similarly, for washed MTS DAG localised in the hypoxic and necrotic inner region of the section (Figure 94b) confirming washing does not redistribute DAG. Results suggest washing MTSs removed salt from the sample reducing the affects of salt suppression whilst the spatial localisation of biological species remained intact.

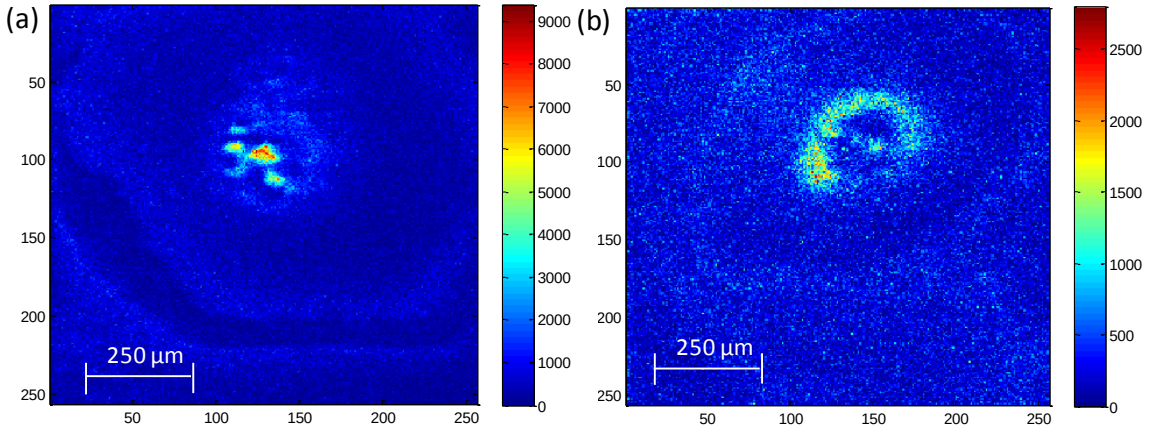

Figure 94: Distribution of diacylglycerol (DAG) *m/z* 607 for (a) unwashed and (b) washed multicellular tumour spheroid (MTS) sections acquired using time-of-flight secondary ion mass spectrometry (ToF-SIMS).

Inspection of the total ion images revealed darker regions relating to the detection of a lower number of ions. This may be caused by sample charging, which has affected the unwashed MTS greater than the washed MTS. Charging is a common issue for ToF-SIMS, and occurs when there are a disproportionate number of primary ions bombarding the surface compared to the number or ions sputtered. Excess positive ions on the sample surface can be compensated for by dosing with low energy electrons onto the surface homogeniously. Washed samples may not have charged to the extent that unwashed samples charged as a consequence of the washing proceedure, which may have improved the ionisation of biological species.

A reason for analysing MTS sections was to determine whether salt suppression was reduced and therefore the ionisation of biological compounds improved. Washing was found to improve the ionisation of biological species such as phosphocholine and DAG. Unexpectedly, an intense salt was present in the washed MTS spectrum. Washing was assumed to remove salt from the sample and therefore intense salt related peaks in the spectra were not expected. An image of a salt peak $Na_2K_2Cl_4$ (*m/z* 263.8) is shown in Figure 95 to localise to the outer region of the washed spheorid. This suggested salt was not completely removed during the washing proceedure and that salt remained on the edge of the sample as residue.

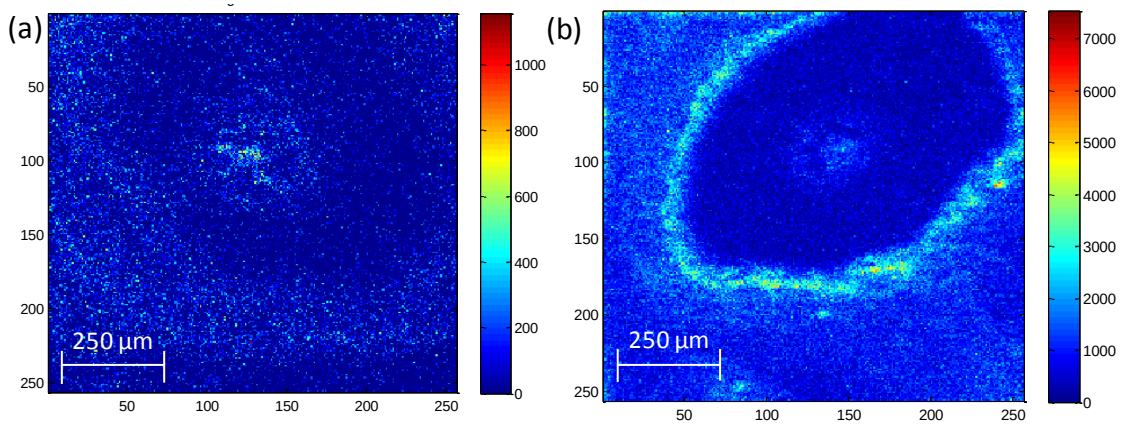

Figure 95: Distribution of salt peak *m/z* 263.8 ($Na_2K_2Cl_4$) for (a) unwashed and (b) washed multicellular tumour spheroid (MTS) sections acquired using time-of-flight secondary ion mass spectrometry (ToF-SIMS).

Overall results suggest washing MTS sections improved the ionisation of biological species with minimal sample redistributed. The intense salt ring around the edge of the MTS suggested more washing was needed to efficiently remove all salt from the substrate surface. To overcome this issue a series of three washes were used to minimise sample charging, and subsequent drying on a rotary spin caster reduced salt depositing around the edge of the MTS (Figure 96b).

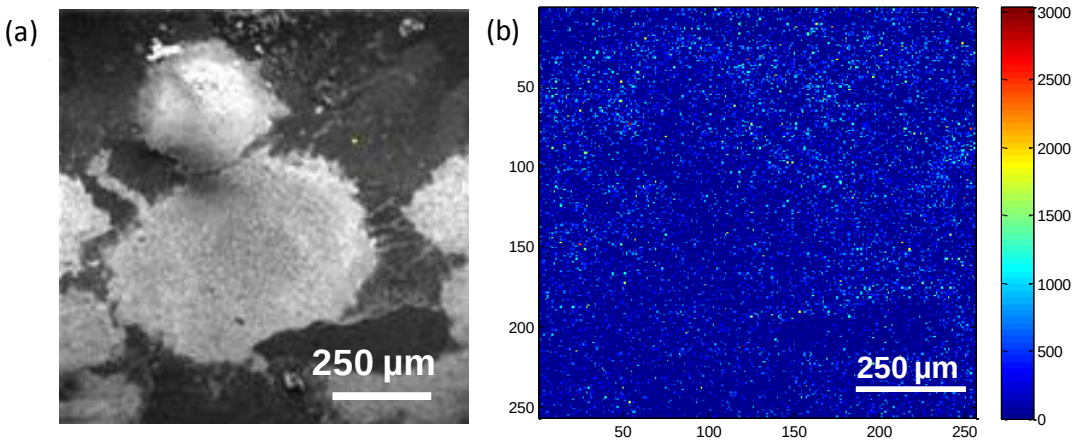

Figure 96: (a) Total ion image of a FaDu multicellular tumour spheroid (MTS) section acquired using time-of-flight secondary ion mass spectrometry (ToF-SIMS). MTS section was treated with 0.1 µM doxorubicin. MTS section received three washes of 0.15 M ammonium formate and dried on a rotary spin caster at 800 rpm (b) localisation of salt related peak *m/z* 263.8.

Furthermore, these spheroids were examined to determine whether metabolites could be spatially localised within specific regions of the MTS. As previously shown, it is possible to localise DAG to specific regions of the MTS. Localisation of metabolites was more challenging potentially due to the concentration of the metabolite available in the sample and ionisation efficiency, which may be lower than for lipids and DAGs. As shown in Figure 97, the individual metabolite fragment peaks of glutamine are present but only a subtle difference between hypoxic and normoxic region is displayed. This could be improved through employing image PCA to identify the patterns in the image relating to the two phenotypes present, high and low oxygen availability, and express these in an image of the two regions.

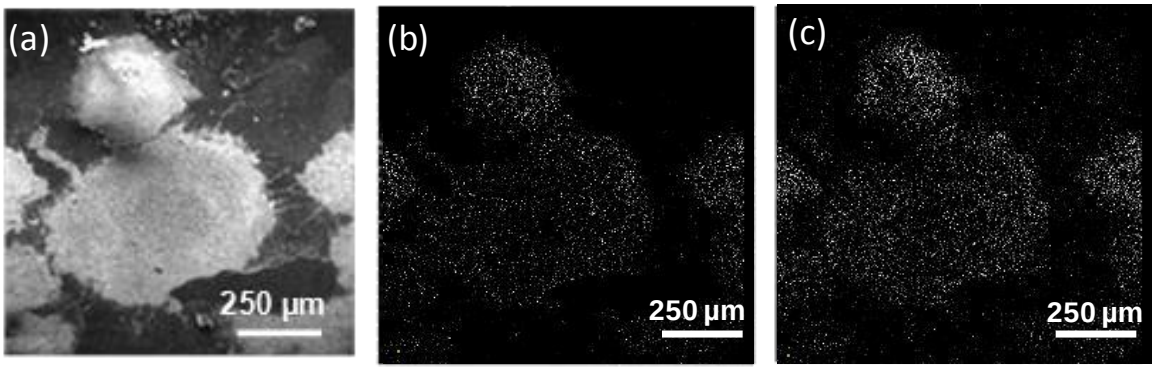

Figure 97: Time-of-flight secondary ion mass spectrometry of a multicellular tumour spheroid (MTS) section (ToF-SIMS) (a) total ion image (b) the distribution of the metabolite glutamine fragment *m/z* 130.05 and (c) the distribution of the metabolite glutamine fragment *m/z* 84.05.

6.2.6 Imaging ToF-SIMS analysis of FaDu MTS to explore the metabolic response to hypoxia-induced chemoresistance in 3D systems

MTSs were studied to determine the underlying metabolic effects contributing to hypoxia-induced chemoresistance. These 3D models mimic the hypoxic environment observed within *in vivo* tumours. MTSs better reflect the *in vivo* tumour microenvironment and therefore coupled with ToF-SIMS imaging it is possible to metabolically phenotype the high and low oxygenated regions. MTSs were prepared from FaDu head and neck carcinoma as MDA-MB-231 single cells did not form spheroids large enough to contain a hypoxic core. Some groups have suggested MDA-MB-231 cells form MTSs with the addition of Matrigel, however the affect of Matrigel on cellular metabolism is unknown, and preliminary experiments failed to generate spheroids large enough to form a hypoxic core[275]. MTSs were cultured until the diameter was ~500µm. As shown in Figure 98, the inner region of the MTS contains a central denser region, which has a limited oxygen supply.

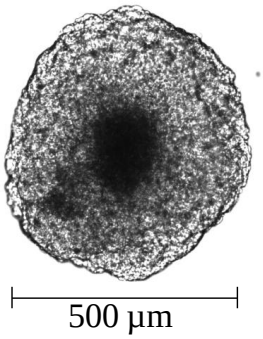

Figure 98: Image of a FaDu multicellular tumour spheroid (MTS) acquired using an Olympus BX51 upright microscope and imaged using a Coolsnap EZ camera.

MTSs received a 24treatment of doxorubicin at doses 0, 0.1 µM or 1 µM. To explore the underlying metabolic response to hypoxia-induced chemoresistance a dose of 0.1 µM doxorubicin, shown in Chapter 3 to inhibit the growth of normoxic cells by ~50 % was used to treat MTS. Furthermore, to explore the mechanisms to overcome hypoxia-induced chemoresistance a higher dose of ~1 µM, shown in Chapter 3 to inhibit the growth of hypoxic cells by ~50 % was used. For each treatment, three biological replicates were acquired and the total ion image of each MTS is shown in Figure 99.

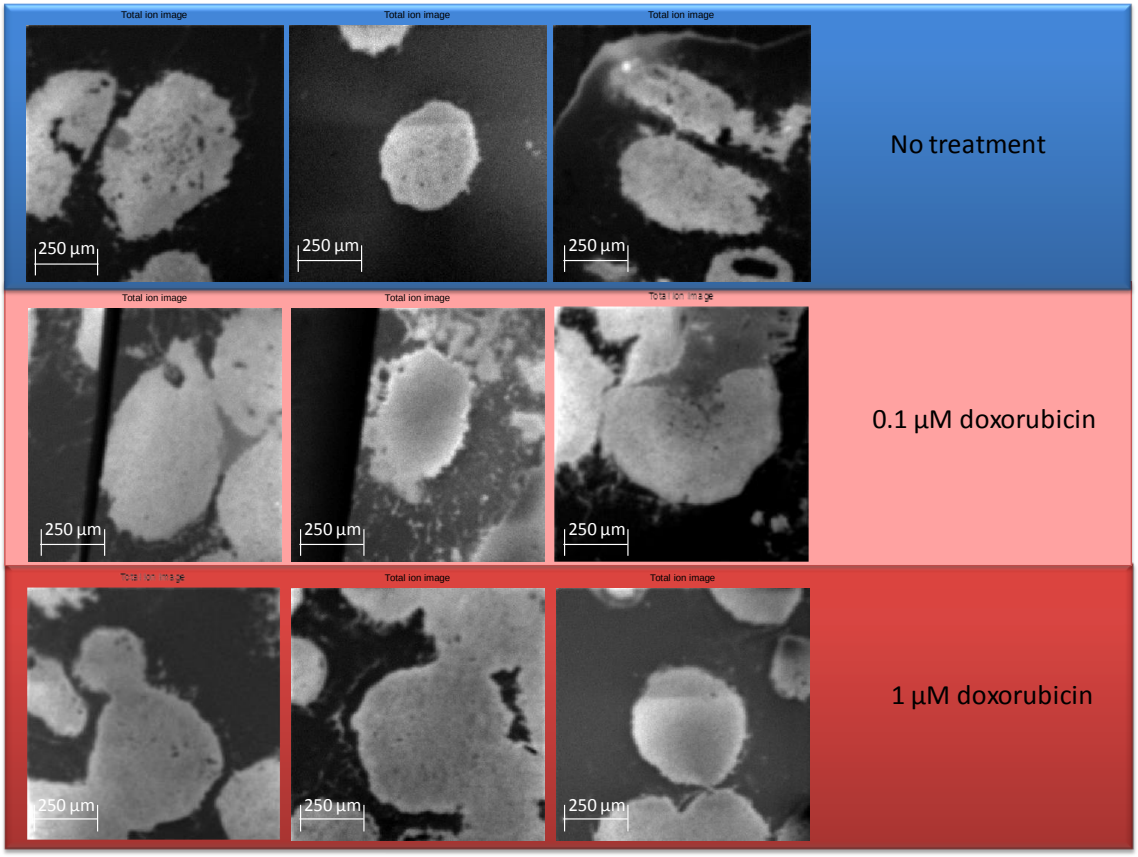

Figure 99: Total ion images of FaDu multicellular tumour spheroid (MTS) sections treated with 0, 0.1 or 1 µM doxorubicin acquired using time-of-flight secondary ion mass spectrometry(ToF-SIMS). Three biological replicates were acquired for each sample type (as shown).

Figure 100 shows the distribution of doxorubicin in MTS following a 24 h exposure of 0, 0.1 or 1 µM. A comparison of the distribution of the molecular ion of doxorubicin (*m/z* 544.25) to an unrelated doxorubicin fragment *m/z* 550.14 suggested the pixels represent background noise for all doses of the drug. This suggests ToF-SIMS spectra of MTS did not include spectral features directly due to doxorubicin, but rather the metabolic differences as a consequence of the action of the drug.

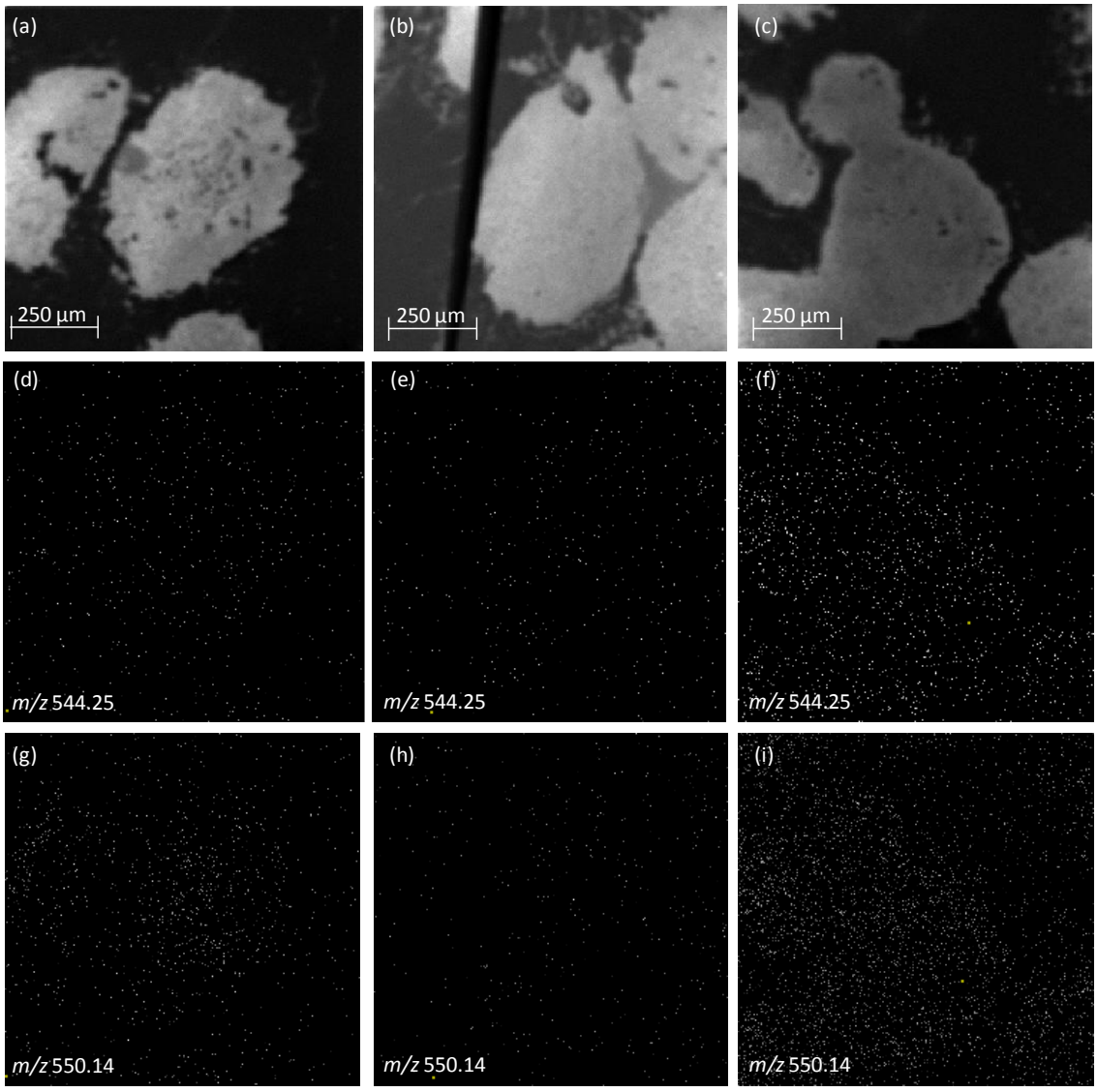

Figure 100: Total ion image of FaDu multicellular tumour spheroid (MTS) sections (a) untreated, (b) treated with 0.1 µM doxorubicin and (c) treated with 1 µM doxorubicin. The distribution of the molecular ion of doxorubicin *m/z* 544.25 for (d) untreated, (e) treated with 0.1 µM doxorubicin and (f) treated with 1 µM doxorubicin. The distribution of an unrelated doxorubicin ion *m/z* 550.14 for (g) untreated, (h) treated with 0.1 µM doxorubicin and (i) treated with 1 µM doxorubicin.

Image PCA was used as a tool to determine the spectral features associated with the hypoxic and normoxic regions of the MTS. As shown in section 6.2.5 metabolite peaks could be imaged and subtle spatial differences were apparent; however image PCA was found to enhance the contrast. Figure 101 shows the scores and loadings plots of the PC that exhibited a difference between the hypoxic inner region and normoxic outer region of the MTS. The loadings plots from each of the three biological replicates were compared to identify whether a fragment was consistently present in all replicates. Only these fragments were considered for metabolite identification.

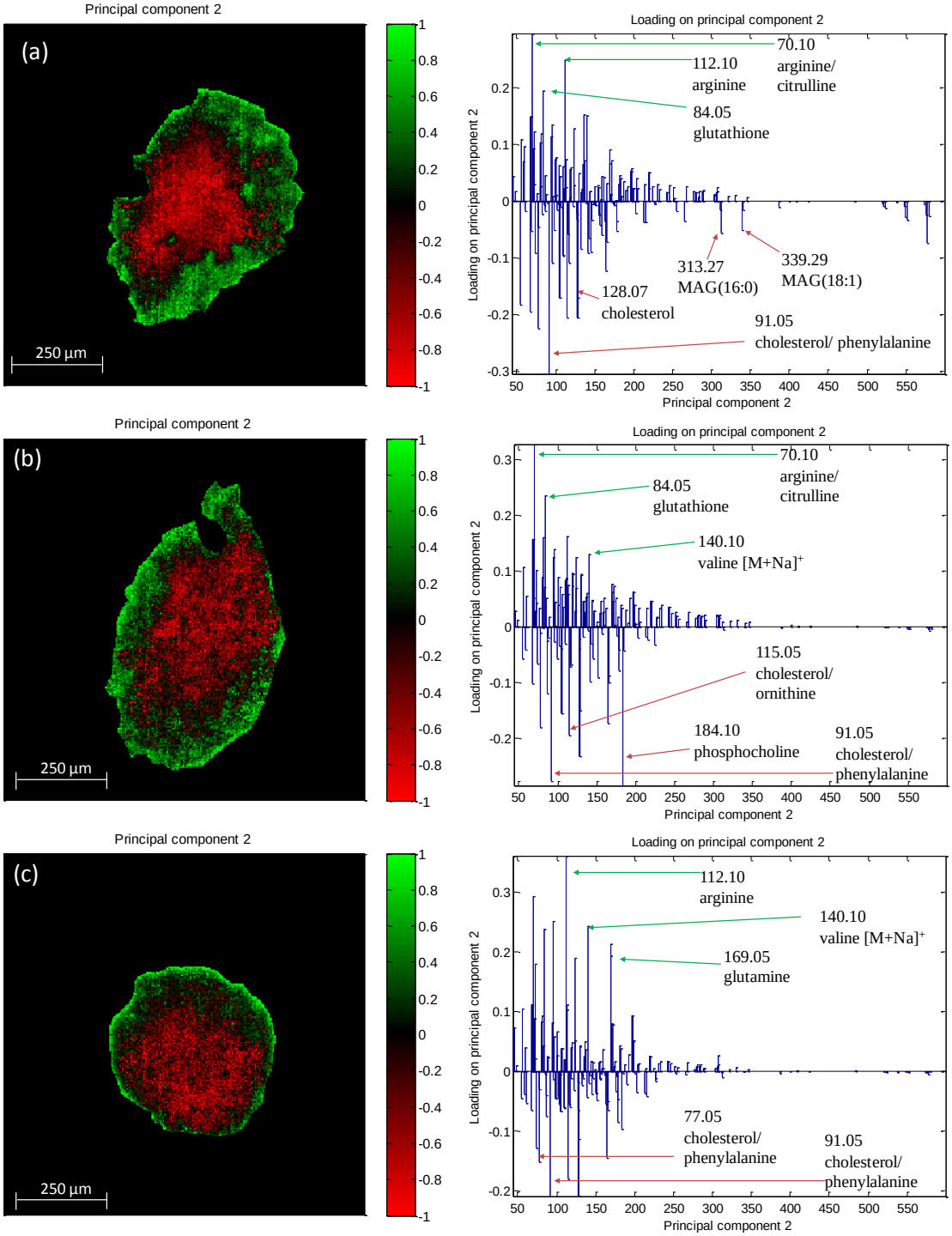

Figure 101: Principal component analysis (PCA) of time-of-flight secondary ion mass spectrometry (ToF-SIMS) data displaying an example of the scores and loadings plot MTS (a) untreated (b) treated with 0.1 µM doxorubicin and (c) treated 1 µM doxorubicin. Percent explained was (a) 34.78 %, (b) 24.49 % and (c) 26.56 %. Intense loadings peaks have been annotated with the *m/z* values and corresponding metabolite.

The loadings were examined to identify metabolites that differ with oxygen tension. Subsequently, drug treated spheroids were examined to identify differences associated with drug treatment. Finally, metabolites that differed exclusively in the lower drug treated MTSs were regarded as resistant features and those differing uniquely in the higher drug treated samples were considered to be the metabolites contributing to overcoming drug resistance.

Metabolites were identified with the criteria that a minimum of 67 % of the fragments, including the molecular ion, must correlate in the same loading direction. Results of the metabolites detected in the three biological replicates for each sample type is shown in Table 27.

Table 27: Metabolites localised in the normoxic and hypoxic region of the multicellular tumour spheroid (MTS) sections when untreated compared to those dosed with 0.1 or 1 µM doxorubicin. N refers to the outer spheroid region and H refers to the inner spheroid region.

Metabolite name	Untreated MTS		MTS + 0.1 µM doxorubicin		MTS + 1 µM doxorubicin		Metabolite response
	N	H	N	H	N	H	
DAG(32:1)				✔		✔	Drug
FA(16:0)			✔		✔		Drug
Glutamine			✔		✔		Drug
Ornithine				✔		✔	Drug
Thiamine			✔		✔		Drug
Thymine			✔		✔		Drug
Tyrosine			✔		✔		Drug
DAG(30:1)		✔					Drug
DAG(36:4)	✔						Drug
MAG(18:1)		✔					Drug
7-ketocholesterol	✔		✔		✔		Oxygen
Adenosine	✔		✔		✔		Oxygen
Arginine	✔		✔		✔		Oxygen
Cholesterol		✔		✔		✔	Oxygen
Citrulline	✔		✔		✔		Oxygen
DAG(32:0)		✔		✔		✔	Oxygen
DAG(34:1)		✔		✔		✔	Oxygen
DAG(34:2)		✔		✔		✔	Oxygen
FA(16:2)	✔		✔		✔		Oxygen
FA(18:1)	✔		✔		✔		Oxygen
FA(18:2)	✔		✔		✔		Oxygen
FA(18:3)	✔		✔		✔		Oxygen
FA(20:4)	✔		✔		✔		Oxygen
Glutathione	✔		✔		✔		Oxygen
Glycerophosphocholine	✔		✔		✔		Oxygen
GSSG	✔		✔		✔		Oxygen
Guanosine	✔		✔		✔		Oxygen
MAG(16:0)		✔		✔		✔	Oxygen
Uracil	✔		✔		✔		Oxygen
Valine	✔		✔		✔		Oxygen
DAG(34:3)		✔				✔	Overcome resistance
PC						✔	Overcome resistance
Citric acid		✔		✔			Drug resistance
Cysteine			✔				Drug resistance
DAG(34:0)		✔		✔			Drug resistance
FA(14:0)			✔				Drug resistance
FA(16:1)			✔				Drug resistance
Glycine			✔				Drug resistance
MAG(16:1)		✔	✔				Drug resistance
Nicotinic acid	✔		✔				Drug resistance
Proline	✔		✔				Drug resistance
Putrescine			✔				Drug resistance
Tryptophan			✔				Drug resistance

Table 27 was explored to find common metabolites that are correlated in the hypoxic or normoxic loading that could be attributed to oxygen availability. Metabolites found to be correlated in the normoxic loading included 7-ketocholesterol, adenosine, arginine, citrulline, fatty acid (FA(16:2)), FA(18:1), FA(18:2), FA(18:3), FA(20:4) glutathione, glycerophosphocholine, GSSG, guanosine, uracil and valine. Those metabolites correlated

in the hypoxic loading included cholesterol, DAG(32:0), DAG(34:1), DAG(34:2) and monoacylglycerol (MAG(16:0)).

Furthermore, Table 27 was examined to revealed common metabolites associated with both 0.1 and 1 µM doxorubicin treatments, which were labelled as drug treatment metabolites (irrespective of the oxygen availability). Metabolites in the normoxic loadings include adenosine, FA(16:0), glutamine, thiamine, thymine and tyrosine and metabolites in the hypoxic loadings were with DAG(32:1) and ornithine. Additionally, metabolites observed only in untreated MTSs were DAG(36:4) in the normoxic loadings and DAG(30:1) and MAG(18:1) in the hypoxic loadings. These metabolites were also assigned as drug related metabolites as the drug caused a biological change causing these metabolites to be absent in the drug treated loadings.

Metabolites associated with hypoxia-induced chemoresistance were indentified through interpreting the loadings for metabolites uniquely present in MTS treated with 0.1 µM doxorubicin. Metabolites in the loadings relating to the normoxic region of drug resistant MTS were cysteine, FA(14:0), FA(16:1), glycine, nicotinic acid, proline, putrescine and tryptophan and hypoxic metabolites were citric acid and DAG(34:0). It was also observed that MAG(16:1) was localised in the hypoxic loadings of the untreated MTSs, however, upon drug treatment this switched and became localised in the normoxic loadings.

Metabolites linked to overcoming hypoxia-induced chemoresistance were interpreted from the loadings of MTS treated with 1 µM doxorubicin. The hypoxic loadings related to overcoming drug resistance contained DAG (34:3) and PC head group.

6.3 Discussion

6.3.1 Metabolite standard spectra

The main objective of this Chapter was to develop ToF-SIMS as a tool to detect metabolites. One of the challenges was to develop the spectral identification of metabolites in ToF-SIMS data. There are many databases available for other mass spectrometry platforms, which are essential for the identification of metabolites in biological samples. For example, the metabolomics study undertaken using GC-MS used two databases to assign metabolites in the data which were the in-house mass spectral and retention index library[132] and the Golm metabolome database mass spectral library[127]. ToF-SIMS would benefit from a metabolite database of standards. To enable the interpretation of metabolites in ToF-SIMS mass spectra, metabolite standard spectra were acquired. Metabolite spectra acquired using ToF-SIMS were compared to LC-ESI-MS^2 spectra in the MassBank database[264]. The metabolite spectra acquired using ToF-SIMS were observed to have a similar fragmentation pattern to the merged LC-ESI-MS^2 spectra. Table 26 contains a column with the fragments common between ToF-SIMS and merged LC-ESI-MS^2. This finding suggested the MassBank database maybe a suitable source for extracting metabolite spectra suitable for interpreting ToF-SIMS. Merged data is an overlay of tandem mass spectra acquired for a metabolite at CID energy ranging from 10-40 eV. This feature is a unique entity of the MassBank database, which makes it the most useful source when compared to other databases currently available. Other databases including Metlin[276] contain tandem mass spectral data at low collision dissociation energy however spectra are not provided in the merged format and therefore all tandem mass spectra for a metabolite would need to be overlaid to interpret ToF-SIMS spectra. This discovery rapidly unlocks metabolite identification of ToF-SIMS data without the need to undertake the time consuming process of acquiring standard spectra for thousands of metabolites. Furthermore, coupling this approach with an algorithm, in a similar approach to the MASCOT algorithm used to identify proteins in tandem MS data[277], may help overcome the difficulties in interpreting ToF-SIMS data. ToF-SIMS tandem mass peaks for each metabolite provided in Table 26 shows no extra fragmentation was acquired in comparison to the ToF-SIMS spectra. It is encouraging that ToF-SIMS alone has enough energy to fragment the ion of interest without the need for tandem mass spectrometry. This was expected and has been previously explained by computational simulation. Simulations describe the primary ion impact to have high energy concentrated to the central area of the crater generating extensive high energy fragmentation, whereas the outer region of the

crater ejects intact molecular molecules[278]. The ejected molecules contain high energy making them likely to fragment further in the vacuum to generate fragmented species similar to that generated in tandem mass spectrometry through CID. This phenomenon has previously been reported for polymeric samples[279]. Tandem mass spectrometry remains to be a useful tool to confirm the presence of an individual metabolite in a complex biological matrix.

6.3.2 Sensitivity and matrix study

Analysis to determine the detection limits of methionine was discovered to be 1 fmol. Munger *et al.* reported the concentration of metabolites in $1.5x10^6$ MRC-5 fibroblast cells was in the nanomolar range for metabolites including citrate, fumarate, malate and pyruvate[280]. Furthermore, Halama *et al.* reported methionine concentration in human cell lines HEK 293, HEK 293, PC3 and MCF7 to be 1.87, 2.53, 1.13 and 1.07 µM respectively for 4 x 105 cells[281]. Thus, the concentration metabolites will vary depending on the number of cells in the lysate, the metabolic activity and size of the cell. Furthermore, this data suggests the sensitivity of the J105 3D chemical imager is within concentrations present in cell lysates. For example, the lowest concentration of methionine detected in the four cell lines (shown in Table 28) was 1.07 µM, which is 1×10^{-6} moles/L suggesting that a detection limit of 1 fmol is adequate to analyse cell lysates. Table 28 shows the comparison of the intracellular concentration of methionine with other metabolites such as alanine, glutamate, phenylalanine and glycine[281].

Table 28: Metabolite concentrations acquired in 4×10^5 cells for four cell lines HEK 293, HepG2, PC3 and MCF7[281].

	Metabolite concentration (µM) in cell lines			
Metabolite	HEK 293	HepG2	PC3	MCF7
Alanine	27.74	24.57	4.11	8.49
Glutamate	29.27	65.86	14.07	22.96
Phenylalanine	3.24	5.59	1.58	1.90
Methionine	1.87	2.53	1.13	1.07
Glycine	42.88	76.60	17.36	20.63

The abundance of methionine is lower than other metabolites reported in the literature[281, 282], which suggests homogeneous standards of metabolites reported in Table 26 would be detected in cell lysates; however the ionisation efficiency must also be considered. The detection of metabolites as a heterogeneous mixture is more complex in SIMS due to the introduction of the matrix effect. GC-MS and LC-MS methods pre-separate the analytes prior to ionisation to overcome the matrix effect.

The ionisation of a metabolite is also influenced by other chemical species present in the sample, which is known as the matrix effect. The matrix effect has been proposed to arise as a result of proton transfer and therefore the $[M+H]^+$ molecular ion intensity and ions forming during gas phase fragmentation will be affected[265]. Although, some small fragments formed through direct fragmentation (as the primary ions impact) are expected to be less sensitive to the matrix effect. Methionine and citric acid were used as an example to show metabolites can influence the ionisation of one another. The metabolite solution was thoroughly mixed to create a homogeneous sample and the whole sample was consumed in the analysis and therefore ionisation differences were attributed exclusively to the matrix effect rather than sample segregation into individual components. Results showed citric acid was suppressed; however there was not a complete loss of the molecular ion or related fragments. Additionally, the extent of suppression or enhancement for all fragments in a species did not occur with the same intensity. For example, the increase in intensity between methionine fragments *m/z* 102.05 and *m/z* 104.05 were very different. Thus, metabolite fragments were used to interpret ToF-SIMS spectra (and not the intensities of the fragment).

6.3.3 Metabolite analysis of MDA-MB-231 cell lysates using ToF-SIMS

Spectra from MDA-MB-231 lysates contained inorganic fragments, some of which were related to salt that is known to cause ion suppression of biological compounds[272]. Ziptips® were explored as a tool to reduce salt in the lysates; however results suggested this also removed the phosphocholine head group (*m/z* 184). Thus, Ziptips® were not useful to prepare lysates for ToF-SIMS analysis. Prior to PCA, all sample spectra were peak picked, using a reference list of peaks of metabolite and lipid fragments, to reduce the intensity of inorganic peaks that can skew MVA. In addition, this pre-processing reduced the large data matrix of raw spectra into a smaller and more manageable set of peaks to ease manual interpretation of the PCA loadings for metabolites and lipids. PCA was used as a tool to reduce the dimensionality of the lysate spectra[172]. PCA is sensitive to data pre-processing and therefore, in this case, data were sum normalised (to account for instrument drift) and square root scaled to minimise the diversity between the most intense peaks from the lesser intense peaks, as low intensity peaks are equally important[172]. The aim of the analysis was to determine whether metabolite similarities for ToF-SIMS and GC-MS associated with the high and low oxygen phenotypes could be recognised. Results were used to determine whether ToF-SIMS was a useful tool for imaging metabolites *in situ*. Of the ToF-SIMS metabolite standard spectra available, glycine, lactic acid, succinic acid, methionine and

valine were previously reported (in Chapter 4) to be low oxygen metabolite markers detected using GC-MS. PCA was used as a tool to simplify chemical interpretation of the spectra through reducing the dimensionality of the dataset and determining peaks that are likely to arise from the same metabolite. Interpretation of the ToF-SIMS loadings, following PCA, revealed glycine, lactic acid and succinic acid to contribute to the hypoxic separation. These three metabolites were all shown to increase in low oxygen samples and therefore would be expected to be in the positive loadings. Methionine, citric acid and valine were not localised to a specific phenotype of low or high oxygen as the metabolite fragments were not consistently in the positive or negative loadings. Since ToF-SIMS does not use a chromatography column to separate the metabolites prior to ionisation, there is overlap of metabolites with similar fragments in ToF-SIMS spectra. For example, methionine fragment (*m/z* 102.05) and a myo-inositol fragment have the same metabolite fragment and thus may not separate consistently in the positive or negative loadings. Advances in instrumentation, such as the development of a C_{60}^+ secondary ion Fourier transform ion cyclotron resonance would improve mass accuracy and thus improve metabolite identification[283]. Metabolite markers of hypoxia discovered using GC-MS were found to have a similar distribution in the loadings plots of PCA of ToF-SIMS data. This cross comparison between platforms suggests ToF-SIMS is able to detect metabolites and that PCA of ToF-SIMS spectra is a suitable tool to determine the spectral differences. Due to the small sample size acquired using ToF-SIMS, DFA was not applicable. This is a limiting factor of ToF-SIMS as the number of samples that can fit onto a sample stub is limited to an area ~3 cm^2 limiting high-throughput analysis of many biological replicates simultaneously. The ability to deposit the sample on the substrate with a smaller diameter may help to overcome this issue, which may be possible through adopting a piezoelectric dispensing system. Overall, analysis suggested ToF-SIMS and PCA are able to show a similar metabolite separation between the high and low oxygenated cells; however common metabolite fragmentation limits the interpretation of PCA loadings of ToF-SIMS datasets.

6.3.4 Investigating hypoxia-induced chemoresistance in FaDu MTS using imaging ToF-SIMS

MTS sections were analysed using ToF-SIMS to investigate the metabolic response of hypoxia-induced chemoresistance *in situ*. ToF-SIMS can be sensitive to sample preparation techniques therefore a washing protocol was developed for MTSs that removed biological salts, whilst preventing the spatial distribution of metabolites. The spatial

distribution of biological compounds was maintained after washing with 0.15 mM ammonium formate and signal intensity was improved. Ammonium formate (0.15 mM) has a balanced pH and osmolarity and has previously been reported as a suitable solution in the preparation of tissue for ToF-SIMS[154, 155, 272]. Drying MTSs on a spin caster was necessary to prevent salt accumulating around the edge of the sample.

The hypoxic region of MTSs generated from the FaDu cell line has been shown to begin approximately 100 µm from the MTS surface as shown in Figure 102[284]. Image PCA was able to identify the hypoxic region and the normoxic region of the MTS sections with and without drug treatment, which is in accordance with literature reports of the location of the hypoxic region for FaDu MTSs[284]. MTSs were treated with ~0.1 or ~1 µM, which were shown in Chapter 3 to be cytotoxic to normoxic and hypoxic FaDu cancer cells respectively. Control MTS remained untreated. Following a 24 h treatment of ~1 µM doxorubicin the MTSs appeared to regress in size compared to the non-treated and ~0.1 µM treated doxorubicin MTSs. This suggests a dose dependent decrease in MTS size, which may be correlated with a decrease in proliferating cells on the outer perimeter[285].

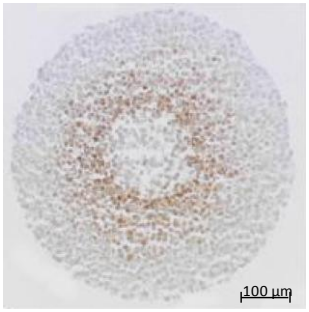

Figure 102: FaDu multicellular tumour spheroid (MTS) section with ~600 µm diameter stained with pimonidazole to show regions of hypoxia (in brown). Pimonidazole binds to thiol-containing proteins, peptides and amino acid markers in hypoxic cells[286]. There is an increase in the intensity towards the centre of the MTS, which diminishes when it reaches the core that has been subjected to necrosis. Image taken from Tupper *et al.*[284].

The aim was to explore the metabolic response of hypoxia-induced chemoresistance in 3D culture systems *in situ*. It is known that doxorubicin poorly penetrates solid tumours decreasing the efficacy of the compound, which cannot be fully understood using *in vitro* cell culture[6]. ToF-SIMS imaging of 3D cultures is a novel tool to study the metabolic response of MTS to low and high doses of doxorubicin *in situ*.

The spheroids were selected from the substrate prior to PCA to minimise skewing the PCA with respect to the silicon surface. Spectra were peak picked prior to image PCA similar to the cell lysates. Data were sum normalised (to account for instrument drift) and square root

scaled to minimise the diversity between the most intense peaks from the lesser intense peaks, as low intensity peaks are equally important[172]. Peak picking the MTS spectra revealed similar results to data that was not peak picked[156]; however more metabolites were identified in the peak picked data through removing inorganic species that can skew PCA.

The metabolic responses were interpreted in the PCA loadings and compared across the drug treatments. Results suggested the metabolic response to drug resistance was mediated by cysteine, FA(14:0), FA(16:1), glycine, MAG(16:1), nicotinic acid, proline, putrescine and tryptophan in the normoxic loadings and citric acid and DAG(34:0) in the hypoxic loading. Glycine has a role in nucleotide and protein synthesis[179] and high levels of glycine in malignant breast cancer tumours has been associated with poor patient prognosis[179]. Cysteine and tryptophan have been suggested to act as an antioxidant, which may reduce the cytotoxic effects of drug induced ROS[72, 242] and thus contributing to drug resistance. Citric acid may be used in the fatty acid synthase pathways as the over expression of fatty acid synthase was associated with chemoresistance in cancer[213]. Furthermore, overcoming doxorubicin resistance was mediated by DAG(34:3) and a PC head group in the hypoxic loading. The response from the inner hypoxic region to overcome resistance may be mediated by a lipid response. Unsaturated fatty acids DAG(34:3) and PC may be indicating lipid peroxidation caused by doxorubicin-induced cytotoxicity[224]. Unsaturated fatty acids have been linked to maintaining membrane fluidity[239], which may allow a greater influx of the drug into the hypoxic region of the MTS, thus increasing cytotoxicity. Furthermore, it was shown in Chapter 4 that this mechanism was also associated with overcoming hypoxia-induced chemoresistance in MDA-MB-231 cells. Thus, increasing levels of unsaturated fatty acids maybe a conserved high drug dose response in solid tumours regardless of the cancer type.

6.4 Conclusion

ToF-SIMS analysis was able to identify a range of metabolites within the spectra of biological samples. Prior to this work, few examples of metabolite detection in ToF-SIMS data were available in the literature[110, 111]. This work has unlocked ToF-SIMS to metabolite analysis in biological systems. ToF-SIMS offers the ability to localise the chemistry of the biological sample *in situ* a capability that other metabolomics platforms such as GC-MS and LC-MS cannot offer. This should enable ToF-SIMS to become a useful tool for both

targeted and untargeted metabolite analysis to localise metabolite markers in biological samples.

ToF-SIMS was shown to be a useful tool to phenotype hypoxic cancer cell lysates, using PCA, with regards to the metabolic response. Additionally, results were comparable with the GC-MS metabolomics study undertaken in Chapter 4. Furthermore, a ToF-SIMS analysis of MTS was able to detect metabolite differences *in situ* when combined with PCA. Image PCA was a useful tool to discriminate between the high and low oxygenated regions of the MTSs and interpreting the loadings revealed the related metabolite patterns contributing to the difference in oxygen availability. In addition, spheroids dosed with 0.1 µM doxorubicin appeared to mediate resistance through upregulating antioxidation mechanisms and increase fatty acid synthesis. Furthermore spheroids dosed with 1 µM doxorubicin overcame resistance as the drug was able to cause lipid peroxidation in the hypoxic region, which may have further increased drug penetration into the hypoxic region.

During the course of metabolite standard analysis it was observed that ToF-SIMS spectra are similar to spectra acquired using LC-ESI-MS^2. This highlights the potential to interpret ToF-SIMS spectra through putitative matching against the molecular ion and related fragmentation pattern from existing metabolite databases. A future development in this area may be to develop computational workflows that would annotate ToF-SIMS spectra using existing metabolomics databases. For example, a Taverna workflow could be employed to merged LC-ESI-MS^2 spectra from existing web-based metabolite databases and further to interpret the loadings of the PCA to determine, which species are present. Furthermore, the workflow could incorporate other useful data processing tools such as the visualisation of metabolite markers within metabolic pathways.

Chapter 7

CONCLUSIONS AND OUTLOOK

7.1 Thesis summary and outlook

The objective of this thesis was to explore the metabolic response of chemotherapy resistance in hypoxic cancer cells and MTSs. This was achieved through studying the metabolome using computational systems biology tools to determine the metabolic network regulation of hypoxia-induced resistance. Many analytical approaches were carried out to generate datasets, which were used to identify metabolite markers and construct metabolic networks to explore the cellular response to hypoxia-induced resistance and to overcome resistance. Network modelling was shown to be an important tool to gain insight into the plethora of interactions a biological system employs in response to a perturbation.

In Chapter 1 an introduction to the thesis was presented reviewing the approach and hypotheses that were studied. The methodology, instrumentation and data processing techniques were described in Chapter 2. Chapter 3 defined key parameters of cell culture that contributed to developing a protocol for metabolomics analysis of large sample numbers. Results from this chapter determined parameters including the appropriate drug dose, cell growth phase and cell seeding density. Furthermore, a preliminary metabolomics study confirmed biomass and metabolite extraction methods used were suitable to detect biological differences between sample types in the intracellular metabolism for four cell passages. In Chapter 4 a large-scale metabolomics study was undertaken using both UHPLC-MS and GC-MS platforms. In this Chapter differences in the metabolome relating to oxygen, low oxygen-induced chemoresistance and overcoming low oxygen-induced chemoresistance responses were elucidated. Statistical analysis and MVA methods were used to identify metabolite markers. This analysis identified novel metabolite markers of hypoxia, hypoxia-induced chemoresistance and overcoming resistance. Results suggested that cancer cells exposed to a low oxygen tension promoted survival through exploiting metabolic pathways including anaerobic respiration, truncation of the TCA cycle, glutaminolysis and autophagy. Doxorubicin treatment in normal oxygen levels suggested three mechanisms of drug action, which included promoting toxicity through lipid peroxidation, targeting N-acetylaspartic acid and decreasing doxorubicin efflux through reducing glutamate uptake. A common pathway of low oxygen induced chemoresistance

was DNA synthesis pathways. Future work could validate the impact of targeting purine and pyrimidine metabolism to overcome low oxygen-induced chemoresistance through generating knockout models. Although metabolic metabolite markers were identified a network-based approach may be more useful to understand fully the relationship between metabolites with respect to the metabolic interactions. Chapter 5 applied network-based correlation analysis to the large-scale GC-MS dataset to generate pair-wise metabolites that differed between sample types. Graph theory was applied to construct metabolic networks of the shortest path connecting correlated metabolites in the EHMN. These networks described the cellular response to low oxygen tensions, drug response in normoxic cells, low oxygen-induced resistance and drug response in low oxygen. This novel method of network-based correlation analysis presented a complementary approach to identifying metabolite markers (in Chapter 4) to determine the topological and dynamic metabolic response. Mechanisms associated with low oxygen metabolism were consistent with existing knowledge however; since not a lot is known about the metabolic regulation of hypoxia-induced chemoresistance, many of the proposed mechanisms discovered were novel. Acquisition of a proteomic dataset may be a future direction of this work to explore the regulatory response with respect to allosteric (metabolic), post-translational and transcriptional regulators. Chapter 6 aimed to develop ToF-SIMS as a tool for metabolite analysis. The mass spectral imaging technique has the ability to localise metabolites within a biological sample, which is a complementary approach to conventional metabolomics platforms. To facilitate metabolite identification in ToF-SIMS, spectra metabolite standards were acquired, which were subsequently used to interpret ToF-SIMS spectra of biological samples. It was observed that ToF-SIMS spectra of metabolites are similar to spectra acquired using LC-ESI-MS^2. This suggests ToF-SIMS spectra could be interpreted using putitative matching against existing metabolite databases. A future development in this area could be to develop computational workflows to annotate ToF-SIMS spectra against existing metabolomics databases. For example, software could be developed to merge LC-ESI-MS^2 spectra from existing web based metabolite databases and use it to interpret the loadings of the PCA. Cell lysates cultured in hypoxic and normoxic conditions identified common metabolite markers in ToF-SIMS and GC-MS datasets. This suggested ToF-SIMS was able to identify metabolites in biological samples. Furthermore, a novel method of preparing and analysing multicellular tumour spheroids was developed to investigate the metabolic response to chemotherapy treatment in the 3D MTSs.

Overall multimodal approaches of metabolite detection in cell biology in combination with a systems biology approach enables a more robust and comprehensive analysis of the system than each of the individual components alone. Developing a method to construct metabolic networks from high-throughput metabolomics datasets unlocked the network-based origin of disease. Furthermore, this novel method can be applied to a multitude of diseases other than tumour hypoxia, which was demonstrated in this thesis. For example, the method could be applied to biological systems, such as the metabolic engineering of yeast. In addition, advances in the spectral interpretation of ToF-SIMS for metabolites will help the technique reach its potential of *in situ* metabolite analysis. This research could be developed further to detect metabolites in single cells enabling the detection of metabolites within an organelle. Thus, metabolite analysis in single cells could be used to study the transformation of a normal cell into a cancer cell and other single cell manipulation studies in areas such as stem cell research and developmental biology.

References

1. Vander Heiden, M.G., Cantley, L.C. & Thompson, C.B. Understanding the Warburg effect: the metabolic requirements of cell proliferation. *Science* **324**, 1029-1033 (2009).
2. Robey, I.F. *et al.* Regulation of the Warburg effect in early-passage breast cancer cells. *Neoplasia* **10**, 745-756 (2008).
3. Strauss, L.G. & Conti, P.S. The applicaitons of PET in clinical oncology. *J. Nucl. Med.* **32**, 623-648 (1991).
4. Bishop, J.M. The molecular-genetics of cancer. *Science* **235**, 305-311 (1987).
5. Tennant, D.A., Duran, R.V. & Gottlieb, E. Targeting metabolic transformation for cancer therapy. *Nat Rev Cancer* **10**, 267-277 (2010).
6. Minchinton, A.I. & Tannock, I.F. Drug penetration in solid tumours. *Nat Rev Cancer* **6**, 583-592 (2006).
7. Brown, J.M. Exploiting the hypoxic cancer cell: mechanisms and therapeutic strategies. *Mol. Med. Today* **6**, 157-162 (2000).
8. Brown, L.M. *et al.* Reversing Hypoxic Cell Chemoresistance in Vitro Using Genetic and Small Molecule Approaches Targeting Hypoxia Inducible Factor-1. *Mol. Pharmacol.* **69**, 411-418 (2006).
9. Sullivan, R. & Graham, C.H. Hypoxia prevents etoposide-induced DNA damage in cancer cells through a mechanism involving hypoxia-inducible factor 1. *Mol. Cancer Ther.* **8**, 1702-1713 (2009).
10. Sullivan, R., Pare, G.C., Frederiksen, L.J., Semenza, G.L. & Graham, C.H. Hypoxia-induced resistance to anticancer drugs is associated with decreased senescence and requires hypoxia-inducible factor-1 activity. *Mol. Cancer Ther.* **7**, 1961-1973 (2008).
11. Wartenberg, M. *et al.* Regulation of the multidrug resistance transporter P-glycoprotein in multicellular tumor spheroids by hypoxia-inducible factor-1 and reactive oxygen species. *FASEB J.*, 02-0358fje (2003).
12. Tredan, O., Galmarini, C.M., Patel, K. & Tannock, I.F. Drug Resistance and the Solid Tumor Microenvironment. *J. Natl. Cancer Inst.* **99**, 1441-1454 (2007).
13. Semenza, G.L. & Wang, G.L. A nuclear factor induced by hypoxia via de novo protein synthesis binds to the human erythropoietin gene enhancer at a site required for transcriptional activation. *Mol. Cell. Biol.* **12**, 5447-5454 (1992).
14. Bertout, J.A., Patel, S.A. & Simon, M.C. The impact of O2 availability on human cancer. *Nat Rev Cancer* **8**, 967-975 (2008).
15. Maxwell, P.H. *et al.* The tumour suppressor protein VHL targets hypoxia-inducible factors for oxygen-dependent proteolysis. *Nature* **399**, 271-275 (1999).
16. Pelengaris, S. & Khan, M. *The Molecular Biology of Cancer*. (Blackwell Pub., 2006).
17. Powis, G. & Prough, R.A. *Metabolism and action of anti-cancer drugs*. (Taylor & Francis, London, New York and Philadelphia; 1987).
18. Mayer, L.D., Bally, M.B. & Cullis, P.R. Uptake of adriamycin into large unilamellar vesicles in response to a pH gradient. *Biochim. Biophys. Acta* **857**, 123-126 (1986).
19. Gewirtz, D.A. A critical evaluation of the mechanisms of action proposed for the antitumor effects of the anthracycline antibiotics adriamycin and daunorubicin. *Biochem. Pharmacol.* **57**, 727-741 (1999).
20. Fornari, F.A., Randolph, J.K., Yalowich, J.C., Ritke, M.K. & Gewirtz, D.A. Interference by doxorubicin with DNA unwinding in MCF-7 breast tumor cells. *Mol. Pharmacol.* **45**, 649-656 (1994).

21. Scheulen, M.E., Kappus, H., Nienhaus, A. & Schmidt, C.G. Covalent protein-binding of reactive adriamycin metabolites in rat-liver and rat-heart microsomes. *J. Cancer Res. Clin. Oncol.* **103**, 39-48 (1982).
22. Ferrari, E., Taillan, B., Dujardin, P. & Morand, P. Cardiotoxicity of anthracyclines - clinical-features, incidence, monitoring. *Presse Med.* **22**, 999-1004 (1993).
23. Vaupel, P., Thews, O. & Hoeckel, M. Treatment resistance of solid tumors - Role of hypoxia and anemia. *Med. Oncol.* **18**, 243-259 (2001).
24. Tredan, O., Galmarini, C.M., Patel, K. & Tannock, I.F. Drug resistance and the solid tumor microenvironment. *J. Natl. Cancer Inst.* **99**, 1441-1454 (2007).
25. Zolzer, F. & Streffer, C. Increased radiosensitivity with chronic hypoxia in four human tumor cell lines. *International Journal of Radiation Oncology*Biology*Physics* **54**, 910-920 (2002).
26. Amellem, O. & Pettersen, E.O. Cell inactivation and cell-cycle inhibition as induced by extreme hypoxia - the possible role of cell-cycle arrest as a protection against hypoxia-induced lethal damage. *Cell Prolif.* **24**, 127-141 (1991).
27. Koshiji, M. *et al.* HIF-1[alpha] induces cell cycle arrest by functionally counteracting Myc. *EMBO J.* **23**, 1949-1956 (2004).
28. Brown, J.M. The Hypoxic Cell. *Cancer Res.* **59**, 5863-5870 (1999).
29. Mellor, H.R. & Callaghan, R. Accumulation and distribution of doxorubicin in tumour spheroids: the influence of acidity and expression of P-glycoprotein. *Cancer Chemother. Pharmacol.* **68**, 1179-1190 (2011).
30. Goode, J.A. & Chadwick, D.J. *pH, Hypoxia and Metastasis*. (John Wiley & Sons, Ltd, New York; 2008).
31. Le Floch, R. *et al.* CD147 subunit of lactate/H+ symporters MCT1 and hypoxia-inducible MCT4 is critical for energetics and growth of glycolytic tumors. *Proc. Natl. Acad. Sci. U. S. A.* **108**, 16663-16668 (2011).
32. Tomiyama, A. *et al.* Critical Role for Mitochondrial Oxidative Phosphorylation in the Activation of Tumor Suppressors Bax and Bak. *J. Natl. Cancer Inst.* **98**, 1462-1473 (2006).
33. Olivier, F. Pyruvate into lactate and back: From the Warburg effect to symbiotic energy fuel exchange in cancer cells. *Radiother. Oncol.* **92**, 329-333 (2009).
34. Chiche, J. *et al.* Hypoxia-Inducible Carbonic Anhydrase IX and XII Promote Tumor Cell Growth by Counteracting Acidosis through the Regulation of the Intracellular pH. *Cancer Res.* **69**, 358-368 (2009).
35. Koukourakis, M.I. *et al.* Hypoxia-regulated Carbonic Anhydrase-9 (CA9) Relates to Poor Vascularization and Resistance of Squamous Cell Head and Neck Cancer to Chemoradiotherapy. *Clin. Cancer. Res.* **7**, 3399-3403 (2001).
36. Swietach, P., Hulikova, A., Patiar, S., Vaughan-Jones, R.D. & Harris, A.L. Importance of Intracellular pH in Determining the Uptake and Efficacy of the Weakly Basic Chemotherapeutic Drug, Doxorubicin. *Plos One* **7**, e35949 (2012).
37. Raghunand, N., Mahoney, B.P. & Gillies, R.J. Tumor acidity, ion trapping and chemotherapeutics: II. pH-dependent partition coefficients predict importance of ion trapping on pharmacokinetics of weakly basic chemotherapeutic agents. *Biochem. Pharmacol.* **66**, 1219-1229 (2003).
38. Lu, C.-W., Lin, S.-C., Chen, K.-F., Lai, Y.-Y. & Tsai, S.-J. Induction of Pyruvate Dehydrogenase Kinase-3 by Hypoxia-inducible Factor-1 Promotes Metabolic Switch and Drug Resistance. *J. Biol. Chem.* **283**, 28106-28114 (2008).
39. Comerford, K.M. *et al.* Hypoxia-inducible Factor-1-dependent Regulation of the Multidrug Resistance (MDR1) Gene. *Cancer Res.* **62**, 3387-3394 (2002).
40. Juliano, R.L. & Ling, V. A surface glycoprotein modulating drug permeability in Chinese hamster ovary cell mutants. *Biochim. Biophys. Acta* **455**, 152-162 (1976).

41. Ueda, K., Cardarelli, C., Gottesman, M.M. & Pastan, I. Expression of a full-length cDNA for the human "MDR1" gene confers resistance to colchicine, doxorubicin, and vinblastine. *Proc. Natl. Acad. Sci. U. S. A.* **84**, 3004-3008 (1987).
42. Aller, S.G. *et al.* Structure of P-Glycoprotein Reveals a Molecular Basis for Poly-Specific Drug Binding. *Science* **323**, 1718-1722 (2009).
43. Sharom, F.J. ABC multidrug transporters: structure, function and role in chemoresistance. *Pharmacogenomics* **9**, 105-127 (2008).
44. Wartenberg, M. *et al.* Down-regulation of intrinsic P-glycoprotein expression in multicellular prostate tumor spheroids by reactive oxygen species. *J. Biol. Chem.* **276**, 17420-17428 (2001).
45. Wartenberg, M. *et al.* Regulation of the multidrug resistance transporter P-glycoprotein in multicellular prostate tumor spheroids by hyperthermia and reactive oxygen species. *Int. J. Cancer* **113**, 229-240 (2005).
46. Gottesman, M.M., Fojo, T. & Bates, S.E. Multidrug resistance in cancer: role of ATP-dependent transporters. *Nat Rev Cancer* **2**, 48-58 (2002).
47. Ogiso, Y., Tomida, A., Lei, S., Oura, S. & Tsuruo, T. Proteasome Inhibition Circumvents Solid Tumor Resistance to Topoisomerase II-directed Drugs. *Cancer Res.* **60**, 2429-2434 (2000).
48. Kang, Y., Greaves, B. & Perry, R.R. Effect of acute and chronic intermittent hypoxia on DNA topoisomerase alpha expression and mitomycin C-Induced DNA damage and cytotoxicity in human colon cancer cells. *Biochem. Pharmacol.* **52**, 669-676 (1996).
49. Wouters, B.G. *et al.* Hypoxia as a target for combined modality treatments. *Eur. J. Cancer* **38**, 240-257 (2002).
50. McKeown, S.R., Cowen, R.L. & Williams, K.J. Bioreductive Drugs: from Concept to Clinic. *Clin. Oncol.* **19**, 427-442 (2007).
51. Rockwell, S., Kennedy, K.A. & Sartorelli, A.C. Mitomycin-C as a prototype bioreductive alkylating agent: In vitro studies of metabolism and cytotoxicity. *International Journal of Radiation Oncology*Biology*Physics* **8**, 753-755 (1982).
52. Zeman, E.M., Brown, J.M., Lemmon, M.J., Hirst, V.K. & Lee, W.W. SR-4233: A new bioreductive agent with high selective toxicity for hypoxic mammalian cells. *International Journal of Radiation Oncology*Biology*Physics* **12**, 1239-1242 (1986).
53. Brown, J.M. & Lemmon, M.J. Potentiation by the hypoxic cytotoxin SR 4233 of cell killing produced by fractionated irradiation of mouse tumors. *Cancer Res.* **50**, 7745-7749 (1990).
54. Rischin, D. *et al.* Tirapazamine, Cisplatin, and Radiation Versus Cisplatin and Radiation for Advanced Squamous Cell Carcinoma of the Head and Neck (TROG 02.02, HeadSTART): A Phase III Trial of the Trans-Tasman Radiation Oncology Group. *J. Clin. Oncol.* **28**, 2989-2995 (2010).
55. Patterson, L.H. Rationale for the use of aliphatic N-oxides of cytotoxic anthraquinones as prodrug DNA binding agents: A new class of bioreductive agent. *Cancer Metastasis Rev.* **12**, 119-134 (1993).
56. McKeown, S.R., Hejmadi, M.V., McIntyre, I.A., McAleer, J.J.A. & Patterson, L.H. AQ4N: An alkylaminoanthraquinone N-oxide showing bioreductive potential and positive interaction with radiation in vivo. *Br. J. Cancer* **72**, 76-81 (1995).
57. Oliver, S.G., Winson, M.K., Kell, D.B. & Baganz, F. Systematic functional analysis of the yeast genome. *Trends Biotechnol.* **16**, 373-378 (1998).
58. Kell, D.B. *et al.* Metabolic footprinting and systems biology: the medium is the message. *Nat Rev Micro* **3**, 557-565 (2005).

59. Nielsen, J. & Jewett, M. The role of metabolomics in systems biology, in *Metabolomics*, Vol. 18. (eds. J. Nielsen & M. Jewett) 1-10 (Springer, Berlin / Heidelberg; 2007).
60. Dunn, W.B. & Ellis, D.I. Metabolomics: Current analytical platforms and methodologies. *TrAC, Trends Anal. Chem.* **24**, 285-294 (2005).
61. Hollywood, K., Brison, D.R. & Goodacre, R. Metabolomics: Current technologies and future trends. *Proteomics* **6**, 4716-4723 (2006).
62. Ma, Y.L., Zhang, P., Yang, Y.Z., Wang, F. & Qin, H.L. Metabolomics in the fields of oncology: a review of recent research. *Mol. Biol. Rep.* **39**, 7505-7511 (2012).
63. Fernie, A.R., Trethewey, R.N., Krotzky, A.J. & Willmitzer, L. Innovation - Metabolite profiling: from diagnostics to systems biology. *Nature Reviews Molecular Cell Biology* **5**, 763-769 (2004).
64. Wishart, D.S. *et al.* HMDB: the Human Metabolome Database. *Nucleic Acids Res.* **35**, D521-D526 (2007).
65. Denkert, C. *et al.* Mass Spectrometry-Based Metabolic Profiling Reveals Different Metabolite Patterns in Invasive Ovarian Carcinomas and Ovarian Borderline Tumors. *Cancer Res.* **66**, 10795-10804 (2006).
66. Sreekumar, A. *et al.* Metabolomic profiles delineate potential role for sarcosine in prostate cancer progression. *Nature* **457**, 910-914 (2009).
67. Kind, T., Tolstikov, V., Fiehn, O. & Weiss, R.H. A comprehensive urinary metabolomic approach for identifying kidney cancer. *Anal. Biochem.* **363**, 185-195 (2007).
68. Bathen, T. *et al.* MR-determined metabolic phenotype of breast cancer in prediction of lymphatic spread, grade, and hormone status. *Breast Cancer Res Treat.* **104**, 181-189 (2007).
69. Troy, H. *et al.* Metabolic profiling of hypoxia-inducible factor-1β-deficient and wild type Hepa-1 cells: effects of hypoxia measured by 1H magnetic resonance spectroscopy. *Metabolomics* **1**, 293-303 (2005).
70. Frezza, C. *et al.* Metabolic Profiling of Hypoxic Cells Revealed a Catabolic Signature Required for Cell Survival. *Plos One* **6**, e24411 (2011).
71. Sterin, M., Cohen, J.S., Mardor, Y., Berman, E. & Ringel, I. Levels of Phospholipid Metabolites in Breast Cancer Cells Treated with Antimitotic Drugs: A 31P-Magnetic Resonance Spectroscopy Study. *Cancer Res.* **61**, 7536-7543 (2001).
72. Wang, J.S. *et al.* Systems toxicology study of doxorubicin on rats using ultra performance liquid chromatography coupled with mass spectrometry based metabolomics. *Metabolomics* **5**, 407-418 (2009).
73. Stephanopoulos, G. & Rigoutos, I. *Systems Biology: Volume II: Networks, Models, and Applications*. (Oxford University Press US, 2007).
74. Hudis, C.A. Trastuzumab - Mechanism of Action and Use in Clinical Practice. *New Engl. J. Med.* **357**, 39-51 (2007).
75. Nesterenko, V.V., Zygmunt, A.C., Rajamani, S., Belardinelli, L. & Antzelevitch, C. Mechanisms of atrial-selective block of Na+ channels by ranolazine: II. Insights from a mathematical model. *Am J Physiol Heart Circ Physiol.* **301**, H1615-H1624 (2011).
76. Stelling, J. Mathematical models in microbial systems biology. *Curr. Opin. Microbiol.* **7**, 513-518 (2004).
77. Taylor, I.W. *et al.* Dynamic modularity in protein interaction networks predicts breast cancer outcome. *Nat Biotech* **27**, 199-204 (2009).
78. Smallbone, K. & Simeonidis, E. Flux balance analysis: A geometric perspective. *J. Theor. Biol.* **258**, 311-315 (2009).

79. Bas, T. *et al.* Can yeast glycolysis be understood in terms of in vitro kinetics of the constituent enzymes? Testing biochemistry. *Eur. J. Biochem.* **267**, 5313-5329 (2000).
80. Herrgard, M.J. *et al.* A consensus yeast metabolic network reconstruction obtained from a community approach to systems biology. *Nat Biotech* **26**, 1155-1160 (2008).
81. Orth, J.D. *et al.* A comprehensive genome-scale reconstruction of Escherichia coli metabolism--2011. *Mol Syst Biol* **7**, 535 (2011).
82. Çalik, P. & Akbay, A. Mass flux balance-based model and metabolic flux analysis for collagen synthesis in the fibrogenesis process of human liver. *Med. Hypotheses* **55**, 5-14 (2000).
83. Kashif, S., Jochen, F. & Lars, K.N. Modeling hybridoma cell metabolism using a generic genome-scale metabolic model of Mus musculus. *Biotechnol. Progr.* **21**, 112-121 (2005).
84. Ma, H.W. *et al.* The Edinburgh human metabolic network reconstruction and its functional analysis. *Mol Syst Biol* **3**, 8 (2007).
85. Duarte, N.C. *et al.* Global reconstruction of the human metabolic network based on genomic and bibliomic data. *Proc. Natl. Acad. Sci. U. S. A.* **104**, 1777-1782 (2007).
86. Hao, T., Ma, H.-W., Zhao, X.-M. & Goryanin, I. Compartmentalization of the Edinburgh Human Metabolic Network. *BMC Bioinformatics* **11**, 393 (2010).
87. Ma, H. & Goryanin, I. Human metabolic network reconstruction and its impact on drug discovery and development. *Drug Discov Today.* **13**, 402 - 408 (2008).
88. Shlomi, T., Benyamini, T., Gottlieb, E., Sharan, R. & Ruppin, E. Genome-Scale Metabolic Modeling Elucidates the Role of Proliferative Adaptation in Causing the Warburg Effect. *PLoS Comp. Biol.* **7**, e1002018 (2011).
89. Li, L., Zhou, X., Ching, W.-K. & Wang, P. Predicting enzyme targets for cancer drugs by profiling human Metabolic reactions in NCI-60 cell lines. *BMC Bioinformatics* **11**, 501 (2010).
90. Shlomi, T., Cabili, M.N., Herrgard, M.J., Palsson, B.O. & Ruppin, E. Network-based prediction of human tissue-specific metabolism. *Nat Biotech* **26**, 1003 - 1010 (2008).
91. Folger, O. *et al.* Predicting selective drug targets in cancer through metabolic networks. *Mol Syst Biol* **7**, 501 (2011).
92. Frezza, C. *et al.* Haem oxygenase is synthetically lethal with the tumour suppressor fumarate hydratase. *Nature* **477**, 225-228 (2011).
93. Camacho, D., de la Fuente, A. & Mendes, P. The origin of correlations in metabolomics data. *Metabolomics* **1**, 53-63 (2005).
94. Steuer, R. Review: On the analysis and interpretation of correlations in metabolomic data. *Brief Bioinform* **7**, 151-158 (2006).
95. Steuer, R., Kurths, J., Fiehn, O. & Weckwerth, W. Observing and interpreting correlations in metabolomic networks. *Bioinformatics* **19**, 1019-1026 (2003).
96. Morgenthal, K., Weckwerth, W. & Steuer, R. Metabolomic networks in plants: Transitions from pattern recognition to biological interpretation. *BioSyst.* **83**, 108-117 (2006).
97. Valcárcel, B. *et al.* A Differential Network Approach to Exploring Differences between Biological States: An Application to Prediabetes. *Plos One* **6**, e24702 (2011).
98. Fukushima, A., Kusano, M., Redestig, H., Arita, M. & Saito, K. Metabolomic correlation-network modules in Arabidopsis based on a graph-clustering approach. *BMC Syst Biol.* **5**, 1 (2011).
99. Vickerman, J.C., Oakes, A. & Gamble, H. Static SIMS studies of catalyst structure and activity. *Surf. Interface Anal.* **29**, 349-361 (2000).

100. Benninghoven, A. Untersuchungen zum Spektrum und den Anfangsenergien negativer Sekundärionen. *Zeitschrift für Physik A Hadrons and Nuclei* **199**, 141-156 (1967).
101. Wong, S.C.C. *et al.* Development of a C60+ ion gun for static SIMS and chemical imaging. *Appl. Surf. Sci.* **203-204**, 219-222 (2003).
102. Ryan, K.E., Wojciechowski, I.A. & Garrison, B.J. Reaction Dynamics Following keV Cluster Bombardment. *The Journal of Physical Chemistry C* **111**, 12822-12826 (2007).
103. Postawa, Z. *et al.* Microscopic Insights into the Sputtering of Ag{111} Induced by C60 and Ga Bombardment. *The Journal of Physical Chemistry B* **108**, 7831-7838 (2004).
104. Gillen, G. *et al.* Depth profiling using C60+ SIMS—Deposition and topography development during bombardment of silicon. *Appl. Surf. Sci.* **252**, 6521-6525 (2006).
105. Ostrowski, S.G., Van Bell, C.T., Winograd, N. & Ewing, A.G. Mass spectrometric imaging of highly curved membranes during Tetrahymena mating. *Science* **305**, 71-73 (2004).
106. Kleinfeld, A., Kampf, J. & Lechene, C. Transport of 13C-oleate in adipocytes measured using multi imaging mass spectrometry. *J. Am. Soc. Mass. Spectrom.* **15**, 1572-1580 (2004).
107. Fletcher, J.S., Lockyer, N.P., Vaidyanathan, S. & Vickerman, J.C. TOF-SIMS 3D Biomolecular Imaging of Xenopus laevis Oocytes Using Buckminsterfullerene (C60) Primary Ions. *Anal. Chem.* **79**, 2199-2206 (2007).
108. Fletcher, J.S., Lockyer, N.P. & Vickerman, J.C. Molecular SIMS imaging; spatial resolution and molecular sensitivity: have we reached the end of the road? Is there light at the end of the tunnel? *Surf. Interface Anal.* **43**, 253-256 (2011).
109. Mas, S. *et al.* Lipid cartography of atherosclerotic plaque by cluster-TOF-SIMS imaging. *Analyst* **132**, 24-26 (2007).
110. Touboul, D. *et al.* MALDI-TOF and cluster-TOF-SIMS imaging of Fabry disease biomarkers. *Int. J. Mass spectrom.* **260**, 158-165 (2007).
111. Kulp, K.S. *et al.* Chemical and biological differentiation of three human breast cancer cell types using time-of-flight secondary ion mass spectrometry. *Anal. Chem.* **78**, 3651-3658 (2006).
112. Baker, M.J. *et al.* Discrimination of prostate cancer cells and non-malignant cells using secondary ion mass spectrometry. *Analyst* **133**, 175-179 (2008).
113. Urquhart, A.J. *et al.* TOF-SIMS Analysis of a 576 Micropatterned Copolymer Array To Reveal Surface Moieties That Control Wettability. *Anal. Chem.* **80**, 135-142 (2007).
114. Fletcher, J.S., Rabbani, S., Henderson, A., Lockyer, N.P. & Vickerman, J.C. Three-dimensional mass spectral imaging of HeLa-M cells – sample preparation, data interpretation and visualisation. *Rapid Commun. Mass Spectrom.* **25**, 925-932 (2011).
115. Chandra, S. & Lorey Ii, D.R. SIMS ion microscopy imaging of boronophenylalanine (BPA) and 13C15N-labeled phenylalanine in human glioblastoma cells: Relevance of subcellular scale observations to BPA-mediated boron neutron capture therapy of cancer. *Int. J. Mass spectrom.* **260**, 90-101 (2007).
116. Colliver, T.L. *et al.* Atomic and Molecular Imaging at the Single-Cell Level with TOF-SIMS. *Anal. Chem.* **69**, 2225-2231 (1997).
117. Mosmann, T. Rapid colorimetric assay for cellular growth and survival: Application to proliferation and cytotoxicity assays. *J. Immunol. Methods* **65**, 55-63 (1983).

118. Cowen, R.L. *et al.* Hypoxia Targeted Gene Therapy to Increase the Efficacy of Tirapazamine as an Adjuvant to Radiotherapy. *Cancer Res.* **64**, 1396-1402 (2004).
119. Bondar, R.J.L. & Mead, D.C. Evaluation of Glucose-6-Phosphate Dehydrogenase from Leuconostoc mesenteroides in the Hexokinase Method for Determining Glucose in Serum. *Clin. Chem.* **20**, 586-590 (1974).
120. Cattaneo, M.V. & Luong, J.H.T. Monitoring glutamine in animal cell cultures using a chemiluminescence fiber optic biosensor. *Biotechnol. Bioeng.* **41**, 659-665 (1993).
121. Barham, D. & Trinder, P. An improved colour reagent for the determination of blood glucose by the oxidase system. *Analyst* **97**, 142-145 (1972).
122. Teng, Q., Huang, W., Collette, T., Ekman, D. & Tan, C. A direct cell quenching method for cell-culture based metabolomics. *Metabolomics* **5**, 199-208 (2009).
123. Saito, K. & Matsuda, F. Metabolomics for Functional Genomics, Systems Biology, and Biotechnology. *Annu. Rev. Plant Biol.* **61**, 463-489 (2010).
124. Halket, J.M. *et al.* Chemical derivatization and mass spectral libraries in metabolic profiling by GC/MS and LC/MS/MS. *J. Exp. Bot.* **56**, 219-243 (2005).
125. Harris, D.C. *Quantitative Chemical Analysis, Sixth Edition*. (W. H. Freeman, 2002).
126. Want, E.J., Nordstrom, A., Morita, H. & Siuzdak, G. From Exogenous to Endogenous: The Inevitable Imprint of Mass Spectrometry in Metabolomics. *Journal of Proteome Research* **6**, 459-468 (2006).
127. Begley, P. *et al.* Development and Performance of a Gas Chromatography−Time-of-Flight Mass Spectrometry Analysis for Large-Scale Nontargeted Metabolomic Studies of Human Serum. *Anal. Chem.* **81**, 7038-7046 (2009).
128. Fiehn, O. *et al.* Metabolite profiling for plant functional genomics. *Nat. Biotechnol.* **18**, 1157-1161 (2000).
129. Dunn, W.B. *et al.* A GC-TOF-MS study of the stability of serum and urine metabolomes during the UK Biobank sample collection and preparation protocols. *Int. J. Epidemiol.* **37**, i23-i30 (2008).
130. Dunn, W.B. *et al.* Procedures for large-scale metabolic profiling of serum and plasma using gas chromatography and liquid chromatography coupled to mass spectrometry. *Nat. Protocols* **6**, 1060-1083 (2011).
131. Wedge, D.C. *et al.* Is Serum or Plasma More Appropriate for Intersubject Comparisons in Metabolomic Studies? An Assessment in Patients with Small-Cell Lung Cancer. *Anal. Chem.* **83**, 6689-6697 (2011).
132. Georgina, A.P. *et al.* Metabolic footprinting as a tool for discriminating between brewing yeasts. *Yeast* **24**, 667-679 (2007).
133. Kopka, J. *et al.* GMD@CSB.DB: the Golm Metabolome Database. *Bioinformatics* **21**, 1635-1638 (2004).
134. Sumner, L. *et al.* Proposed minimum reporting standards for chemical analysis. *Metabolomics* **3**, 211-221 (2007).
135. Steuer, R., Morgenthal, K., Weckwerth, W. & Selbig, J. A Gentle Guide to the Analysis of Metabolomic Data Metabolomics, in, Vol. 358. (ed. J.M. Walker) 105-126 (Humana Press, 2007).
136. Smilde, A.K., van der Werf, M.J., Bijlsma, S., van der Werff-van-der Vat, B.J.C. & Jellema, R.H. Fusion of mass spectrometry-based metabolomics data. *Anal. Chem.* **77**, 6729-6736 (2005).
137. Fenn, J.B., Mann, M., Meng, C.K., Wong, S.F. & Whitehouse, C.M. Electrospray ionization for mass-spectrometry of large biomolecules. *Science* **246**, 64-71 (1989).
138. Li, Q. *et al.* Smad4 inhibits tumor growth by inducing apoptosis in estrogen receptor-alpha-positive breast cancer cells. *J. Biol. Chem.* **280**, 27022-27028 (2005).

139. Makarov, A. Electrostatic Axially Harmonic Orbital Trapping: A High-Performance Technique of Mass Analysis. *Anal. Chem.* **72**, 1156-1162 (2000).
140. Smith, C.A., Want, E.J., O'Maille, G., Abagyan, R. & Siuzdak, G. XCMS: Processing mass spectrometry data for metabolite profiling using Nonlinear peak alignment, matching, and identification. *Anal. Chem.* **78**, 779-787 (2006).
141. Brown, M. *et al.* Automated workflows for accurate mass-based putative metabolite identification in LC/MS-derived metabolomic datasets. *Bioinformatics* **27**, 1108-1112 (2011).
142. Thomson, J.J. Rays of Positive Electricity. *Philosophical Magazine* **20**, 752-767 (1910).
143. Vickerman, J.C. & Briggs, D. *ToF-SIMS: surface analysis by mass spectrometry*. (IM Publications LLP Chichester; 2001).
144. Groenewold, G.S. *et al.* Static SIMS investigation of tetraethylammonium bromide on soil particles using ReO4− and Ga+ projectiles. *Int. J. Mass Spectrom. Ion Processes* **174**, 129-142 (1998).
145. Kotter, F. & Benninghoven, A. Secondary ion emission from polymer surfaces under Ar+, Xe+ and SF5+ ion bombardment. *Appl. Surf. Sci.* **133**, 47-57 (1998).
146. Davies, N. *et al.* Development and experimental application of a gold liquid metal ion source. *Appl. Surf. Sci.* **203-204**, 223-227 (2003).
147. Weibel, D. *et al.* A C60 Primary Ion Beam System for Time of Flight Secondary Ion Mass Spectrometry: Its Development and Secondary Ion Yield Characteristics. *Anal. Chem.* **75**, 1754-1764 (2003).
148. Touboul, D., Kollmer, F., Niehuis, E., Brunelle, A. & Laprévote, O. Improvement of Biological Time-of-Flight-Secondary Ion Mass Spectrometry Imaging with a Bismuth Cluster Ion Source. *J. Am. Soc. Mass. Spectrom.* **16**, 1608-1618 (2005).
149. Wojciechowski, I.A. & Garrison, B.J. Sputtering of water ice induced by C60 bombardment: onset of plume formation. *The Journal of Physical Chemistry A* **110**, 1389-1392 (2005).
150. Russo Jr, M.F., Wojciechowski, I.A. & Garrison, B.J. Sputtering of amorphous ice induced by C60 and Au3 clusters. *Appl. Surf. Sci.* **252**, 6423-6425 (2006).
151. Wucher, A. Molecular secondary ion formation under cluster bombardment: A fundamental review. *Appl. Surf. Sci.* **252**, 6482-6489 (2006).
152. Fletcher, J.S. *et al.* A New Dynamic in Mass Spectral Imaging of Single Biological Cells. *Anal. Chem.* **80**, 9058-9064 (2008).
153. Bagshaw, R.D., Callahan, J.W. & Mahuran, D.J. Desalting of In-Gel-Digested Protein Sample with Mini-C18 Columns for Matrix-Assisted Laser Desorption Ionization Time of Flight Peptide Mass Fingerprinting. *Anal. Biochem.* **284**, 432-435 (2000).
154. Malm, J., Giannaras, D., Riehle, M.O., Gadegaard, N. & SjoÌˆvall, P. Fixation and Drying Protocols for the Preparation of Cell Samples for Time-of-Flight Secondary Ion Mass Spectrometry Analysis. *Anal. Chem.* **81**, 7197-7205 (2009).
155. Jones, E.A., Lockyer, N.P. & Vickerman, J.C. Depth Profiling Brain Tissue Sections with a 40 keV C60+ Primary Ion Beam. *Anal. Chem.* **80**, 2125-2132 (2008).
156. Kotze, H.L. *et al.* ToF-SIMS as a tool for metabolic profiling small biomolecules in cancer systems. *Surf. Interface Anal.*, available online (2012).
157. Winder, C.L., Gordon, S.V., Dale, J., Hewinson, R.G. & Goodacre, R. Metabolic fingerprints of Mycobacterium bovis cluster with molecular type: implications for genotype-phenotype links. *Microbiology* **152**, 2757-2765 (2006).
158. Kim, D.-H. *et al.* Combining metabolic fingerprinting and footprinting to understand the phenotypic response of HPV16 E6 expressing cervical carcinoma cells exposed to the HIV anti-viral drug lopinavir. *Analyst* **135**, 1235-1244 (2010).

159. Martens, H., Nielsen, J.P. & Engelsen, S.B. Light Scattering and Light Absorbance Separated by Extended Multiplicative Signal Correction. Application to Near-Infrared Transmission Analysis of Powder Mixtures. *Anal. Chem.* **75**, 394-404 (2003).
160. Chambers, J., Cleveland, W., Kleiner, B. & Tukey, P. *Graphical Methods for Data Analysis*. (Duxbury Press, Wadsworth; 1983).
161. Hogg, R.V. & Ledolter, J. *Engineering Statistics*. (MacMillan, New York; 1987).
162. Dudoit, S., Shaffer, J.P. & Boldrick, J.C. Multiple hypothesis testing in microarray experiments. *Statistical Science* **18**, 71-103 (2003).
163. Storey, J.D. A direct approach to false discovery rates. *J. Roy. Stat. Soc. Ser. B. (Stat. Method.)* **64**, 479-498 (2002).
164. Benjamini, Y. & Hochberg, Y. Controlling the False Discovery Rate: A Practical and Powerful Approach to Multiple Testing. *Journal of the Royal Statistical Society. Series B (Methodological)* **57**, 289-300 (1995).
165. Nichols, T. & Hayasaka, S. Controlling the familywise error rate in functional neuroimaging: a comparative review. *Stat. Methods Med. Res.* **12**, 419-446 (2003).
166. Thomas, V.P. What's wrong with Bonferroni adjustments. *BMJ* **316**, 1236-1238 (1998).
167. Nakagawa, S. A farewell to Bonferroni: the problems of low statistical power and publication bias. *Behav. Ecol.* **15**, 1044-1045 (2004).
168. Krzanowski, W.J. *Principles of Multivariate Analysis: A User's Perspective*. (Oxford University Press, New York; 1988).
169. Wold, S., Esbensen, K. & Geladi, P. Principal component analysis. *Chemometrics Intellig. Lab. Syst.* **2**, 37-52 (1987).
170. Goodacre, R. *et al.* Proposed minimum reporting standards for data analysis in metabolomics. *Metabolomics* **3**, 231-241 (2007).
171. Fletcher, J.S. *et al.* Rapid discrimination of the causal agents of urinary tract infection using ToF-SIMS with chemometric cluster analysis. *Appl. Surf. Sci.* **252**, 6869-6874 (2006).
172. Tyler, B.J., Rayal, G. & Castner, D.G. Multivariate analysis strategies for processing ToF-SIMS images of biomaterials. *Biomaterials* **28**, 2412-2423 (2007).
173. Alsberg, B.K., Goodacre, R., Rowland, J.J. & Kell, D.B. Classification of pyrolysis mass spectra by fuzzy multivariate rule induction-comparison with regression, K-nearest neighbour, neural and decision-tree methods. *Anal. Chim. Acta* **348**, 389-407 (1997).
174. Rodgers, J.L. & Nicewander, W.A. Thirteen Ways to Look at the Correlation Coefficient. *The American Statistician* **42**, 59-66 (1988).
175. Stuart, A. *Kendall's advanced theory of statistics*. (Griffin, London; 1987).
176. Steuer, R. in Institute of physics, Vol. PhD 130 (University of Potsdam, Potsdam; 2005).
177. Keating, S.M., Bornstein, B.J., Finney, A. & Hucka, M. SBMLToolbox: an SBML toolbox for MATLAB users. *Bioinformatics* **22**, 1275-1277 (2006).
178. Shannon, P. *et al.* Cytoscape: A software environment for integrated models of biomolecular interaction networks. *3rd International Conference on Systems Biology 2002; Dec 13-15; Stockholm, Sweden*, 2498 - 2504 (2002).
179. Cao, M.D. *et al.* Predicting long-term survival and treatment response in breast cancer patients receiving neoadjuvant chemotherapy by MR metabolic profiling. *NMR Biomed.* **25**, 369-378 (2011).
180. Cuperlović-Culf, M., Barnett, D.A., Culf, A.S. & Chute, I. Cell culture metabolomics: applications and future directions. *Drug Discov Today.* **15**, 610-621 (2010).

181. Ahn, W.S. & Antoniewicz, M.R. Metabolic flux analysis of CHO cells at growth and non-growth phases using isotopic tracers and mass spectrometry. *Metab. Eng.* **13**, 598-609 (2011).
182. Pichot, C.S. *et al.* Dasatinib synergizes with doxorubicin to block growth, migration, and invasion of breast cancer cells. *Br. J. Cancer* **101**, 38-47 (2009).
183. Smith, L. *et al.* The analysis of doxorubicin resistance in human breast cancer cells using antibody microarrays. *Mol. Cancer Ther.* **5**, 2115-2120 (2006).
184. Matthews, N.E., Adams, M.A., Maxwell, L.R., Gofton, T.E. & Graham, C.H. Nitric Oxide-Mediated Regulation of Chemosensitivity in Cancer Cells. *J. Natl. Cancer Inst.* **93**, 1879-1885 (2001).
185. Doublier, S. *et al.* HIF-1 activation induces doxorubicin resistance in MCF7 3-D spheroids via P-glycoprotein expression: a potential model of the chemo-resistance of invasive micropapillary carcinoma of the breast. *BMC Cancer* **12**, 4 (2012).
186. Song, X. *et al.* Hypoxia-induced resistance to cisplatin and doxorubicin in non-small cell lung cancer is inhibited by silencing of HIF-1 alpha gene. *Cancer Chemother. Pharmacol.* **58**, 776-784 (2006).
187. Beppu, K., Nakamura, K., Linehan, W.M., Rapisarda, A. & Thiele, C.J. Topotecan Blocks Hypoxia-Inducible Factor-1Î± and Vascular Endothelial Growth Factor Expression Induced by Insulin-Like Growth Factor-I in Neuroblastoma Cells. *Cancer Res.* **65**, 4775-4781 (2005).
188. Calvani, M., Rapisarda, A., Shoemaker, R.H. & Melillo, G. Topotecan inhibits HIF-1{alpha}, but not HIF-2{alpha}, and hypoxia-induced angiogenesis in human endothelial cells. *AACR Meeting Abstracts* **2005**, 263-264 (2005).
189. Lee, K. *et al.* Anthracycline chemotherapy inhibits HIF-1 transcriptional activity and tumor-induced mobilization of circulating angiogenic cells. *Proc. Natl. Acad. Sci. U. S. A.* **106**, 2353-2358 (2009).
190. DiPaola, R.S. To Arrest or Not To G2-M Cell-Cycle Arrest. *Clin. Cancer. Res.* **8**, 3311-3314 (2002).
191. Amellem, O., Loffler, M. & Pettersen, E.O. Regulation of cell-proliferation under extreme and moderate hypoxia - the role of pyrimidine (deoxy)nucleotides. *Br. J. Cancer* **70**, 857-866 (1994).
192. Winder, C.L. *et al.* Global Metabolic Profiling of Escherichia coli Cultures: an Evaluation of Methods for Quenching and Extraction of Intracellular Metabolites. *Anal. Chem.* **80**, 2939-2948 (2008).
193. De Beer, E.L., Bottone, A.E. & Voest, E.E. Doxorubicin and mechanical performance of cardiac trabeculae after acute and chronic treatment: a review. *Eur. J. Pharmacol.* **415**, 1-11 (2001).
194. Goodacre, R. *et al.* Rapid identification of urinary tract infection bacteria using hyperspectral whole-organism fingerprinting and artificial neural networks. *Microbiology* **144**, 1157-1170 (1998).
195. Chouhan, R. & Bajpai, A.K. Real time in vitro studies of doxorubicin release from PHEMA nanoparticles. *Journal of Nanobiotechnology* **7**, 5 (2009).
196. Campbell, J.A. The influence of O2-tension in the inspired air upon the O2-tension in the tissues. *The Journal of Physiology* **60**, 20-29 (1925).
197. Hayflick, L. The limited in vitro lifetime of human diploid cell strains. *Exp. Cell Res.* **37**, 614-636 (1965).
198. Counter, C.M. *et al.* Telomere shortening associated with chromosome instability is arrested in immortal cells which express telomerase activity. *EMBO J.* **11**, 1921-1929 (1992).
199. Harris, A.L. Hypoxia - A key regulatory factor in tumour growth. *Nature Reviews Cancer* **2**, 38-47 (2002).

200. Cortes-Funes, H. & Coronado, C. Role of anthracyclines in the era of targeted therapy. *Cardiovasc. Toxicol.* **7**, 56-60 (2007).
201. Kanehisa, M. *et al.* From genomics to chemical genomics: new developments in KEGG. *Nucleic Acids Res* **34**, D354 - D357 (2006).
202. Bristow, R.G. & Hill, R.P. Hypoxia and metabolism: Hypoxia, DNA repair and genetic instability. *Nat Rev Cancer* **8**, 180-192 (2008).
203. Baggetto, L.G. Deviant energetic metabolism of glycolytic cancer cells. *Biochimie* **74**, 959-974 (1992).
204. Gerweck, L.E., Kozin, S.V. & Stocks, S.J. The pH partition theory predicts the accumulation and toxicity of doxorubicin in normal and low-pH-adapted cells. *Br. J. Cancer* **79**, 838-842 (1999).
205. Triba, M.N. *et al.* Metabolomic profiling with NMR discriminates between biphosphonate and doxorubicin effects on B16 melanoma cells. *NMR Biomed.* **23**, 1009-1016 (2010).
206. Frederiksen, L.J. *et al.* Chemosensitization of Cancer In vitro and In vivo by Nitric Oxide Signaling. *Clin. Cancer. Res.* **13**, 2199-2206 (2007).
207. Bordel, S., Agren, R. & Nielsen, J. Sampling the Solution Space in Genome-Scale Metabolic Networks Reveals Transcriptional Regulation in Key Enzymes. *PLoS Comput Biol* **6**, e1000859 (2010).
208. Voet, D. & Voet, J.G. *Biochemistry*. (John Wiley & Sons, Hoboken; 2004).
209. Tannock, I.F. & Rotin, D. Acid pH in Tumors and Its Potential for Therapeutic Exploitation. *Cancer Res.* **49**, 4373-4384 (1989).
210. Kuhajda, F.P. Fatty-acid synthase and human cancer: new perspectives on its role in tumor biology. *Nutrition* **16**, 202-208 (2000).
211. Baron, A., Migita, T., Tang, D. & Loda, M. Fatty acid synthase: A metabolic oncogene in prostate cancer? *J. Cell. Biochem.* **91**, 47-53 (2004).
212. Hunt, D.A., Lane, H.M., Zygmont, M.E., Dervan, P.A. & Hennigar, R.A. mRNA Stability and Overexpression of Fatty Acid Synthase in Human Breast Cancer Cell Lines. *Anticancer Res.* **27**, 27-34 (2007).
213. Swinnen, J.V. *et al.* Selective activation of the fatty acid synthesis pathway in human prostate cancer. *Int. J. Cancer* **88**, 176-179 (2000).
214. Hochachka, P.W., Rupert, J.L., Goldenberg, L., Gleave, M. & Kozlowski, P. Going malignant: the hypoxia-cancer connection in the prostate. *Bioessays* **24**, 749-757 (2002).
215. Cao, M. *et al.* Prognostic value of metabolic response in breast cancer patients receiving neoadjuvant chemotherapy. *BMC Cancer* **12**, 39 (2012).
216. Abel, K., Anderson, R.A. & Shears, S.B. Phosphatidylinositol and inositol phosphate metabolism. *J. Cell Sci.* **114**, 2207-2208 (2001).
217. Wise, D.R. *et al.* Hypoxia promotes isocitrate dehydrogenase-dependent carboxylation of α-ketoglutarate to citrate to support cell growth and viability. *Proc. Natl. Acad. Sci. U. S. A.* **108** 19611-19616 (2011).
218. Sutherland, G.R., Tyson, R.L. & Auer, R.N. Truncation of the Krebs cycle during hypoglycemic coma. *Medicinal Chemistry* **4**, 379-385 (2008).
219. Gardner, P.R., Raineri, I., Epstein, L.B. & White, C.W. Superoxide Radical and Iron Modulate Aconitase Activity in Mammalian Cells. *J. Biol. Chem.* **270**, 13399-13405 (1995).
220. Matsuno, T. & Goto, I. Glutaminase and Glutamine Synthetase Activities in Human Cirrhotic Liver and Hepatocellular Carcinoma. *Cancer Res.* **52**, 1192-1194 (1992).
221. Mazurek, S. *et al.* Tumor M2-PK and glutaminolytic enzymes in the metabolic shift of tumor cells. *Anticancer Res.* **20**, 5151-5154 (2000).

222. Dang, C.V. Glutaminolysis: Supplying carbon or nitrogen or both for cancer cells? *Cell Cycle* **9**, 3884-3886 (2010).
223. Sato, K. *et al.* Autophagy is activated in colorectal cancer cells and contributes to the tolerance to nutrient deprivation. *Cancer Res.* **67**, 9677-9684 (2007).
224. Bagchi, D., Bagchi, M., Hassoun, E.A., Kelly, J. & Stohs, S.J. Adriamycin-induced hepatic and myocardial lipid peroxidation and DNA damage, and enhanced excretion of urinary lipid metabolites in rats. *Toxicology* **95**, 1-9 (1995).
225. Meliksetian, M.B., Davtyan, T.K., Chirkowa, I.V., Alexanyan, Y.T. & Ignatova, T.N. Alterations in immunoglobulin synthesis during adriamycin-induced apoptosis in mouse hybridoma cells. *Cell Biol. Int.* **21**, 69-74 (1997).
226. Broxterman, H.J., Pinedo, H.M., Kuiper, C.M., Schuurhuis, G.J. & Lankelma, J. Glycolysis in p-glycoprotein-overexpressing human-tumor cell-lines - effects of resistance-modifying agents. *FEBS Lett.* **247**, 405-410 (1989).
227. Friedman, M. The Use of Ranks to Avoid the Assumption of Normality Implicit in the Analysis of Variance. *Journal of the American Statistical Association* **32**, 675-701 (1937).
228. Baslow, M.H. N-Acetylaspartate in the Vertebrate Brain: Metabolism and Function. *Neurochem. Res.* **28**, 941-953 (2003).
229. Baslow, M.H. & Yamada, S. Identification of N-acetylaspartate in the Lens of the Vertebrate Eye: A New Model for the Investigation of the Function of N-acetylated Amino Acids in Vertebrates. *Exp. Eye Res.* **64**, 283-286 (1997).
230. Kolwijck, E. *et al.* N-acetyl resonances in in vivo and in vitro NMR spectroscopy of cystic ovarian tumors. *NMR Biomed.* **22**, 1093-1099 (2009).
231. Boss, E.A. *et al.* High-resolution proton nuclear magnetic resonance spectroscopy of ovarian cyst fluid. *NMR Biomed.* **13**, 297-305 (2000).
232. Sauer, H., Putz, V., Fischer, K., Hescheler, J. & Wartenberg, M. Increased doxorubicin uptake and toxicity in multicellular tumour spheroids treated with DC electrical fields. *Br. J. Cancer* **80**, 1204-1213 (1999).
233. Sadzuka, Y., Yamashita, Y. & Sonobe, T. Effects of Glutamate Transporter Inhibitors on the Antitumor Activity of Doxorubicin. *Clin. Cancer. Res.* **8**, 3943-3947 (2002).
234. Hao, X.-Y., Bergh, J., Brodin, O., Heltman, U. & Mannervik, B. Acquired resistance to cisplatin and doxorubicin in a small cell lung cancer cell line is correlated to elevated expression of glutathione-linked detoxification enzymes. *Carcinogenesis* **15**, 1167-1173 (1994).
235. Poirson-Bichat, F., Gonçalves, R.A.B., Miccoli, L., Dutrillaux, B. & Poupon, M.F. Methionine Depletion Enhances the Antitumoral Efficacy of Cytotoxic Agents in Drug-resistant Human Tumor Xenografts. *Clin. Cancer. Res.* **6**, 643-653 (2000).
236. James, S.J., Miller, B.J., McGarrity, L.J. & Morris, S.M. The effect of folic acid and/or methionine deficiency on deoxyribonucleotide pools and cell cycle distribution in mitogen-stimulated rat lymphocytes. *Cell Prolif.* **27**, 395-406 (1994).
237. Kotlyar, A.B. & Vinogradov, A.D. Interaction of the membrane-bound succinate dehydrogenase with substrate and competitive inhibitors. *Biochim. Biophys. Acta* **784**, 24-34 (1984).
238. Longnus, S.L., Wambolt, R.B., Barr, R.L., Lopaschuk, G.D. & Allard, M.F. Regulation of myocardial fatty acid oxidation by substrate supply. *Am J Physiol Heart Circ Physiol.* **281**, H1561-H1567 (2001).
239. Hulbert, A.J. Life, death and membrane bilayers. *J. Exp. Biol.* **206**, 2303-2311 (2003).
240. Caron, R.M. & Hamilton, J.W. Developmentally specific effects of the DNA cross-linking agent mitomycin C on phosphoenolpyruvate carboxykinase gene expression

in vivo: Correlation with changes in chromatin structure within the promoter region of the gene. *J. Biochem. Mol. Toxicol.* **12**, 325-337 (1998).
241. Ihnat, M.A. *et al.* Suppression of P-glycoprotein expression and multidrug resistance by DNA cross-linking agents. *Clin. Cancer. Res.* **3**, 1339-1346 (1997).
242. Aruoma, O.I., Halliwell, B., Hoey, B.M. & Butler, J. The antioxidant action of taurine, hypotaurine and their metabolic precursors. *Biochem. J* **256**, 251-255 (1988).
243. Wang, J. *et al.* Dependence of Mouse Embryonic Stem Cells on Threonine Catabolism. *Science* **325**, 435-439 (2009).
244. Hanahan, D. & Weinberg, R.A. The Hallmarks of Cancer. *Cell* **100**, 57-70 (2000).
245. Hanahan, D. & Weinberg, Robert A. Hallmarks of Cancer: The Next Generation. *Cell* **144**, 646-674 (2011).
246. Weckwerth, W. & Fiehn, O. Can we discover novel pathways using metabolomic analysis? *Curr. Opin. Biotechnol.* **13**, 156-160 (2002).
247. Barabasi, A.-L., Gulbahce, N. & Loscalzo, J. Network medicine: a network-based approach to human disease. *Nat Rev Genet* **12**, 56-68 (2011).
248. Tomaiuolo, M., Bertram, R. & Houle, D. Enzyme isoforms may increase phenotypic robustness. *Evolution* **62**, 2884-2893 (2008).
249. Warburg, O. Origin of cancer cells. *Science* **123**, 309-314 (1956).
250. Ullah, M.S., Davies, A.J. & Halestrap, A.P. The plasma membrane lactate transporter MCT4, but not MCT1, is up-regulated by hypoxia through a HIF-1 alpha-dependent mechanism. *J. Biol. Chem.* **281**, 9030-9037 (2006).
251. Gnanapragasam, A. *et al.* Adriamycin induced myocardial failure in rats: protective role of Centella asiatica. *Mol. Cell. Biochem.* **294**, 55-63 (2007).
252. Zeng, L. *et al.* Saturated Fatty Acids Modulate Cell Response to DNA Damage: Implication for Their Role in Tumorigenesis. *Plos One* **3**, e2329 (2008).
253. Sasaki, T., Holeyfield, K.C. & Uitto, J. Doxorubicin-induced inhibition of prolyl hydroxylation during collagen biosynthesis in human skin fibroblast cultures. Relevance to imparied wound healing. *The Journal of Clinical Investigation* **80**, 1735-1741 (1987).
254. Phang, J.M., Donald, S.P., Pandhare, J. & Liu, Y.M. The metabolism of proline, a stress substrate, modulates carcinogenic pathways. *Amino Acids* **35**, 681-690 (2008).
255. Spivey, K.A. *et al.* A role for collagen XXIII in cancer cell adhesion, anchorage-independence and metastasis. *Oncogene* **31**, 2362-2372 (2012).
256. Majumdar, S., Gunda, S., Pal, D. & Mitra, A.K. Functional Activity of a Monocarboxylate Transporter, MCT1, in the Human Retinal Pigmented Epithelium Cell Line, ARPE-19. *Mol. Pharm.* **2**, 109-117 (2005).
257. Sonveaux, P. *et al.* Targeting lactate-fueled respiration selectively kills hypoxic tumor cells in mice. *The Journal of Clinical Investigation* **118**, 3930-3942 (2008).
258. Jukanti, R., Devraj, G., Shashank, A.S. & Devraj, R. Biodistribution of ascorbyl palmitate loaded doxorubicin pegylated liposomes in solid tumor bearing mice. *J. Microencapsulation* **28**, 142-149 (2011).
259. Brown, A., van den Berg, J.A. & Vickerman, J.C. The application of secondary Ion mass spectrometry to surface analysis of semiconductor substrates and devices. *Surf. Interface Anal.* **9**, 309-317 (1986).
260. Brown, A. & Vickerman, J.C. A comparison of positive and negative ion static SIMS spectra of polymer surfaces. *Surf. Interface Anal.* **8**, 75-81 (1986).
261. Carado, A. *et al.* C60 Secondary Ion Mass Spectrometry with a Hybrid-Quadrupole Orthogonal Time-of-Flight Mass Spectrometer. *Anal. Chem.* **80**, 7921-7929 (2008).
262. Passarelli, M.K. & Winograd, N. Lipid imaging with time-of-flight secondary ion mass spectrometry (ToF-SIMS). *Biochim. Biophys. Acta* **1811**, 976-990 (2011).

263. Vickerman, J.C., Briggs, D. & Henderson, A. *The Static SIMS Library version 4* (Surfacespectra Ltd, Manchester; 2006).
264. Horai, H. *et al.* MassBank: a public repository for sharing mass spectral data for life sciences. *J. Mass Spectrom.* **45**, 703-714 (2010).
265. Jones, E.A., Lockyer, N.P. & Vickerman, J.C. Suppression and enhancement of non-native molecules within biological systems. *Appl. Surf. Sci.* **252**, 6727-6730 (2006).
266. Fletcher, J.S., Kotze, H.L., Armitage, E.G., Lockyer, N.P. & Vickerman, J.C. Time-of-Fight Secondary Ion Mass Spectrometry for Metabolomics – An Assessment of the Challenges for Metabolite Identification and Quantification. *Metabolomics (Submitted)* (2012).
267. Barnes, C.A. *et al.* Identifying Individual Cell Types in Heterogeneous Cultures Using Secondary Ion Mass Spectrometry Imaging with C60 Etching and Multivariate Analysis. *Anal. Chem.* **84**, 893-900 (2012).
268. Li, J. *et al.* Purification, identification and profiling of serum amyloid A proteins from sera of advanced-stage cancer patients. *Journal of Chromatography B-Analytical Technologies in the Biomedical and Life Sciences* **889**, 3-9 (2012).
269. Erve, J.C.L., Beyer, C.E., Manzino, L. & Talaat, R.E. Metabolite identification in rat brain microdialysates by direct infusion nanoelectrospray ionization after desalting on a ZipTip and LTQ/Orbitrap mass spectrometry. *Rapid Commun. Mass Spectrom.* **23**, 4003-4012 (2009).
270. Wartenberg, M. *et al.* Reactive oxygen species-linked regulation of the multidrug resistance transporter P-glycoprotein in Nox-1 overexpressing prostate tumor spheroids. *FEBS Lett.* **579**, 4541-4549 (2005).
271. Roberts, D.L. *et al.* Contribution of HIF-1 and drug penetrance to oxaliplatin resistance in hypoxic colorectal cancer cells. *Br. J. Cancer* **101**, 1290-1297 (2009).
272. Piwowar, A.M., Lockyer, N.P. & Vickerman, J.C. Salt Effects on Ion Formation in Desorption Mass Spectrometry: An Investigation into the Role of Alkali Chlorides on Peak Suppression in Time-of-Flight-Secondary Ion Mass Spectrometry. *Anal. Chem.* **81**, 1040-1048 (2009).
273. Berman, E.S.F. *et al.* Preparation of single cells for imaging/profiling mass spectrometry. *J. Am. Soc. Mass. Spectrom.* **19**, 1230-1236 (2008).
274. Nygren, H. *et al.* A cell preparation method allowing subcellular localization of cholesterol and phosphocholine with imaging TOF-SIMS. *Colloids Surf. B. Biointerfaces* **30**, 87-92 (2003).
275. Ivascu, A. & Kubbies, M. Rapid Generation of Single-Tumor Spheroids for High-Throughput Cell Function and Toxicity Analysis. *J. Biomol. Screen.* **11**, 922-932 (2006).
276. Smith, C.A. *et al.* METLIN - A metabolite mass spectral database. *Ther. Drug Monit.* **27**, 747-751 (2005).
277. Perkins, D.N., Pappin, D.J.C., Creasy, D.M. & Cottrell, J.S. Probability-based protein identification by searching sequence databases using mass spectrometry data. *Electrophoresis* **20**, 3551-3567 (1999).
278. Garrison, B.J. & Postawa, Z. Computational view of surface based organic mass spectrometry. *Mass Spectrom. Rev.* **27**, 289-315 (2008).
279. Leggett, G.J., Vickerman, J.C., Briggs, D. & Hearn, M.J. Surface studies by static secondary ion mass spectrometry: cluster ion formation studied by tandem mass-spectrometric techniques. *J. Chem. Soc., Faraday Trans.* **88**, 297-309 (1992).
280. Munger, J. *et al.* Systems-level metabolic flux profiling identifies fatty acid synthesis as a target for antiviral therapy. *Nat Biotech* **26**, 1179-1186 (2008).
281. Halama, A., Moller, G. & Adamski, J. Metabolic Signatures in Apoptotic Human Cancer Cell Lines. *Omics-a Journal of Integrative Biology* **15**, 325-335 (2011).

282. Psychogios, N. *et al.* The Human Serum Metabolome. *Plos One* **6**, e16957 (2011).
283. Smith, D.F., Robinson, E.W., Tolmachev, A.V., Heeren, R.M.A. & Pasa-Tolic, L. C-60 Secondary Ion Fourier Transform Ion Cyclotron Resonance Mass Spectrometry. *Anal. Chem.* **83**, 9552-9556 (2011).
284. Tupper, J., Greco, O., Tozer, G.M. & Dachs, G.U. Analysis of the horseradish peroxidase//indole-3-acetic acid combination in a three-dimensional tumor model. *Cancer Gene Ther.* **11**, 508-513 (2004).
285. Monazzam, A. *et al.* Application of the multicellular tumour spheroid model to screen PET tracers for analysis of early response of chemotherapy in breast cancer. *Breast Cancer Res.* **9**, R45 (2007).
286. Varia, M.A. *et al.* Pimonidazole: A Novel Hypoxia Marker for Complementary Study of Tumor Hypoxia and Cell Proliferation in Cervical Carcinoma. *Gynecol. Oncol.* **71**, 270-277 (1998).